On the Changing Upper-Ocean Stratification - Trends and Variability of the Upper-Ocean Structure during the Argo Observation Period

Dissertation

zur Erlangung des Doktorgrades

der Mathematisch-Naturwissenschaftlichen Fakultät
der Christian-Albrechts-Universität zu Kiel

vorgelegt von

Marisa Roch

Kiel, 2023

GEOMAR
Helmholtz-Zentrum für Ozeanforschung Kiel

CAU
Christian-Albrechts-Universität zu Kiel

Erster Gutachter:	Prof. Dr. Peter Brandt
Zweiter Gutachter:	Prof. Dr. Arne Biastoch

Tag der mündlichen Prüfung:	18.12.2023

Abstract

The warming climate is causing an increasing ocean stratification as a consequence of intensified ocean surface warming. Changes in ocean stratification affect, e.g., ocean ventilation, mixed layer entrainment, heat exchange and air-sea interactions. In turn, stratification changes play a role for carbon uptake, oxygen distribution and nutrient fluxes which are crucial for marine ecosystems. However, it is still uncertain how exactly these physical and biological processes will be affected. Additionally, the effects of stratification changes probably vary from region to region.

This thesis addresses the recent decadal changes of the upper-ocean structure by focusing on the ocean surface mixed layer as well as the vertical stratification maximum. As a boundary between the atmosphere and the upper-ocean, the ocean surface mixed layer plays a crucial role in setting up the upper-ocean structure. Below the mixed layer, the vertical stratification maximum acts as a gateway between the upper-ocean and the ocean interior.

Taking advantage of the excessive Argo observation dataset from 2006-2022, it is possible to examine the decadal variability and recent changes of the upper-ocean for the period of the most intense warming to-date. In particular, the southeastern tropical Atlantic Ocean (10°S-20°S, 5°W-15°E) shows a continuous warming and freshening trend of the mixed layer for the time period of 2006-2020. The resulting surface density reduction influences the upper-ocean stratification that is found to strengthen by 30 % in this region. Consequently, the stratification is observed to shift from a subtropical stratification toward a more tropical stratification with warmer and fresher surface waters and a subsurface salinity maximum. Additionally, wind stress curl-induced isopycnal heave, generating squeezing of density layers, contributes to the increasing upper-ocean stratification. This region in the southeastern tropical Atlantic is of great interest as it contains a high-productive marine ecosystem. Possible consequences for the productivity and fish species off Angola and Namibia are discussed.

Based on the method introduced for evaluating upper-ocean stratification changes in the southeastern tropical Atlantic, a procedure is developed to determine the vertical stratification maximum from the Argo array. The Argo observation dataset allows for investigating changes of the mixed layer and the vertical stratification maximum on global scales. The observations from 2006-2021 suggest highly variable signals among different regions. Nevertheless, a general statement can be made, indicating an increasing summer stratification maximum in the Northern and Southern Hemispheres, while the winter stratification maximum only strengthens in the Northern Hemisphere. On global average, the summer and winter vertical stratification maxima are observed to intensify by 7-8 % during the period of 2006-2021, proposing a de-coupling of the upper-ocean from the ocean interior. The intensifying stratification is found to be accommmpanied by mainly a warmer and partly fresher mixed layer. Although the mixed layer is warming in most areas, the global mixed layer is found to deepen by $4\,m$. Most reasonable causes are changes in the wind parameters. Within this thesis a data product of the global ocean's vertical stratification maximum is created, representing the current mean state as well as recent changes during the hitherto most intense warming period. This product can be used for investigating discrepancies between observations and models.

Changes in the upper-ocean structure have an impact on the potential vorticity of the water column. The northeastern tropical Atlantic encompasses a region of high potential vorticity which plays an important role for the size of the exchange window between the subtropical-tropical oceans, as a part of the subtropical cell. This thesis establishes a relation between the decadal variability of North Atlantic Oscillation and the zone of high potential vortictiy. During positive phases of the North Atlantic Oscillation, intensified trade winds result in isopycnal heave and squeezing of density layers. Thereby, the potential vorticity is strengthened. Analyses of the Sverdrup streamfunction and geostrophic velocities within the thermocline layer indicate enhanced flow via the western boundary toward the equator while the velocities in the ocean interior are reduced. At the same time, the intensified trade winds during the positive phase of the North Atlantic Oscillation result in a strengthening Equatorial Undercurrent as observed from the mooring site at 0°, 23°W as well as higher subduction rates of the density range supplied into the Equatorial Undercurrent.

This thesis aims to enrich the knowledge on the changing upper-ocean structure. As there are still many open questions, it is important to not only study long-term climate change signals but also improve our understanding of changes happening on decadal timescales.

Zusammenfassung

Die Klimaerwärmung verursacht eine sich verstärkende Schichtung des Ozeans als Folge der stärker werdenden Erwärmung der Oberfläche des Ozeans. Änderungen in der Ozeanschichtung können unter anderem die Ventilation des Ozeans, die Deckschichtentstehung, den Wärmeaustausch und die Wechselwirkung von Ozean und Atmosphäre beeinflussen. Daher spielen Änderungen der Schichtung eine große Rolle für die Aufnahme von Kohlenstoff, die Sauerstoffverteilung und Nährstoffflüsse, welche entscheidend für marine Ökosysteme sind. Allerdings ist es immer noch unsicher, wie genau diese physikalischen und biologischen Prozesse beeinflusst werden. Hinzukommt, dass die Effekte womöglich von Region zu Region verschieden sind.

Diese Thesis befasst sich mit den jüngsten dekadischen Änderungen der Struktur des oberen Ozeans. Der Fokus liegt hierbei auf der ozeanischen Deckschicht sowie dem vertikalen Schichtungsmaximum. Die ozeanische Deckschicht spielt als Grenze zwischen der Atmosphäre und dem oberen Ozean eine entscheidene Rolle darin, die Struktur des oberen Ozeans zu bestimmen. Unterhalb der Deckschicht befindet sich das vertikale Schichtungsmaximum, welches als Gateway zwischen dem oberen Ozean und dem tiefen Ozean agiert.

Unter Nutzung des umfangreichen Argo-Beobachtungsdatensatzes von 2006-2022 ist es möglich, die dekadische Variabilität und die jüngsten Veränderungen des oberen Ozeans für die Zeitperiode der bis heute stärksten Erwärmung zu untersuchen. Insbesondere zeigt der südöstliche tropische Atlantik (10°S-20°S, 5°W-15°E) einen kontinuierlichen Trend hin zu einer wärmeren und frischeren Deckschicht für die Zeit von 2006-2020. Die daraus resultierende Dichtereduktion beeinflusst die Schichtung des oberen Ozeans, welche in dieser Region um 30 % angestiegen ist. Infolgedessen wurde beobachtet, dass sich die ursprüngliche subtropische Schichtung zu einer tropischen Schichtung verschiebt. Das bedeutet, dass an der Oberfläche wärmeres und frischeres Wasser ist und dass unterhalb der Oberfläche sich ein Salzmaximum befindet. Weiter wurde durch Wind-Stress-Curl hervorgerufenes Anheben der Dichteflächen eine Stauchung der Dichteschichten verursacht, was wiederherum zu der Stärkung der Schichtung des oberen Ozeans beigetragen hat. Diese Region im südöstlichen tropischen Atlantik ist von großem Interesse, da es sich hier um ein sehr produktives marines Ökosystem handelt. Mögliche Konsequenzen für die Produktivität und die Fischarten vor Angola und Namibia werden diskutiert.

Basierend auf der zuvor genutzten Methode um Schichtungsänderungen im oberen Ozean des südöstlichen tropischen Atlantiks zu untersuchen, wurde ein Verfahren weiterentwickelt, um das Schichtungsmaximum mit dem Argo Array zu bestimmen. Der Argo-Beobachtungsdatensatz erlaubt die Untersuchung von Änderungen der Deckschicht sowie des vertikalen Schichtungsmaximums auf globalen Skalen. Die Beobachtung von 2006-2021 zeigen regional sehr variierende Signale. Nichtsdestotrotz kann eine generelle Aussage getroffen werden, dass das Sommer-Schichtungsmaximum in der Nord- und Südhemisphäre stärker wird, während das Winter-Schichtungsmaximum nur in der Nordhemisphäre zunimmt. Im globalen Mittel wird von 2006-2021 eine Zunahme von 7-8 % des Sommer- und auch Winter-Schichtungsmaximums beobachtet. Dies deutet auf eine Entkopplung des oberen Ozeans vom tiefen Ozean hin. Die sich verstärkende Schichtung geht vor allem mit einer wärmeren und teilweise frischeren Deckschicht einher. Obwohl die Deckschicht in fast allen Regionen wärmer wird, vertieft die globale Deckschicht sich um $4\,m$. Die plausibelsten Gründe dafür sind Änderungen in den Wind Parametern. Innerhalb dieser Arbeit wird ein Datenprodukt des globalen vertikalen Schichtungsmaximums kreiert, welches den aktuellen mittleren Zustand sowie die jüngsten Änderungen in der bis heute stärksten Erwärmungsperiode beschreibt. Dieses Produkt kann genutzt werden, um die Unterschiede zwischen Beobachtungen und Modellen zu untersuchen.

Änderungen in der Struktur des oberen Ozeans haben einen Einfluss auf die potentielle Wirbelstärke der Wassersäule. Im nordöstlichen tropischen Atlantik gibt es eine Region mit hoher potentieller Wirbelstärke, welche für die Größe des Austauschfensters zwischen dem subtropischen und dem tropischen Ozean als Teil der Subtropischen Zelle eine große Rolle spielt. Diese Thesis findet eine Verbindung zwischen der dekadischen Variabilität der Nordatlantischen Oszillation und der Region mit hoher potentieller Wirbelstärke. Während der positiven Phasen der Nordatlantischen Oszillation sorgen stärkere Passatwinde zu einer Anhebung von Isopyknen, was zu einer Stauchung der Dichteflächen führt. Dadurch verstärkt sich die potentielle Wirbelstärke. Analysen der Sverdrup Stromfunktion und der geostrophischen Gechwindigkeiten in der Thermoklinenschicht weisen auf eine erhöhten Strömung entlang des westlichen Randes zum Äquator hin, während die Geschwindigkeiten in der Mitte des Ozeans geschwächt sind. Gleichzeitig sorgen die stärkeren Passatwinde während der positiven Phase der Nordatlantischen Oszillation für einen zunehmenden Äquatorialen Unterstrom. Dies wird mithilfe von Verankerungsdaten bei $0^\circ, 23^\circ$W beobachtet. Außerdem werden höhere Subduktionsraten des Dichtebereichs gefunden, welcher den Äquatorialen Unterstrom speist.

Ziel dieser Arbeit ist es, das Wissen über die sich änderende Struktur des oberen Ozeans zu erweitern. Da es immer noch viele offene Fragen zu diesem Thema gibt, ist es wichtig nicht nur die Langzeit-Klimaänderungen zu untersuchen, sondern auch das Verständnis von Änderungen auf dekadischen Zeitskalen zu verbessern.

Contents

List of Figures

List of Abbreviations

ABF	Angola-Benguela Front
AC	Angola Current
ADCP	Acoustic Doppler current profiler
ALACE	Autonomous Lagrangian Circulation Explorer
AMOC	Atlantic Meridional Overturning Circulation
ASCAT	Advanced Scatterometer
BCC	Benguela Coastal Current
BGC	BioGeoChemical
BLLCJ	Benguela low-level Coastal Jet
BOC	Benguela Oceanic Current
CMEMS	Copernicus Marine Environmental Monitoring Service
CMIP	Coupled Model Intercomparison Project
CTD	Conductivity-Temperature-Depth
CTW	Coastally Trapped Wave
COM	Climate Observations and Monitoring
ENSO	El Niño-Southern Oscillation
EOF	Empirical Orthogonal Function
ERA-I	ECMWF Re-Analysis Interim
EUC	Equatorial Undercurrent
GCUC	Gabun-Congo Undercurrent
GPCP	Global Precipitation Climatology Project
GSW	Gibbs SeaWater
IPSL	Institut Pierre Simon Laplace
IQR	Interquartile range
IRD	Institut de Recherche pour le Développement
JAS	July-September
JFM	January-March
ML	Mixed Layer
MLD	Mixed Layer Depth
MLPD	Mixed Layer Potential Density
MLS	Mixed Layer Salinity
MLT	Mixed Layer Temperature
NAO	North Atlantic Oscillation
NBC	North Brazil Current
NBUC	North Brazil Undercurrent
NEC	North Equatorial Current
NECC	North Equatorial Countercurrent
NEUC	North Equatorial Undercurrent
NPP	Net primary production
nSEC	Northern branch of the South Equatorial Current
OAFlux	Objectively Analyzed air-sea fluxes
ONI	Ocean Niño Index
PC	Principle Component
pchip	piecewise cubic Hermite interpolating polynomial
PV	Potential Vorticity
SACW	South Atlantic Central Water
SAOD	South Atlantic Ocean Dipole
SASH	South Atlantic Subtropical High
SEC	South Equatorial Current
SECC	South Equatorial Countercurrent
SETA	Southeastern tropical Atlantic Ocean
SEUC	South Equatorial Undercurrent
SST	Sea Surface Temperature
sSEC	Southern branch of the South Equatorial Current
STC	Subtropical Cells
T-S	Temperature-Salinity
VGPM	Vertically Generalized Production Model
WHOI	Woods Hole Oceanographic Institution
WOCE	World Ocean Circulation Experiment

Chapter 1

Introduction

Covering 71 % of the Earth's surface, the ocean plays an important role in the climate system. The ocean interacts with the atmosphere, exchanging heat, freshwater and momentum, forcing climate variability on a variety of scales. In particular, the upper-ocean is a crucial element in this connection, as it represents a gateway between the atmosphere and the ocean interior affecting physical as well as biogeochemical processes. The development of the upper-ocean density structure is involved in various processes: heat and freshwater fluxes, diffusive and turbulent mixing, convection, upwelling and downwelling processes, advection of water mass characteristics due to the wind-driven and general circulation as well as internal waves, Rossby and Kelvin waves (Fiedler et al., 2013). The upper-ocean density structure modulates vertical mixing (Cronin et al., 2013) and thus, it is crucial for the formation of the surface mixed layer (e.g., Yamaguchi and Suga, 2019). The mixed layer, limited by the atmosphere at the top and by a density gradient at the base of the mixed layer, influences ocean ventilation and thereby, regulates exchanges of heat, freshwater, oxygen and carbon (e.g., Bopp et al., 2015; Schmidtko et al., 2017; Oschlies et al., 2018). The upper-ocean structure is also important for the biological productivity as it determines how much light is available for photosynthesis but also regulates the nutrient flux from below to the euphotic zone (e.g., Falkowski et al., 1998; Echevin et al., 2008; Xue et al., 2022). Changes in the upper-ocean structure can therefore impact a variety of processes. Knowing and understanding the physical changes in the upper-ocean structure is vital, in order to specify possible consequences as a result of the on-going climate warming.

In the following, drivers of the large-scale circulation are introduced in Section 1.1. In Section 1.2 the upper-ocean structure, including the surface mixed layer and pycnocline layer, is described and in Section 1.3 climate variability is presented. Finally, the motivation, objectives and outline of this thesis are portrayed in Section 1.4

1.1 What drives the large-scale ocean circulation?

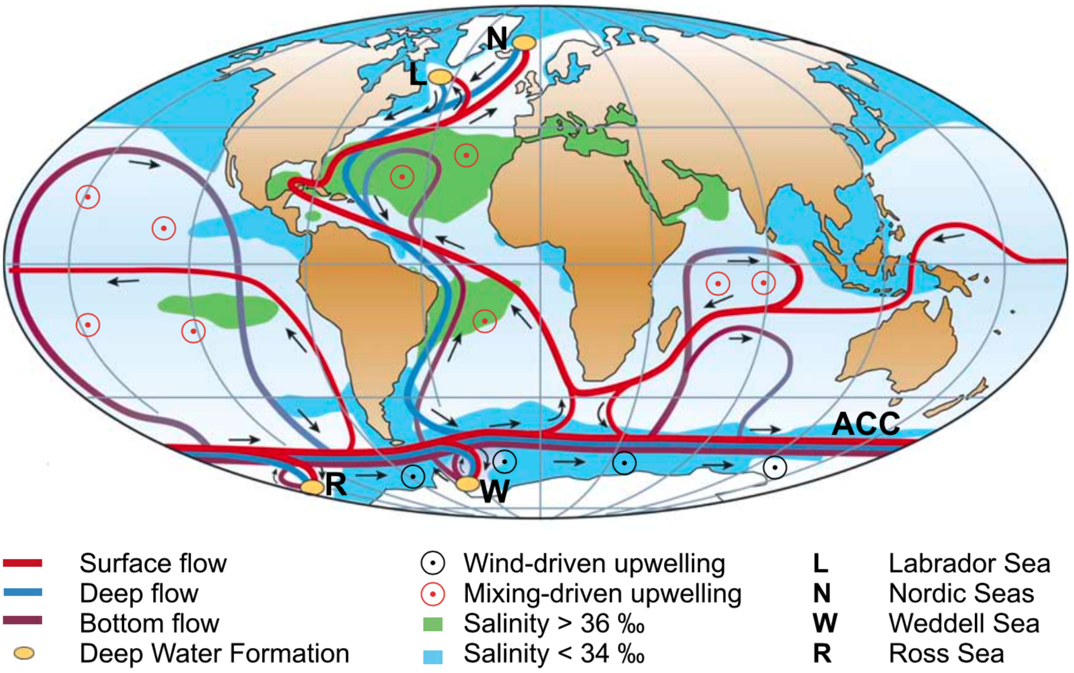

Figure 1.1: Schematic representing the *Great Conveyer Belt*. Deep water formation regions are marked by yellow dots (Labrador Sea, Nordic Seas, Weddel Sea and Ross Sea). The Atlantic depicts a northward flow of warm and saline waters to the Labrador Sea and Nordic Seas, where deep water masses are formed which then return southward. In the Ross Sea and Weddel Sea, additional deep water is formed which is denser than the North Atlantic Deep Water and, hence, recirculates at even greater depth. The schematic is created by Rahmstorf (2002) and adapted by Kuhlbrodt et al. (2007).

Many different processes can move oceanic water masses including wind-driven and thermohaline processes on larger scale but also tidal and gravitational forces. Coupled to atmospheric forcings via buoyancy fluxes (heat and freshwater fluxes), the thermohaline circulation is driven by density differences (Rahmstorf, 2002). In the Atlantic Ocean, as a part of the thermohaline circulation, warm and saline waters are transported northward (red line in Figure 1.1) in the upper-ocean to the formation regions of deep water in the North Atlantic: the Labrador Sea and Nordic Seas (yellow dots in Figure 1.1, Rahmstorf (2002); Kuhlbrodt et al. (2007); Lumpkin and Speer (2007)). In these regions, sea ice forms which increases salinity of the surrounding water. This contributes to a great density increase as a result of large oceanic heat loss to the atmosphere. Due to larger density at the surface, the water column starts to overturn (i.e., convect), deep water masses (North Atlantic Deep Water) are formed and return southward at depth (blue line in Figure 1.1). More deep water is formed in the Southern Ocean in the Weddell Sea and Ross Sea (Antarctic Bottom Water). This water mass is denser and thus, spreads even deeper in the ocean basins than the North Atlantic Deep Water (purple line in Figure 1.1) (Rahmstorf, 2002; Kuhlbrodt et al., 2007; Lumpkin and Speer, 2007).

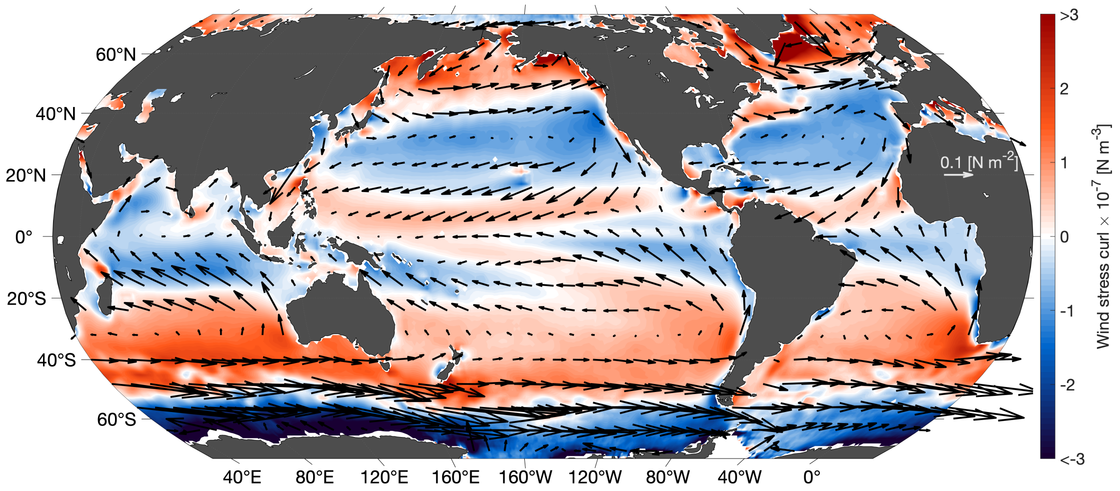

Figure 1.2: Mean wind stress curl (color shading) and mean absolute wind stress (arrows) for the period of 2007-2022. Monthly wind stress data is taken from E. U. Copernicus Marine Environmental Monitoring Service (CMEMS). Blue shading in Northern Hemisphere denotes areas of negative wind stress curl and therefore, downward Ekman pumping. Red shading in Northern Hemisphere shows positive wind stress curl and thus, upward Ekman suction. In the Southern Hemisphere the signs are reversed: positive wind stress curl generates downward Ekman pumping, and negative wind stress curl produces upward Ekman suction.

The upper-ocean circulation, however, is mainly wind-driven and wind stress, the force of wind acting on the ocean surface, is probably the most crucial force generating ocean circulation (Huang, 2010a). Examples for wind-driven circulations are the large-scale gyres in the subtropical and polar regions. Large-scale wind stress patterns are dominated by easterly trade winds in the subtropics north and south of the equator (Figure 1.2). Poleward of the trade winds, strong westerlies can be found in the mid-latitudes (Figure 1.2). While the trade wind system is rather steady, the westerlies are more variable. Wind stress curl creates zones of convergence and divergence of water, so-called Ekman convergence/divergence (Figure 1.2), which then in turn, produce interior equatorward and poleward transport of water (referred to as Sverdrup transport), respectively. The subtropical oceans are dominated by Ekman convergence zones which result in downwelling of water from the ocean surface down to the interior. Ekman divergence zones are found in the subpolar regions, which generate upwelling of water from below to the surface. These upwelling and downwelling processes are described as Ekman suction and Ekman pumping, respectively.

1.2 Vertical Structure of the Upper-Ocean

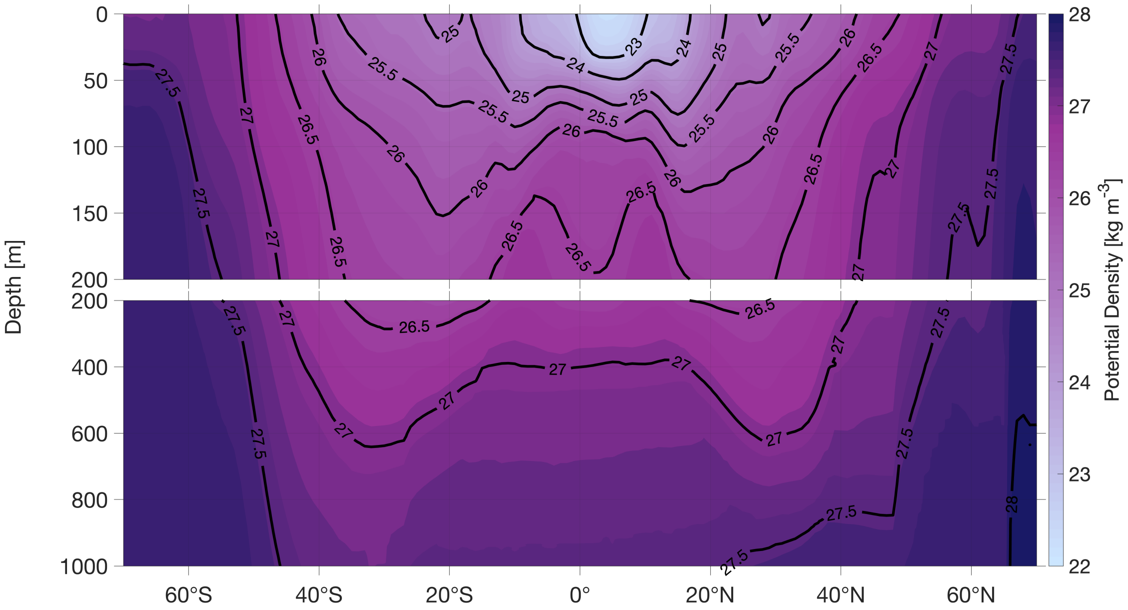

Figure 1.3: Zonal mean potential density section of the upper 1000 *m* in the Atlantic Ocean. This graph is obtained from the Argo observation dataset for the time period of 2006-2021 (Argo, 2021).

The ocean is stratified in density in the vertical. A water column is stable stratified when water with lower density can be found on top of water with higher density. In most of the world ocean's, the density structure is mainly regulated by the vertical structure of temperature (Sprintall and Cronin, 2009; Talley et al., 2011e). As most of the solar heat enters the ocean surface, the surface layer of the ocean is warmer and less dense than the deep ocean (cf. zonal mean potential density field of the Atlantic Ocean in Figure 1.3) and as a consequence of the continuous input of solar radiation, a stable ocean stratification is maintained. A stable stratification affects vertical mixing: the larger the vertical density gradient and hence the higher the stratification is, the more difficult it is to mix the water column and layers of large gradients act as barriers. Therefore, ocean stratification can modulate the vertical exchange of heat, oxygen, carbon and nutrients (Rhein et al., 2013; Li et al., 2020; Keeling et al., 2010; DeVries et al., 2017). Consequently, stratification has an influence on biological productivity, phytoplankton abundance as well as fisheries (Lozier et al., 2011; Fiedler et al., 2013; Llort et al., 2019).

Due to excess solar heating in the tropics and oceanic heat loss at the poles, the tropical oceans contain lighter surface waters than the higher latitudes (Figure 1.3). The regions are, however, connected via the isopycnal surfaces: Water masses are formed at the ocean surface via air-sea interactions and then follow isopycnal surfaces into the deep ocean, subduct underneath lighter isopycnals and bend toward the equator. This is the basic concept of the cold water sphere subducting underneath the warm water sphere, following Wüst (1949). The region, where isopycnals are reaching the surface are so-called isopycnal outcrops. Typically, the isopycnals feature a bowl-shape in the upper-ocean in the subtropics, indicating the presence of the wind-driven subtropical gyres and subtropical convergence zones (Figure 1.2, 1.3).

Based on the density stratification, the ocean can be separated into several types of layers: the surface mixed layer, a so-called pycnocline layer and the deep ocean (Sprintall and Cronin, 2009; Talley et al., 2011e). In the following, the mixed layer and the pycnocline layer are described in more detail.

1.2.1 Mixed Layer

At the ocean surface, there exists the surface mixed layer, which is the upper boundary layer connecting the upper-ocean with the atmosphere. In the mixed layer, water mass characteristics are well-mixed and therefore, relatively homogeneous from the surface to the mixed layer base such that almost no vertical density gradient exists. Mixing of this layer is a result of atmospheric forces acting on the ocean surface. These forces include wind and buoyancy loss induced by either cooling or evaporation (e.g., Talley et al., 2011e; Sprintall and Cronin, 2009). If the surface layer is stable stratified, wind stress can create turbulence that mixes this layer and dissolves the vertical density gradient, resulting in a rather uniform density within the mixed layer. The influence of wind on to the ocean decreases with depth. Usually, the impact of wind does not reach further than 100-150 m (e.g., Talley et al., 2011e). Mixing can also occur due to heat loss or evaporation, resulting in a density increase at the ocean surface. If the density at the surface is now higher than at depth, this unstable constellation will result in an overturn of this layer and thereby, generating deeper mixed layers (e.g., Talley et al., 2011d).

In contrast, heat and freshwater input cause a density reduction at the surface. The vertical density gradient is then larger and the water column is more stable stratified. Assuming all other forces remain the same, this leads to a shoaling of the mixed layer as more energy is now required to mix the stable stratified water column (e.g., Talley et al., 2011d).

Since the mixed layer connects the atmosphere to the ocean, the mixed layer dynamics play a role for ocean ventilation and setting water mass properties, modulating oxygen concentrations, carbon uptake and heat content of the ocean but also in determining the light availability for photosynthesis (Falkowski et al., 1998; Boyce et al., 2010; Bopp et al., 2015; Schmidtko et al., 2017; Oschlies et al., 2018). The heat content in turn, affects air-sea interactions such as tropical storms and precipitation patterns (Balaguru et al., 2016; Vincent et al., 2014). Hence, observing and understanding mixed layer variations on seasonal to multidecadal timescales is of great importance, as it plays a large role in our climate system. Indeed, the mixed layer development is a rather complex mechanism, since there are stabilizing as well as de-stabilizing forces at play and interacting with each other (Sallée et al., 2021). To date, the mean state and the variability of the mixed layer depth (MLD) are not well-depicted in climate models (Fox-Kemper et al., 2023; Treguier et al., 2023). This is however required, in order to suggest consequences of the on-going climate change.

The variability of the mixed layer forcing factors (wind stress, heat and freshwater fluxes) leads to temporal mixed layer variations on daily to seasonal timescales and to spatial mixed layer variations with generally deep mixed layers at high latitudes and shallow mixed layers in the tropical oceans (Sprintall and Cronin, 2009). Most regions have thinner mixed layers in the warm summer season and largest MLD can be found at the end of the winter (Sprintall and Cronin, 2009).

The seasonal cycle of MLD and mixed layer temperature (MLT) can be investigated with three-months mean fields for January-March, April-June, July-September and October-December (Figure 1.4 derived from the Argo observation dataset, Argo, 2021). The Northern Hemisphere shows coolest and deepest mixed layers in boreal winter (January-March) which are then shoaling and warming during boreal spring (Figure 1.4). Warmest and minimum mixed layers are found in July-September for the Northern Hemisphere and deepen again in boreal fall. For the Southern Hemisphere, shallowest and warmest mixed layers can be found in austral summer, i.e., January-March, and maximum depth as well as coldest mixed layers are obtained in July-September (Figure 1.4). Note, the mixed layer varies on average between 10-60 m depth but reaches greatest depth exceeding 200 m in the subpolar North Atlantic in January-March and in the Southern Ocean in July-September (Figure 1.4).

1.2.2 Pycnocline layer

While within the mixed layer, the density does not change much, below the mixed layer base, the density strongly increases and which is where the pycnocline can be found. A pycnocline is defined by a sharp density gradient and hence, a high stratification. Since the temperature structure most of the time dominates the density structure, many studies often refer to a thermocline (i.e., a large temperature decrease with depth). However, there are regions, where the salinity structure also plays a role in setting the density structure. This is the case for the tropics and high latitudes, where there exist a subsurface salinity maximum, creating a halocline (Sprintall and Cronin, 2009; Talley et al., 2011f). Therefore, it is often more suitable to use the term pycnocline. In the context of this thesis, most of the time this layer is called pycnocline and refers to density, thermocline is used when referring to temperature. However, to stay consistent with the phrasing of some fundamental concepts, sometimes thermocline is used although it is at the same time a pycnocline.

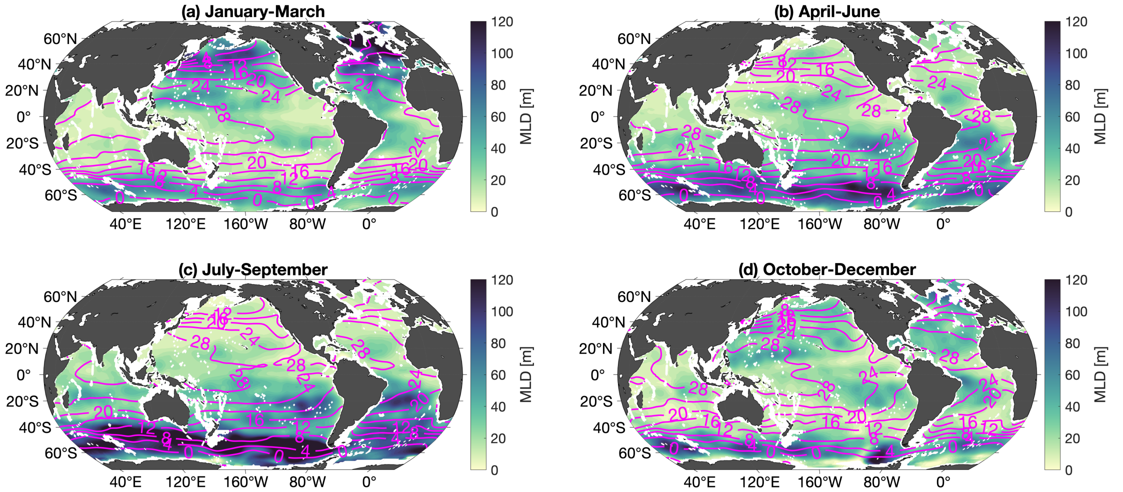

Figure 1.4: Seasonality of mixed layer depth and temperature. Seasonal means of mixed layer temperature (MLT, labeled pink contour lines) and mixed layer depth (MLD, color shading) for **(a)** January-March, **(b)** April-June, **(c)** July-September and **(d)** October-December. These fields are derived from Argo observation for the period of 2006-2021. Mixed layer properties are estimated following the algorithm of Holte and Talley (2009). Note, this is the same procedure of calculating mean fields as in Chapter 4. The mean fields of MLT and MLD for January-March and July-September are from the in Chapter 4 produced dataset.

It should be noted, that there exist several types of pycnoclines. At the ocean surface, a diurnal pycnocline is present which is related to the ocean diurnal warm layer (Huang, 2010a). Below the shallow summer mixed layer, a seasonal pycnocline can be found. The seasonal pycnocline is coupled to the seasonal cycle of the mixed layer, formed by mixed layer detrainment during spring when the mixed layer becomes shallower and it detrains its waters into the seasonal pycnocline. In fall, the water from the seasonal pycnocline contributes to the deepening of the mixed layer and disappears until winter (Huang, 2010b; Sprintall and Cronin, 2009).

Another type of pycnocline is the permanent pycnocline, often also called the main pycnocline/thermocline. It is found at depth of $100\,m$-$800\,m$ (e.g., Feucher et al., 2019) and is solely present equatorward of the subtropical convergence zone. It is formed by subduction of late-winter mixed layer properties (Stommel, 1979; Huang, 2010b) mainly associated with Ekman pumping (Karstensen and Quadfasel, 2002b). The water mass prevalent in the permanent pycnocline is the central water which has a linear temperature-salinity relation. As the isopycnals, which are part of the permanent pycnocline, outcrop between the subtropical and subpolar gyres, no permanent pycnoclines can be found in the subpolar gyres (e.g., Huang, 2010a). Within the permanent pycnocline, the subducted water masses are transported equatorward as a result of the Sverdrup dynamics. Following the pattern of the upper-ocean isopycnal surfaces, the permanent pycnocline features a bowl-like shape within the subtropical oceans and becomes shallower toward the equator.

In some areas of the subtropical gyres, an additional water mass can be found on top of the permanent pycnocline: so-called mode waters (Hanawa and Talley, 2001; Feucher et al., 2019). In general, mode waters consist of a large volume of homogeneous water mass characteristics (i.e., pycnostads) and hence, are associated with low stratification and potential vorticitiy (Hanawa and Talley, 2001). In contrast to central water masses, mode waters consists of one dot in the temperature-salinity relation but can depict a large volume within the water column.

Below the pycnocline layer, the deep ocean or ocean interior can be found where only weak density variations can be found (Talley et al., 2011a). The pycnocline layer is therefore essential for the connection of the upper-ocean and the deep ocean and for the ocean ventilation (Sprintall and Cronin, 2009; Cronin et al., 2013).

Within the framework of this thesis, a local pycnocline defined by the vertical stratification maximum is examined. The vertical stratification maximum defines the largest vertical density gradient of the water column. It is found in the upper-ocean below the mixed layer and within the pycnocline layer (shallower than $500\,m$ in most areas). Depending on the region and season, the vertical stratification maximum can represent different types of pycnoclines (e.g., seasonal pycnocline in summer). However, it is a parameter which is relevant for the coupling between the surface ocean and the deep ocean no matter which region and it can influence how deep the mixed layer can actually reach (e.g., Fiedler et al., 2013; Cronin et al., 2013).

1.3 Climate Variability

Variations in the climate system can be initiated by natural, internal and external forcing or by anthropogenic external forcing (Latif and Keenlyside, 2009; Talley et al., 2011c). Internal variability is caused by interactions within the climate system. External variability requires forcing from outside of the climate system, such as volcanic eruptions, variations of solar radiation at the top of the atmosphere and anthropongenic greenhouse gas emissions (Latif, 2009). Natural climate variability acts on seasonal to millenial timescales (Latif and Keenlyside, 2009).

The ocean plays a vital part in the Earth's climate system, as it not only stores but also exchanges heat, freshwater, momentum and biogeochemical components with the atmosphere. Interactions between the ocean and the atmosphere are responsible for many variations in both of these climate system components (e.g., Yu et al., 2020). Indeed, variability in the ocean occurs in all types of quantities, such as temperature, salinity, sea level, ocean currents and circulation (e.g., Cronin et al., 2012). Temporal variations in the ocean range from seconds (e.g., surface waves), to hours (diurnal cycle, tides, internal waves, inertial oscillations), days (eddies and storm-event induced variability), months (seasonal cycle), years (El Niño-Southern Oscillation events, variability of the large-scale gyres), decades (North Atlantic Oscillation, Pacific Decadal Oscillation and meridional overturning circulation), multidecadal (Atlantic Multidecadal Oscillation) and longer (anthropogenically-forced changes) (Cronin et al., 2012; Talley et al., 2011c). Due to the non-linear relations of some of these processes, variations at one scale can impact variability on other scales and therefore, it is challenging to distinguish between the variability of the different timescales (Franzke et al., 2020, 2022; Cronin et al., 2012).

Within the framework of this thesis, the focus will be on climate variability of the upper-ocean on timescales ranging from interannual to decadal. As described above, on seasonal timescales the relation between atmospheric forcing, the mixed layer and upper-ocean stratification is well-understood: heat loss and stronger winds for instance dissolve the upper-ocean stratification and produce deeper mixed layers in winter while with increasing solar radiation in summer, shallower mixed layers are generated as a result of enhanced stratification. However, the variability of the upper-ocean structure including the mixed layer and the vertical stratification maximum on interannual to decadal timescales requires more research. Knowing variability of the upper-ocean also on decadal timescales is crucial for understanding the signals of climate change and predicting possible consequences. Observational long-term trends of the past 50-60 years detect large changes in the upper-ocean including a warming sea surface, an increasing upper-ocean stratification and a summertime mixed layer deepening (Bulgin et al., 2020; Garcia-Soto et al., 2021; Sallée et al., 2021; Yamaguchi and Suga, 2019). As the link between these observed signals is not yet fully understood, analyzing interannual to decadal variability can help improving the knowledge of the processes acting in the upper-ocean.

Variability on these timescales can often be linked to climate modes. On interannual timescales, the El Niño-Southern Oscillation (ENSO, Philander, 1983) is the most dominant mode of climate variability (Latif and Keenlyside, 2009) which is defined by anomalously warm (El Niño) or cold (La Niña) sea surface temperatures (SSTs) in the tropical Pacific cold tongue. The Southern Oscillation describes a seesaw in sea level pressure between the eastern and western tropical Pacific which then leads to variations in the trade winds (e.g., Wang et al., 2017). During an El Niño event, weaker easterly trade winds cause a reduction of the slope of the equatorial thermocline and thereby, lead to warmer SST anomalies in the Pacific cold tongue and a weaker east-west SST gradient (Latif and Keenlyside, 2009; Wang et al., 2017). In addition, the atmospheric Walker circulation is then weakened (Latif and Keenlyside, 2009) which in turn amplifies the initial warm SST anomalies. This feedback mechanism between the ocean and atmosphere is also referred to the Bjerknes feedback (Bjerknes, 1969). During a La Niña event, the normal state of the equatorial Pacific is amplified: stronger trade winds push the warm SSTs toward the west, steepen the thermocline slope and thereby, upwell colder water in the east of the equatorial Pacific (Latif and Keenlyside, 2009). In these conditions the

Walker circulation in the atmosphere is stronger. Even though ENSO's centre of action is located in the tropical Pacific Ocean, it also influences the global climate via atmospheric teleconnections. For instance, during El Niño events, South America shows anomalously high precipitation while in Australia and Indonesia droughts occur (Latif and Keenlyside, 2009). Also, ENSO influences the hurricane activity in the North Atlantic and the West African Monsoon (Rodríguez-Fonseca et al., 2016).

On decadal timescales, the North Atlantic Oscillation (NAO) is one of the most dominant atmospheric climate modes (Hurrell, 1995; Hurrell et al., 2003). The NAO mode is defined by the pressure difference between the North Atlantic subtropical high and the North Atlantic subpolar low and is thereby responsible for changes of the westerlies and the northeast trades over the North Atlantic (e.g., Hurrell, 1995; Pinto and Raible, 2012). During a positive NAO phase, the subpolar low and subtropical high are intensified, causing warmer and more moist conditions over northern Europe and eastern North America, but colder and drier weather in the Mediterranean (Hurrell, 1995; Visbeck et al., 2001; Pinto and Raible, 2012). As a result of stronger westerlies and northeast trade winds, the SST pattern in the North Atlantic is affected: cold SST anomalies in the North Atlantic subpolar region and in the northern tropical Atlantic and warm SST anomalies in the area of the subtropical gyre (e.g., Wanner et al., 2001; Pinto and Raible, 2012). When the NAO is in its negative phase, the pressure difference between the subpolar low and subtropical high is decreased, the westerlies and northeast trade winds are weaker, leading to colder and drier weather over northern Europe, but wet conditions over the Mediterranean (e.g., Hurrell, 1995; Wanner et al., 2001; Pinto and Raible, 2012). The tripole SST anomaly pattern in the North Atlantic shows reversed signs compared to the positive NAO phase (e.g., Wanner et al., 2001; Pinto and Raible, 2012). The NAO further affects many areas of the world via atmospheric teleconnections but it also influences many ocean sites (Visbeck et al., 2001).

During this thesis, ENSO and NAO are the most relevant climate modes. Nonetheless, there exist many more climate modes acting on different timescales. Next to ENSO and NAO, some of the most known are the Atlantic Niño and the Atlantic Meridional Mode on interannual timescales, the Pacific Decadal Oscillation on decadal timescales as well as the Atlantic Multidecadal Oscillation on multidecadal timescales (e.g., Talley et al., 2011c).

Knowing about these climate modes and their impacts on the ocean and the climate system is crucial. On the one hand, if the data shows variations mirroring the patterns of a climate mode, possible consequences can be projected. On the other hand, separating the features of climate modes from signals of the observed data, allows to detect trends in the data that are not superimposed by the variability of the climate modes.

1.4 Motivation, Objectives and Outline

1.4.1 Motivation and Objectives

Climate is changing and as a result of the on-going climate warming and the proceeding anthropogenic greenhouse gas forcing, the ocean has taken up 93 % of the excess heat since 1955 (Church et al., 2011; Levitus et al., 2012; Rhein et al., 2013). The largest heat uptake is observed in the upper-ocean above the permanent pycnocline (e.g., Häkkinen et al., 2016) and consequently, the upper-ocean is becoming more stratified (e.g., Rhein et al., 2013; Yamaguchi and Suga, 2019).

Climate models suggest that strengthening stratification is associated with shallower mixed layers, weaker ventilation and reduced vertical mixing, and hence less nutrient supply to the euphotic zone (Keeling et al., 2010; Capotondi et al., 2012; Rhein et al., 2013; Kwiatkowski et al., 2020). Besides, with rising sea surface temperatures in the subtropical oceans, the outcrop regions of isopycnals are expected to move poleward, thereby shoaling the ventilated layers and leading to a deoxygenation below the tropical thermocline (Oschlies et al., 2018).

However, observations indicate ocean surface warming might regionally not be accompanied by intensifying stratification (Somavilla et al., 2017). Apart from that, a paradox is observed: large-scale deeper mixed layers occur along with strengthened upper-ocean stratification (Somavilla et al., 2017; Sallée et al., 2021). Suggested causes for the mixed layer deepening are wind stress changes, e.g., intensified Ekman pumping in the subtropical gyres (Somavilla et al., 2017) and wind-driven internal wave turbulence (Sallée et al., 2021). Globally, stratification has been increasing since the 1960s (up to 6.1 % in the upper 200 m (Yamaguchi and Suga, 2019) and 5.3 % in the upper 2000 m of the water column (Li et al., 2020)). Half of the upper-ocean stratification increase is found in the tropical oceans (Yamaguchi and Suga, 2019).

Observations suggest that the relation between mixed layer and upper-ocean stratification changes are not yet fully understood and mismatch with model predictions. Therefore, the knowledge about the on-going processes has to be improved. There is no general consent on which stratification measure to use for which purpose. Definitions of stratification include the density difference from the surface to 200 m (e.g., Somavilla et al., 2017; Yamaguchi and Suga, 2019), averaging the Brunt-Väisälä frequency over the upper 2000 m (e.g., Li et al., 2020) or focusing on the Brunt-Väisälä frequency at the base of the mixed layer and combining mixed layer and stratification changes (Sallée et al., 2021). Each of these methods has advantages and disadvantages. Averaging over a depth range causes a loss of the vertical density structure. Nevertheless, it is a useful parameter to compare for instance to ocean heat content changes of the same depth interval. However, this thesis focuses on the upper-ocean structure, in particular on the mixed layer and the vertical stratification maximum. As the MLD and the depth of the vertical stratification maximum significantly vary regionally and seasonally, the investigation specifically examines these individual parameters at their specific depths and not over an average depth range. This assures to maintain the upper-ocean structure during the analysis which is essential for understanding the underlying physical processes.

This thesis aims to investigate the decadal variability of the upper-ocean in terms of stratification, mixed layer and water mass changes during the Argo observation period (2006-2022), in order to enrich the understanding of recent changes of the upper-ocean. Although many studies find an enhancing stratification, there is still a lacking knowledge of processes acting in the upper-ocean and coupling the surface with the ocean interior. Additionally, the MLD as well as its variability are so far not well described in coupled models (e.g., Fox-Kemper et al., 2023; Treguier et al., 2023). This is however required, in order to suggest possible consequences as a result of the on-going climate change (Treguier et al., 2023). Therefore, it is essential to investigate the recent mean state as well as the decadal variability of the mixed layer properties as well as the vertical stratification maximum.

With the extensive Argo observation dataset, it is now possible to investigate ocean variability below the sea surface for a time period of 17 years. While these years are subject to the largest warming rates (e.g., Garcia-Soto et al., 2021; Bulgin et al., 2020; Yamaguchi and Suga, 2019), the Argo period is too short to directly link the observed changes to global warming. Instead, interannual to decadal variability is the dominant driver of changes on the timescales covered by the Argo period. Natural climate variability on these timescales (5-20 years) is often linked to climate modes, e.g., the ENSO as a dominant mode on interannual, or the NAO on decadal timescales. Understanding and detecting upper-ocean variability on decadal timescales helps to propose possible impacts under climate change.

In particular, this thesis focuses on causes and consequences of upper-ocean stratification changes in specifically the tropical Atlantic but also providing a global overview on upper-ocean changes. Understanding the decadal variability of the upper-ocean stratification as well as its regional differences in the variability patterns can help improving model-observation discrepancies and enriching the comprehension of potential feedback mechanisms acting due to climate warming. In this context, after introducing scientific background relevant for this thesis (Chapter 2), the following research questions will be addressed:

- How did the upper-ocean stratification change in the southeastern tropical Atlantic during the Argo observation period? What are the reasons for the observed changes? How do they impact the marine ecosystem in the southeastern tropical Atlantic? (Chapter 3)
- What are common characteristics of the vertical stratification maximum in summer and winter season? How did the vertical stratification maximum and mixed layer characteristics change globally during the Argo observation period in summer and winter seasons, respectively? What causes the observed large-scale patterns and what are possible implications? (Chapter 4)
- What is the impact of the North Atlantic Oscillation (NAO) on the physical processes in the upper-ocean of the subtropical-tropical Atlantic Ocean? How is the decadal variability of isopycnals related to the potential vorticity barrier? Does the variability of the potential vorticity barrier have an influence on subtropical-tropical pathways? (Chapter 5)

1.4.2 Outline

For the analyses, the vast amount of Argo observations of temperature, salinity and pressure from 2006 onward are utilized. Argo observations enable a three-dimensional view of the global oceans from the surface to 2000 m depth since 2006 (Roemmich et al., 2015; Desbruyères et al., 2017; Johnson et al., 2022). In Chapter 2, the scientific background on fundamental concepts, the ventilated thermocline, heave and spice analysis and the Argo observation dataset is described. Chapter 3 addresses the southeastern tropical Atlantic changing from subtropical to tropical conditions. This region experiences the largest stratification increase in the tropical Atlantic during the period of 2006-2019. Causes for this stratification rise and potential impacts on the marine ecosystem are discussed. Based on the in Chapter 3 introduced procedure of estimating the vertical stratification maximum from Argo profiles, a method for detecting the vertical stratification maximum globally is developed further in Chapter 4. Here, the mean state and decadal changes of summer and winter vertical stratification maxima during 2006-2021 are analyzed and compared to mixed layer property variations. In Chapter 5 the NAO's impact on upper-ocean isopycnals in the tropical Atlantic is discussed and resulting consequences on potential vorticity variability in the eastern tropical North Atlantic and on the subtropical-tropical pathways are investigated. Chapter 6 summarizes the results and returns to the research questions, before giving an outlook.

Chapter 2

Scientific Background

This chapter provides some of the scientific background required for understanding this thesis. At first, fundamental concepts of describing the large-scale ocean circulation are introduced (Section 2.1). Second, in Section 2.2, concepts of the ventilated thermocline are explained. The procedure of analyzing heave and spice is presented in detail in Section 2.3. This chapter finishes with the introduction of the Argo observation dataset (Section 2.4).

2.1 Fundamental Concepts

In this section the theoretical concepts of Geostrophic balance, Ekman balance and Sverdrup relation are briefly described.

2.1.1 Geostrophic Balance

The momentum equations, following Newton's second law of motion, describe the ocean dynamics. Assuming a flow in steady state as well as a homogeneous, frictionless fluid, allow to neglect nonlinear advection terms and time derivatives of the momentum equations. Then the momentum equations reduce to one of the most fundamental concepts in physical oceanography, the balance of pressure gradient and Coriolis force (e.g., Cushman-Roisin and Beckers, 2009b). This is termed the geostrophic balance and is given by:

$$\begin{aligned} fu_g &= -\frac{1}{\rho_0}p_y \\ -fv_g &= -\frac{1}{\rho_0}p_x \end{aligned} \tag{2.1}$$

where f is the Coriolis parameter which includes the β-plane approximation of varying Coriolis parameter with latitude, u_g and v_g are the zonal and meridional geostrophic velocity components, ρ_0 is the reference density and p is the pressure. Note, that p_x and p_y are the partial derivatives of p. In a non-rotating system, the flow would solely be directed from high to low pressure. As result of the Coriolis force (i.e., the rotating Earth), the geostrophic flow is isobaric, implying that the flow follows streamlines of constant pressure, rotating clockwise around a high pressure and anticlockwise around a low pressure in the Northern Hemisphere (e.g., Cushman-Roisin and Beckers, 2009b). In the Southern Hemisphere, the flow is directed in the opposite direction. This is due to the deflection of the pressure gradient force to the right on the Northern Hemisphere and to the left on the Southern Hemisphere.

2.1.2 Ekman Dynamics

So far, frictional forces were neglected. However, the ocean surface is subject to wind stress forcing which drives the wind-driven circulation. Including wind stress forcing in the steady state momentum equations yield the following flow (e.g., Marshall and Plumb, 2008):

$$\begin{aligned} fu &= -\frac{1}{\rho_0}p_y + \frac{1}{\rho_0}\tau_z^y \\ -fv &= -\frac{1}{\rho_0}p_x + \frac{1}{\rho_0}\tau_z^x \end{aligned} \tag{2.2}$$

where τ^x, τ^y are the zonal and meridional components of the surface wind stress. Note, the wind stress in this equation shows a dependence on depth z. Wind forcing only acts on the ocean to a certain depth H_E, the so-called Ekman layer depth (e.g., Marshall and Plumb, 2008).

Separating the horizontal flow $(u, v) = (u_g, v_g) + (u_{Ek}, v_{Ek})$ into its geostrophic and Ekman parts, yields the Ekman balance, i.e., the balance between Coriolis and wind stress (frictional) forcing (e.g., Talley et al., 2011b):

$$\begin{aligned} fu_{Ek} &= \frac{1}{\rho_0}\tau^y \\ -fv_{Ek} &= \frac{1}{\rho_0}\tau^x \end{aligned} \tag{2.3}$$

At the surface of the Ekman layer, the water is deflected from the wind direction due to the Coriolis force. The angle is about 45° to the right of the wind in the Northern Hemisphere and to the left of the wind in the Southern Hemisphere (Talley et al., 2011b). Down to the Ekman depth, the flow becomes weaker and is deflected in each layer according to friction and the Coriolis force. This creates the so-called Ekman spiral (Ekman, 1905).

Vertical integration of the Ekman flow above the Ekman depth H_E defines the Ekman transport (e.g., Talley et al., 2011b):

$$\begin{aligned} U_E &= \frac{\tau^y}{\rho_0 f} \\ V_E &= -\frac{\tau^x}{\rho_0 f} \end{aligned} \tag{2.4}$$

The Ekman transport (defined from the surface down to the Ekman depth) is oriented 90° to the right/left to the wind stress on the Northern/Southern Hemisphere, respectively (Talley et al., 2011b). Due to the prevailing wind systems, regions of Ekman convergences and divergences are created. The trade winds generate a poleward Ekman transport and the westerlies trigger equatorward Ekman transport, leading to Ekman convergence in the subtropical oceans in between. This results in so-called Ekman pumping, i.e., wind stress curl-driven downwelling (compare to negative wind stress curl regions in the Northern Hemisphere and positive wind stress curl regions in the Southern Hemisphere in Figure 1.2). In regions of Ekman divergence, e.g., in the subpolar gyres, Ekman suction (wind stress curl-driven upwelling) is generated.

Mathmatically, the Ekman pumping velocity w_{Ek} can be derived from the vertical integration of the continuity equation ($u_x + v_y + w_z = 0$) from the surface to Ekman depth and by using the expressions for the Ekman flow from Eq. 2.4 (Talley et al., 2011b). Furthermore, the vertical veloctiy at the sea surface $w_{z=0}$ is assumed to be zero (e.g., Talley et al., 2011b). Then, the Ekman pumping velocity becomes:

$$w_{Ek} = \frac{1}{\rho_0}\left[\left(\frac{\tau^y}{f}\right)_x - \left(\frac{\tau^x}{f}\right)_y\right] \tag{2.5}$$

2.1.3 Sverdrup Balance

Interior flow directions can be derived following the planetary vorticity balance introduced by Sverdrup (1947), nowadays also called the Sverdrup balance. Taking the curl of the geostrophic velocity components in Eq. 2.1 and making use of the continuity equation $u_x + v_y + w_z = 0$, the Sverdrup relation can be derived following Talley et al. (2011g):

$$\beta v = f w_z \tag{2.6}$$

where $\beta = \frac{df}{dy}$ (β-plane approximation) stemming from $f = f_0 + \beta y$ with $f_0 = 2\Omega\sin(\Phi_0)$, Φ_0 is the latitude and Ω is the angular rotation rate of the Earth. The partial derivative w_z refers to vertical stretching/squeezing of the water column. Any change of w_z has to be compensated by an adjustment of potential vorticity as one assumes conversation of potential vorticity. Focusing on large-scale ocean circulation, the relative vorticity contribution can be neglected as it is much smaller than the planetary vorticity component. Therefore, any stretching/squeezing of the water column will lead to a meridional movement toward a larger/smaller Coriolis parameter f, respectively (Talley et al., 2011g).

The vertical stretching and squashing of the water column is generated by the Ekman pumping velocity (Eq. 2.5). Besides, it is assumed that for the ocean bottom the vertical velocity is zero. Then, the meridional transport V is defined by the vertical integration of Eq. 2.6 from Ekman layer depth to ocean bottom. Adding the meridional Ekman transport component V_E from Eq. 2.4 yields the meridional Sverdrup transport (e.g., Cushman-Roisin and Beckers, 2009a):

$$V_{Sv} = \frac{1}{\rho_0 \beta_0} \left(\tau_x^y - \tau_y^x \right) \tag{2.7}$$

This is also defined as the flat-bottom Sverdrup relation and it shows that the meridional ocean interior transport can be defined solely by the wind stress curl (Cushman-Roisin and Beckers, 2009a). Therefore, the Sverdrup transport is a combination of the Ekman and geostrophic flows and accounts for the entire water column. The Sverdrup transport is, however, not initially mass balanced. This happens in the form of a return flow at the western boundaries when including horizontal friction in the momentum equations which was implemented by Stommel (1948) and Munk (1950).

2.2 Concepts of the Ventilated Thermocline

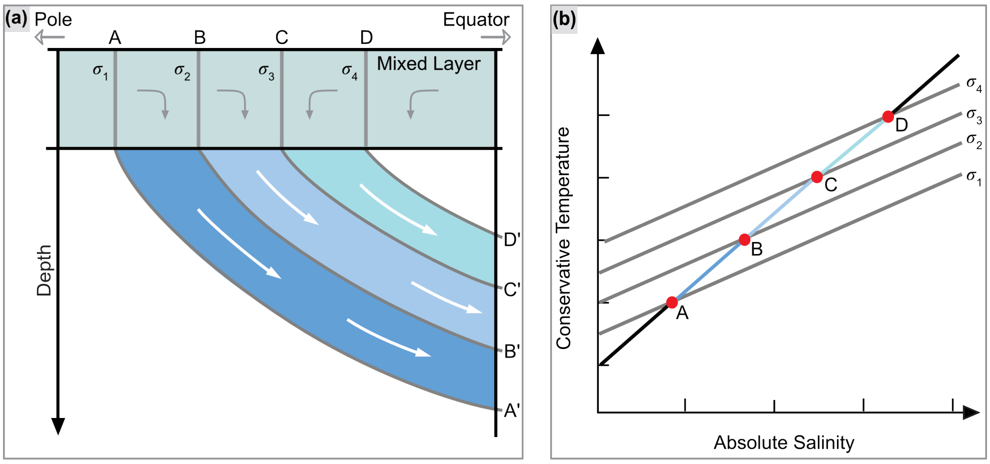

Figure 2.1: Schematic showing the central water mass formation in the subtropical convergence zone occuring on isopycnal surfaces following the concept of Iselin (1939). **(a)** Surface convergence in the mixed layer leads to subduction by downward Ekman pumping along isopycnals ($\sigma_1, \sigma_2, \sigma_3, \sigma_4$). The characteristics in positions A, B, C, D at the surface along a meridional section are re-found in a vertical section located equatorward at A', B', C' and D'. **(b)** Temperature-salinity diagram shows both the meridional and the vertical temperature-salinity relation in one. A, B, C and D and the labeled isopycnals (gray lines, $\sigma_1, \sigma_2, \sigma_3, \sigma_4$) resemble the same characteristics as in **(a)**. The schematic is adapted from Tomczak and Godfrey (1994).

Ventilation is a way of setting a subsurface layer into motion (e.g., Huang, 2010c). Iselin (1939) postulated the first conceptualized model of the thermocline. He suggested that the subtropical permanent thermocline waters have their origin at higher latitudes, as the surface temperature-salinity relation at higher latitudes mirrors the vertical relation at lower latitudes (Figure 2.1). This basically implies that the meridional temperature-salinity diagram is resembled as the vertical temperature-salinity diagram in the subtropics/tropics (Figure 2.1 b). Colder waters from the poles are subducted along isopycnals equatorward underneath lighter surface waters. Thereby, a linear temperature-salinity relation is generated which characterizes the central water masses. Stommel (1979) further suggested only late-winter properties from the mixed layer make it into the permanent thermocline and demonstrated that Ekman pumping occurs along isopycnal surfaces into the deep geostrophic flow. To date, this phenomenon is referred to as the *Stommel demon*. Stommel (1979) himself stated that a demon must be responsible for the subduction of only late-winter properties.

Based on these concepts, Luyten et al. (1983) developed a multi-layer model of the ventilated thermocline. In the subtropics, the surface layer is subject to Ekman pumping. Once subducted to the subsurface layer, the water particles are shielded from Ekman pumping and maintain their potential vorticity (Luyten et al., 1983). According to Sverdrup dynamics, the subsurface flow is equatorward. The flow then follows streamlines of potential vorticity. Due to the conservation of potential vorticity f/h with f being the Coriolis parameter and h the layer depth, the subsurface flow is equatorward. Along the eastern boundary, Luyten et al. (1983) assumed constant subsurface layer thickness. This stems from the boundary condition, that there cannot be a geostrophic flow across the eastern boundary. Hence, potential vorticity conservation cannot hold at the eastern boundary, which implies that there is no flow along the eastern boundary. Therefore, Luyten et al. (1983) introduced so-called shadow zones along the eastern boundary, which are poorly ventilated regions. The model of Luyten et al. (1983) provided the base of the concept of the so-called subtropical cells (STCs). STCs are shallow meridional overturning cells, connecting the subtropcial subduction zones with the upwelling regimes along the equator and upwelling-domes in the tropics (Zhang et al., 2003; Schott et al., 2004).

2.3 Heave and Spice Analysis

Heat and freshwater fluxes as well as wind forcing acting onto the ocean surface are altered as a result of climate variability and climate change. Bindoff and McDougall (1994) considered the impact of different atmospheric forcing on the mixed layer and the subsurface once the water is subducted. Atmospheric forcing can affect the subsurface of the ocean by three different processes: *pure warming*, *pure freshening* and *pure heaving*

(Bindoff and McDougall, 1994). Changing characteristics of temperature and salinity can be analyzed in the reference frame of depth as well as of isopycnals. Both of these reference frames will be used in the following sections.

Pure warming and *pure freshening* are associated with subduction of warmer and fresher waters from the mixed layer, respectively. Once subducted into the thermocline, these waters will cause changes at depth levels as well as on density surfaces (also referred to as spice changes). *Pure heaving* is the vertical displacement of isopycnals which has no signature in the temperature-salinity relation on isopycnals (i.e., no variation in spice), yet when in the reference frame of depth this mechanism can have an impact on the characteristics (Bindoff and McDougall, 1994). In the following, the different processes will be explained for different types of stratification, i.e., stability ratios $R_\rho = \frac{\alpha\theta_z}{\beta S_z}$. α and β denote the thermal expansion and haline contraction coefficients, respectively. θ_z and S_z refer to the vertical gradients of conservative temperature and absolute salinity, respectively. The following stability ratios are considered: $1 < R_\rho < \infty$ which is associated with saline surface waters above fresher subsurface waters and $-\infty < R_\rho < 0$, associated with fresher surface waters above more saline subsurface waters. Both scenarios are stable stratified in temperature, i.e., warm waters on top of colder waters. In most of the oceans, the permanent thermocline consists of the stability ratio of $1 < R_\rho < \infty$ (Bindoff and McDougall, 1994), which is also referred to a typical subtropical stratification.

2.3.1 Pure Warming

Assume an intensifying heat flux acting on the ocean surface while the freshwater flux and the subduction rate remain unchanged. In turn, the mixed layer warms and its density decreases. This implies that a parcel, that is now subducted, happens to be on a lighter density surface than without the warming. Moreover, the initial denser isopycnal surface is suppressed downward as it is replaced by the lighter density surface on top (Bindoff and McDougall, 1994). However, during such a warming process at depth, different changes can be observed in the isopycnal frame of reference.

Therefore, the warming process at a specific depth is now considered in the temperature-salinity space. Imagining the subtropical stratification ($1 < R_\rho < \infty$) at first, i.e., warm and saline water on top of colder and fresher water. Then, a warming at a certain depth will shift the initial thermocline (thin blue line in Figure 2.2a) to a new position (thick blue line in Figure 2.2a). The warming at depth (orange arrow) can be examined as a vector summation between a positive heave component, i.e., a downward movement of the initial density surface due to a new lighter density surface on top (blue arrow), and a negative spice contribution (green arrow). Negative spice implies that the water mass characteristics on an isopycnal at the new thermocline location appear now cooler and fresher than at the same isopycnal at the initial thermocline position (Figure 2.2a, Bindoff

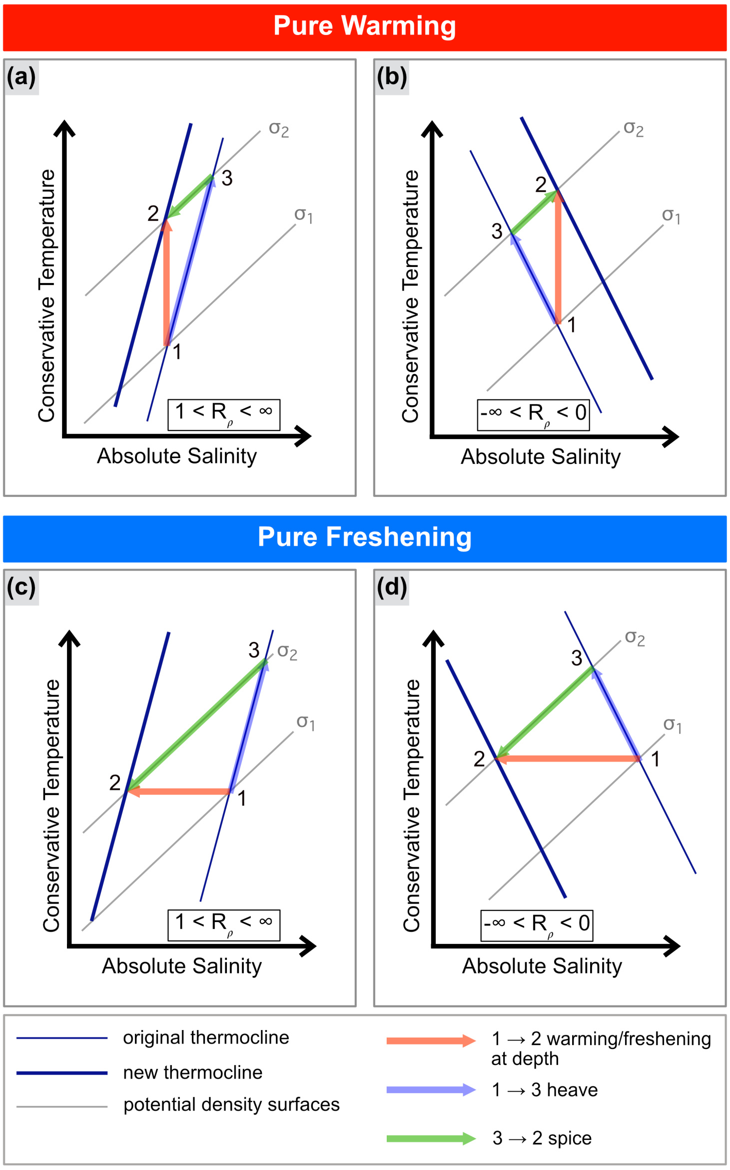

Figure 2.2: Temperature-Salinity (T-S) relation of a pure warming process **(a, b)** and a pure freshening process **(c, d)** for different types of stratification/stability ratios: **(a)** and **(c)** consider $1 < R_\rho < \infty$ which is a typical subtropical stratification and in **(b)** and **(d)** $-\infty < R_\rho < 0$ which can be observed in the tropics and high latitudes. The thin blue line shows the original thermocline, the thick blue line denotes the new thermocline after the pure warming/freshening process. Gray lines indicate the potential density surfaces. Position 1 denotes the starting point, position 2 depicts the T-S condition at the same depth after the warming/freshening process. Orange arrows (1–2) show the warming/freshening process, green arrows (3-2) reveal the spice component (i.e., change of water mass characteristics on a density surface), i.e., the change of density characteristics, and blue arrows (1-3) show the heave component, i.e., the vertical displacement of an isopycnal. This figure is adapted from Bindoff and McDougall (1994); Häkkinen et al. (2016). **(a)** and **(c)** have been similarly published in Roch et al. (2021).

and McDougall (1994); Häkkinen et al. (2016)). Depending on the stratification/stability ratio R_ρ, the spice component (change of water mass properties on an isopycnal) can be negative or positive.

Following the decomposition of Bindoff and McDougall (1994), a change of conservative temperature θ at a certain depth z is defined by:

$$\left.\frac{d\theta}{dt}\right|_z = \left.\frac{d\theta}{dt}\right|_n - \left.\frac{dz}{dt}\right|_n \frac{d\theta}{dz} \tag{2.8}$$

where the first part of the equation on the right side is the spice component (the change of temperature along an isopycnal surface n) and the second part is the heave component (the change of the vertical displacement of this neutral density surface times the vertical temperature gradient, Bindoff and McDougall (1994)).

For a stratification where warm and fresh water is layered above cool and saline water, as for instance in the tropics or at high latitudes, the stability ratio becomes $-\infty < R_\rho < 0$. Then the vector summation between heave and spice for a pure warming process differs from the one of the subtropical stratification (Figure 2.2b). For this type of stratification ($-\infty < R_\rho < 0$), the warming is again characterized by positive heave (blue arrow from position 1 to 3), but this is now superimposed by positive spice (green arrow from position 3 to 2, Figure 2.2b). This implies that at the new thermocline location, water mass characteristics on an isopycnal are found to be warmer and more saline than on the same isopycnal at the original thermocline position (Bindoff and McDougall, 1994). The analysis shows that even though a warming is observed at depth, it does not necessarily indicate a warming on isopycnal surfaces. Differences between these two types of reference frames have to be kept in mind. The sign of the spice contribution depends on the type of stratification and the stability ratio.

2.3.2 Pure Freshening

Similarly to the *pure warming* process, *pure freshening* can be analyzed. Now assume an anomalous freshwater input at the surface and no change of temperature. Consequently, a freshening of the mixed layer and thus a density decrease at the surface will be observed. Again, the subduction rate is supposed to stay the same as prior to the freshening signal. For the subtropical stratification ($1 < R_\rho < \infty$), a freshening at a specific depth shifts the original thermocline to a new position (orange arrow, Figure 2.2c). This can be analyzed as the sum of positive heave (blue arrow, Figure 2.2c) and negative spice (green arrow, Figure 2.2c). This is the same as for the *pure warming* in a subtropical stratification.

For a tropical or subpolar stratification ($-\infty < R_\rho < 0$), *pure freshening* behaves different than the *pure warming* process. Positive heave accounts for the freshening at depth (blue arrow, Figure 2.2d), however, it is corrected by a negative spice component (green arrow). Hence, the water mass characteristics on the new thermocline position appear now cooler and fresher than on the same density surface as before (Bindoff and McDougall, 1994; Häkkinen et al., 2016).

A change of absolute salinity S_A at a specific depth is defined accordingly to the change of conservative temperature from Eq. 2.8 (Bindoff and McDougall, 1994):

$$\left.\frac{dS_A}{dt}\right|_z = \left.\frac{dS_A}{dt}\right|_n - \left.\frac{dz}{dt}\right|_n \frac{dS_A}{dz} \tag{2.9}$$

2.3.3 Pure Heaving

Pure warming and *pure freshening* assume no change in subduction rates. Changing rates of subduction into and out of layers between isopycnals will alter the vertical position of isopycnal surfaces (Figure 2.3a). This can be generated by wind stress changes, variations in water mass renewel rates as well as by adjustment due to Rossby waves (Bindoff and McDougall, 1994). The vertical movement of isopycnals without changing the water mass characteristics on the isopycnal surfaces (i.e., spice, Figure 2.3) is the so-called *pure heaving* process (Bindoff and McDougall, 1994). Nevertheless, *pure heaving* is associated with a temperature or salinity change at depth. This implies for *pure heaving* the Eqs. 2.8 and 2.9 become the following (Bindoff and McDougall, 1994);

$$\begin{aligned} \left.\frac{d\theta}{dt}\right|_z &= -\left.\frac{dz}{dt}\right|_n \frac{d\theta}{dz} \\ \left.\frac{dS_A}{dt}\right|_z &= -\left.\frac{dz}{dt}\right|_n \frac{dS_A}{dz} \end{aligned} \tag{2.10}$$

Wind stress is a highly varying parameter in our climatic system (Huang, 2015). If the wind forcing changes, the wind-driven circulation will adapt in turn. Examples of wind stress changes are intensified wind stress curl-driven upwelling or downwelling of isopycnals occurring due to anomalous Ekman suction or Ekman pumping, respectively. Since the upwelling and downwelling of isopycnals does not happen to be the same for all isopycnals, the vertical displacement of isopycnals changes the distance between the isopycnals and leads to stretching and squeezing of isopycnal layers. This in turn alters the stratification of the water column (Huang, 2015). Stretching of isopycnal layers produces weaker stratification whereas squeezing of isopycnal layers results in enhanced stratification. Furthermore, potential vorticity is required to adapt to ensure conservation. In the ocean interior, relative potential vorticity is negligible (e.g., Talley, 1988). Therefore, potential vorticity is solely f/h. Squeezing or stretching of isopycnal layers moves the water column equatorward or poleward, respectively (Huang, 2010a).

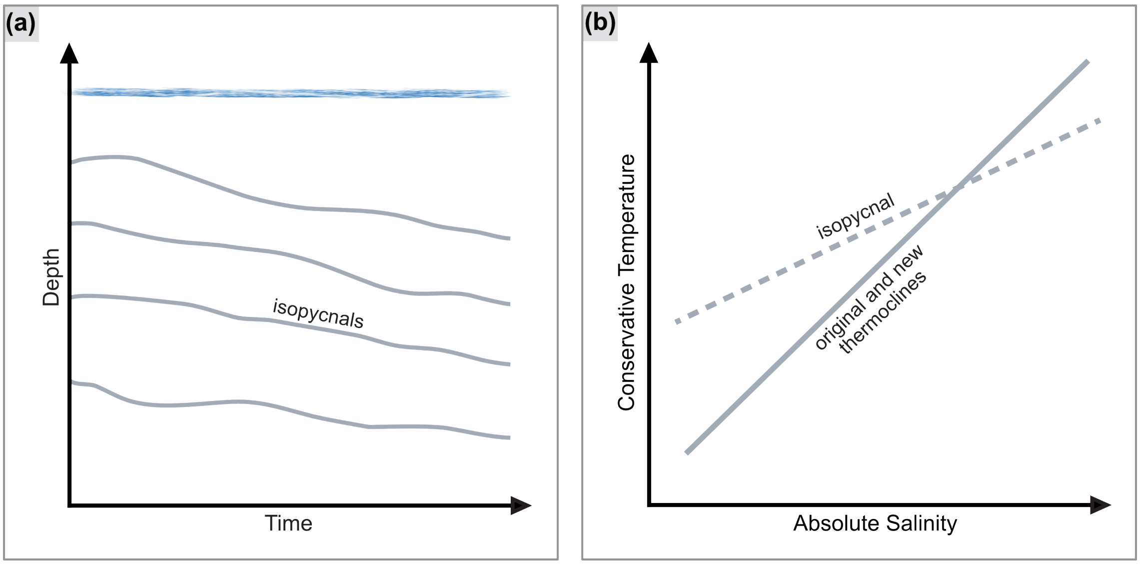

Figure 2.3: Schematic representing the *pure heaving* process. **(a)** Time evolution of vertical displacements of isopycnals and therefore, height changes between the surfaces. **(b)** The characteristics of the subducted water in **(a)** remain the same on the isopycnals. Hence, the temperature-salinity frame does not change. Note, this figure is adapted from Bindoff and McDougall (1994).

Huang (2015) presented several types of possible heaving modes in the world oceans as a result of wind stress anomalies in certain regions. Focusing on interannual and decadal timescales, he studied the dynamical consequences as a result of heaving of the permanent thermocline. In quasi steady-state, the thermocline is shallow in the subpolar gyres as well as at the equator, while it is deep in the centre of the subtropical gyres. Two of Huang (2015) scenarios will be presented in the following. The first case assumes relaxed easterlies at the equator (Figure 2.4a). As a consequence, the thermocline at the equator rises. Hence, the warm water above has to be distributed to the north and south of the equator, which leads to a downward displacement of the thermocline in the extratropics. Below the thermocline, cold water is transported to the equator in order to balance the effect of the upper-ocean poleward distribution of warm water (Figure 2.4a).

For the second case, anomalous weak wind stress is induced in the region of Northern Hemisphere subtropical gyre. This leads to reduced Ekman pumping in this region and produces a shoaling of the thermocline in the Northern Hemisphere subtropics (Figure 2.4b). Upper-ocean warm water will be transported toward the poles and the equator while cold water in the deep layers will propagate to the subtropics (Huang, 2015). Such a thought-experiment can be done for any kind of wind stress change. Consequently, the meridional and vertical redistribution of heat content and water masses is one of the most important changes related to the *pure heaving* process.

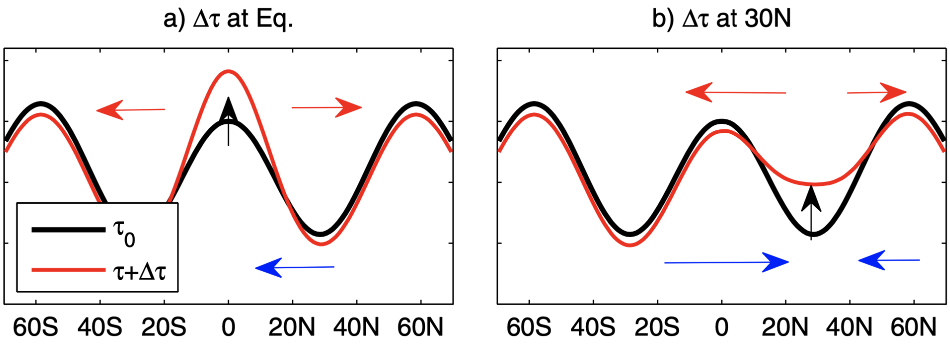

Figure 2.4: Heaving modes in an idealized two-hemisphere ocean as a result of wind stress forcing **(a)** at the equator and **(b)** at 30°N. τ indicates the mean wind stress and $\Delta\tau$ the wind stress anomaly. Note that depending on the forcing $\Delta\tau$ can be negative or positive. Black lines indicate steady state thermocline position. Red lines denote the new thermocline position as a consequence of wind stress forcing. Black arrows show the vertical movement of the thermocline. Red/blue arrows demonstrate the redistribution of warm/cold water above/below the thermocline. This figure is adapted from Huang (2015).

Indeed, observations show that ocean heat content changes are mainly driven by wind-driven heaving (vertical displacement of isopycnals) on interannual, decadal and multi-decadal timescales whereas spice contributions are found to be weak (Häkkinen et al., 2016; Desbruyères et al., 2017). Changes of isopycnal heave have been identified to increase the volume of subtropical mode waters (Häkkinen et al., 2015, 2016) and during the Argo period, subtropical mode waters are suggested to be warming hot spots of the upper-ocean (Kolodziejczyk et al., 2019). Within the framework of this thesis, the observational dataset of Argo will be used to analyze heaving of isopycnals, spice variations on the isopycnals as well as changes of mixed layer characteristics. Thereby, all three of the above introduced components will be intensively studied with the aim to improve the understanding of recent upper-ocean stratification changes.

2.4 Argo Observations

This thesis is mainly based on the extensive Argo observation dataset. This dataset is obtained from autonomous profiling floats measuring hydrographic parameters mainly in the upper 2000 m of the water column in the world oceans. In the following a description of the history of Argo observations and the operation mode of Argo floats is provided. Argo is an international scientific program which developed from the World Ocean Circulation Experiment (WOCE) project in the 1990's (Roemmich et al., 1998). Argo's aim is to survey the upper-ocean changes and variability on monthly to decadal timescales, in particular in terms of heat and freshwater storage (Roemmich et al., 1998). Together with satellite data, it provides a three-dimensional view on the upper-ocean. In order to evaluate the ocean's role in the climate system, persistent global observations are needed

Figure 2.5: First map of the Gulf Stream created by Benjamin Franklin and Timothy Folger (Franklin et al., 1768). This figure can be accessed via the Library of Congress (https://www.loc.gov/resource/g9112g.ct000753/?r=-0.355,-0.08,1.588,0.991,0, accessed 01. October 2023).

(Johnson et al., 2022). Before the Argo project started, such observational datasets were barely available and required high costs. First useful oceanographic observations were reported by Benjamin Franklin in 1770: ocean temperature measurements obtained from ship voyages between Europe and the English colonies were analyzed to define the location of the Gulf Stream (Folger (1787); Johnson et al. (2022), Figure 2.5).

The *Challenger* expedition from 1872 to 1876 provided the first measurements of temperature down to more than $1000\,m$ depth of the global oceans. More than 250 measurement stations were taken in the World Oceans (Wyville Thomson and Murray, 1885). Carrying on oceanographic measurements, it was only in the 1980s that scientists achieved a dataset of some high-quality measurements of temperature and salinity, including a few tracer and biogeochemical samples (Johnson et al., 2022). Most of the subsurface ocean was still unobserved. In order to obtain a better knowledge about the subsurface ocean, oceanographers invoked the WOCE project. The goal was to assemble ship-based measurements of the world oceans at several thousand stations (Johnson et al., 2022). Within the scope of WOCE an Autonomous Lagrangian Circulation Explorer (ALACE) was deployed (Davis et al., 1992). ALACE was some kind of an early version of the later developed Argo floats, drifting freely and descending down to $1000\,m$ depth and back to the surface, submitting its location to satellites (Johnson et al., 2022). With the position tracking, one could receive a velocity vector form the displacements with a 10-day resolution. In the end-1990s, ALACE floats additionally received conductivity-temperature-salinity sensors (Lavender et al., 2000). This is how the idea of the Argo

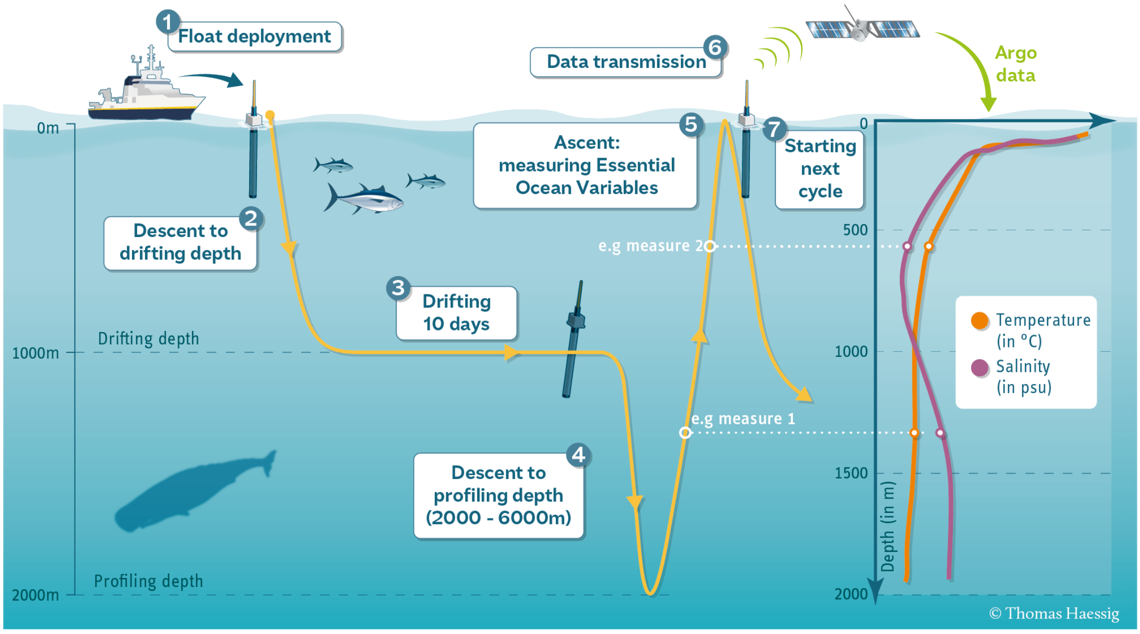

Figure 2.6: Schematic indicating the work flow of an Argo float. Once the float is deployed (1), it sinks to a drifting depth of 1000 m (2). At this depth the float is drifting for about 10 days (3) until it descends down to 2000 m (4) (or if the float is part of the deep Argo program, it moves down to 6000 m). The float then moves up to the surface again (5). During its ascent, hydrographic parameters are measured, which are then transmitted to satellites (6). After completion of data transmission, the float proceeds with the next cycle (7). This figure is from Argo (2023b) (https://argo.ucsd.edu/how-do-floats-work/, date accessed: 23.08.23).

observation project started. With autonomous profiling floats, Argo is now measuring temperature, conductivity and pressure of the upper 2000 m of the water column and provides information on the ocean circulation.

The Argo project started deploying floats in the year 2000 and since then the oceans are continuously filled with floats. The name Argo was created since the float array collaborates with the Jason earth observing satellites which determine the shape of the ocean surface. In the Greek mythology, *Jason* sailed with his ship *Argo* to find the golden fleece in the Black Sea (Argo, 2023b). Argo is part of the Global Ocean and Global Climate Observing System and there are 30 nations involved in the project. To date, almost 4000 floats are active in the world's oceans and in 2020 on average 12,000 profiles were obtained per month (Argo, 2023b). Argo coverage goal in the global oceans is about one float per 3° × 3° box for regions beyond 2000 m depth.

Within a 10-day cycle, an Argo float typically moves down from the surface to a drifting depth of 1000 m where it remains for about 9 days. This is followed by another descent to 2000 m before the float rises to the surface again. On the ascent, the float measures temperature, conductivity and pressure. Once the float is at the surface, the data is transmitted to satellites (Figure 2.6). From the displacement positions, integral velocity data over the 10-day period can be obtained. An Argo float lives for about 4-5 years (Argo, 2023b).

The Argo project started with the Core Argo program which consists of the float behavior and measurements described above. Since some years, two more missions are provided by Argo: BioGeoChemical (BGC) Argo and Deep Argo. Both missions are in their rough beginnings. Deep Argo works similar to the Core Argo mission, just that floats reach 4000-6000 m deep. BGC Argo surveys biogeochemical variables (Argo, 2023a). However, in this thesis the biogeochemical parameters of BGC Argo are not taken into account. Deep Argo profiles are found within the immense dataset. Since the research focuses on the upper-ocean, only upper-ocean measurements are included in the analyses.

The Argo observational dataset allows for the computation of hydrographic climatologies (e.g., Schmidtko et al., 2013; Roemmich et al., 2009). With the extending length of the dataset, it is now possible to investigate interannual to decadal ocean variability (e.g., Roemmich et al., 2015; Desbruyères et al., 2017; Johnson et al., 2022). Additionally, Argo data is used to improve ocean and weather forecasts as well as to validate the present ocean state in climate models (King et al., 2020).

In the context of this thesis, decadal changes and climate variability are assessed from the Argo dataset for upper-ocean variables including mixed layer parameters and the upper-ocean stratification. Note that the MLD can be determined with different methods. Often used are threshold methods (e.g., Kara et al., 2000; de Boyer Montégut et al., 2004) which define the base of the mixed layer at the depth where temperature or density changed by a fixed value compared to the surface. Another possible procedure to detect MLDs is the gradient method (e.g., Lukas and Lindstrom, 1991). This method is based on the assumption that the mixed layer is followed by a large gradient of temperature or density associated to the thermocline or pycnocline (Holte and Talley, 2009). Throughout this thesis, the mixed layer algorithm of Holte and Talley (2009) is applied. This algorithm combines the threshold and gradient methods and thereby, yields a collection of possible MLDs. The algorithm then analyzes other features of the water column (e.g., seasonal thermocline and seasonal pycnocline) to determine the final estimate of the MLD (Holte and Talley, 2009).

Based on Argo observations, regional analysis in the southeast tropical Atlantic will provide new insights into the open ocean changes off Angola/Namibia (Chapter 3). A dataset of the vertical stratification maximum, as a useful variable for model validation, is determined. With this data product, decadal changes are evaluated in the global oceans (Chapter 4). In Chapter 5, the North Atlantic Oscillation's impact on the decadal variability of upper-ocean isopycnals in the subtropical-tropical Atlantic is investigated.

Chapter 3

Southeastern Tropical Atlantic Changing From Subtropical to Tropical Conditions

As a high-productive ecosystem just north of the Benguela upwelling system, the coastal region off Angola has received a lot of scientific attention. Most studies, however, focus on the continental slope and shelf region, particularly analyzing coastally trapped waves on seasonal timescales (e.g., Ostrowski et al., 2009; Bachèlery et al., 2016) or the extreme events occurring in this region, called Benguela Niños, which act on interannual timescales (e.g., Shannon et al., 1986; Imbol Koungue et al., 2019). This Chapter aims at investigating the decadal variability of upper-ocean stratification in the open ocean of the southeast tropical Atlantic. The focus is on larger scale water mass and stratification changes. Additionally, potential impacts for the marine ecosystem are discussed.

The manuscript was published in *Frontiers in Marine Science: Physical Oceanography* in November 2021.

Roch, M., Brandt, P., Schmidtko, S., Vaz Velho, F. and Ostrowski, M. (2021). Southeastern Tropical Atlantic Changing From Subtropical to Tropical Conditions. *Front. Mar. Sci.* 8; 748383. doi: 10.3389/fmars.2021.748383

The candidate carried out all the analyses, produced all the figures and authored the manuscript from the first draft to the final published version.

Abstract

A warming and freshening trend of the mixed layer in the upper southeastern tropical Atlantic Ocean (SETA) is observed by the Argo float array during the time period of 2006–2020. The associated ocean surface density reduction impacts upper-ocean stratification that intensified by more than 30 % in the SETA region since 2006. The initial typical subtropical stratification with a surface salinity maximum is shifting to more tropical conditions characterized by warmer and fresher surface waters and a subsurface salinity maximum. During the same period isopycnal surfaces in the upper 200 m are shoaling continuously. Observed wind stress changes reveal that open ocean wind curl-driven upwelling increased, however, partly counteracted by reduced coastal upwelling due to weakened alongshore southerly winds. Weakening southerly winds might be a reason why tropical surface waters spread more southward reaching further into the SETA region. The mixed layer warming and freshening and associated stratification changes might impact the marine ecosystem and pelagic fisheries in the Angolan and northern Namibian upwelling region.

3.1 Introduction

The southeastern tropical Atlantic (SETA: 10–20°S, 5°W–15°E) encompasses a highly-productive ecosystem off Angola which is located just north of one of the major global coastal upwelling regions: the Benguela upwelling system (Ostrowski et al., 2009; Kopte et al., 2017). In the SETA region the thermal Angola-Benguela Front (ABF) evolves around 15–17°S where warm, tropical waters encounter cooler, subtropical waters from the Benguela upwelling system (Shannon et al., 1987; Siegfried et al., 2019). At the ABF the poleward Angola Current meets the northward Benguela Coastal Current (Siegfried et al. (2019) indicated schematically in Figure 3.1a). Siegfried et al. (2019) showed that the Angola Current is fed with tropical South Atlantic Central Water (SACW) via the eastward flowing Equatorial Undercurrent (EUC), the South Equatorial Undercurrent (SEUC) and the South Equatorial Countercurrent (SECC) (Figure 3.1a). These currents and the location of the ABF undergo large seasonal variations and hence the area influenced by the presence of tropical SACW varies as well (Rouault, 2012).

On seasonal time scales the variability of the Angola Current is affected by coastally trapped waves (CTWs) excited by remote equatorial forcing (Ostrowski et al., 2009; Bachèlery et al., 2016; Kopte et al., 2018; Tchipalanga et al., 2018). The seasonal upwelling and downwelling phases in the SETA region coincide with the corresponding four seasonal wave propagations of the CTWs. March and October are marked by downwelling and July–August and December-January by upwelling phases (Ostrowski et al., 2009). CTWs excite sea surface temperature (SST) anomalies via the thermocline feedback which can affect air-sea interactions such as heat fluxes and precipitation patterns (Shannon et al., 1986; Rouault et al., 2018).

On top of the seasonal cycle, the SST along the coast of Angola and Namibia can experience extreme warm events, the so-called Benguela Niños (Shannon et al., 1986). During these interannual warm events, the ABF is shifted anomalously poleward (Florenchie et al., 2004; Rouault et al., 2007, 2018; Lübbecke et al., 2010). Thereby, tropical SACW extends into the northern part of the Benguela upwelling region (Lübbecke et al., 2010; Siegfried et al., 2019).

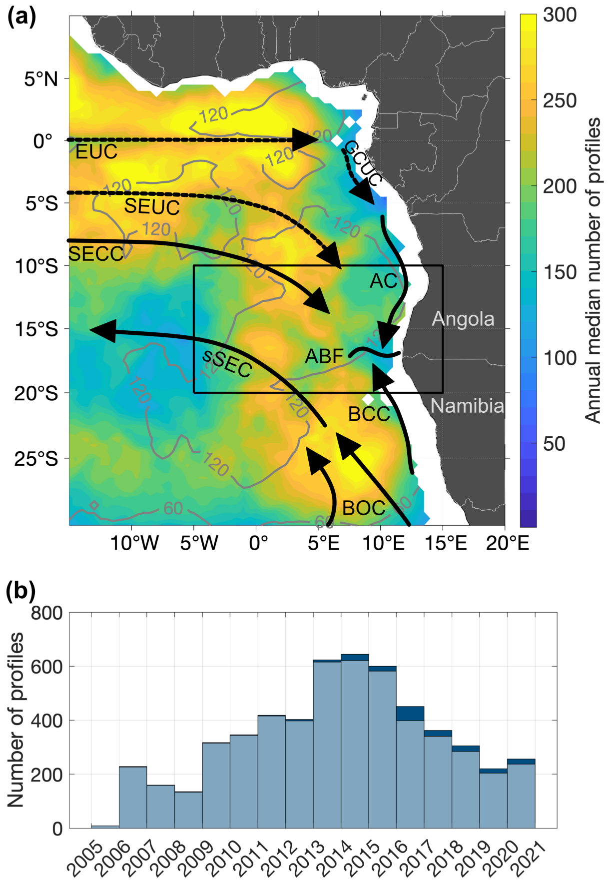

Figure 3.1: **(a)** Median annual number of Argo profiles for the time period of 2006–2020. Mapping radii are ellipses with 3° in latitude and 8° in longitude at the equator changing exponentially toward circles with 6° radii in latitude and longitude at 20°S. Gray contour lines show the standard deviation of the median annual number. The black box shows the southeastern tropical Atlantic (SETA) region (10–20°S, 5°W–15°E). Additionally, currents are schematically indicated (solid arrows imply surface currents and dashed arrows thermocline currents): Equatorial Undercurrent (EUC), South Equatorial Undercurrent (SEUC), South Equatorial Countercurrent (SECC), Angola Current (AC), Benguela Coastal Current (BCC), Benguela Oceanic Current (BOC), southern branch of the South Equatorial Current (sSEC), and Gabun-Congo Undercurrent (GCUC). Besides, the location of the Angola-Benguela Front (ABF) is depicted. Shelf regions below 2,000 *dbar* have been blanked out. **(b)** Dark blue bars indicate the overall number of Argo profiles in the SETA region per year. Light blue bars above depict the number of Argo profiles that pass the good interquartile range filter of the vertical stratification maximum in the SETA region per year.

Meteorologically, the SETA region is situated on the northeastern flank of the South Atlantic Subtropical High (SASH) and therefore, the wind pattern is influenced by the southeast trades (Peterson and Stramma, 1991). In the northern part of the SETA region the mainly southerly wind is considerably weak (Risien et al., 2004; Fennel et al., 2012; Lübbecke et al., 2019; Zeng et al., 2021). Besides, in austral winter when SSTs are lowest, the upwelling favorable winds are weakest and thus, the shallowing of the thermocline occurring during that part of the year is not wind-driven. Instead, enhanced biological productivity off Angola in austral winter is mainly associated with the propagation of an upwelling CTW (e.g., Ostrowski et al., 2009; Rouault, 2012; Lübbecke et al., 2019). Mixing dominantly induced by internal tides (Zeng et al., 2021) transfers the CTW upwelling signal toward the surface to further modulate near coastal SST (Imbol Koungue and Brandt, 2021) and transport nutrients upward into the euphotic zone.

In the southern part of the SETA region the wind situation differs as the southerly wind is substantially stronger. This equatorward wind weakens toward the coast and thereby produces a negative wind stress curl which leads to wind curl- driven upwelling, especially off Namibia (Fennel et al., 2012; Lübbecke et al., 2019).

Upwelling is generally considered to be the upward advection forced by Ekman dynamics (via alongshore winds and wind stress curl) and CTWs (Fennel and Lass, 2007; Fennel et al., 2012). CTWs can be generated both locally and thereby partly reducing the effect of local wind-forced upwelling (Fennel and Lass, 2007) or remotely, e.g., by equatorial forcing (Bachèlery et al., 2016). Nutrients that are important for primary productivity can be transported upward by upwelling and mixing, whereas mixing was shown to be particularly effective during upwelling CTW phases (Zeng et al., 2021).

Superimposed on the wide-spread southerly wind component in the SETA region associated with the southeast trades is the atmospheric Benguela low-level coastal jet (BLLCJ, Patricola and Chang (2017)). Low-level coastal jets are marked by strong coast-parallel equatorward winds in eastern boundary upwelling systems. Attributed to the geometry of the coastline, the BLLCJ constitutes of two local maxima in terms of frequency of occurrence around 26 and 17.5°S (Patricola and Chang, 2017; Lima et al., 2019a). The BLLCJ is formed in between the SASH and the Angolan thermal low pressure. The co-existence of these two pressure systems results in strong pressure gradient and forces the equatorward winds (Lima et al., 2019a). According to Patricola and Chang (2017), an intensification of the SASH and a shift toward the African continent strengthens the BLLCJ. The meridional wind stress component is then enhanced in the southern part, but decreasing offshore and to the north of this region.

In the high-productive SETA region both, upwelling and mixing are of great importance for small pelagic fish stocks since upward transport of nutrients directly impact primary production (Ostrowski et al., 2009; Tchipalanga et al., 2018). The extreme warm and frequently occurring Benguela Niños can have dramatic consequences for the marine ecosystem and its productivity. During a major warm event in 1995 e.g., sardinella *Sardinella aurita* and sardine *Sardinops sagax* showed a large reduction in biomass with increased mortality in Angolan waters and a southward migration to Namibian coastal waters (Gammelsrød et al., 1998). Besides, Potts et al. (2014) reported an intensified warming over the last three decades with dramatic consequences for some fish species and poleward habitat shifts. For a recent review of the impact of climate variability on the plankton, pelagic and demersal fish communities in the Benguela upwelling system the reader is referred to Jarre et al. (2015). Additionally, Jarre et al. (2015) give an outlook on possible changes of the ecosystem related to climate warming.

In general, upwelling and mixing are affected by upper- ocean stratification. Processes such as ocean ventilation and entrainment into the mixed layer depend on the density gradient at the base of the mixed layer and thus on stratification. In this study, we make use of an extensive Argo float dataset to focus on decadal variability of upper-ocean stratification. Our aim is not to investigate processes on the continental slope and shelf, as the Argo floats cannot represent the shelf region. In particular, we cannot study the effects of Benguela Niños and CTWs by using Argo data. Instead, we focus on larger scale water mass and stratification changes and discuss their possible impact on the marine ecosystem.

The common assumption based on climate projections is that global warming will result in a more stratified ocean due to enhanced warming of the ocean surface, often associated with mixed layer shoaling, reduced ventilation and weaker vertical mixing (Keeling et al., 2010; Capotondi et al., 2012; Rhein et al., 2013). Consequently, less upward nutrient supply to the euphotic zone and declining dissolved oxygen concentration are expected (Capotondi et al., 2012; Ito et al., 2019). Hence, impacts on marine ecosystems can be large. Previous work on upper-ocean stratification has mainly focused on climate models and some of these proposed feedbacks are not that straight forward as many different factors play a role. Ventilation processes for example can be further influenced by changes of the wind-driven circulation and heaving (Huang, 2015). Besides, there can be large regional differences and there are observations indicating deeper mixed layers in regions with enhanced stratification (Somavilla et al., 2017; Sallée et al., 2021). This is counterintuitive and could balance the predicted reduction of vertical mixing. It reveals the general lack of understanding of how physical and biological processes are shifting due to climate warming.

Two recent studies showed increasing global stratification since the 1960s. Yamaguchi and Suga (2019) found a $40\,\%$ increase of global stratification in the upper $200\,m$, about half of this enhancement is observed in the tropical oceans. Li et al. (2020) highlight that the global stratification in the upper $2,000\,m$ depth is strengthening by $0.9\,\%$ per decade ($5.3\,\%$ in total) during the period 1960–2018. Their estimate detects largest stratification increases of 5–18 % in the upper $150\,m$.

When investigating upper-ocean stratification, it is necessary to examine mixed layer properties. Directly below the mixed layer the pycnocline/thermocline representing the vertical stratification maximum is situated. The dynamics of these two components, i.e., the mixed layer and the stratification maximum below, can be linked to each other. However, for the global ocean the evolution of water mass properties at the base of the mixed layer is much less studied than the surface warming (Clément et al., 2020).

The continuous growth of Argo observations in recent years allows us to investigate the tropical Atlantic Ocean in terms of upper-ocean stratification changes, its causes as well as its consequences for physical ocean dynamics and marine ecosystems. In this study we will focus on the SETA region as it encompasses a highly productive ecosystem and hence, investigation of upper-ocean stratification in terms of climate variability in this region is of major economic importance for the Angolan and Namibian fisheries. We aim to provide a better understanding of possible physical changes as a result of climate change and their relation to marine ecosystems.

3.2 Data and Methods

3.2.1 Argo Observations and Stratification Estimate

The Argo project currently contains about 4,000 floats measuring hydrographic properties in the upper $2,000\,m$ within a 10-day cycle. For this study Argo observations of the upper $200\,m$ from 2006 to 2019 (Argo, 2019) are used. Prior 2006 the gaps in the data are too large (Roemmich et al., 2015; Desbruyères et al., 2017). Only profiles reaching at least $1000\,m$ depth and flagged good are utilized. The tropical Atlantic from 30°N–30°S holds 121,126 profiles in the observation period. Here, we applied an interquartile range (IQR) filter, excluding data 1.5 times the IQR above/below the first/third quartile. Analyses of potential temperature, absolute salinity and potential density are performed using TEOS-10 (McDougall and Barker, 2011). Additionally, conservative temperature is estimated for the calculation of the Brunt–Väisälä frequency. Note that specifically for the analysis of the SETA region (10°S–20°S, 5°W–15°E) we extended the time series with Argo observations until November 2020, in order to overcome a gap in the data in this particular region in the mid of the year of 2019 (Argo, 2020). The SETA region constitutes 5,477 profiles from 2006 to 2020.

Argo profiles are interpolated vertically using a modified Akima piecewise cubic Hermite interpolation (makima method) as implemented in MATLAB (2019). The algorithm of Akima was first introduced by Akima (1970). Makima is a mixture of the spline and pchip interpolation methods (MathWorks Inc., 2019). Advantages are that makima respects monotonicity compared to the spline method, yet it does not cut off undulations like a pchip method. Using various vertical interpolation schemes, we found that the errors as seen in Supplementary Figure 3.14b are smallest using the makima method. Furthermore, a linear or piecewise cubic method has maxima and minima centered on measured vertical depth levels. This would lead to a bias using float data, since floats (in particular the ones that transmit the data via ARGOS, as most of them still do) have specific target depth at which they measure the oceanic properties. Thus, for the analysis of vertical maxima and minima using float data, an interpolation scheme that may have local maxima and minima between measurements is necessary and therefore, we chose the makima method. First, all profiles are interpolated on an even $0.01\,kg\,m^{-3}$ density grid and second, this is followed by an interpolation on an even $1\,dbar$ pressure grid.

The pressure interpolated profiles are used to determine the Brunt–Väisälä frequency as a measure for stratification. Argo profiles have a varying vertical resolution which impacts the estimate of the Brunt–Väisälä frequency. In order to obtain the best-possible stratification estimate with Argo measurements, we subsampled a high-resolution Conductivity-Temperature-Depth (CTD) profile from a recent cruise in the equatorial Atlantic (Meteor cruise M158, Brandt et al. (2021)) onto the vertical resolution of all available Argo profiles for this study. The CTD profile was taken at 0°, 11°W in October 2019 and covers a vertical sampling rate of $1\,dbar$. The above explained makima interpolation method was applied to the temperature and salinity profiles subsampled according to the vertical resolution of measured Argo profiles. In a next step the Brunt–Väisälä frequency was computed on the even pressure grid. With this we derived a large amount of artificial Argo profiles which are based on the same Brunt–Väisälä frequency profile. However, they deviate from each other since they are based on different vertical resolutions. Finally, the vertical maximum in the upper $200\,m$ of the water column was determined.

By assuming the CTD vertical stratification maximum being the "true" value, we analyzed the dependence of the vertical stratification maximum on the vertical sampling rate of the Argo profiles. The deviations are large (Supplementary Figure 3.14). However, by using the above described IQR filter and a 15-dbar window for computations, the errors were largely reduced (Supplementary Figure 3.14). This smoothing length scale was done by trial and error always in comparison to the CTD reference value. In addition, this smoothing length scale is required for the study of background stratification, ignoring other small-scale features that influence the stratification. 15-dbar seems to be the ideal range for this study as it is the balance between minimizing the noise and preserving the shape of the stratification profile (Feucher, 2016).

Mixed layer properties are determined by using the algorithm by Holte and Talley (2009). This algorithm is based on a hybrid method which combines threshold and gradient methods to specify the best mixed layer properties (Holte and Talley, 2009).

Mapping is accomplished using a least squares method which takes the uneven distribution of Argo profiles into account. Despite generally fewer profiles in the South Atlantic (Figure 3.1a), the histogram of the SETA region indicates more than 300 profiles per year from 2009 to 2018. Influence radii of the anomalies of stratification and mixed layer properties have been checked with a semivariogram analysis, in order to evaluate the spatial bias. This yielded that the spatial bias of the profiles in the SETA region is generally small. Results from 2006 to 2008 and from mid 2019 should be taken with caution due to the relatively small number of Argo profiles available (Figure 3.1b). The histogram also shows the number of profiles per year that pass the IQR filter for the vertical stratification maximum (Figure 3.1b). From those 5,477 available profiles in the SETA region 5,297 profiles pass the IQR filter. Trends and time series of Argo observations are always computed from anomalies relative to the seasonal mean. Seasonal means are calculated on a 15-day grid resolution using overlapping 3-month means (i.e., ±45 days). In order to test statistical significance of the trends, the 95 % confidence limits were determined by multiplying the t-value of the Student's t distribution for 95 % significance with the standard error of the trend. In case the slopes of the upper and lower confidence limits are of the same sign, the trend is assigned to be of 95 % statistical significance.

3.2.2 Wind Stress Data

To investigate changes of wind speed, zonal and meridional wind stress components the wind product Global Ocean Wind L4 Reprocessed Monthly Mean Observations from Copernicus Marine environment monitoring service (CMEMS) is used (Wind and TAC, 2018). The measurements are based on ASCAT scatterometers on METOP-A and METOP-B satellites with the processing level L4. This product is composed of three different ASCAT products (Bentamy, 2020) spanning the global ocean with a spatial resolution of $0.25° \times 0.25°$. It encompasses monthly means which are estimated from at least 25 daily values at each grid point (Bentamy and Fillon, 2012). The observation period covers May 2007–December 2019. With the meridional and zonal wind stress components, the wind stress curl is computed as well. To reduce noise, the data has been transformed on a $0.5° \times 0.5°$ horizontal grid by taking the mean of all points within ±2° in longitudinal and latitudinal direction around each grid point. The anomalies of the wind data are evaluated by subtracting the monthly means provided by CMEMS from the time series.

3.2.3 Heat Flux and Freshwater Products

In order to compare the results to heat and freshwater fluxes different products are used. First of all, the Objectively Analyzed air-sea fluxes (OAFlux) for the Global Oceans from Woods Hole Oceanographic Institution (WHOI) is used[1] (Yu et al., 2008). The horizontal resolution of the data is $1° \times 1°$ in latitude and longitude and is available as a monthly mean from 1958 until present. OAFlux latent and sensible heat fluxes are computed with

---

[1] https://oaflux.whoi.edu/data-access/

the COARE bulk flux algorithm and surface meteorological properties (Yu et al., 2008). For this analysis, latent heat flux, evaporation and specific humidity are used for the time period of 2006–2019.

In addition, TropFlux latent heat flux and specific humidity are compared to OAFlux data (Praveen Kumar et al., 2012). TropFlux heat fluxes are calculated from the COARE v3 algorithm. In contrast to OAFlux, TropFlux uses ERA-I and therefore, the two datasets are to some extent not related to each other (Praveen Kumar et al., 2012). According to Praveen Kumar et al. (2012), TropFlux and OAFlux are the best-performing heat flux products. TropFlux horizontal resolution is identical to OAFlux, the monthly estimates from 2006 to 2018 are used.

Furthermore, monthly precipitation estimates from the Global Precipitation Climatology Project (GPCP) Version 2.3 are analyzed (Adler et al., 2018; Pendergrass et al., 2020). This data set has a horizontal resolution of $2.5^\circ \times 2.5^\circ$ and data from 2006 to 2019 is used. GPCP combines several satellite measurements and gauge data.

Similar as for the wind data, the heat flux, evaporation and precipitation data are available as monthly estimates. Anomalies are computed by subtracting the corresponding monthly climatology. Finally, with these anomalies the linear decadal trends are computed.

3.2.4 Net Primary Production

Stratification changes are compared to net primary production data from the Ocean Productivity site[2] (Behrenfeld and Falkowski, 1997). The data is based on the Eppley Vertically Generalized Production Model (VGPM) which uses MODIS chlorophyll, SST data, SeaWiFs PAR and estimates of the euphotic zone depth. Net primary production is available for the period of 2002–2019 as monthly values and this study focusses on the years 2006–2019. The horizontal resolution is $1/6^\circ$ in latitude and longitude but the net primary production was re-gridded on a $0.5^\circ \times 0.5^\circ$ spatial grid to reduce noise.

3.3 Theoretical Background

3.3.1 Pure Warming and Freshening Processes in Terms of Heave and Spice

To investigate possible causes for stratification changes it is important to understand that depending on the mean temperature and salinity distribution different processes can dominate. The most common cause for increasing upper- ocean stratification is surface

---

[2] http://sites.science.oregonstate.edu/ocean.productivity/index.php

warming, i.e., surface density reduction. Surface warming can be explored in terms of a vector summation between heave and spice (Bindoff and McDougall, 1994; Häkkinen et al., 2016). However, the sign of heave and spice depends strongly on the stability ratio in the region.

The SETA region encompasses a typical subtropical stratification, i.e., warm and saline water layered above cool and fresh water. Then a pure warming or pure freshening process (i.e., a density reduction) at a fixed depth can be interpreted by using a T-S diagram as follows: in case of a pure warming process (Figure 3.2a, orange arrow) the original thermocline (thin blue line) is shifted to a new position (thick blue line). This results into positive heaving, i.e., the original density surface is sinking downward and is replaced by a lower density on top.

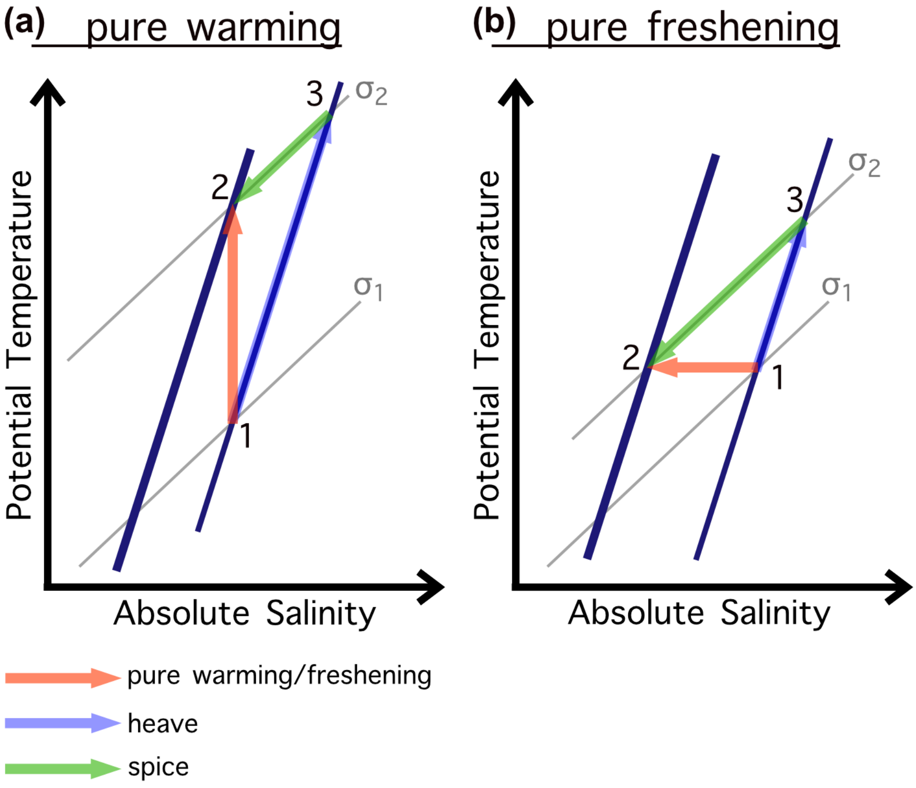

Figure 3.2: T-S relation schematic for a pure warming process **(a)** and a pure freshening process **(b)** for a subtropical stratification (adapted from Bindoff and McDougall (1994); Häkkinen et al. (2016)). Thin blue line indicates initial thermocline, thick blue line the new thermocline. Gray lines show the potential density surfaces (σ_1 as the initial density surface and σ_2 as the density surface at the same depth after the warming/freshening process with σ_2 being smaller and thus lighter than σ_1). 1 indicates the initial starting point, 2 reveals the T-S condition at the same depth after warming/freshening. Orange arrows (1–2) denote the warming/freshening process, green arrows indicate the spice component (3–2) and blue arrows the heave component (1–3).

This heaving is then corrected by a negative spice contribution which is the temperature and salinity change on a density surface. Thus, a parcel at position 2 appears now cooler and fresher than a parcel at position 3 at the same density on the original thermocline (Figure 3.2, following Bindoff and McDougall (1994); Häkkinen et al. (2016)).

The same processes are active for a pure freshening (Figure 3.2b). Instead, a cooling or salinification at a fixed depth results in negative heave and positive spice, i.e., an upward displacement of the isopycnals and warm/saline conditions on the initial density surface (not shown). Note the described cases above are the simplest ones. Observed water mass changes will always be a combination of both.

3.3.2 Pure Heaving Process

Another process that can influence the vertical stratification is pure heaving, e.g., due to changes of wind stress curl. This mechanism is not associated with imprints in the T-S diagram (Bindoff and McDougall, 1994). If wind stress curl-driven upwelling intensifies, isopycnals will rise upward and thereby reducing the height difference between near-surface isopycnals (Figure 3.3) and correspondingly increasing the near-surface stratification or Brunt–Väisälä frequency. In case the height difference between isopycnals is increasing, the stratification decreases. Heaving can thereby alter vertical stratification and additionally may lead to shifts in the heat content (Huang, 2015).

3.4 Results

3.4.1 Decadal Trends of the Tropical Atlantic

This section will deal with mean fields and decadal trend maps of vertical stratification maximum, its depth, mixed layer properties, the vertical displacement and spice of isopycnals in the tropical Atlantic. In order to receive an overview about the on-going changes and explain why we particularly focus on the SETA region (10–20°S, 5°W–15°E) for a more detailed analysis, the maps of the vertical stratification maximum and its depth are computed for the entire tropical Atlantic from 30°N to 30°S. All other maps are confined to a smaller region in the eastern tropical Atlantic ranging from 10°N–30°S, 15°W–20°E which includes the SETA region and is still large enough to explain some observed larger-scale patterns.

The vertical stratification maximum is located just below the mixed layer and is within the depth range of the thermocline. The mean of the vertical stratification maxima shows largest values within 10°N and 10°S especially close to the eastern boundary (Figure 3.4a). These areas largely coincide with areas where the mean depth of the stratification maximum is shallowest (Figure 3.4b).

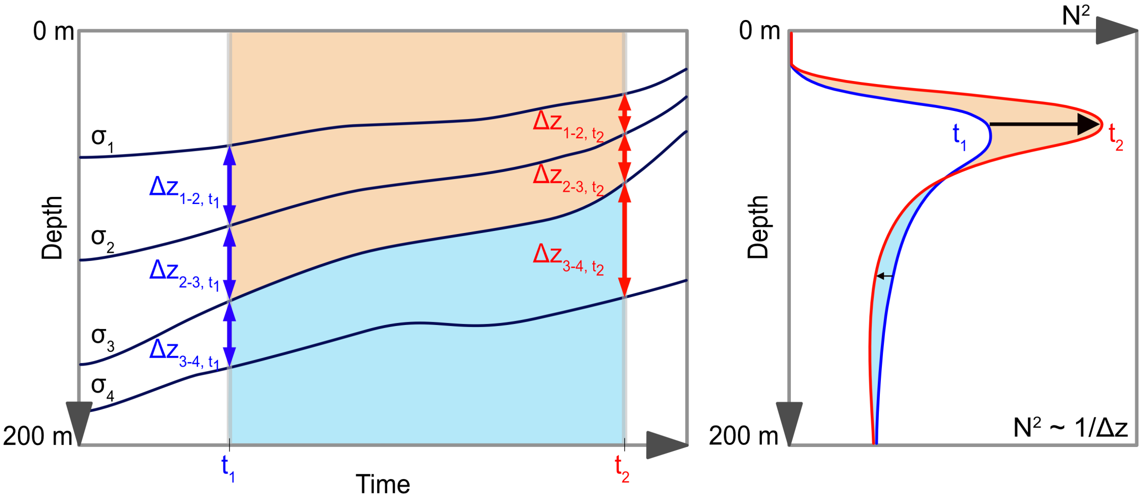

Figure 3.3: Schematic of a pure heaving process as a result of intensified wind curl-driven upwelling. Dark blue lines indicate different isopycnals (σ_1, σ_2, σ_3, and σ_4) whose depth is changing over time. Due to the upwelling of the isopycnals, the height difference Δz between two isopycnals changes over time (compare time steps t_1 and t_2). If the Δz decreases as for the upper two pairs of isopycnals (Δz_{1-2}, Δz_{2-3}) from time step t_1 (blue double arrows) to t_2 (red double arrows), the stratification in terms of the Brunt–Väisälä frequency N^2 increases as indicated in the **right panel** by the typical stratification profile. Here the blue line of the N^2 profile corresponds to the time step t_1 as in the **left panel**. The red profile indicates the profile for t_2. In both panels the depth range where stratification increases, is shaded light orange. In contrast, if the height difference becomes larger over time as for the lower pair of isopycnals (Δz_{3-4}), stratification will be reduced. The depth range where stratification decreases is marked light blue in both panels.

The decadal trend reveals an increase of stratification in the eastern tropical North Atlantic and in most of the tropical South Atlantic away from the equatorial band with maximum increase in the region of SETA (10–20°S, 5°W–15°E) with an intensification of up to 30 % (Figure 3.4c). Besides, where the stratification maximum intensifies, its depth is shoaling (Figure 3.4d). The described increase of stratification in the SETA region as well as in the northeastern tropical Atlantic (Figure 3.4c) are of 95 % statistical significance.

To better characterize the above results, decadal trends of surface mixed layer characteristics have been calculated for the smaller region in the eastern tropical Atlantic (10°N–30°S, 15°W–20°E) (Figure 3.5). On average, the MLD can be found only slightly above the vertical stratification maximum. The equatorial region reveals a deepening of the mixed layer, a cooling and salinification and thus, an increase in density. Further south in the SETA region the MLT is rising, MLS is reducing and the MLD is shoaling (Figure 3.5). Indeed, at the depth of the vertical stratification maximum the patterns of temperature, salinity and density changes are similar (not shown).

In order to understand the acting processes, it is important to not only investigate changes on depth levels but also on density surfaces. Therefore, we inspect the trends of

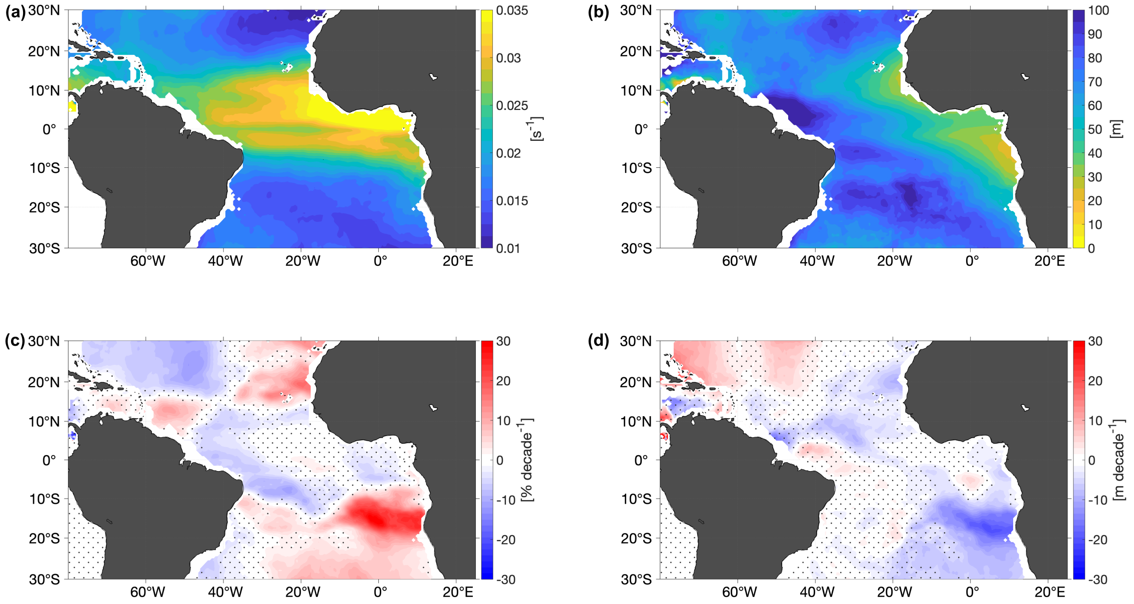

Figure 3.4: **(a)** Mean of vertical stratification maxima inferred from Argo for the time period of 2006–2019. **(b)** Mean depth of the vertical stratification maximum from **(a)**. Panels **(c,d)** decadal trend of **(a,b)**, respectively. Trends are computed from the anomalies relative to the seasonal mean. Please note, positive trend of depth refers to a deepening. Areas where the trend is not of 95 % significance are stippled. Shelf regions below 2, 000 $dbar$ are blanked out.

the vertical displacement (i.e., heave) and the spice of two different isopycnals (25.5 and 26.0 $kg\,m^{-3}$).

These isopycnals are chosen as they are surrounding the vertical stratification maximum in the SETA region. The results of the decadal heave trend show that in most of the southeastern tropical Atlantic these two isopycnals, lying within the upper 150 m, are shoaling (Figures 3.6a,b). The strongest upwelling of the isopycnals is within 10° offshore in the SETA region whereas there is weaker upwelling along the coast (Figures 3.6a,b). Spice trends are relatively weak with a range of up to $\pm 0.2\,g\,kg^{-1}\,\mathrm{decade}^{-1}$ (Figures 3.6c,d). Nevertheless, from the African coastline to 5°W–0° the spice is reducing. Westward of the Greenwich meridian the spice trend is increasing (Figures 3.6c,d).

3.4.2 Regional Analysis of the Southeastern Tropical Atlantic Ocean Region

In this section the SETA region (10–20°S, 5°W–15°E) is investigated in more detail by analyzing its time series. SETA is the region which undergoes the largest stratification increase within the entire tropical Atlantic during the Argo period. In fact, the 6 months running median time series of the percental change of the stratification maximum confirms the observed decadal trend in the SETA region as it continuously intensifies. From 2006 to 2016 the stratification increased by 40 % (Figure 3.7a). From 2016 until the beginning of 2020 the stratification intensified by almost another 20 %. The time series of the depth anomaly onto the mean depth of the stratification maximum shows that the depth is indeed shoaling (around 50 m from 2006 to 2020, Figure 3.7b). The same accounts for the MLD which is on average 20–40 m above the depth of the vertical stratification maximum (Figure 3.7b).

The time series of MLT anomaly reveals almost 3°C temperature rise in the SETA region from 2006 to 2018 (Figure 3.7c). This temperature increase is followed by a minimum of almost -1°C in mid of 2019. At the end of 2019 and beginning of 2020 the MLT depicts a large maximum by around 3.5°C which is by far the greatest peak of the MLT timeseries. MLS is decreasing over time (more than 0.5 $g\,kg^{-1}$), however, there is a negative peak in

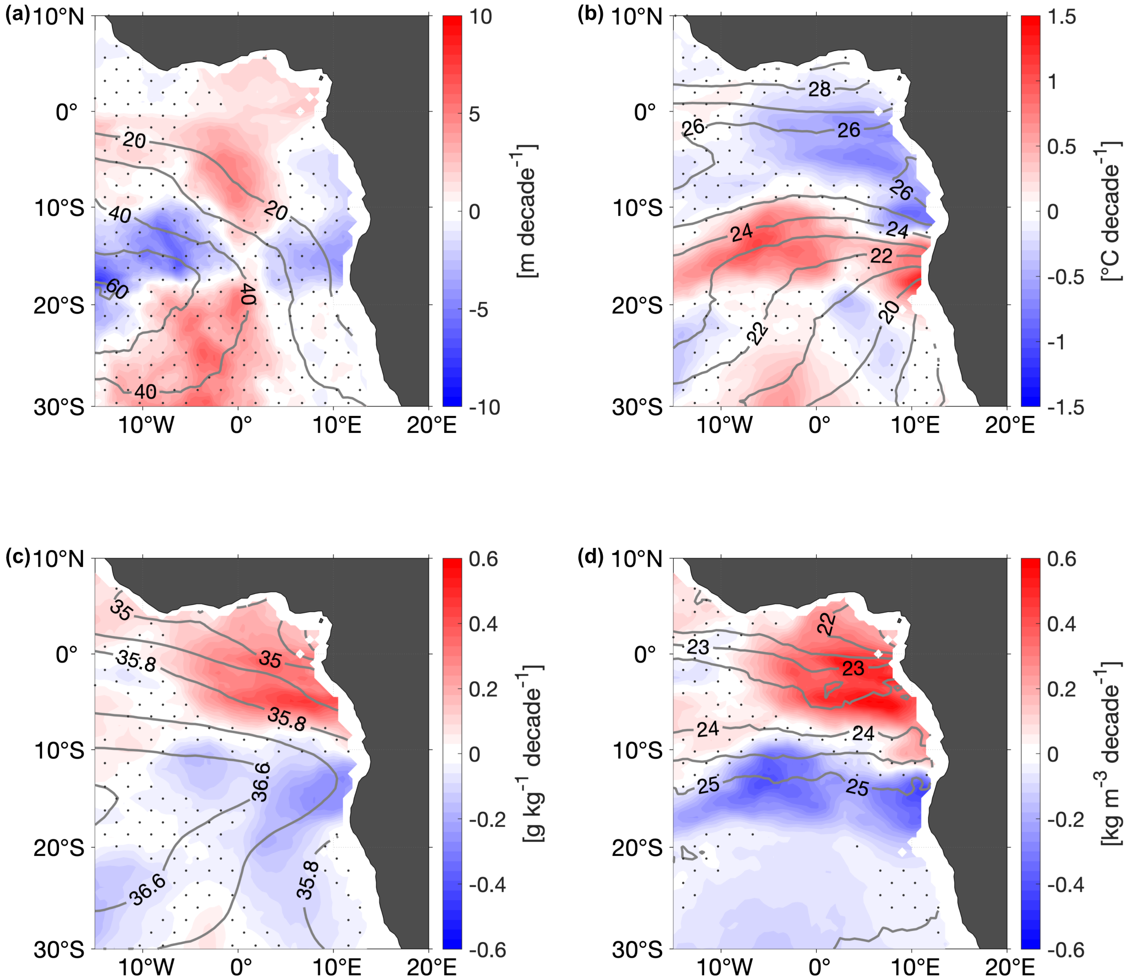

Figure 3.5: Decadal trend of **(a)** mixed layer depth (MLD), **(b)** mixed layer temperature (MLT), **(c)** mixed layer salinity (MLS), and **(d)** mixed layer potential density anomalies from Argo for the time period of 2006–2019. Trends are computed from the anomalies relative to the seasonal mean. Mixed layer properties have been estimated with the Holte and Talley algorithm (Holte and Talley, 2009). Gray contour lines show the mean fields for the period of 2006–2019, respectively. Areas where the trend is not of 95 % significance are stippled. Please note, positive trend of MLD refers to a deepening of the mixed layer. Shelf regions below 2,000 $dbar$ are blanked out.

2008 (Figure 3.7c). Thus, as the mixed layer is becoming warmer and fresher, the density is decreasing (Figure 3.7a). The warming and freshening can be found at the depth of the vertical stratification maximum as well even though not as pronounced as in the mixed layer (not shown).

Shown as well are the time series of salinity anomalies on the isopycnals 25.5, 26.0, and 26.5 $kg\,m^{-3}$ (spice anomalies). The pattern of the time series of spice changes along the 25.5 and 26.0 $kg\,m^{-3}$ isopycnal surfaces is similar to that of MLS (Figure 3.7d). We observe the negative peak in 2008 and since 2011 the spice is decreasing. The spice on the 26.5 $kg\,m^{-3}$ isopycnal is increasing over time indicating that at larger depths different processes are active.

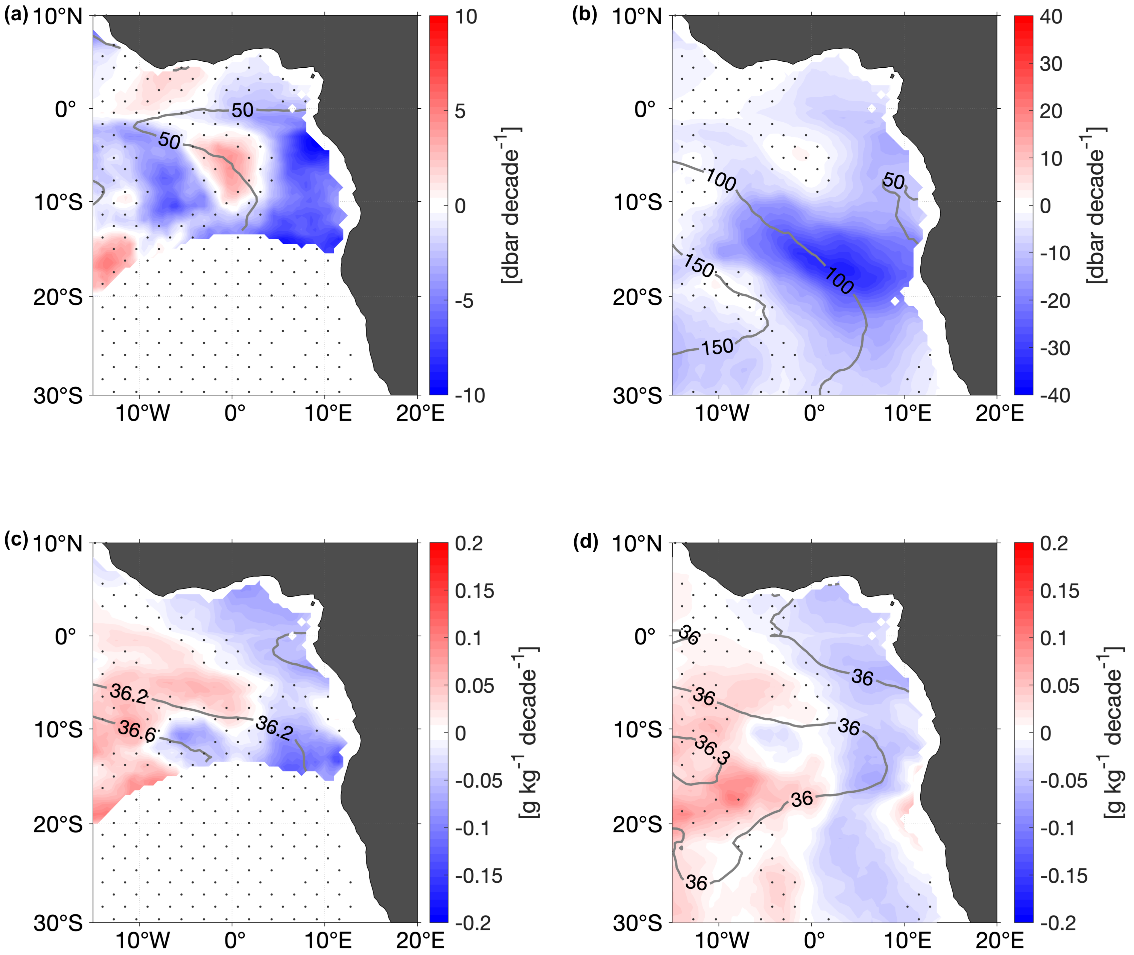

Figure 3.6: Decadal trend of pressure of the isopycnal surfaces **(a)** 25.5 $kg\,m^{-3}$ and **(b)** 26.0 $kg\,m^{-3}$ and decadal trend of absolute salinity on the isopycnal surfaces **(c)** 25.5 $kg\,m^{-3}$ and **(d)** 26.0 $kg\,m^{-3}$ from Argo for the time period of 2006–2019. Trends are computed from the anomalies relative to the seasonal mean. Gray contour lines show the mean fields on each isopycnal surface for the time period of 2006–2019. Areas where the trend is not of 95 % significance are stippled. Please note, positive trend of pressure of isopycnals surfaces refers to a deepening of the isopycnals. Shelf regions below 2,000 $dbar$ are blanked out.

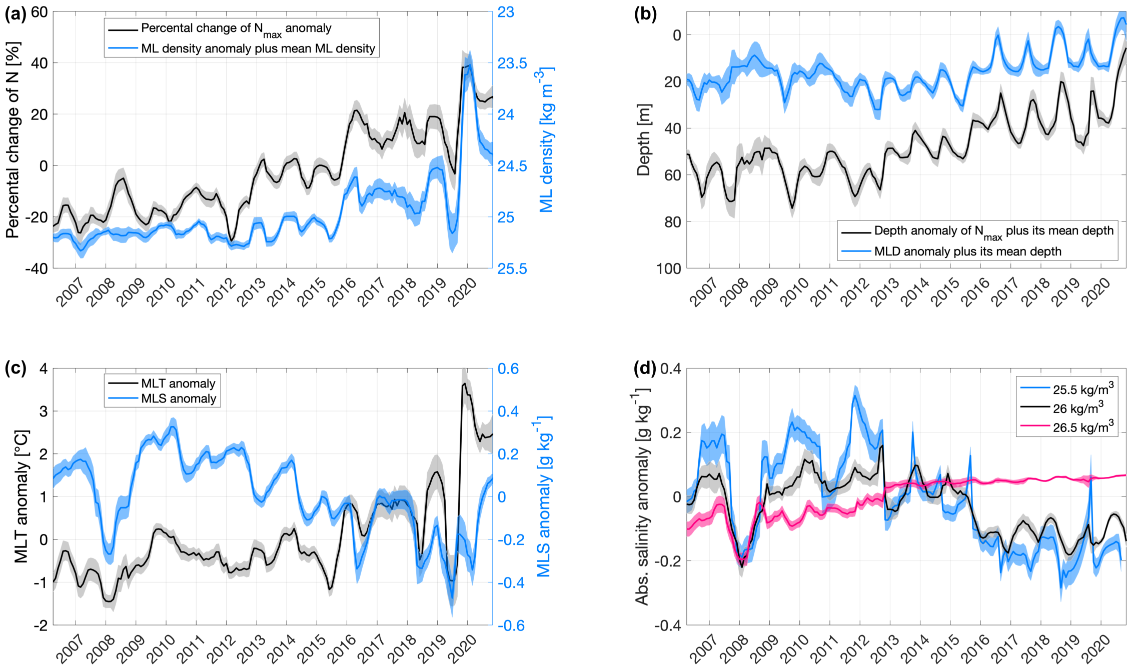

Figure 3.7: Six months running median of **(a)** percental change of stratification anomaly of its vertical maximum N_{max} (black line, left y-axis) and mixed layer (ML) density anomaly plus mean ML density (blue line, right y-axis), **(b)** depth anomaly of the vertical stratification maximum plus its mean depth (black line, left y-axis) and mixed layer depth (MLD) anomaly plus mean MLD (blue line, right y-axis), **(c)** mixed layer temperature (MLT) anomaly (black line, left y-axis) and mixed layer salinity (MLS) anomaly (blue line, right y-axis) and **(d)** salinity anomaly on the isopycnal surfaces (i.e., spice anomaly) in SETA (10–20°S, 5°W–15°E). In **(d)** blue line denotes the 25.5 $kg\,m^{-3}$ isopycnal, black line the 26.0 $kg\,m^{-3}$ isopycnal and pink line the 26.5 $kg\,m^{-3}$ isopycnal. All anomalies are computed relative to the seasonal mean. Shading shows the corresponding 95 % confidence interval.

In order to visualize salinity, temperature and stratification changes within the upper 200 m of the water column in the SETA region, a T-S diagram for annual averages of the Argo temperature and salinity profiles was drawn (Figure 3.8). The derived T-S diagram highlights a typical subtropical stratification with warm, saline water layered above cool, fresh water on average in the SETA region. The annual mean profiles indicate that the water column becomes more stratified during the observing period (Figure 3.8). However, this does not happen constantly on all depth levels. Largest changes are indeed found in the near-surface waters where the conditions are changing toward warmer and especially fresher characteristics. This confirms the observed mixed layer changes. Since 2009 this shift happens to be continuous and thus, the upper water column is becoming more stratified (Figure 3.8).

The T-S diagram reveals that in deeper levels the stratification is becoming slightly weaker (Figure 3.8). This is supported by mean Brunt–Väisälä frequency profiles for three time periods: 2006–2010, 2011–2015, and 2016–2020 which indicate a continuous increase of stratification in the upper 60 $dbar$ and a decrease below 60 $dbar$ (Figure 3.9b).

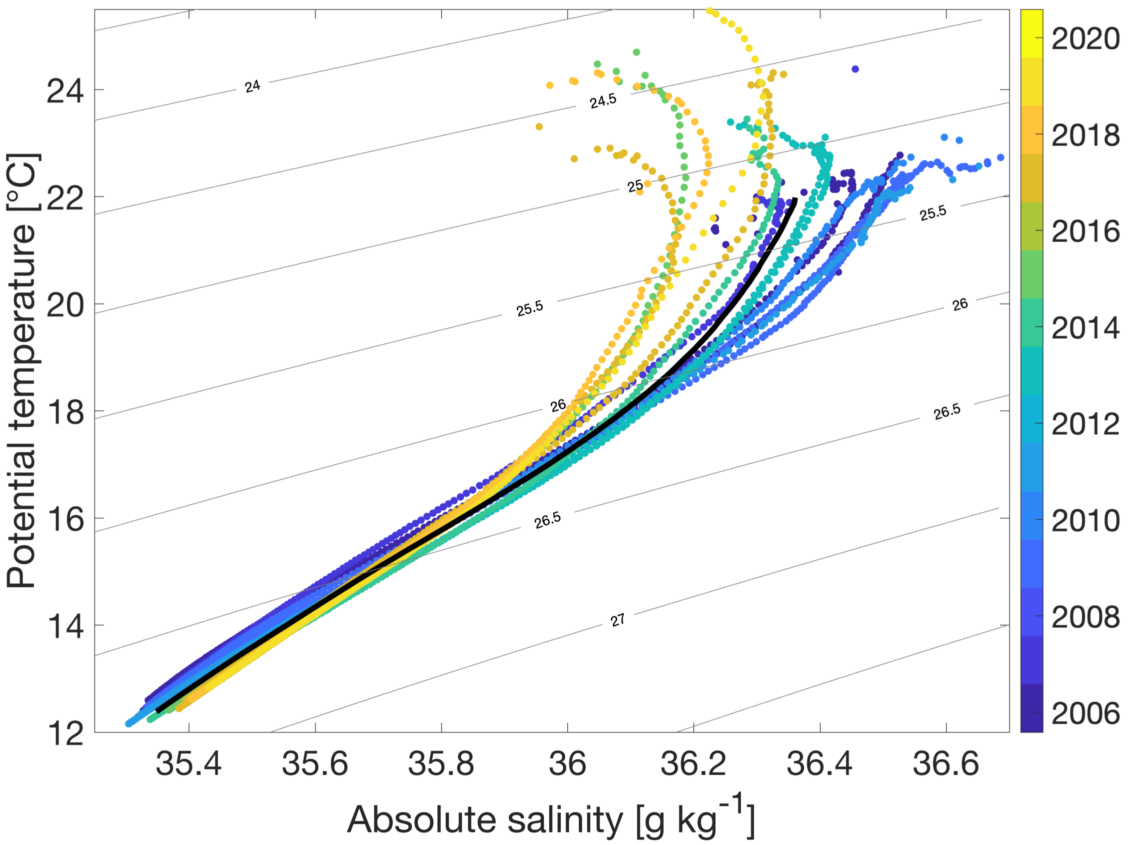

Figure 3.8: T-S diagram of annual mean potential temperature and absolute salinity values of the upper 200 m in the SETA region (10–20°S, 5°W–15°E). Black line indicates the mean of the time period of 2006–2020.

In comparison to the stratification profiles, the time series of the 6 months running median pressure anomaly of the three isopycnal surfaces 25.5, 26.0, and 26.5 $kg\,m^{-3}$ plus their corresponding mean pressure are shown. We can see how the isopycnals change their vertical position and how the stratification profile alters in the respective depth over the corresponding time period (Figure 3.9a). The time series indicate a steady upward displacement of the three isopycnals. However, the height difference between the isopycnals changes differently (Figure 3.9a). This is especially visible from the slope of the corresponding trend lines (Figure 3.9a). We find that in the depth range of the largest stratification increase, the isopycnals surfaces 25.5 and 26.0 $kg\,m^{-3}$ are becoming closer to each other. Whereas below, the height difference between the 26.0 and the 26.5 $kg\,m^{-3}$ enlarges. This is the same depth range where stratification weakens.

3.4.3 Decadal Wind Stress Changes in the Southeastern Tropical Atlantic Ocean Region

In this section we contrast the prior findings of the decadal changes in the SETA region with changes of the wind stress curl, zonal and meridional wind stress components as well as wind speed. Starting with the decadal trend maps of these four variables in the eastern tropical Atlantic to achieve an overview (Figure 3.10), we discover that close to the African coast in the South Atlantic east of the mean zero-line, the wind stress curl reveals a negative trend. This implies the wind stress curl in this region is becoming more negative. West of the zero-line the wind stress curl anomaly shows a positive trend (Figure 3.10a).

The decadal trend of the wind speed anomaly shows an increase in the southern part of SETA, whereas in the northern part of SETA and around SETA the trend of wind speed is negative (Figure 3.10b). Comparing this to the zonal wind stress component, we find a negative trend in the area of intensified wind speed in SETA, i.e., intensified easterlies. The positive trend is surrounded by westerly trend. The meridional wind stress component which is on average directed northward in the SETA region depicts a negative trend in the northern part of this region, thus, indicating a weakening of southerly winds.

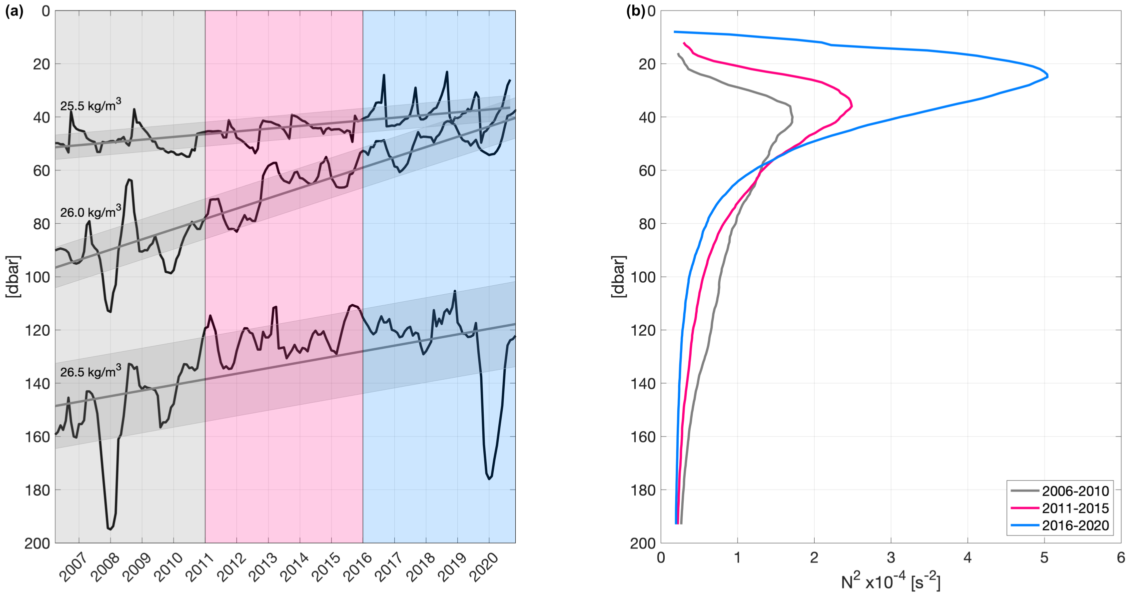

Figure 3.9: **(a)** Six months running median pressure anomaly of three isopycnals (25.5, 26.0, and 26.5 $kg\,m^{-3}$) plus their corresponding mean pressure in the SETA region (10–20°S, 5°W–15°E). For each isopycnal the linear trend (gray line) and its standard error are shown (gray shading around the linear trend lines). Shaded areas indicate the time periods for the corresponding mean Brunt–Väisälä frequency profile of the upper 200 $dbar$ in **(b)**. Gray shows the mean for the time of 2006–2010, pink denotes the mean of 2011–2015 and blue indicates the period of 2016–2020.

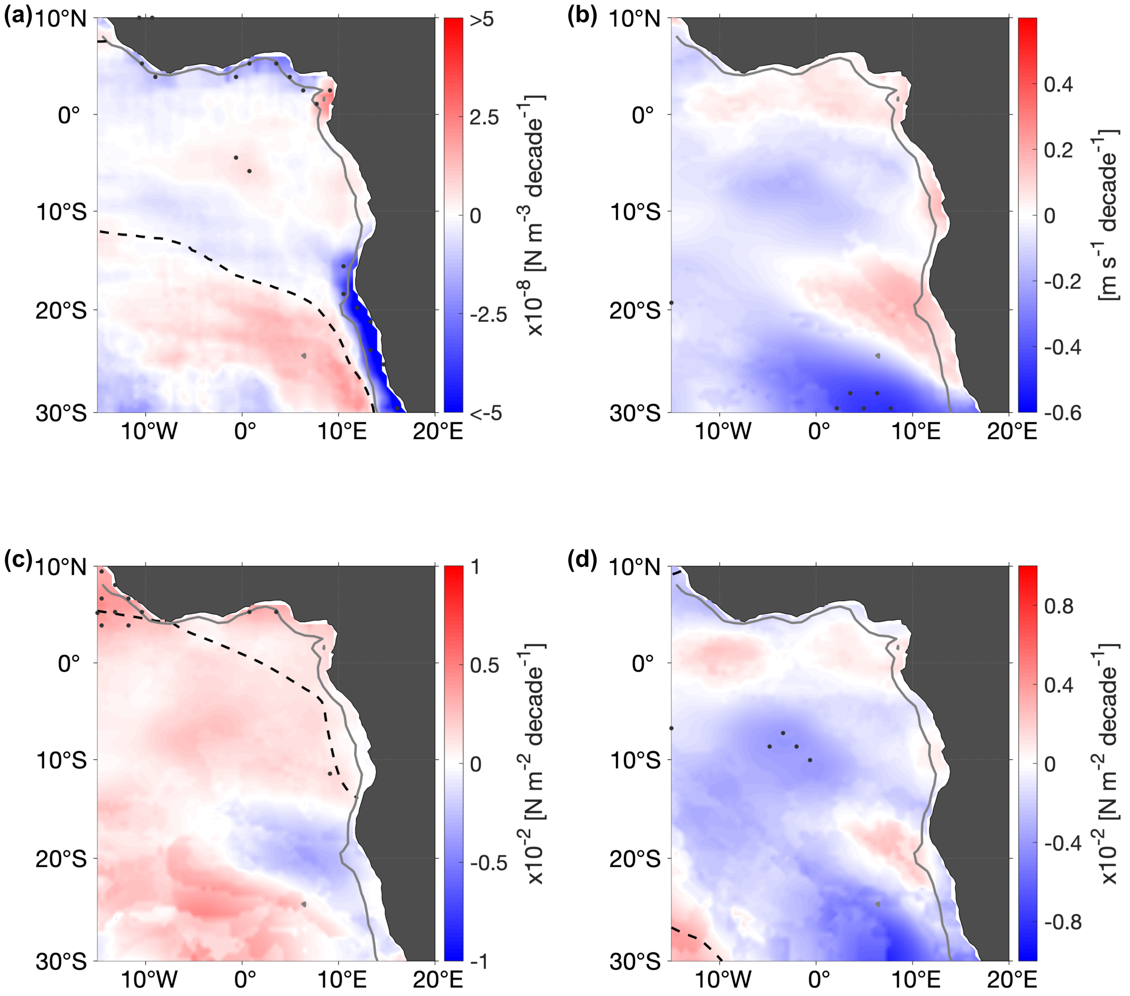

Figure 3.10: Decadal trend of **(a)** wind stress curl, **(b)** wind speed, **(c)** zonal wind stress component, and **(d)** meridional wind stress component from monthly values from Copernicus Marine environment monitoring service (CMEMS) from ASCAT scatterometers on METOP-A and METOP-B satellites for the time period of 2007–2019. Trends are computed from the anomaly relative to the monthly mean. Black dashed lines indicate the zero-lines of the corresponding mean fields, respectively. Areas where the trend is of 95 % significance are stippled. Gray line marks the 2,000 *dbar* isobath of the shelf regions.

In the southern part of SETA, the wind stress anomaly shows a slight increase of the northward component (Figure 3.10d).

Focusing on the wind stress curl and the meridional wind stress component, the zonal sections of the 6 months running mean of the two components in the SETA region, show that indeed within 500 *km* of the coast the wind stress curl becomes more negative. In contrast, since 2009 meridional wind stress anomalies shift from northward to southward anomalies within about 200 *km* of the coast. Since 2017 again more northward anomalies are observed (Figure 3.11).

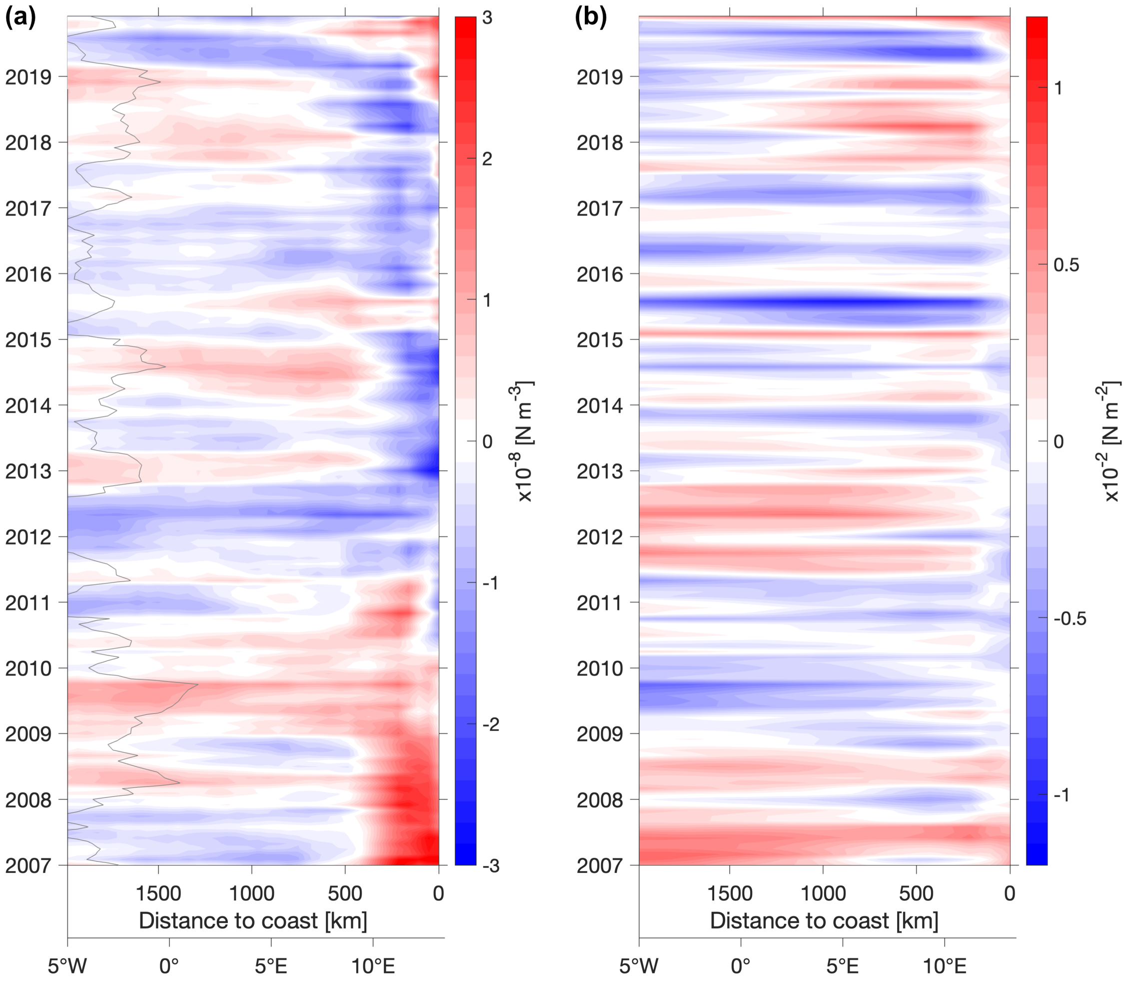

Figure 3.11: Six months running mean of **(a)** wind stress curl anomaly and **(b)** meridional wind stress anomaly meridionally averaged in SETA (10–20°S, 5°W–15°E) as a function of distance to the coast (at about 13.5°E) and time as inferred from Copernicus Marine environment monitoring service. Anomalies are computed relative to the monthly mean of the period of 2007–2019. Gray contour line in **(a)** indicates the zero-line of the mean wind stress curl, i.e., east of this line the mean wind stress curl is negative while west of this line it is positive.

3.4.4 Analysis of Latent Heat Fluxes, Evaporation and Specific Humidity

In order to investigate a possible forcing of the observed mixed layer changes, in this section decadal trends of latent heat flux, precipitation, specific humidity and evaporation are evaluated for the eastern tropical Atlantic. It is important to point out that the latent heat flux and specific humidity differ substantially among the two analyzed products.

The trend of OAFlux latent heat flux shows positive values in almost the entire eastern tropical Atlantic, i.e., the oceanic latent heat loss is reduced (Figure 3.12a). Only a region around 10°S, 10°W shows an increase in oceanic latent heat loss as well as an area south of 20°S close to the Namibian coast. Accordingly, decreasing evaporation trends are observed where latent heat loss is reduced (Figure 3.12c). Contrary, oceanic latent heat loss from

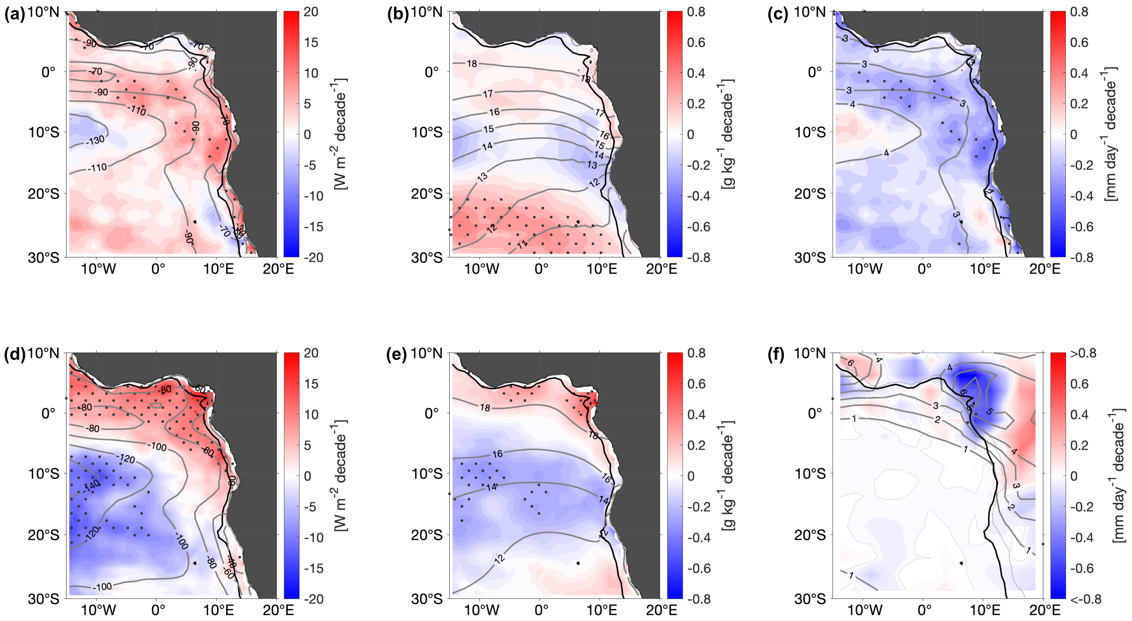

Figure 3.12: Decadal trend of **(a)** latent heat flux anomaly, **(b)** specific humidity anomaly, and **(c)** evaporation anomaly from OAFlux data (2006–2019) and **(d)** latent heat flux anomaly and **(e)** specific humidity anomaly from TropFlux data (2006–2018) as well as **(f)** precipitation anomaly of GPCP data (2006–2019). All anomalies are computed relative to the corresponding monthly means. Note, a negative latent heat flux indicates that the ocean loses heat. Gray contour lines show the corresponding mean field. Areas where the trend is of 95 % significance are stippled. Black line indicates the 2,000 *dbar* isobath of the shelf region.

TropFlux shows an increase south of 5°S away from the coast. North of 5°S including the Gulf of Guinea and along the coast the latent heat loss is decreasing (Figure 3.12d).

In addition, the trend of specific humidity of OAFlux reveals increasing humidity in the equatorial region while south of that region humidity is found to be reduced. Southward from 15◦S humidity increases again (Figure 3.12b). For the TropFlux product humidity increases in the Gulf of Guinea and within the coastal regions extending southward to about 10°S (Figure 3.12e). The reduction of specific humidity is spatially larger than in OAFlux and even reaches up to 25–30°S. These differences among OAFlux and TropFlux highlight the uncertainties in the heat flux trends.

Besides, GPCP precipitation trend demonstrates a decline of precipitation in the area of the equatorial region, while slightly south of it the precipitation increases (Figure 3.12f). The Congo drainage basin reveals intensified precipitation rates.

3.4.5 Primary Production

The SETA upwelling system is a key region of enhanced nutrient supply to the euphotic zone that fuels local primary productivity. This section contrasts the observed signals in stratification with rates of net primary production derived from satellite observations. The mean field of net primary production for the period of 2006–2019 shows elevated

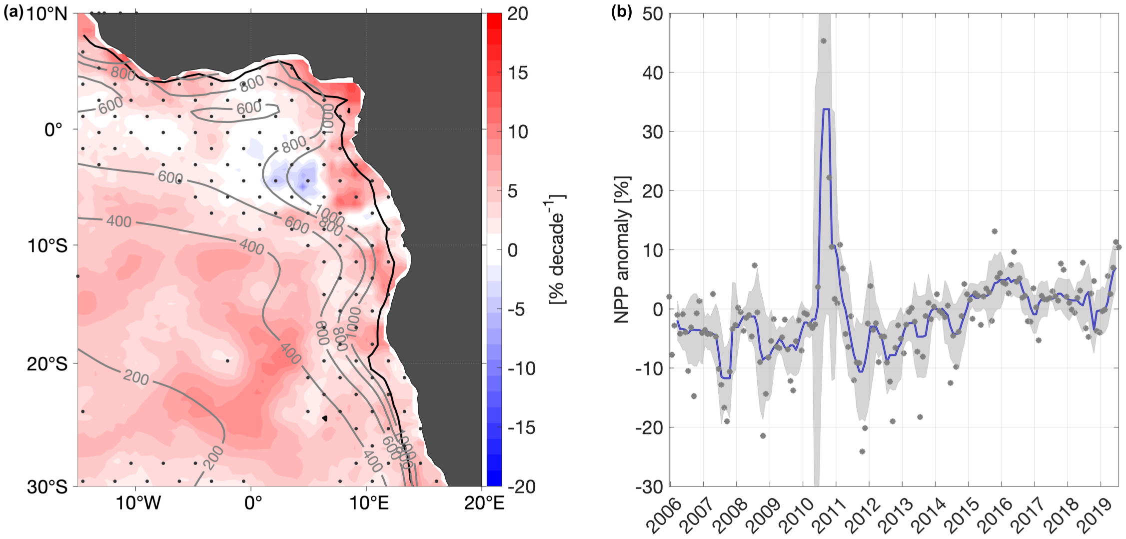

Figure 3.13: **(a)** Decadal trend of net primary production (NPP) deduced from satellite observations from Ocean Productivity site for the time period of 2006–2019. The decadal trend has been evaluated from the anomalies relative to the corresponding monthly means. Areas where the trend is not of 95 % significance are stippled. The gray contour lines in **(a)** show the mean NPP field. The black contour line indicates the 2,000 *dbar* isobath of the shelf region. **(b)** Six months running median NPP anomaly in SETA region (10–20°S, 5°W–15°E) in percent (blue line). Anomalies are computed to the monthly mean. Shading denotes the standard deviation and dots refer to the given monthly values from the product.

values especially within the eastern boundary regions and in the equatorial upwelling region (Figure 3.13a). The decadal trend pattern from the time series reveals that primary productivity in open ocean is increasing around 5–10 % per decade almost everywhere in the eastern tropical Atlantic (Figure 3.13a). Specifically, in the SETA region primary production is intensifying as well (Figure 3.13a). North of the SETA region primary production depicts a small decreasing trend. The overall trend pattern correlates with the trend of the vertical stratification maximum except from the equatorial region, i.e., in general there is higher productivity in regions with enhanced stratification and shoaling stratification maximum (cf. Figures 3.4c,d, 3.13a).

Taking a closer look at the 6 months running median percental change of the net primary production in the SETA region, the time series of the median shows a maximum of above 30 % primary production in 2010 (Figure 3.13b). Except from this maximum the primary productivity seems to increase in the SETA region. For the years 2012–2019 the productivity is continuously enhancing (Figure 3.13b).

3.5 Discussion

3.5.1 Physical Processes Leading to the Observed Stratification Changes

The findings of this study highlight locally large stratification increases within the upper 200 m in the tropical Atlantic Ocean for the Argo observation period of 2006–2019. Especially within the SETA region (10–20°S, 5°W–15°E) we observe an almost 60 % intensification of the vertical stratification maximum from 2006 to 2020. This enhanced stratification is related to a warming, freshening and shoaling of the mixed layer. It represents a shift from subtropical stratification with salinity maximum water at the top toward a tropical stratification with warm and fresh surface waters (Figure 3.8). Mixed layer characteristics in the SETA region steadily change over time, i.e., changes are not confined to some single years. We observe a continuous warming of the mixed layer of 3°C during the years of 2006–2018 as well as a freshening of more than $0.5\, g\, kg^{-1}$ from 2009 to 2020 (Figure 3.7). The MLT timeseries revealed a substantial temperature drop in 2019 which was followed by a warm mixed layer event at the end of the year (Figure 3.7). The negative MLT anomaly might be a result of an uneven distribution of the Argo profiles. The warm event in the beginning of 2020 can be associated to a Benguela Niño according to the classification given in Imbol Koungue et al. (2019).

Following the method of Bindoff and McDougall (1994) a pure warming or a pure freshening at a fixed depth for a typical subtropical stratification, as in the SETA region identified, should be the vector summation of negative spice and positive heave. Indeed, we observe the decline of spice on the isopycnals surrounding the vertical stratification maximum (Figure 3.7d). Yet, the isopycnals are rising (implying a negative heave, Figure 3.9a) and not deepening as anticipated for a pure warming or freshening process. Maximum upwelling of the isopycnals is observed about 10° offshore in the SETA region (Figure 3.6). Hence, another process has to be involved in the stratification increase. Wind stress curl-driven changes can lead to pure heaving (i.e., vertical adjustment of isopycnals) which is not associated with signatures in the T-S diagram (Bindoff and McDougall, 1994; Huang, 2015). In fact, we found an already negative wind stress curl becoming more negative in the SETA region, i.e., wind curl-driven upwelling is favored. As upwelling intensifies, isopycnals slope upward just as the time series show (Figure 3.9a). This suggests that the wind curl-driven upwelling is superimposed onto the pure warming and freshening processes discovered in the mixed layer and is obviously having a larger effect on the vertical displacement of the isopycnals. Besides, the heave mechanism does not contradict the stratification increase. The upper isopycnals are rising and thereby the distance between the 25.5 and the $26.0\, kg\, m^{-3}$ is reducing and correspondingly the Brunt–Väisälä frequency is increasing (Figure 3.9). For the $26.5\, kg\, m^{-3}$ isopycnal different processes seem to be involved. This deeper isopycnal is shoaling too, however, the distance between the 26.0 and the 26.5 $kg\,m^{-3}$ isopycnals is becoming larger. Furthermore, the spice on the 26.5 $kg\,m^{-3}$ isopycnal is slightly increasing (Figure 3.7). This indicates that stratification changes do not happen constantly at all depth levels which is confirmed by the T-S diagram with annual mean profiles of temperature and salinity (Figure 3.8) and by the mean Brunt–Väisälä frequency profiles for three different time periods (Figure 3.9b). At deeper levels (at the depth around the 26.5 $kg\,m^{-3}$ isopycnal) the stratification is decreasing slightly (Figure 3.9).

Partly in contrast to the above noted findings related to the wind stress curl is that the meridional wind stress shows a shift from northward to southward anomalies within 200 km of the coast. This implies downwelling favorable conditions close to coast. However, southward wind stress anomalies could result in an increasing southward extent of near-equatorial surface waters approaching the SETA region and thereby altering the primarily subtropical stratification in the SETA region to more tropical conditions. In addition, we can compare the decadal trend pattern of wind speed and zonal wind stress, where the southern part of the SETA region reveals a slight intensification of the southeast trades. However, this area is surrounded by a westerly (positive) zonal wind stress trend, implying a weakening of the trades. Overall, it seems that the SASH is moving or extending poleward and thereby changing the prevailing winds near the African coast (Figure 3.11). Indeed, Zilli et al. (2019) found the SASH is extending further southwestward in the period of 2005–2014 compared to 1979–1991. Their results indicate that the shift produces a cyclonic anomaly of the wind over the tropical South Atlantic. Hence, this fits well to our observation of negative wind stress curl anomaly in the SETA region. Associated with the change of the SASH, the BLLCJ might have been modified, too. According to Patricola and Chang (2017), the BLLCJ shows a large intraseasonal variability linked to the SASH. Intense jet events are found to be aligned with a strengthened SASH and increased equatorward meridional wind stress 5–10° offshore from the coast in the SETA region. Further offshore and to the north of this region, however, they found that the meridional wind stress is reduced. This pattern is similar to what our results show on decadal timescales and thus, indicates that during the observational period of our study the BLLCJ might have strengthened and led to the associated wind stress changes. In addition, future projections of Lima et al. (2019b) also show that as a result of global warming the SASH is going to intensify and therefore amplify the pressure gradient toward the Angolan low pressure. This is further associated with a poleward movement of the SASH and is assumed to cause a wind speed increase around 26°S whereas north of 17.5°S the wind speed is going to be reduced.

Nonetheless, careful attention must be taken with satellite wind products as they often do not represent coastal areas very well. The statistical significance test shows how uncertain these products are which is a problem for climatic studies. Despite this uncertainty, it is still important to point out that the isopycnals are continuously shoaling which has to be a result of intensified wind curl-driven upwelling. It indicates that the observed wind stress data has to be trustworthy to some extent.

Changes of the latent heat flux, evaporation and specific humidity strongly depend on the used product (Figure 3.12). Following the decadal trends from OAFlux, the freshening of the mixed layer could be associated with a decreased oceanic latent heat loss and thus, reduced evaporation. Conversely, latent heat flux and humidity trends from TropFlux actually indicate a decline in humidity in most of the tropical South Atlantic and increased oceanic latent heat loss. Only close to the coast and in the equatorial region the heat loss is reduced. This would rather be a sign for a salinification of the mixed layer. The large uncertainty of the heat flux products makes it difficult to interpret our findings of the mixed layer changes. Also, the test of significance mirrors the great uncertainty of these products.

The GPCP precipitation data shows a rising trend in the drainage area of the Congo River. This might enhance river input and thus increase freshwater fluxes into the ocean. However, caution must be taken as precipitation data in the tropical regions is uncertain. In fact, different precipitation products show inconsistent variabilities in the tropical oceans (Sun et al. (2018) and references herein). The mean precipitation pattern is well-represented with GPCP data. Yet, there are large variations in regions with a small amount of gauge stations (Sun et al. (2018) and references herein). Besides, the significance analysis reveals barely anywhere significant trends. It is unfortunate that the meteorological data are so uncertain which makes it difficult to interpret and explain results from a climatic study like this one.

Despite the fact, that the Argo time series of the SETA region indicate mostly a steady increase or decline, we must be aware that there are uncertainties due to either an uneven distribution of the floats within the region as well as a minimum number of profiles in 2008. However, the time period of 2009–2018 shows an amount of 300 profiles and more per year allowing to achieve confident results.

As a matter of climate change, stratification is expected to increase due to the warming of ocean's surface (Capotondi et al., 2012). Yamaguchi and Suga (2019) and most recently Li et al. (2020) highlighted the continuous enhancement of the stratification in the global oceans since the 1960s with largest impacts within the upper 200 m in the tropics. Comparing their global results to our findings of the last 13 years, does not yield guarantee that the increased stratification in the SETA region is a result of the on-going global warming. Probably, the much larger trends in the SETA region compared to the global trends suggest still internal climate variability as the main reason. However, also a poleward migration of the SASH that could be forced by climate warming would contribute to enhanced warming. Thus, also the superposition of different climate-warming induced processes could result in the observed regionally enhanced trends.

3.5.2 Comparison of Stratification and Mixed Layer Changes to Observations of Primary Productivity

Changes in the upper-ocean stratification matter as they affect not only physical ocean dynamics such as ocean ventilation processes but also biogeochemical and ecological activities such as nutrient fluxes and fisheries. Nevertheless, the consequences of increased stratification for upwelling regions are not yet fully understood (Jarre et al., 2015). The SETA upwelling system is a key region for enhanced nutrient supply to the euphotic zone and hence, a core nutrient source for high coastal primary productivity. The nutricline is just below the mixed layer depth and within the depth range of the vertical stratification maximum in this region. The location of the nutricline was checked from individual profiles (Schlitzer, 2021). The common assumption is that increased stratification as a result of global warming will weaken mixing processes that are responsible for the upward nutrient flux to the surface waters and thereby reducing the primary production (Capotondi et al., 2012). In contradiction, our findings reveal that the net primary productivity is actually rising since 2012 in the SETA region and thereby correlating with the increase in stratification but also warming, freshening and shoaling of the mixed layer as well as the depth of the stratification maximum. In fact, this fits to enhanced observed long-term trends of chlorophyll-a data off Angola and northern Benguela recently reported by Lamont et al. (2019). Additionally, Jarre et al. (2015) discussed increased chlorophyll-a in Northern Benguela from 2006 to 2010 which was found along with a warming of the sea surface and decreased coastal upwelling. They assume that the upwelling was still in favor for primary productivity and anomalous downwelling not strong enough to suppress mixing. Actually, our findings for the SETA region indicate increased wind curl-driven upwelling associated with shoaling depths of the stratification maximum and the mixed layer. This process could instead enhance the nutrient supply into the euphotic zone and could thus explain the rising rates of primary productivity in recent years.

Furthermore, given that except from the equatorial region the trends of primary production and stratification seem to coincide, this highlights the uncertainties and lack of understanding that we are still dealing with concerning the linkage between stratification and primary production. In fact, Lozier et al. (2011) identified that there exists a direct relationship between stratification and primary productivity on seasonal time scales. Nevertheless, they concluded that on longer time scales the two variables cannot be linked so easily anymore.

Our time series shows an outstanding event in 2010 of above 30 % increase of primary productivity. According to Bachèlery et al. (2016), interannual variations in biogeochemistry (such as nitrate and oxygen) off Angola, Namibia and Benguela are mainly generated by remote equatorial forcing due to CTWs. These variations of nitrate and oxygen have a large influence on the chlorophyll and primary productivity. Indeed, Bachèlery et al.

(2016) state that off Angola these events are responsible for up to 30 % of the mean primary productivity. Hence, such an event could have contributed to this large maximum in primary productivity in 2010. An indicator for this could be the cold event in 2010 prior to the Benguela Niño in 2011 (Imbol Koungue et al., 2019). However, this is something we cannot prove with Argo observations as they are not able to represent CTWs.

Given that the net primary productivity data is based on a satellite product, the findings should be treated with caution. Satellite products of primary production are based on empirical models as from Behrenfeld and Falkowski (1997) and are no direct measurement. These models use satellite measurements of chlorophyll and SST. Satellites only measure the surface layer (Robinson, 2010). Hence, we do not know about the primary productivity at greater depth or if there is a vertical shift of biomass. There might be a compression of the primary productivity near the surface in case of thinner mixed layers, which would be better visible in satellite data. Nevertheless, compared to situations with thicker mixed layers, this could still imply a reduction of vertically integrated primary productivity.

3.5.3 Possible Implications for the Pelagic Fishes

Understanding the consequences of enhanced stratification on primary productivity is key as this will have further impact on the marine food web. In fact, small pelagic fishes are sensitive to climate variability (Bakun et al., 2015; López-Parages et al., 2020; Peck et al., 2021). For instance, variations in temperature and food availability can lead to migrations of small pelagic fishes and to changes of their behavior (Brochier et al., 2018; López-Parages et al., 2020). Our observed stratification transition from subtropical to tropical conditions associated with a warmer mixed layer is likely to impact the small pelagic fishes in the SETA region. We now propose a hypothesis on the physics-to-fish relation in this region, in particular concerning the coexistence of the sardinellas *S. aurita* preferring the warm tropical waters north of the ABF and the sardines *S. sagax* favoring cooler temperatures south of the ABF (BCC, 2012). The two stocks migrate seasonally following their temperature and habitat preferences, with the SETA region being the preferred habitat for adult sardinella during austral summer (Boley and Fréon, 1980). As a result of the warming mixed layer and increasing stratification, the ABF is shifting southward. This gives the tropical sardinellas the possibility to migrate southward to stay within their best spawning and feeding environment on an all-year basis. There are indications that the tropical sardinellas of all age classes may have colonized this region during the recent decade. Indeed, Ekau et al. (2018) observed a southward shift of sardinella larvae from southern Angola to northern Namibia in the past few years. Ostrowski and Barradas (2018) reported the increasing incidence of juvenile sardinellas in trawl catches from this region during recent years. Additionally, the Benguela Current Convention (BCC, 2012) reported an increasing biomass of sardinellas off Angola and at the same time, a reduction of sardine biomass off Angola associated with a southward shift of the ABF. Sardinellas and sardines are in no feeding competition but they favor different hydrographic conditions. Besides the hydrographic parameters, there are other factors, such as the bathymetry, that impact the distribution of sardinellas and sardines which cannot be neglected.

To conclude, our results regarding the warming mixed layer and thereby stratification increase, suggest an evolution from sardine to sardinella habitat in the SETA region. Therefore, fishermen will have to adapt to new circumstances which probably will lead to economic consequences. According to Bearak and Mooney (2019), six to seven species off Angola have almost disappeared in recent years from fishermens' catches in the SETA waters, leading to substantial disturbances for the fishing industry of Southern Angola.

3.6 Conclusion

To summarize, this study gives an insight about recent stratification increase related to a change from subtropical toward tropical conditions in the SETA upwelling region. This is associated with mixed layer warming and freshening as well as intensified wind stress curl-driven upwelling. The impact on biological processes is still lacking of knowledge. Nevertheless, this study indicates, that the relationship between stratification and primary production is not that straight forward as previously thought. In contrast to climate projections, the satellite-derived primary production shows an increasing trend, which, however, remains to be verified by *in situ* data.

3.7 Data Availability Statement

Publicly available datasets were analyzed in this study. This data can be found here: Argo (2019). Argo float data and metadata from Global Data Assembly Centre (Argo GDAC) – Snapshot of Argo GDAC of November 13th 2019. SEANOE. https://doi.org/10.17882/42182#68322; Argo (2020). Argo float data and metadata from Global Data Assembly Centre (Argo GDAC) – Snapshot of Argo GDAC of November 25th 2020. SEANOE. https://doi.org/10.17882/42182#78698; Brandt, Peter, Hahn, Johannes, Schmidtko, Sunke, Tuchen, Franz Philip, Kopte, Robert, Kiko, Rainer, Bourlès, Bernard, Czeschel, Rena, and Dengler, Marcus. (2021). Data and scripts used in "Atlantic Equatorial Undercurrent intensification counteracting warming induced deoxygenation" (Version 2) [Data set]. Zenodo. https://doi.org/10.5281/zenodo.4478285; Climate Data Guide: GPCP (Monthly): Global Precipitation Climatology Project. https://climatedataguide.ucar.edu/climate-data/gpcp-monthly-global-precipitation-climatology-project; Ocean Productivity Site: http://orca.science.oregonstate.edu/1080.by.2160.monthly.hdf.eppley.m.chl.m.sst.php; TropFlux – Indian National Centre for Ocean Information Services: latent heat and specific humidity: https://incois.gov.in/tropflux/tf_products.jsp; WHOI OAFlux: latent heat, evaporation and specific humidity: https://oaflux.whoi.edu/data-access/; Wind TAC (2018): *WIND_GLO_PHY_CLIMATE_L4_REP*_012_003 – Global Ocean Wind L4 Reprocessed Monthly Mean Observations, E.U. Copernicus Marine Service Information. Available at: https://resources.marine.copernicus.eu/?option=com_csw&view=details&product_id=WIND_GLO_PHY_CLIMATE_L4_REP_012_003.

3.8 Acknowledgements

We acknowledge the WHOI OAFlux project (http://oaflux.whoi.edu) funded by NOAA Climate Observations and Monitoring (COM) program for providing the global ocean heat flux and evaporation products and TropFlux data which is produced under a collaboration between Laboratoire d'Océanographie et du climat : Expérimentations et Approches Numériques (LOCEAN) from Institut Pierre Simon Laplace (IPSL, Paris, France) and National Institute of Oceanography/CSIR (NIO, Goa, India), and supported by Institut de Recherche pour le Développement (IRD, France) for the heat flux product. TropFlux relies on data provided by the ECMWF Re-Analysis interim (ERA-I) and ISCCP projects. Additionally, we acknowledge the Climate Data Guide: GPCP (Monthly): Global Precipitation Climatology Project. Achieved from https://climatedataguide.ucar.edu/climate-data/gpcp-monthly-global-precipitation-climatology-project. Furthermore, this study has been conducted using E. U. Copernicus Marine Service Information for the wind stress product.

3.9 Supplementary Material

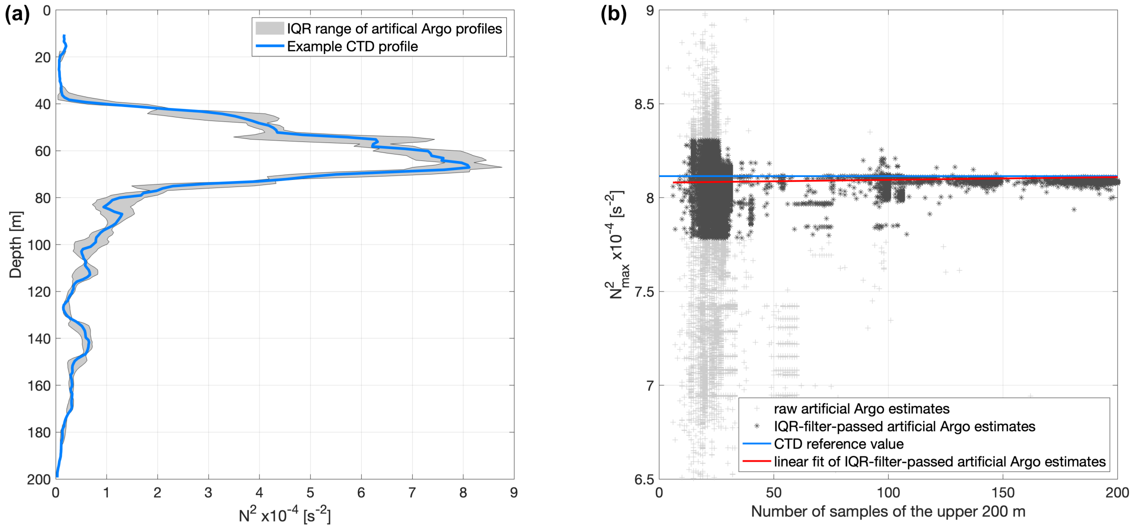

Supplementary Figure 3.14: **(a)** Example profile from Brunt-Väisälä frequency N^2 with CTD measurements from a recent cruise in the equatorial Atlantic (Meteor Cruise M158, Brandt et al. (2021)). This profile is assumed to be the "true" profile for the artificial Argo profiles. Grey shading shows the range of artificial Argo estimates of the Brunt-Väisälä frequency that passed the good interquartile range (IQR) filter. **(b)** Estimate of vertical stratification maximum as a function of the number of samples of one Argo profile of the upper 200 m calculated with a 15-dbar window and makima interpolated temperature and salinity values. Light grey crosses denote the estimate of vertical stratification maximum for each raw artificial Argo profile. Dark grey crosses indicate the estimate of vertical stratification maximum for the good interquartile range (IQR) filter-passed artificial Argo profiles. Blue line indicates the CTD reference value, i.e., the assumed "true" value. Red line shows the linear fit of the IQR filter-passed artificial Argo estimates..

Chapter 4

Recent large-scale mixed layer and vertical stratification maxima changes

In Chapter 3, upper-ocean stratification changes in the southeastern tropical Atlantic were investigated and demonstrated a substantial shift from subtropical to a more tropical stratification. The method of evaluating the vertical stratification maximum from Argo observations introduced in Chapter 3 is further developed in this Chapter and applied to the global ocean. Here, recent global changes of the mixed layer and vertical stratification maxima during the Argo observation period (2006-2021) are examined, in order to understand whether there is a general de-coupling of the upper-ocean from the ocean interior. The vertical stratification maximum is subject to different processes in different regions, however, it is a variable that can be easily determined and therefore is a useful parameter to compare to models. The analysis differentiates between summer and winter seasons, as different mechanisms are at play in each season. Possible causes for the observed differences in regional changes will be discussed.

The manuscript was published in *Frontiers in Marine Science: Physical Oceanography* in October 2023.

Roch, M., Brandt, P., and Schmidtko, S. (2023). Recent large-scale mixed layer and vertical stratification maxima changes. *Front. Mar. Sci.* 10; 1277316. doi: 10.3389/fmars.2023.1277316

The candidate carried out all the analyses, produced all the figures and authored the manuscript from the first draft to the final published version.

Abstract

The warming climate is causing a strengthening of ocean stratification. Ocean stratification, in turn, has significant impacts on physical, biogeochemical and ecological processes, such as ocean circulation, ventilation, air-sea interactions, nutrient fluxes, primary productivity and fisheries. How these processes are affected in detail by changing stratification still remains uncertain and are likely to vary locally. Here, we investigate the state and trend of different parameters characterizing the stratification of the global upper-ocean which can be derived from Argo profiles for the period 2006-2021. Among those parameters are mixed layer depth, magnitude and depth of the vertical stratification maximum. The summertime stratification maximum has increased in both hemispheres, respectively. During wintertime, the stratification maximum has intensified in the Northern Hemisphere, while changes in the Southern Hemisphere have been relatively small. Comparisons to mixed layer characteristics show that a strengthening stratification is mainly accompanied by a warming and freshening of the mixed layer. In agreement with previous observational studies, we find a large-scale mixed layer deepening that regionally contributes to the increasing stratification. Globally, the vertical stratification maximum strengthens by 7-8 % and the mixed layer deepens by $4\,m$ during 2006-2021. This hints to an ongoing de-coupling of the surface ocean from the ocean interior. The investigated changes can help determine the origin of existing model-observation discrepancies and improve predictions on climate change impact on upper-ocean ecology and biogeochemistry.

4.1 Introduction

The intensity of upper-ocean stratification has profound impact on the climatic system as it modifies or shapes physical mechanisms at work and the marine ecosystem. The vertical transfer of heat, matter and momentum in the ocean, including ventilation, upwelling and entrainment into the mixed layer are affected by the density distribution below the mixed layer and therefore depend on the stratification (Capotondi et al., 2012; Cronin et al., 2013). Mixed layer dynamics impact air-sea exchange of carbon (Bopp et al., 2015) and influence deoxygenation processes in the subtropical-tropical oceans (Schmidtko et al., 2017; Oschlies et al., 2018). Upwelling and mixing in turn play a key role for the nutrient supply to the euphotic zone which further influences phytoplankton abundance and fisheries (e.g., Fiedler et al., 2013; Llort et al., 2019). Additionally, upper-ocean stratification changes play a role in upper-ocean heat content and air-sea interactions which in turn can influence phenomena such as tropical storms or rainfall (Balaguru et al., 2016).

This study aims to address recent changes of the vertical stratification maximum and mixed layer properties from Argo observations for the time period of 2006-2021 (Argo, 2021). Due to its tight relation to the mixed layer, the vertical stratification maximum is a gateway for ocean ventilation and nutrient supply to the euphotic zone.

The upper-ocean can be described by three layers: the surface mixed layer, the seasonal and permanent pycnocline (Sprintall and Cronin, 2009). Additionally, a transient layer located directly below the surface mixed layer is often employed to describe exchange processes between the mixed layer and the ocean interior (Ferrari and Boccaletti, 2004; Johnston and Rudnick, 2009). It is sometimes part of the seasonal pycnocline. The surface mixed layer is characterized by well-mixed hydrographic properties and undergoes a seasonal cycle, being typically deeper in winter and shallower in summer. The mixed layer properties are subject to atmospheric forcings, such as wind, heat and freshwater (Sprintall and Cronin, 2009). These forcings lead to mixed layer variations on all timescales and result in a mean latitudinal mixed layer depth distribution, being deep at high latitudes and shallow in the tropical oceans (Sprintall and Cronin, 2009).

Below the mixed layer, density increases strongly with depth, creating local maxima in the vertical density gradient (Sprintall and Cronin, 2009). This transition layer is characterized by high vertical shear and connects the highly turbulent surface mixed layer with the weakly turbulent ocean interior (Ferrari and Boccaletti, 2004; Johnston and Rudnick, 2009; Kaminski et al., 2021). During summer, the seasonal pycnocline is within the transient layer. The seasonal pycnocline forms during spring from detrainment of the shoaling mixed layer and entrains its waters back into the deepening winter mixed layer. It is the midterm memory of the upper-ocean by which summer conditions impact the start and/or strength of winter processes (Sprintall and Cronin, 2009; Huang, 2010b). Below, there exists the permanent pycnocline. Owing to the seasonal cycle of the mixed layer, the permanent pycnocline develops from late-winter properties of the deep winter mixed layer only: when isopycnal outcrops are closest to the equator and the mixed layers are deepest in late winter, there is a time frame of 1-2 months, where water from the mixed layer reaches the permanent pycnocline (Williams and Meijers, 2019). The permanent pycnocline separates the upper from the deep ocean on an all-year basis (Iselin, 1939; Stommel, 1979; Williams et al., 1995; Sprintall and Cronin, 2009; Huang, 2010b; Feucher et al., 2019). Note, subduction is a non-local process, i.e., since the water, detrained from the mixed layer, is moving downstream by currents. Hence, the late winter properties found in the permanent pycnocline originate from a different location as where they are subducted (Huang, 2010b).

However, not in all areas of the world oceans these types of seasonal and permanent pycnoclines are present, e.g., in the high polar regions no permanent pycnocline exists (Sprintall and Cronin, 2009). In the tropical ocean a shallow pycnocline (thermocline) exists in all seasons since there is only a weak seasonal cycle of the mixed layer depth.

Towards the subtropics and high latitudes, the seasonality increases and thus induces the above discussed seasonal pycnocline above the permanent pycnocline (e.g., Wyrtki, 1964; Fiedler and Talley, 2006). Thus, a separation into seasonal and permanent pycnoclines is not always possible.

The maximum vertical density gradient can be detected via the Brunt-Väisälä frequency as the vertical stratification maximum which has an influence on e.g., buoyancy and heat budgets, but also plays a role for oxygen and nutrient distributions (Fiedler et al., 2013). Regionally and seasonally, the vertical stratification maximum can have a severely different meaning in the water column, as it may locally be the transition from the mixed layer to the seasonal or permanent pycnocline, or e.g., in summer be part of the seasonal pycnocline itself.

Climate models project an intensifying stratification, accompanied by mixed layer shoaling. This is associated with a reduced ocean ventilation under the global warming scenario (e.g., Keeling et al., 2010; Capotondi et al., 2012; Rhein et al., 2013; Kwiatkowski et al., 2020). Consequences of strengthened stratification and poleward movement of outcropping areas of isopycnals due to subtropical ocean surface warming are suggested to lead to a shallowing of subducted ventilated layers and an oxygen loss below the tropical thermocline (Oschlies et al., 2018). Furthermore, assuming thinner mixed layers, lateral induction, an important process in the mode water formation, could decline (Oschlies et al., 2018).

Observational evidence suggests that these relationships are ambiguous and the causes of stratification changes in a warming world are not yet fully understood. Despite ocean surface warming, stratification does not strengthen everywhere (Somavilla et al., 2017). Large-scale mixed layer deepening is counterintuitive to enhanced stratification owing to changes in buoyancy forcings and wind-driven Ekman pumping (Somavilla et al., 2017). Observations indicate summertime mixed layer deepening accompanied by enhanced stratification below the mixed layer base (Sallée et al., 2021). Two methodically-different studies show stratification has been increasing since the 1960s (Yamaguchi and Suga, 2019; Li et al., 2020): Stratification has been rising by 3.3-6.1 % in the upper 200 m and it has been intensifying in 40 % of the global oceans (Yamaguchi and Suga, 2019). The upper 2000 m of the water column are experiencing an enhanced stratification of 5.3 % with greatest increase in the upper 150 m (5-18 %) (Li et al., 2020). All above studies investigated stratification over a large depth range or at the base of the mixed layer. Despite both methods reveal an increase of stratification in the various parts of the water column, they have specific advantages and limitations. All stratification analyses that average over a depth range have to deal with a loss of the vertical density structure and thus, limit the understanding of the processes at play. The pycnocline locations and mixed layer depths vary globally, hence such a method regionally misses profound stratification maxima changes wherever the mixed layer is deeper or much shallower than the evaluated depth range (Sallée et al., 2021). Nevertheless, an advantage of a depth-range-averaged stratification measure is its ability to relate it to ocean heat content variations in the same depth range.

This investigation concentrates on the vertical stratification maximum which is defined as a local pycnocline and is thought to play a key role for the exchange between the mixed layer and the interior ocean as well as for how deep the mixed layer can reach. Our method frames the true maximum of the vertical stratification of the local water column which does not have to be the first local maximum below the mixed layer as studied recently by Sérazin et al. (2023). Indeed, the vertical stratification maximum location is highly variable among regions and summer and winter season. Therefore, it cannot be assigned to a specific layer for the global ocean. It depends on the region, in which upper-ocean layer the vertical stratification maximum is located. In general, it can be part of the transition layer when the maximum is found just below the mixed layer and its magnitude is comparable to the one in the transition layer. But in regions, where the stratification maximum is much deeper than the mixed layer and larger in magnitude than the transition layer stratification, it is hardly determining the transition layer. Here, we do not aim for a layer thickness, yet we focus on the location and magnitude of the vertical stratification maximum for its simplicity of determining this variable.

The vertical stratification maximum is a part of the ocean that has not yet been investigated in detail. In contrast to seasonal and permanent pycnoclines, it is a variable which is well-defined in all areas of the ocean and related to exchange processes between the surface mixed layer and ocean interior. The vertical stratification maximum is located at a depth that can be easily determined and is therefore a parameter that is well-comparable to models. It is not subject to the high variability as found for the base of the mixed layer. Making excessive use of the vast amount of Argo observations (Argo, 2021), we map summer and winter vertical stratification maxima. This dataset represents the mean state of the vertical stratification maxima in the past 16 years and gives detailed insights about the variability of the summer and winter stratification maxima on multi-year time scales. The last decade (2010-2019) is of especially large interest since the ocean surface warming has intensified by $0.280 \pm 0.068°\text{C}\,\text{decade}^{-1}$ compared to the warming rate of $0.062 \pm 0.013°\text{C}\,\text{decade}^{-1}$ of the last 120 years (1900-2019) (Garcia-Soto et al., 2021). With the Argo observations we are able to investigate the decade of accelerated warming in more detail and explore regional differences in stratification and mixed layer changes as well as their possible causes. It is not possible to directly link the observed changes of stratification and mixed layer characteristics to climate warming as a short time period of 16 years is subject to natural climate variability, too. We aim to provide a data product of an upper-ocean variable that can be easily compared to model and reanalysis outputs for validation and process analysis.

4.2 Data and Methods

4.2.1 Argo Observations

As hydrographic dataset we use Argo observations from 2006-2021 (Argo, 2021). The Argo floats are profiling the upper 2000 m and since 2006 the Argo coverage has overcome larger gaps and it allows for global analyses (Roemmich et al., 2015; Desbruyères et al., 2017). Here, we use profiles that are identified as good data by the quality control procedures (QC=1), taking only those from the adjusted data mode into account. Additional quality controls applied are the following: pressure profiles have to be continuous and reach at least 1000 $dbar$, vertical profiles may not have a pressure difference between two adjacent pressure points larger than 150 $dbar$ and more than 20 sample points have to be present in the upper 2000 $dbar$. Globally, 1,559,383 profiles pass this quality check. Temporal and spatial distributions of the Argo profiles have been checked (Supplementary Figure 4.11). Some regions as the central subtropical South Pacific and south of 60°S should be evaluated with more caution as the number of profiles and maximum time span is observed to be reduced (Supplementary Figure 4.11). Conversion of in situ measurements into absolute salinity, conservative temperature and potential density is done using TEOS-10 (McDougall and Barker, 2011). Note that the vertical resolution of an individual Argo profile is usually not distributed uniformly over the water column, but generally has a higher resolution in the upper 500 $dbar$. The median pressure difference between two adjacent pressure measurements in the upper 500 $dbar$ of all profiles is 5-6 $dbar$. Since in most regions the vertical stratification maximum is confined to the upper 500 $dbar$ of the ocean, it is well-detected by most profiles. For each profile mixed layer depth, temperature and salinity are estimated by the Holte and Talley algorithm (Holte and Talley, 2009) which evaluates the mixed layer characteristics by a combination of threshold and gradient (Holte and Talley, 2009).

Argo profile treatment and stratification estimate

Vertical resolution among Argo profiles varies. Particularly, the newer Iridium floats contain a higher vertical sampling rate than the older ARGOS floats. In order to overcome this irregularity of vertical sampling, we interpolate all profiles on an isopycnal grid prior to our analysis of the vertical stratification maxima. We chose the isopycnal interpolation for this study as it maintains the vertical stratification (Schmidtko et al., 2013) and hence, this formulation mitigates possible errors of the vertical stratification maximum. Statistical comparison shows that isopycnal gridding on average performs better than isobaric gridding (Supplementary Figure 4.12). This is due to the non-linearity of the equation of state for seawater which is accounted for by the isopycnal gridding performed in theta-salinity space, but not by the isobaric gridding.

For the measure of stratification, we choose the square of the Brunt-Väisälä frequency, N^2, following the definition in TEOS-10 (IOC et al., 2010; McDougall and Barker, 2011):

$$N^2 = g^2 \rho \frac{\beta dS_A - \alpha dT}{dP} \tag{4.1}$$

where g is the gravitational acceleration, ρ is the potential density, α and β refer to the thermal expansion and saline contraction coefficients, respectively. dT and dS_A are differences in conservative temperature and absolute salinity over a pressure difference dP (IOC et al., 2010). This function, implemented in the Gibbs SeaWater (GSW) Oceanographic Toolbox of the International Thermodynamic Equation of State – 2010 (IOC et al., 2010) originates from the definition by Gill (Gill, 1982) (cf. his equation 3.7.9). This way of calculating the Brunt-Väisälä frequency is proposed to be the desired one when conservative temperature and absolute salinity profiles are interpolated or fitted beforehand which is the case for our study (McDougall and Barker, 2014).

In the following we provide a step-by-step guide on our interpolation scheme and the determination of the vertical stratification maximum.

Step 1: The profiles of conservative temperature, absolute salinity and pressure are interpolated on an isopycnal grid. This grid consists of 433 levels ranging from $20.0\,kg\,m^{-3}$ to $29.5\,kg\,m^{-3}$. The isopycnal grid is assigned into several subsets of different intervals between isopycnals with increasing resolution for higher density levels. Lower density levels ($20.0\,kg\,m^{-3} - 23.95\,kg\,m^{-3}$) have a grid space difference of $0.12\,kg\,m^{-3}$. This grid interval becomes smaller over several subsets down to $0.005\,kg\,m^{-3}$ for isopycnal levels larger than $28.15\,kg\,m^{-3}$. This isopycnal grid has been chosen in order to be able to resolve the vertical structure in subpolar regions and the Mediterranean Sea. These regions contain much higher density values from surface to bottom and to assure a reasonable grid spacing, the isopycnal intervals are decreasing for higher isopycnal levels. The isopycnal levels and intervals are chosen by the compromise of taking the computational efficiency and a sufficiently well-resolved upper-ocean into account.

For the interpolation we applied the modified Akima piecewise cubic Hermite interpolation [makima method (MathWorks Inc., 2019; MATLAB, 2019)] which is based on the algorithm from Akima (Akima, 1970) and combines the interpolation schemes of cubic spline and the piecewise cubic Hermite interpolating polynomial (pchip) (MathWorks Inc., 2019). To determine vertical maxima and minima from an individual profile, an interpolation scheme is required which allows for local maxima and minima between measurements (Roch et al., 2021). The makima method enables undulations in contrast to the pchip method and at the same time prevents artificial spline maxima between identical samples.

Step 2: Some profiles cover only part of the density range due to outcropping isopycnals. This is handled mathematically by using mixed layer properties above the surface for ease of computational analysis. Note that on an isopycnal grid the mixed layer does not need

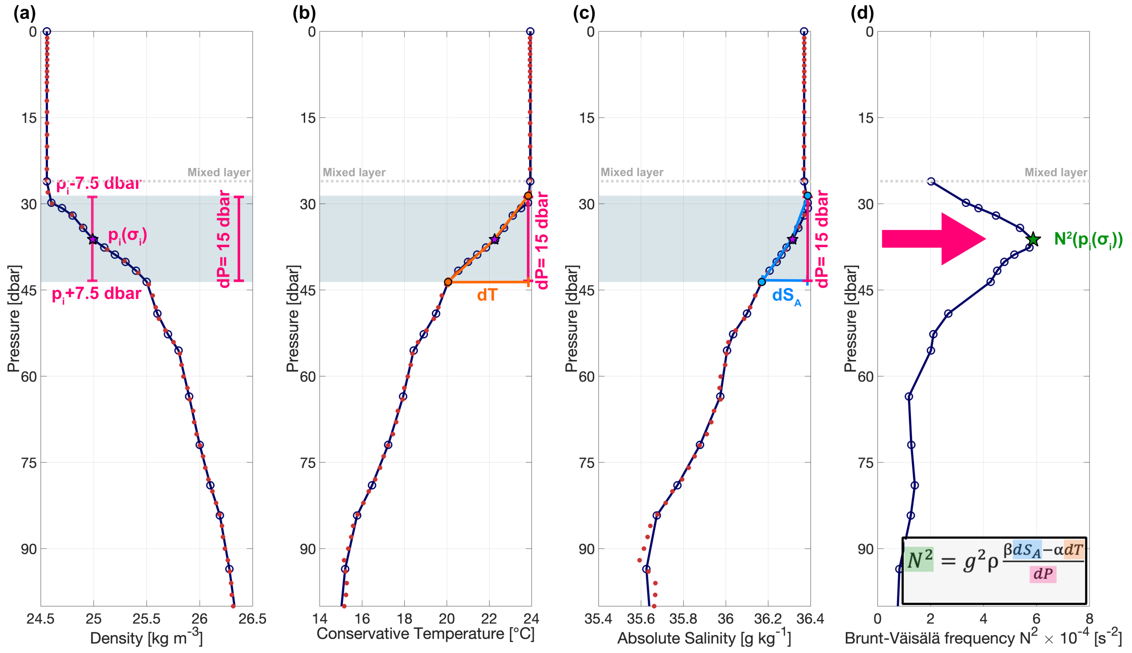

Figure 4.1: Density-interpolated Argo profile. Snapshot of an example Argo profile after applying density-interpolation for **(a)** pressure, **(b)** conservative temperature, **(c)** absolute salinity and **(d)** the therefrom resultant squared Brunt-Väisälä frequency profile. The blue lines with bullets show the profiles received after makima interpolation method on the isopycnal grid. The bullets denote the chosen isopycnal grid and red dots refer to the un-interpolated measurement points of the Argo profile. Additionally, the mixed layer is indicated by the grey dotted line. The light blue shaded bar as well as the pink vertical lines in **(a-c)** indicate the dP=15-dbar window chosen for the computation of the Brunt-Väisälä frequency. The density-interpolated pressure grid point $p_i(\sigma_i)$ is found at the center of these bars and marked by a purple star **(a-c)**. Due to the 15-dbar window, we achieve three different points: $p_i(\sigma_i)$ and $p_i \pm 7.5\,dbar$. As indicated by the orange lines in **(b)** for temperature and by the blue lines in **(c)** for salinity, it is linearly interpolated among the corresponding three points. From this three-point interpolation, dT [horizontal orange line in **(b)**] and dS_A [horizontal blue line in **(c)**] can be computed for each corresponding dP=15-dbar window. Following the equation for the Brunt-Väisälä frequency in **(d)**, the resulting Brunt-Väisälä frequency profile is achieved. The green star in **(d)** corresponds to the grid point indicated by the purple stars in **(a-c)**.

any other grid points than at the mixed layer base and at the surface since the density in the mixed layer is the same at all depth levels (Figures 4.1a-c).

Step 3: For the calculation of the Brunt-Väisälä frequency, we set $dP = 15\,dbar$ in Eq. 4.1. We choose the constant window size of 15-dbar instead of the layer thickness between isopycnals, in order to maintain a comparable parameter and to avoid troubleshooting with globally varying isopycnal depths and layer thicknesses. The constant window size is applied to each isopycnal grid point σ_i (i referring to the isopycnal level).

The pressure at each isopycnal grid point, $p_i(\sigma_i)$, is the midway pressure point to which the final estimate of N^2 will be referenced. Then, the corresponding upper and lower limits of the 15-dbar window are defined as follows: $[p_i(\sigma_i) - 7.5\,dbar,\, p_i(\sigma_i) + 7.5\,dbar]$

(Figure 4.1a). Together with the midway pressure point $p_i(\sigma_i)$ this results in three vertical points.

Step 4: To determine the salinity and temperature values for the upper and lower limits of the 15-dbar window, linear interpolation between the nearest grid points of the isopycnal grid is applied. The difference between the determined values at the upper and lower limits provides dT (horizontal orange bar in Figure 4.1b) and dS_A (horizontal blue bar in Figure 4.1c) corresponding to $dP = 15\,dbar$ (Figures 4.1a-c by the vertical pink bar). dT and dS_A are individual for each isopycnal grid point σ_i.

Step 5: dT, dS_A and $dP = 15\,dbar$ are then inserted into Eq. 4.1. From Eq. 4.1 the square of the Brunt-Väisälä frequency, N^2, is obtained as a function of the isopycnal grid and the corresponding pressure $p_i(\sigma_i)$ (Figure 4.1d). This procedure provides Brunt-Väisälä frequency profiles that are vertically smoothed as a result of the 15-dbar window. This filter allows for a good representation of local maxima and minima of the vertical profiles but reduces small-scale noise and variability which would become dominant for smaller vertical windows.

Step 6: Finally, the vertical stratification maximum and its depth are derived from each Brunt-Väisälä frequency profile as the maximum value and the depth of the corresponding isopycnal grid point.

This method does yield different results compared to taking stratification directly below the mixed layer (Sallée et al., 2021) into account as for 73 % of the Argo profiles the vertical stratification maximum is found deeper than within the 15 m layer below the mixed layer base. Additionally, our method estimates stratification on an isopycnal grid which is in contrast to all above-noted methodically-different studies. Isopycnal gridding benefits over isobaric gridding as it does not create artificial water masses, but maintains water mass properties and the vertical stratification (Lozier et al., 1994; Schmidtko et al., 2013). Since averaging errors are significantly reduced when using isopycnal instead of isobaric schemes, Lozier et al. (1994) proposed the use of potential density surfaces for creating hydrographic climatologies.

Note, for the isopycnal heave analysis, isopycnal coordinates are converted to depth coordinates. This is done via linear interpolation on an even depth grid with a 5m-stepwidth from the sea surface to 1000 m. A transformation to depth surfaces is necessary, in order to compare the isopycnal displacements to the mixed layer depth and pycnocline depth changes during the zonal analyses.

Since the density distributions vary among the Atlantic, Pacific and Indian Oceans, we applied the zonal heave analysis for each ocean separately. We exclude the Mediterranean Sea from the calculation for the Atlantic Ocean as it has much higher density than the rest of the subtropical North Atlantic.

Mapping processes and trend calculations

Mapping of the individual parameters (vertical stratification maximum, its depth, mixed layer temperature, salinity and depth) is done on a 1° × 1° grid in latitude and longitude. For each grid point data within an ellipse is taken into account. To preserve the more zonal structures in low latitudes, along the equator 6° radius in latitude and 14° radius in longitude is the maximum distance of used data. The elliptic radii gradually change toward circle radii at 20°N/S following an exponential function, while preserving the spatial area of the ellipses and circles. For each grid point and parameter to be mapped an interquartile range (IQR) filter is used, excluding data outside 1.5 times the IQR above the third quartile or 1.5 times the IQR below the first quartile. This is equivalent to a 99.3 % standard deviation filter on a normal distribution.

In order to account for the different distances of the profiles to the grid points, we include a distance weighting function in the mapping process (Schmidtko et al., 2013):

$$w_i = \exp\left\{ - \left[\frac{\Delta d_i}{L}\right]^2 \right\} \tag{4.2}$$

where Δd is the distance between each profile location and the corresponding grid point i, and L is the spatial decorrelation scale which is defined to be $500\,km$.

In addition, we de-weighted El Niño and La Niña years by including the Ocean Niño Index (ONI) (Trenberth and National Center for Atmospheric Research Staff, 2020). The ONI index was downloaded from the Climate Data Guide. The ONI index applies a three-month running mean on the SST anomalies in the Niño 3.4 region (5°N-5°S, 170°W-120°W). With the inclusion of the ONI index, our weighting function becomes:

$$w_i = \exp\left\{ - \left(\Delta\mathrm{ONI}^3 + \left[\frac{\Delta d_i}{L}\right]^2 \right) \right\} \tag{4.3}$$

with $\Delta\mathrm{ONI} = \left[\frac{|\mathrm{ONI}|_{-0.3}}{0.3}\right]$ for $|\mathrm{ONI}| \geq 0.3$ and $\Delta\mathrm{ONI} = 0$ for $|\mathrm{ONI}| < 0.3$.

The mean field is calculated using a least squares model regression. For each grid point of the mean field to be mapped linear fits in longitude and latitude as well as a quadratic fit for latitude are applied as well as a linear fit in time are eliminated referenced to the year 2005. This is done with the data from January-February-March and July-August-September, respectively.

Trends are then calculated from the local anomalies relative to the above-described mean field of the corresponding season. For the trend we apply a least squares model regression which with linear fits in longitude, latitude and time referenced to the grid point and year 2005. The derived gradient in time is used as trend.

We test for statistical significance of the trend fields by multiplying the t-value of the Student's t distribution for 95 % significance with the standard error estimate of the trend model's least square solution. This gives us the 95 % confidence limits. The trends are then defined to be of 95 % statistical significance if the slopes of the upper and lower confidence limits are of the same sign.

For completeness the fields of the standard errors of the trends of the vertical stratification maximum, its depth and for the three mixed layer properties are included in the Supplementary Material (Supplementary Figures 4.13, 4.14).

For the estimation of trends of global zonal means of the vertical stratification maximum, its depth and the mixed layer depth as well as for the isopycnal heave analysis for the Atlantic, Pacific and Indian zonal means, a different weighting function is applied. Here, all profiles within ±7° from the latitude grid point are included and the following distance weighting function is then used:

$$w_i = \exp\left\{ - \left(\Delta\mathrm{ONI}^3 + \left[\frac{\Delta\mathrm{lat}}{2^\circ}\right]^2 \right) \right\} \tag{4.4}$$

The de-weighting of El Niño and La Niña (first term of the equation) remains the same as in the mapping process.

Global estimates of vertical stratification maximum, its depth and the mixed layer depth anomalies

To analyze the global mean changes, we combine all profiles from the two seasons (JAS and JFM) and estimate the global 2-year median and the IQR of the vertical stratification maxima, their depths and the mixed layer depths anomalies. The anomalies are computed relative to the nearest grid point's mapped mean, corresponding to the season. The percental change of the vertical stratification maximum is determined relative to the nearest grid point's mapped mean.

4.3 Results

4.3.1 Seasonal mean state of the vertical stratification maxima

We are focussing our analysis on the Argo period to minimize temporal bias due to temporal and spatial heterogenous sampling in previous decades. The most pronounced vertical stratification maximum is found in the tropical oceans, especially on the eastern side of the basins in both seasons (up to $16 \times 10^{-4}\, s^{-2}$, Figure 4.2). Poleward, stratification intensity decreases and experiences a seasonal cycle. Both hemispheres show enhanced stratification in its respective summer months (July-September (JAS) in the Northern

Hemisphere, January-March (JFM) in the Southern Hemisphere), compared to its winter season. The Southern Hemisphere has overall weaker stratification ($< 2 \times 10^{-4}\,s^{-2}$) of the summer and winter stratification maxima (Figure 4.2).

High stratification values are accompanied by shallow depths of the vertical stratification maxima in most areas. The depths in the tropical oceans range from around $40 - 100\,m$, shoaling from west to east. The Northern Hemisphere reveals a distinct seasonal cycle of the depth of the stratification maximum with around $40\,m$ in JAS (Figure 4.2a) and deeper than $200\,m$ in JFM (Figure 4.2b). A similar cycle is found in the Southern Ocean, where its depths span from $60 - 100\,m$ in JFM, reaching beyond $600\,m$ in JAS (Figure 4.2).

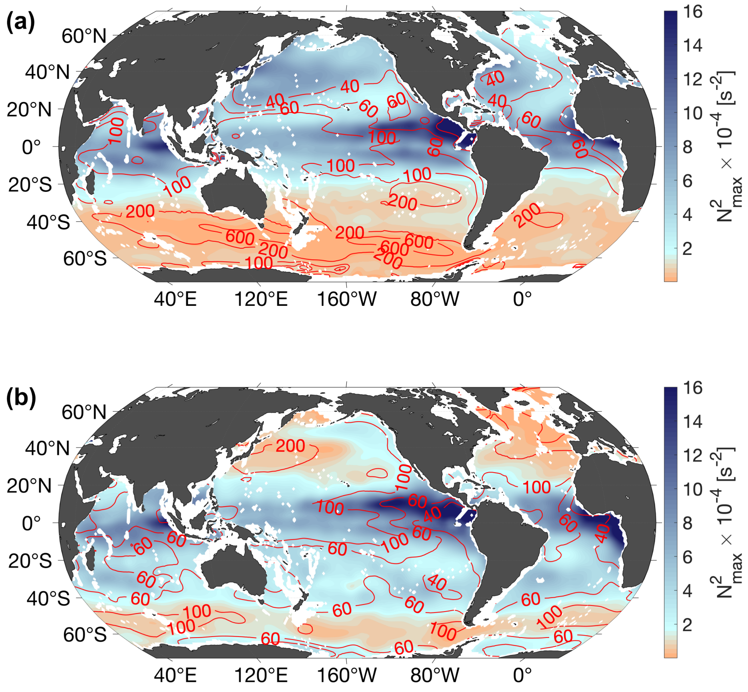

Figure 4.2: Mean vertical stratification maximum and its depth. **(a)** Mean vertical stratification maximum in July-September and **(b)** in January-March. Red contour lines mark the corresponding mean depth in meters.

4.3.2 Observed changes in vertical stratification maxima strength and depth

The above mean state residuals of monthly data (Figure 4.2) are used to derive multi-year trends of depth and stratification strength (Figure 4.3).

The North Pacific Ocean is undergoing substantial changes by vast increasing stratification in both seasons ($1.5 \times 10^{-4}\,s^{-2}\,\text{decade}^{-1}$ equivalent to 40-50 % decade^{-1} in JAS) especially around 10°N stratification increases by $2.5 \times 10^{-4}\,s^{-2}\,\text{decade}^{-1}$ (equivalent to $\sim 10\,\%\,\text{decade}^{-1}$, Figure 4.3). On the contrary, the increase of the South Pacific Ocean stratification maximum is small in JAS and in many areas the trend is not statistically

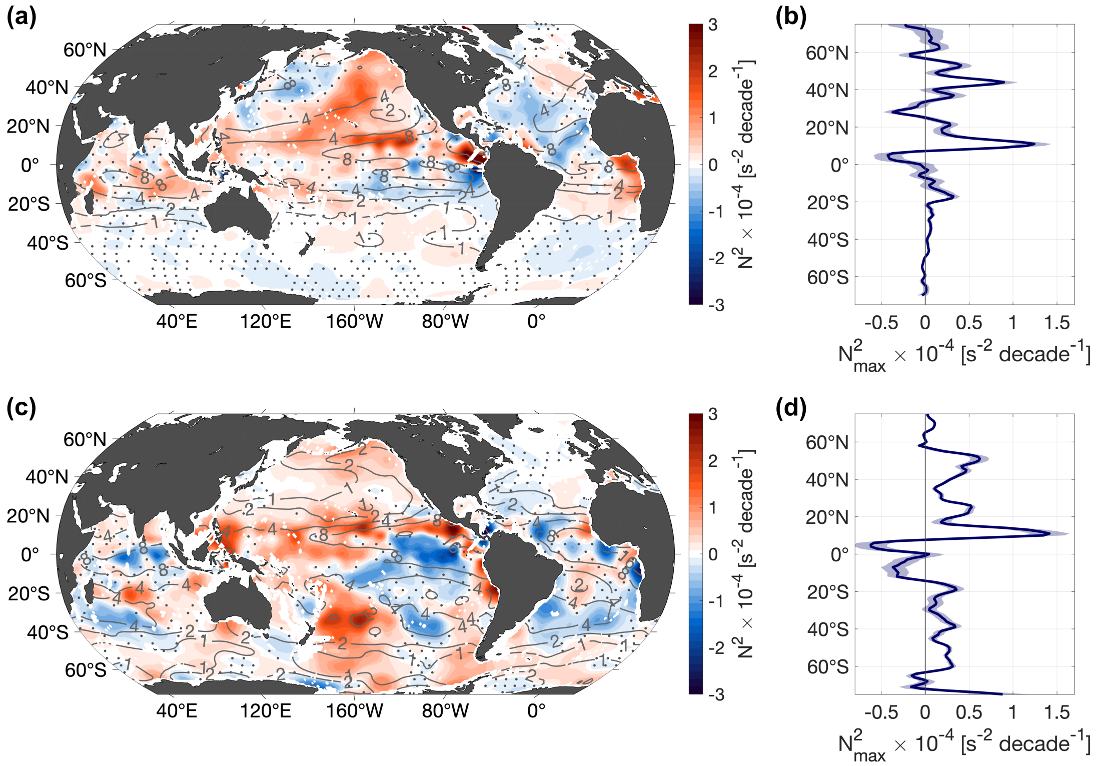

Figure 4.3: Trend of vertical stratification maximum. **(a)** Trend of vertical stratification maximum in July-September and **(b)** trend of the corresponding zonal mean. **(c, d)** same as in **(a, b)** but for January-March. Contour lines in **(a, c)** show the respective mean vertical stratification maximum given in $\times 10^{-4} s^{-2}$. Labels of the contours have to be multiplied by 10^{-4}. Dotted areas refer to where the trend is not of 95 % significance. Shading in **(b, d)** depicts the 95 % confidence interval.

significant (see Methods). In JFM the South Pacific Ocean reveals a dipole pattern with a large rise of stratification in the southwest ($3 \times 10^{-4}\, s^{-2}$ decade^{-1}) and a decline in the central-eastern tropical South Pacific Ocean. Along the eastern continental slope, the eastern boundary upwelling system experiences enhanced stratification. The stratification maximum in the eastern equatorial Pacific decreases intensely in JFM ($-2 \times 10^{-4}\, s^{-2}$ decade^{-1}, Figure 4.3).

Changes in the Atlantic Ocean are substantially different compared to those in the Pacific Ocean. The subtropical North Atlantic Ocean is marked by reduced stratification in JAS ($-0.6 \times 10^{-4}\, s^{-2}$ decade^{-1}, Figure 4.3a) and slightly less in JFM (Figure 4.3c). Only the Senegalo-Mauritanian upwelling region shows strengthening stratification in JFM. Poleward of 40°N, the northeastern North Atlantic stratification is slightly increasing during JAS. In JFM this positive trend is weaker but reaches further south. The eastern tropical Atlantic stratification intensifies ($> 2 \times 10^{-4}\, s^{-2}$ decade^{-1}) in JAS and shows a less clear picture in JFM. The South Atlantic is dominated by a north-south dipole in JAS with strengthening stratification equatorward of 20°S and a weakly, significantly decreasing trend further south (Figure 4.3a). In JFM, we find declining stratification around 30°S-40°S and no continuous large-scale changes otherwise (Figure 4.3c).

The Indian Ocean has no large-scale areas of significant trends. Nonetheless, the JAS stratification north of 20°S reveals a positive trend. In JFM, the tropical Indian Ocean depicts a decreasing stratification maximum. South of the tropics, a small east-west dipole shows reduced stratification in the west and opposite in the east (Figure 4.3c).

To address a more global aspects of upper-ocean stratification changes, zonal mean fields of the observed trends are estimated. The trend of the global zonal mean of vertical stratification maxima is mostly positive in the Northern Hemisphere for both seasons (Figures 4.3b, d). The North Pacific dominates over the reversed trend in the Atlantic Ocean. Around 30°N the decreasing stratification of the North Atlantic Ocean becomes apparent in the trend of the zonal mean, in particular in JAS due to the larger magnitude of decrease in Atlantic Ocean stratification. The Southern Hemisphere encompasses almost no trends in the zonal mean in JAS (Figure 4.3b), while the summer JFM trend of the zonal mean shows a statistically significant strengthening stratification (Figure 4.3d).

There are many smaller scale regions that defy these general patterns. Owing the mapping scales, the oceanic structure might even be more heterogenous, despite the large-

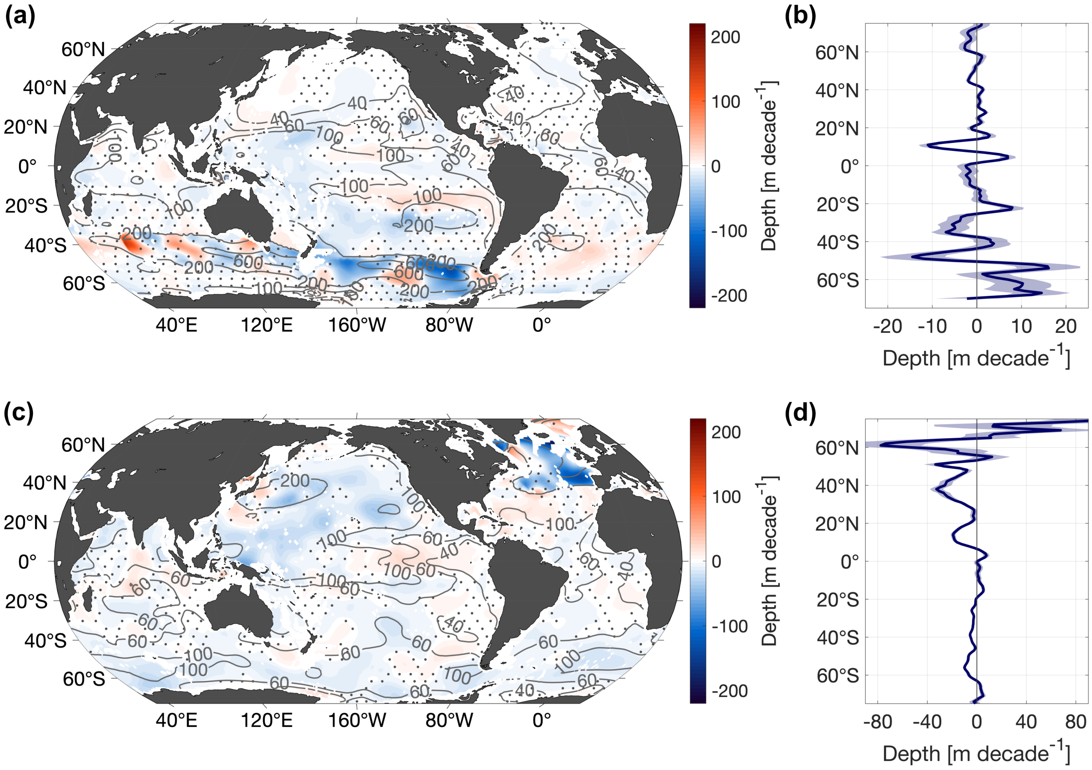

Figure 4.4: Trend of depth of the vertical stratification maximum. **(a)** Trend of the depth of the vertical stratification maximum in July-September and **(b)** trend of the corresponding zonal mean. **(c, d)** same as in **(a, b)** but for January-March. Contour lines in **(a, c)** show the respective mean fields in m. Dotted areas refer to where the trend is not of 95 % significance. Shading in **(b, d)** depicts the 95 % confidence interval.

scale variation taking place. Summarizing the detailed description above, the observed overarching patterns are the Northern Hemisphere stratification intensification in summer and winter while the Southern Hemisphere becomes more stratified in summer only.

Next to stratification strength, the depth of the vertical stratification maximum is of importance. For both seasons, its depth trend indicates a large-scale shoaling in many regions of the global oceans (5-20 $m\,\mathrm{decade}^{-1}$, Figure 4.4). Some areas as the tropical Pacific or the subtropical North Atlantic depict a deepening instead. Yet, in most areas the trends are not significant. Largest changes are observed in the Southern Ocean along the Antarctic Circumpolar Current in JAS and in the subpolar North Atlantic Ocean in JFM (Figures 4.4a, c). The trend of the zonal mean of the depth of the vertical stratification maximum in JAS shifts sign around 55°S. This can be linked to meridional shifts of the frontal zone which is found to be migrating southward and is associated to enhanced and poleward displaced westerly winds (Fyfe and Saenko, 2006; Chapman et al., 2020). Weak but statistically significant shoaling is present in the North Pacific Ocean during both seasons. The zonal mean trends of the stratification maximum depth demonstrate a surprising strong symmetry between the hemispheric respective seasons: Weak summer stratification maximum depth changes and pronounced shoaling during winter (Figures 4.4b, d).

4.3.3 Mixed layer variations

To better understand the origin of the observed changes of the vertical stratification maximum, we investigate changes of the mixed layer representing the interface between the stratified ocean and atmosphere. The parameters analyzed here include the mixed layer temperature (MLT), mixed layer salinity (MLS, Figure 4.5) and mixed layer depth (MLD, Figure 4.6). Mixed layer density changes can be inferred from the respective salinity and temperature trends. MLT and MLS trend patterns are similar in both seasons. The mixed layer is experiencing a vast and intense warming on the order of 1°C decade^{-1} (Figures 4.5a, c). This warming is exceeded in the northeastern North Pacific in JAS and southwestern South Pacific in JFM (2°C decade^{-1}). The mixed layer is cooling in few regions in the Southern Ocean and the subpolar North Atlantic during both seasons. The subpolar North Atlantic has recently been exposed to a cooling period which is suggested to arise from a slowdown of the Atlantic Meridional Overturning Circulation and to be associated to the North Atlantic Oscillation (Robson et al., 2016; Caesar et al., 2018; Bulgin et al., 2020). This mixed layer cooling occurs where the stratification is decreasing in the subpolar North Atlantic and its impact is weakened by the exhibited mixed layer freshening. The freshening trend is most likely associated with the freshwater flux of glacial melt and melting sea ice (de Steur et al., 2018; Rühs et al., 2021). Further isolated intense cooling is observed in the eastern tropical Pacific cold tongue area in

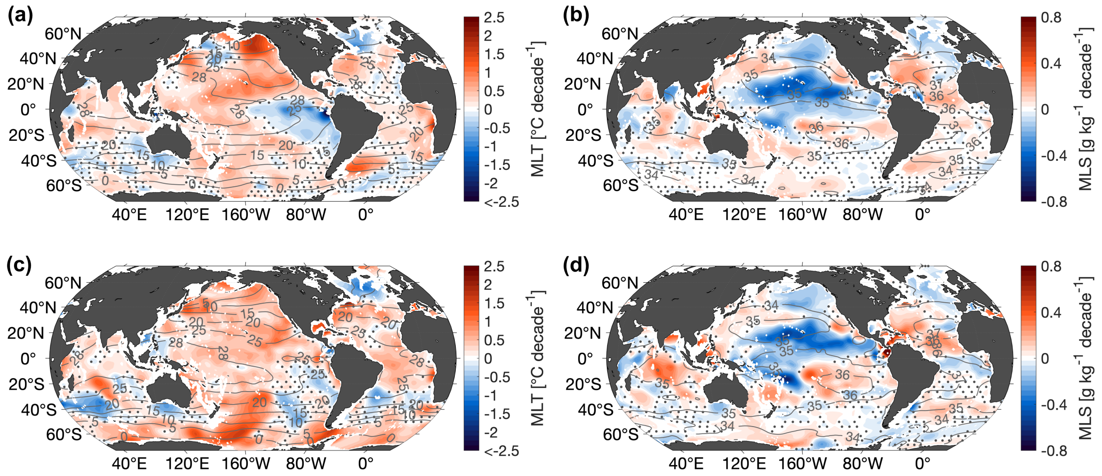

Figure 4.5: Trends of temperature and salinity of the mixed layer. **(a)** Trend of mixed layer temperature and **(b)** mixed layer salinity in July-September. **(c, d)** same as in **(a, b)** but for January-March. Labelled contour lines show the corresponding mean field in $°C$ and $g\,kg^{-1}$ correspondingly. Dotted areas refer to where the trend is not of 95 % significance.

JAS (2.5°C decade^{-1}). A cooling of the Pacific cold tongue is observed since the 1980s (e.g., Jiang and Zhu, 2020; Latif et al., 2023). It is suggested to result from strengthened atmospheric deep convection over the warm pool regions in the western Pacific and south of North America, leading to anomalous vertical circular circulation and thereby causing a westward shift of the Walker circulation (Jiang and Zhu, 2020). This produces a strong divergence over the eastern Pacific, shoaling the thermocline and thus, enhanced cooling of the Pacific cold tongue. Recently, Latif et al. (2023) found that intensifying trade winds impact ocean dynamical processes and air-sea heat exchange, and thereby, counterbalance the externally forced sea surface temperature warming. Another potential reason for the cold tongue cooling might be related to the Pacific Decadal Oscillation. It was mostly in a negative phase during our observation period which manifests in a large-scale cooling in the tropical Pacific (Latif et al., 2023).

The mixed layer is freshening in the subtropical North and tropical West Pacific Ocean in both seasons ($0.5\,g\,kg^{-1}$ decade^{-1}, Figures 4.5b, d). A potential cause for the salinity decrease is enhanced freshwater flux in the central Pacific Ocean (Ke-xin and Fei, 2022). In the South Pacific Ocean, the salinity maximum water is becoming more saline which is consistent with the findings of Bingham et al. (2019). For the period of 2011-2019 they found advection changes of the subtropical gyre, South Equatorial Undercurrent, Ekman transport and Ekman pumping leading to a more saline salinity maximum water.

A synopsis of the MLT, MLS and vertical stratification maximum changes indicate enhancing stratification when the mixed layer is warming and freshening at the same time and thus, leading to a density reduction (e.g., subtropical North Pacific Ocean in both seasons, Figures 4.3, 4.5). When MLT and MLS show counterbalancing changes, it depends on which component has the largest effect on density and in turn, lead to the observed stratification adjustment (Supplementary Figure 4.17). In the subtropical North Atlantic Ocean, northwest of the salinity maximum, MLS increases (0.3 $g\,kg^{-1}$ decade^{-1}; Figures 4.5b, d), coexistent with the reduction of stratification in JAS and JFM (Figures 4.3). The location of the more saline mixed layer could be a result of the poleward shift of the North Atlantic salinity maximum formation region recently suggested for the period of 1979-2012 (Yu et al., 2018; Liu et al., 2019).

The counterbalancing effect of salinity in the North Atlantic becomes more evident from thermal and haline contributions to the trend of vertical stratification maximum (Supplementary Figure 4.17). In both seasons the trend of the haline contribution is negative while the trend of the thermal contribution is weakly negative in JAS and weakly positive in JFM in the North Atlantic (Supplementary Figure 4.17).

Also, the MLS of the tropical Indian Ocean increases, especially in JFM. Yet, it is the MLT changes that mainly mirror the stratification changes in the Indian Ocean. MLT trend patterns are comparable to the trend pattern of the Indian Ocean heat content anomaly for the upper 700 m presented by Roxy et al. (2020). Decadal variations of upper-ocean heat content in the Indian Ocean are linked to a La Niña-like climate shift and intensified heat transport via the Indonesian Throughflow (Liu et al., 2016).

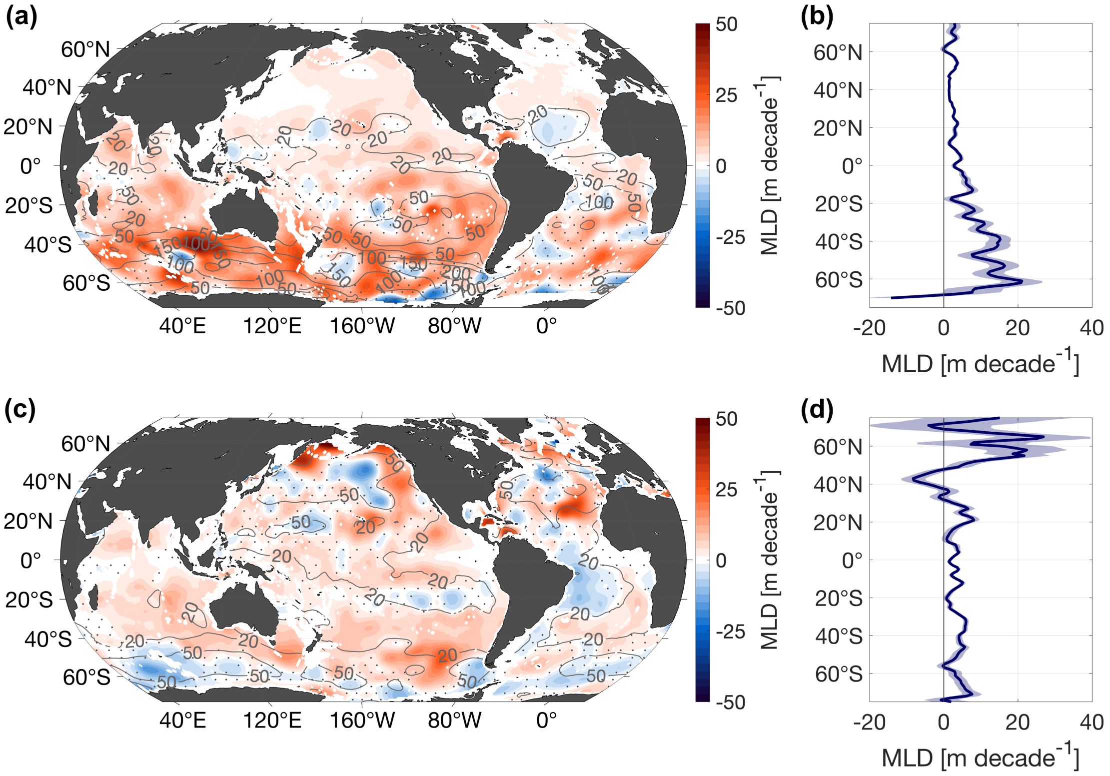

Figure 4.6: Trend of mixed layer depth. **(a)** Trend of the mixed layer depth in July-September and **(b)** trend of the corresponding zonal mean. **(c, d)** same as in **(a, b)** but for January-March. Contour lines in **(a, c)** show the respective mean fields. Dotted areas refer to where the trend is not of 95 % significance. Shading in **(b, d)** depicts the 95 % confidence interval.

The Southern Ocean depicts weak and barely significant MLS trends. Therefore, Southern Ocean MLT changes seems to be the main contributor to the observed stratification change (cf. Supplementary Figure 4.17). Nonetheless, since stratification changes in JAS are weak although MLT is rising, an impact by salinification cannot be ruled out.

The last mixed layer parameter examined, the MLD, is deepening globally in a surprising uniform pattern with few variations and a distinct seasonal pattern (Figure 4.6). Summer mixed layers are slightly deepening (5-10 m decade^{-1}) while winter mixed layers show a more pronounced deepening (30-50 m decade^{-1}) in both hemispheres. The trends of the zonal means also portray this symmetric behavior (Figures 4.6b, d).

4.3.4 Strain and isopycnal heave

Stratification changes of its vertical maximum may not only arise from changing mixed layer characteristics, but also from isopycnal heave and associated strain changes [vertical displacement of isopycnals (Bindoff and McDougall, 1994; Huang, 2015; Roch et al., 2021)] within the stratified ocean. Due to isopycnal movement, vertical density gradients change by squeezing/stretching of the isopycnal layers. This leads to enhanced/reduced stratification and affects the vertical stratification maximum. Basin-wide zonal mean trends show

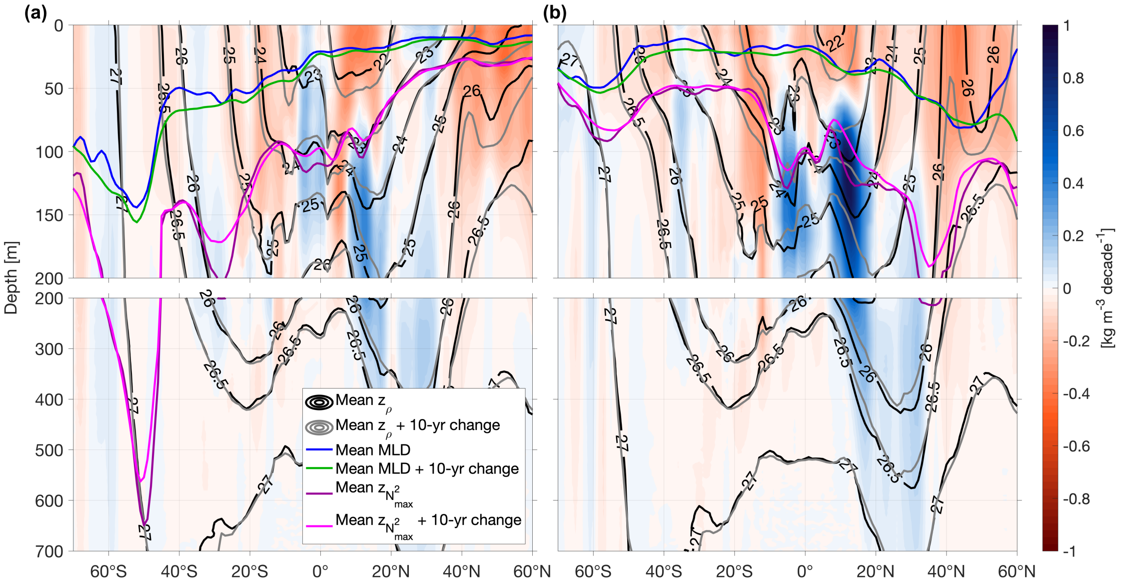

Figure 4.7: Changes of isopycnal heave in Pacific Ocean. **(a)** Trend of density in the Pacific in July-September and **(b)** in January-March for the time period of 2006-2021. Note, reddish colors imply a density reduction (i.e., warming and/or freshening) and blue colors a density enhancement. Additionally, zonal mean depths of isopycnals are shown in black, and mean depths plus 10-year changes in grey. The 10-year changes are derived from the trend. Blue lines show the zonal mean mixed layer depth (MLD), green lines refer to the mean MLD plus 10-year changes. Purple lines denote the zonal mean pycnocline depth ($z_{N^2_{max}}$) and pink lines the corresponding mean depth plus 10-year changes.

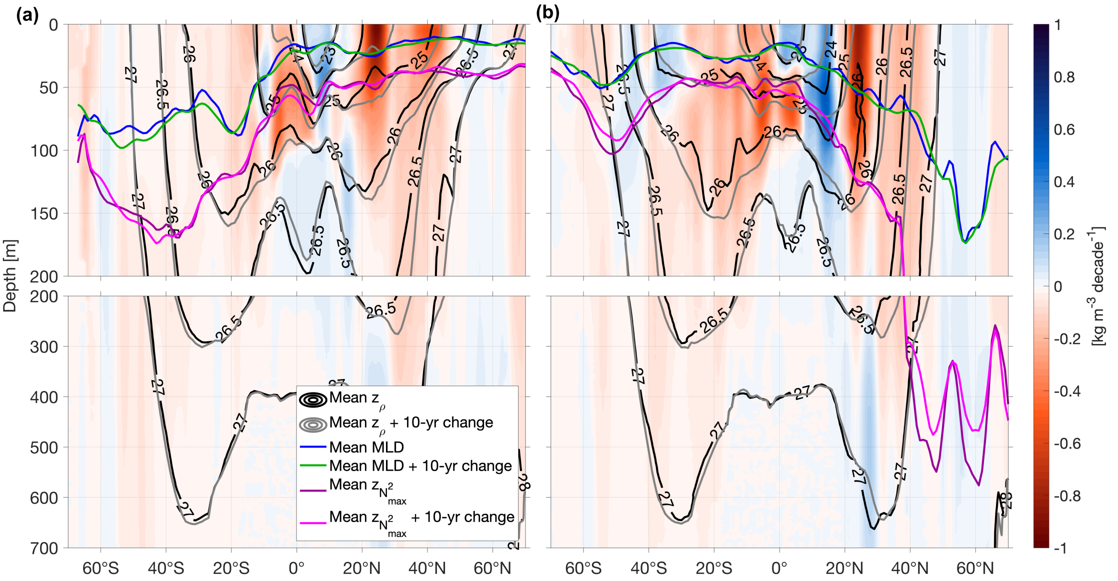

Figure 4.8: Changes of isopycnal heave in Atlantic Ocean. **(a)** Trend of density in the Atlantic in July-September and **(b)** in January-March for the time period of 2006-2021. Note, reddish colors imply a density reduction (i.e., warming and/or freshening) and blue colors a density enhancement. Additionally, zonal mean depths of isopycnals are shown in black, and mean depths plus 10-year changes in grey. The 10-year changes are derived from the trend. Blue lines show the zonal mean mixed layer depth (MLD), green lines refer to the mean MLD plus 10-year changes. Purple lines denote the zonal mean pycnocline depth ($z_{N^2_{max}}$) and pink lines the corresponding mean depth plus 10-year changes.

different isopycnal behavior among the three oceans and are compared to corresponding zonal mean trends of MLD and stratification maximum depth (Figures 4.7–4.9).

In many areas of the Pacific and Atlantic Oceans, we observe a mixed layer density reduction corresponding to a poleward migration and a downward movement of the isopycnals below the MLD (Figures 4.7, 4.8). Around the depth of the stratification maximum within the equatorial-subtropical North Pacific Ocean, the density trend is changing its sign (shoaling isopycnals: $20\,m\,\text{decade}^{-1}$, Figure 4.7). These opposing density trends in the upper and lower layers, lead to squeezing of isopycnal layers and corresponding volume changes. This is observed in both seasons in the subtropical North Pacific Ocean and contributing to the observed stratification increases (Figure 4.3). In the subtropical South Pacific isopycnal heave is weak in both seasons. Opposing behavior of the Pacific Ocean MLD and stratification maximum depth in JAS and JFM lead to a squeezing of the layer in between (Figure 4.7).

In the Atlantic Ocean, the uneven isopycnal deepening induces a stretching of the isopycnal layers at the depth of the vertical stratification maximum (particularly within 20°N-30°N, Figure 4.8). Maximum deepening is observed on the 26.5 $kg\,m^{-3}$- and 26.0 $kg\,m^{-3}$-isopycnals in the centers of the North and South Atlantic subtropical gyres, respectively, in both seasons. Since we observe the largest deepening at depth in the subtropics, this implies that next to the surface density reduction, another process has to be involved.Wind

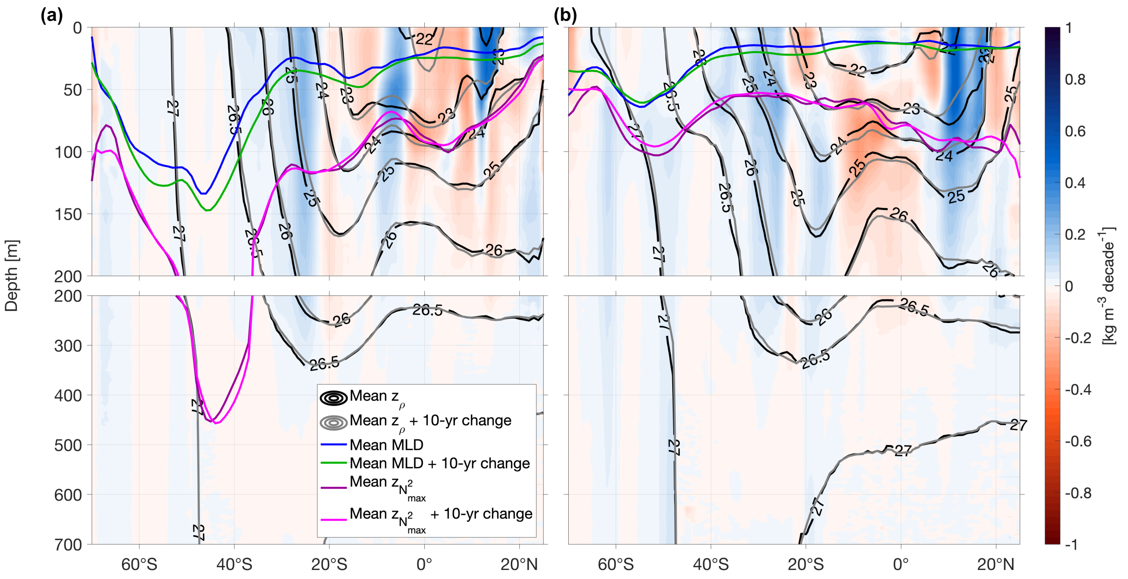

Figure 4.9: Changes of isopycnal heave in Indian Ocean. **(a)** Trend of density in the Indian Ocean in July-September and **(b)** in January-March for the time period of 2006-2021. Note, reddish colors imply a density reduction (i.e., warming and/or freshening) and blue colors a density enhancement. Additionally, zonal mean depths of isopycnals are shown in black, and mean depths plus 10-year changes in grey. The 10-year changes are derived from the trend. Blue lines show the zonal mean mixed layer depth (MLD), green lines refer to the mean MLD plus 10-year changes. Purple lines denote the zonal mean pycnocline depth ($z_{N^2_{max}}$) and pink lines the corresponding mean depth plus 10-year changes.

stress curl changes can induce pure heaving (Bindoff and McDougall, 1994; Huang, 2015). Indeed, the deepening of isopycnals in the subtropical gyres indicate downwelling favorable conditions which fits to identified long-term intensification of the North Atlantic's subtropical high (Li, 2012). Besides, observations indicate that volume anomalies of water masses within the North Atlantic Subtropical gyre as a result of transport divergence are associated with both: variations of thermocline depth and Ekman pumping (Evans et al., 2017). This points to wind-induced heave being a driver of the transport anomalies (Evans et al., 2017).

North of the equator (0°-20°N), increasing density leads to an isopycnal shoaling which further contributes to stretching of the layers surrounding the stratification maximum and therefore decreasing the stratification at this depth.

In the Atlantic Ocean, mixed layer and summer stratification maximum changes of the zonal mean mirror the changes described above (Figures 4.4, 4.6, 4.8). Below, the winter stratification maximum in the South Atlantic is deepening whereas the winter stratification maximum in the Northern Hemisphere is shoaling (almost 100 m decade^{-1}, Figure 4.7).

Density changes in the Indian Ocean vary from the patterns found in the other oceans. Poleward of 20°S in the Indian Ocean, a large-scale density increase is accompanied by an equatorward migration of isopycnal outcrops and a weak upwelling of isopycnals within the subtropics (Figure 4.9) during both seasons. The equatorial Indian Ocean is dominated by density reduction. Thus, the isopycnals are moving downward. North of 10°N, density is increasing again and the isopycnals are shoaling over time. These findings go along with a pronounced mixed layer deepening (10-20 m decade^{-1}), particularly in JAS.

4.3.5 Mean global changes of the vertical stratification maximum and the MLD

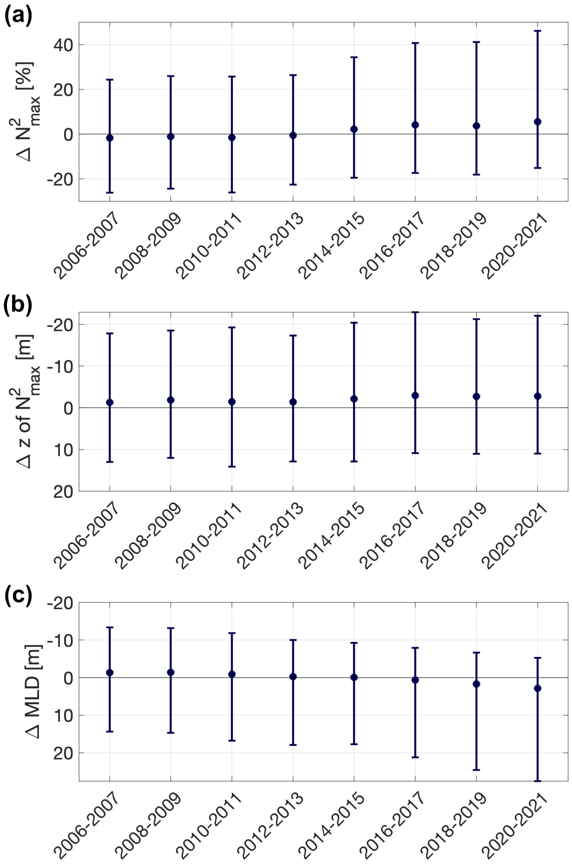

Figure 4.10: Global 2-year median of the vertical stratification maximum, its depth and MLD. Global 2-year median anomalies of the **(a)** vertical stratification maximum **(b)** its depth and **(c)** of the mixed layer depth (MLD). Anomalies are computed relative to the seasonal nearest grid point's mean. Bars show the corresponding upper and lower limits of the interquartile range.

To provide global estimates of stratification changes of the upper-ocean, a 2-year median and IQR of all available profiles' vertical stratification maxima, their depths and MLD anomalies during JAS and JFM are derived (Figure 4.10). For the Argo period, the global median of the vertical stratification maximum shows an intensification of 7-8 %

while the median of the MLD indicates a deepening of $4\,m$. Also, the lower and upper ends of the IQR of these two variables show a stratification increase and mixed layer deepening (Figure 4.10). The upper limits of the IQR of the data are changing even stronger than the median indicating a strong shift in the distribution. The depth of the vertical stratification maximum however, does not show a significant change when taking a global 2-year median.

The increase of the stratification maximum of 7-8 % is comparable to the strengthening of 6.1 % of the upper $200\,m$ of the water column by Yamaguchi and Suga (2019). Yet, their estimate is for the time period of 1960-2017 while our is for the years of 2006-2021 only. Currently, we are in the state of an intensified ocean surface warming (Garcia-Soto et al., 2021) and also the analysis of Yamaguchi and Suga (2019) showed an immense stratification increase for the period of 2010-2017. Therefore, it is possible that we observe such a large stratification increase in a rather short time period.

4.4 Discussion

4.4.1 Contributions of MLT, MLS and isopycnal heave to stratification changes

Our trend analysis of Argo data for the period 2006-2021 shows that on average the vertical stratification maximum in the Northern Hemisphere is strengthening in summer and winter whereas the Southern Hemisphere stratification maximum intensifies in summer (JFM) only (Figure 4.3). This is accompanied by mixed layer deepening and warming throughout both seasons. Due to thicker mixed layers, the volume between the MLD and stratification maxima is contracting during both, winter and summer. The large-scale warming of the mixed layer of $1°\mathrm{C}\,\mathrm{decade}^{-1}$ is consistent with satellite sea surface temperature data from 1981-2018 (Bulgin et al., 2020). Mixed layer warming rates among four consecutive periods from the 37-year time series demonstrate the largest warming trend during the period of 2010-2018 (with regionally trends up to $4°\mathrm{C}\,\mathrm{decade}^{-1}$) (Bulgin et al., 2020).

In general, the findings reveal stratification increases can be linked to surface density reduction mainly due to mixed layer warming and partly freshening as well as to squeezing of isopycnal layers (i.e., pure heave) at the depth of the vertical stratification maximum (e.g., subtropical North Pacific). Nevertheless, the global maps highlight several regional differences of stratification changes during the analyzed period indicating that decadal to multidecadal climate variability is most likely responsible for some of the observed variations. The results show warming of the ocean surface does not necessarily imply intensifying stratification maxima on decadal time scales as it was demonstrated for longer time periods (1990-2015 by Somavilla et al., 2017). In some regions the mixed layer warming-induced density reduction is counterbalanced by a salinity increase which then in turn occurs along with a reduction of stratification if the salinity increase is large enough (e.g., subtropical North Atlantic, Figures 4.3, 4.5, Supplementary Figure 4.17). It should be noted that our findings of the MLS changes do not suggest an amplification of the hydrological cycle as determined by Durack and Wijffels (2010). However, this can be attributed to the different investigated time periods and observation lengths. It is most likely that we here observe a multi-year climate variability as we focus on the past 16 years. Mixed layer changes may be associated with variations in advection and freshwater fluxes (Sprintall and Cronin, 2009). Apart from MLT and MLS variations, stratification is impacted by isopycnal heave. Stretching and squeezing of isopycnal layers is caused by wind stress curl changes (Bindoff and McDougall, 1994; Huang, 2015) and the related volume changes affect the stratification (e.g., contraction of volume in the North Pacific leading to enhanced stratification and stretching of isopycnals in the North Atlantic causing a reduction of stratification, Figures 4.3, 4.7, 4.8).

4.4.2 Mixed layer deepening and stratification increase

Changes of stratification have been addressed by analyzing MLT, MLS and isopycnal heave. The large-scale vast mixed layer deepening will be addressed in the following. Mixed layer deepening might modulate upper-ocean stratification. As indicated in the introduction, model studies have suggested that on-going warming and ocean stratification intensification may lead to thinner mixed layers (Capotondi et al., 2012). Recent observations indicate long-term intensifying stratification (Yamaguchi and Suga, 2019; Li et al., 2020; Sallée et al., 2021) does not have to go along with thinner mixed layers (Somavilla et al., 2017; Sallée et al., 2021). In fact, the summer mixed layer is deepening for the period 1970-2018 (Sallée et al., 2021). For the much shorter Argo observation period, we identify a significant mixed layer deepening in most regions as well as on global scale. Whether this is part of the ongoing long-term deepening trend or a period of climate variability remains to be investigated with the prolonging observations of the Argo array.

We observe a symmetric seasonal mixed layer deepening in both hemispheres. This large-scale deepening is more pronounced in winter than in summer and only small limited regions defy the global trend. Warmer and thicker mixed layers contribute to a stronger vertical stratification maximum. This can be explained as follows: oceanic warming from atmospheric forcing creates a vertical temperature gradient and thus density gradient, leading to a pronounced increase of depth average stratification and a slight increase of the stratification maximum. A subsequent wind-induced deepening of the upper well-mixed layer reduces the distance between the bottom of mixed layer and vertical stratification maximum. This contraction results in an upward shift and strengthening of the vertical stratification maximum. In summer, the stratification maximum demonstrates only weak changes whereas the winter stratification maximum shows a pronounced shoaling trend. This generates a squeezing of the layer between the deepening mixed layer and the vertical stratification maximum, being more intense during winter.

As the mixed layer deepens, the mixed layer heat content increases stronger than expected from sea surface warming of satellite measurements alone. Larger ocean heat content could contribute to enhanced hurricane activity (Trenberth et al., 2018). Since the winter mixed layer thickens stronger than the summer mixed layer, the seasonal cycle of the MLD is amplified, which impacts the subduction of mode waters. The largest winter MLD increases are situated poleward of 40°. Mode waters are mainly formed by the lateral induction part of the subduction equation (Marshall et al., 1993; Hanawa and Talley, 2001; Karstensen and Quadfasel, 2002a). If the seasonal cycle and the meridional gradient of the MLD are enhancing, lateral induction is intensifying and subtropical mode water volume increases due to isopycnal heaving (Häkkinen et al., 2015, 2016). These processes may help to explain why mode waters are identified as warming hot spots during the Argo period (Kolodziejczyk et al., 2019).

Possibilities of increased MLD are changing buoyancy fluxes, but since the mixed layer is warming the buoyancy fluxes would yield the wrong sign. Therefore, we conclude wind is likely the main contributor. There are two mechanisms by which wind might contribute to enhanced MLD: increased turbulent mixing due to stronger winds and increased Ekman convergence due to intensified cyclonic wind stress curl. It is well-known that global trend analysis of wind is uncertain with a tendency to increased wind speeds over the ocean (Torralba et al., 2017). We investigated changes of the wind speed and its variability of different products (Supplementary Figures 4.15, 4.16). Despite the high uncertainty of wind products, the results indicate wind changes from current wind datasets cannot explain the nearly unanimous global mixed layer deepening. Some regions as in the Northern Hemisphere in JFM indicate enhanced wind speed and variability which might contribute to thicker winter mixed layers. Yet, there are also many areas, where the wind variability seems to decrease. Intensifying subtropical highs are suggested in a warming climate (Li et al., 2012). Besides, observations (2005-2014) indicate an intensifying South Pacific Gyre Circulation caused by anomalous Ekman convergence (Roemmich et al., 2016). Such changes are associated with wind stress curl changes driving Ekman convergences and therefore impacting MLD.

The question why the mixed layer is deepening cannot be solved within this study. Nevertheless, changes of the wind fields are a possible contributor. Different wind regimes rule in different places and in different seasons. Other parameters of wind can have an influence, such as frequency, maximum magnitudes, timings, midlatitude winter storms, tropical cyclones, etc. To just name a few variables that highlight the difficulties we have to deal with.

The described and analyzed large-scale pattern indicate various forces at play in the upper-ocean stratification, with MLT increase playing into most observed changes. Nevertheless, regional differences are large and regionally as well as temporally varying forces can play an important role. The identified changes cannot solely be linked to one global trend. While the data used here is deweighting ENSO, other climate variations, as Pacific Decadal Oscillation, Atlantic Meridional Oscillation, Southern Annular Mode, North Atlantic Oscillation play a role in determining the regional to basin scale trend patterns.

The Argo project allows us to investigate upper-ocean changes for the past 16 years. Uncertainties from this product have to be kept in mind. There might be gaps in the data in some regions for some periods. For example, the central subtropical South Pacific has some regions where the maximum time span within a 2° × 2° grid box covered by Argo profiles is 6 years or less (Supplementary Figure S1). Trends in areas like this should be treated with caution. Nevertheless, most areas show a sufficient amount and time span of available profiles per grid box (Supplementary Figure 4.11). Besides, the estimated trends have been compared to actual time series of JAS and JFM vertical stratification maximum and MLD anomalies (Supplementary Figures 4.18-4.21). The regional time series confirm that the identified trend yields reasonable results. Indeed, many regions reveal continuous intensification of the vertical stratification maximum as well as ongoing mixed layer deepening. Hence, for the Argo observation period of 16 years we are able to show significant trends of upper-ocean stratification and mixed layer properties. To determine whether these changes and regional differences are part of the ongoing climate warming, the Argo time series has to be continuously updated.

4.5 Conclusion

For the Argo observation period, the vertical stratification maximum is intensifying on a global average by 7-8 %. Even though there are large regional differences, the global signal suggests an increasing de-coupling of the surface ocean from the ocean interior in the past 16 years. The observed modified stratification can be associated with a warmer and thicker mixed layer. The salinity changes either contribute or counteract the warming-induced density reduction, depending on the region. Additionally, the isopycnal heave plays a role in adjusting the vertical stratification maximum and is likely to have been impacted by wind stress curl-driven changes. The deepening of the mixed layer and squeezing of the layers below down to the vertical stratification maxima in summer and winter, have the potential to impact mode water formation processes, ocean ventilation and mixing, and further biological consequences. Impacts on nutricline, subsurface oxygen levels and therefore the marine ecosystem are expected to be manifold and regionally diverse. The presented analysis can help identify model – observation discrepancies concerning

MLD and stratification, determine its causes and help to improve model predictions and projections. Since many ecological and biogeochemical processes in the upper-ocean are impacted by MLD and stratification, their correct representation in climate models is necessary to better understand looming changes to ecosystem and biogeochemistry in the ocean.

4.6 Data Availability Statement

The analyzed datasets are publicly available. This data can be found here: Argo (2021). Argo float data and metadata from Global Data Assembly Centre (Argo GDAC) - Snapshot of Argo GDAC of December 10st 2021. SEANOE. doi: 10.17882/42182#90179. The Ocean Nino Index (ONI) by Trenberth and National Center for Atmospheric Research Staff (2020): https://psl.noaa.gov/data/correlation/oni.data.

All necessary codes for this study are available at: Roch, Marisa, Brandt, Peter, & Schmidtko, Sunke. (2023). Software used in "Recent large-scale mixed layer and vertical stratification maxima changes" (Version 3). Zenodo. https://doi.org/10.5281/zenodo.8382701.

Datasets used in the Supplementary Materials: M158 CTD data from Brandt, Subramaniam, Schmidtko, Krahmann (2022): Physical oceanography (CTD) during METEOR cruise M158. PANGAEA, https://doi.org/10.1594/PANGAEA.952354. CCMP wind data from Remote Sensing Systems (Wentz et al., 2015): https://www.remss.com/measurements/ccmp/. ERA5 data by Hersbach et al. (2018): https://cds.climate.copernicus.eu/cdsapp#!/dataset/reanalysis-era5-single-levels?tab=overview and the global wind product of E. U. Copernicus Marine Service Information: https://data.marine.copernicus.eu/product/WIND_GLO_WIND_L4_REP_OBSERVATIONS_012_006/description.

4.7 Acknowledgements

We acknowledge the use of the Argo observation dataset, the ONI by Trenberth and National Center for Atmospheric Research Staff (2020), the use of CCMP wind data from Remote Sensing Systems (Wentz et al., 2015), the use of ERA5 data by Hersbach et al. (2018) and the use of the global wind product of E. U. Copernicus Marine Service Information.

4.8 Supplementary Material

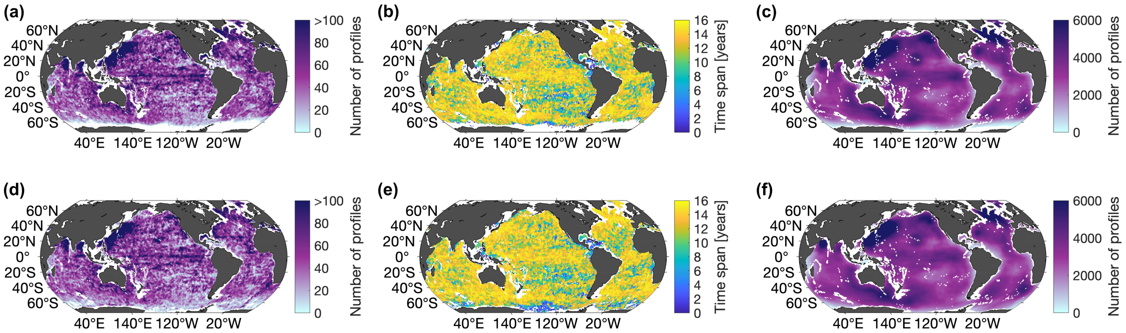

Supplementary Figure 4.11: Spatial and temporal distribution of Argo profiles. **(a)** Number of profiles per 2° × 2° grid box in July-September from 2006-2021. **(b)** Maximum time span of available Argo profiles per 2° × 2° grid box from in July-September from 2006-2021. **(b)** Number of profiles included in the mapping procedure for the climatological mean of July-September season for each grid point. **(d)-(f)** Same as above just for January-March season.

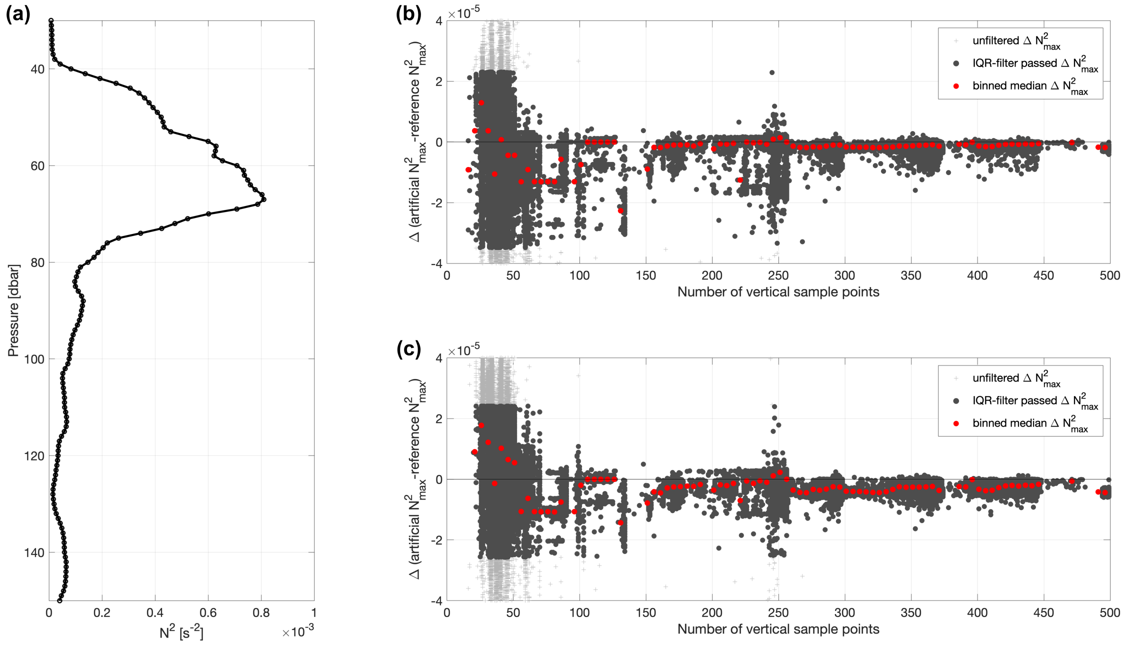

Supplementary Figure 4.12: Comparison of stratification maxima derived using isopycnal and isobaric gridding. **(a)** Reference squared Brunt-Väisälä frequency profile obtained from a CTD station at 0°, 11°W from the M158 cruise in September-October 2019 (Brandt, Subramaniam, Schmidtko, Krahmann (2022): Physical oceanography (CTD) during METEOR cruise M158. PANGAEA, https://doi.org/10.1594/PANGAEA.952354). This profile is assumed to be the ”true” profile. Temperature, salinity, pressure and potential density from this high-resolution CTD profile with 1 *dbar* vertical resolution are subsampled creating artificial Argo profiles, using the different vertical grids from 245,730 Argo profiles taken in the Atlantic Ocean (40°N-40°S). **(b)** Difference between the estimates of the vertical stratification maximum of artificial Argo profiles determined from isopycnal gridded fields and the vertical stratification maximum obtained from the reference profile as function of the number of vertical sample points of the Argo profiles in the upper 500 m. **(c)** Same as in **(b)** but when deriving the vertical stratification maximum of artificial Argo profiles determined from isobaric gridded fields. Both types of grids are determined by applying the makima interpolation scheme onto the density/pressure grid of the reference CTD profile for isopycnal/isobaric gridding, respectively, and the corresponding vertical stratification maxima of the resulting artificial Argo profiles are estimated following the step-by-step procedure in the Data and Method Section. Light gray crosses show profiles that did not pass the IQR filter. Note that not all values are visible, as these graphs represent a zoomed view. Dark gray dots show the profiles that pass the IQR and red dots denote the binned median. Bin size is 5 vertical sample points.

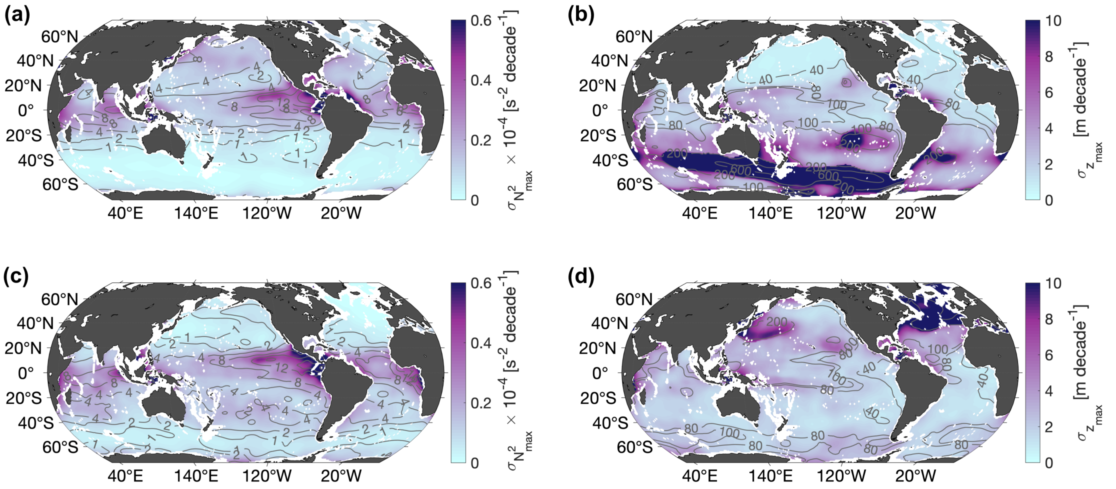

Supplementary Figure 4.13: Standard errors for the vertical stratification maximum and its depth. **(a)** Standard error for the trend of the vertical stratification maximum in July-September and in **(b)** for its depth. **(c)-(d)** Same as above but for the January-March season. Contour lines show the corresponding mean field in each panel.

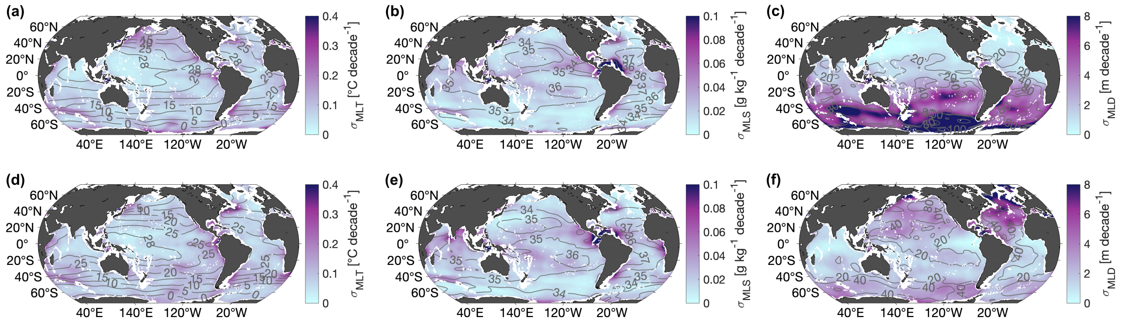

Supplementary Figure 4.14: Standard errors for mixed layer temperature, salinity and depth. **(a)** Standard error of trends of mixed layer temperature, **(b)** mixed layer salinity and **(c)** mixed layer depth in July-September. **(d)-(f)** Same as above but for January-March season. Contour lines show the corresponding mean field in each panel.

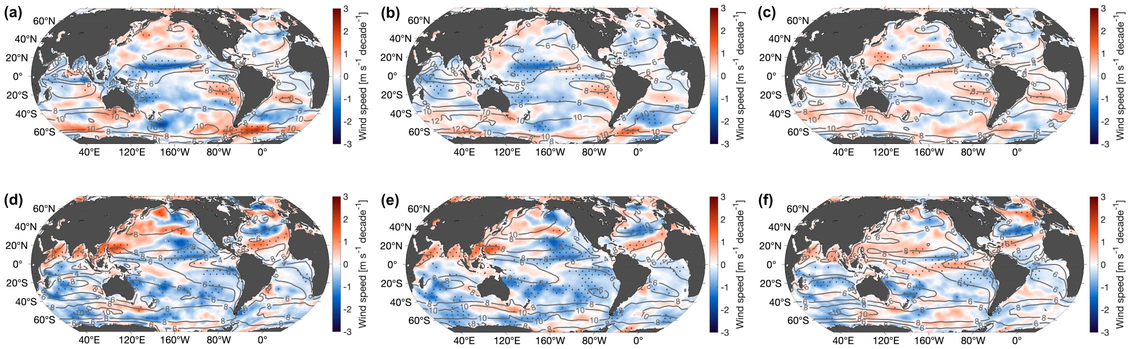

Supplementary Figure 4.15: Trend of wind speed. Trend of wind speed in July-September from **(a)** CCMP (Cross-calibrated multi-platform wind vector analysis, CCMP V2.0 dataset from Remote Sensing Systems (Wentz et al., 2015)) for the period of 2006-2019, **(b)** the Global Ocean Wind L4 Reprocessed 6 hourly Observations from Copernicus Marine Environmental Monitoring Service for the period of 2006-2019 (see Bentamy et al., 2022) and **(c)** ERA5 (combined 10 m zonal and meridional wind speed components, Hersbach et al. (2018)) for the period of 2006-2021. **(d)-(f)** Same as **(a)-(c)** but for January-March. Dotted areas show where the trend is within the 95 % confidence interval. All three products have been converted on a 1° × 1° spatial grid by taking the mean of all available points surrounding the grid point in 3° radii in latitudinal and longitudinal direction. The 6-hourly values were averaged onto daily means. The trends are calculated from daily wind speed anomalies relative to their corresponding seasonal means: June-September and January- March. ENSO years are de-weighted.

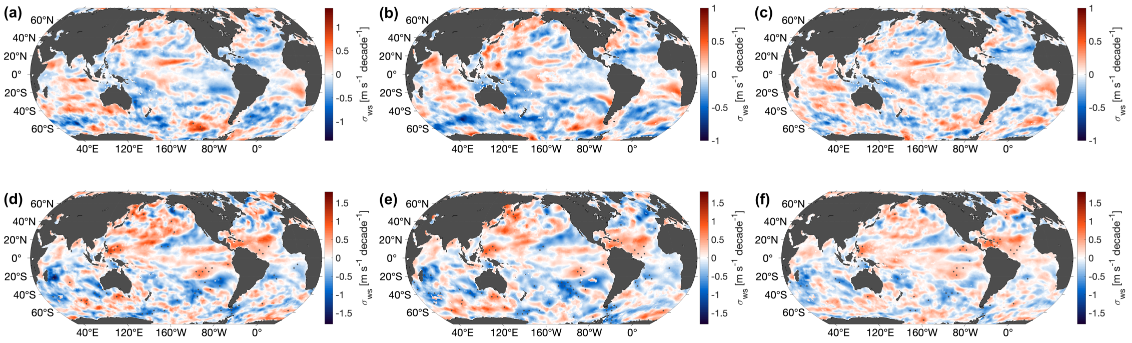

Supplementary Figure 4.16: Trend of wind speed variability. Trend of wind speed standard deviation in July-September from **(a)** CCMP (Cross-calibrated multi-platform wind vector analysis, CCMP V2.0 dataset from Remote Sensing Systems (Wentz et al., 2015)) for the period of 2006-2019, **(b)** the Global Ocean Wind L4 Reprocessed 6 hourly Observations from Copernicus Marine Environmental Monitoring Service for the period of 2006-2019 (see Bentamy et al., 2022) and **(c)** ERA5 (combined 10 m zonal and meridional wind speed components, Hersbach et al. (2018)) for the period of 2006-2021. **(d)-(f)** Same as **(a)-(c)** but for January-March. Dotted areas show where the trend is within the 95 % confidence interval. All three products have been converted on a 1° × 1° spatial grid by taking the mean of all available points surrounding the grid point in 3° radii in latitudinal and longitudinal direction. The 6-hourly values were averaged onto daily means. The standard deviation from daily wind speed anomalies is calculated for each year's three months period: June-September and January-March. The anomalies are determined by subtracting the July-September or January-March mean from the daily values, respectively. Hence, we achieve the annual standard deviation for the two three-months-periods and thus, are able to assess the linear 10-year trend. ENSO years are de-weighted as during the Argo analysis.

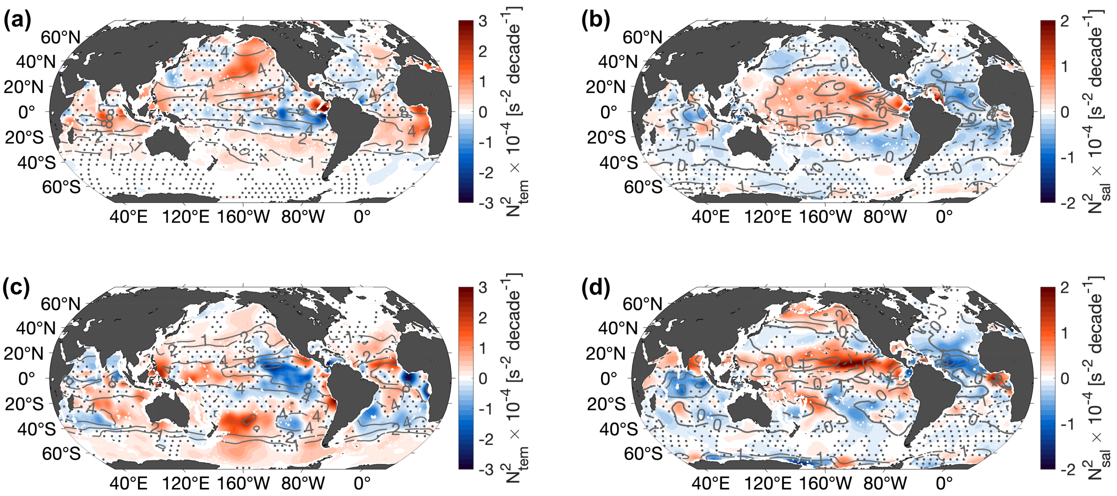

Supplementary Figure 4.17: Thermal and haline contributions to the vertical stratification maximum trend. **(a)** Trend of the thermal contribution to the vertical stratification maximum trend in July-September. **(b)** Trend of saline contribution to the vertical stratification maximum trend in July-September. **(c)-(d)** Same as **(a)-(b)** but for January-March season. The trends are calculated from anomalies relative to their corresponding seasonal means: June-September and January-March. ENSO years are de-weighted. Dotted areas show where the trend is within the 95 % confidence interval. Contour lines show the corresponding mean field $\times 10^{-4}\, s^{-2}$.

We compute profiles of Brunt-Väisälä frequency N^2 following TEOS-10 (IOC et al., 2010; McDougall and Barker, 2011):

$$N^2 = g^2 \rho \frac{\beta dS_A - \alpha dT}{dP}$$

where 4 is the gravitational acceleration, ρ is the potential density, α and β refer to the thermal expansion and saline contraction coefficients, respectively. The Brunt-Väisälä frequency can be approximated as a linear combination of its haline and thermal contributions, N^2_{sal} and N^2_{tem}:

$$N^2 = N^2_{tem} + N^2_{sal} \,\text{with}\, N^2_{tem} = -g^2 \rho \frac{\alpha \Delta T}{\Delta P} \,\text{and}\, N^2_{sal} = g^2 \rho \frac{\beta \Delta S}{\Delta P}$$

This is similar to the procedure performed by Sallée et al. (2021) except from that we use the pressure formulation and not the depth coordinates.

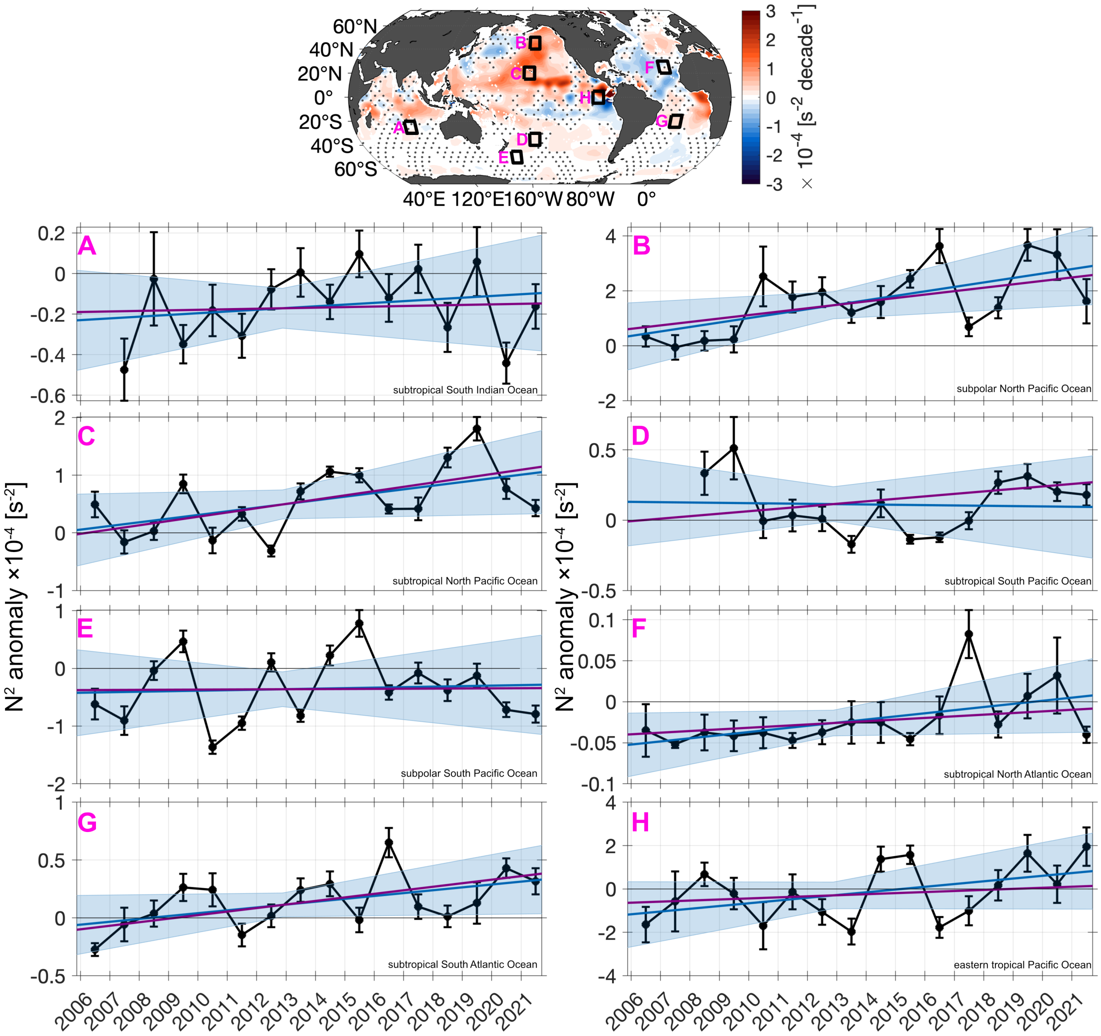

Supplementary Figure 4.18: Regional time series of vertical stratification maximum in July-September. Top: Trend of vertical stratification maximum in July-September (as in Figure 4.3a). Dotted areas show where the trend is not of 95 % significance. Black boxes with pink labels mark the corresponding regions for which the median time series (black) for July-September is shown below in **(A)-(H)**. Black lines with dots mark the July-September median anomaly for each year relative to the seasonal mean. Error bars denote the 95 % confidence interval. Blue lines indicate the corresponding trend of the July-September anomalies. Shading denotes its 95 % confidence level. Purple lines refer to the corresponding trend from our product we determined via the least square method (as in Figure 4.3a)) for the center grid point within the respective regional box.

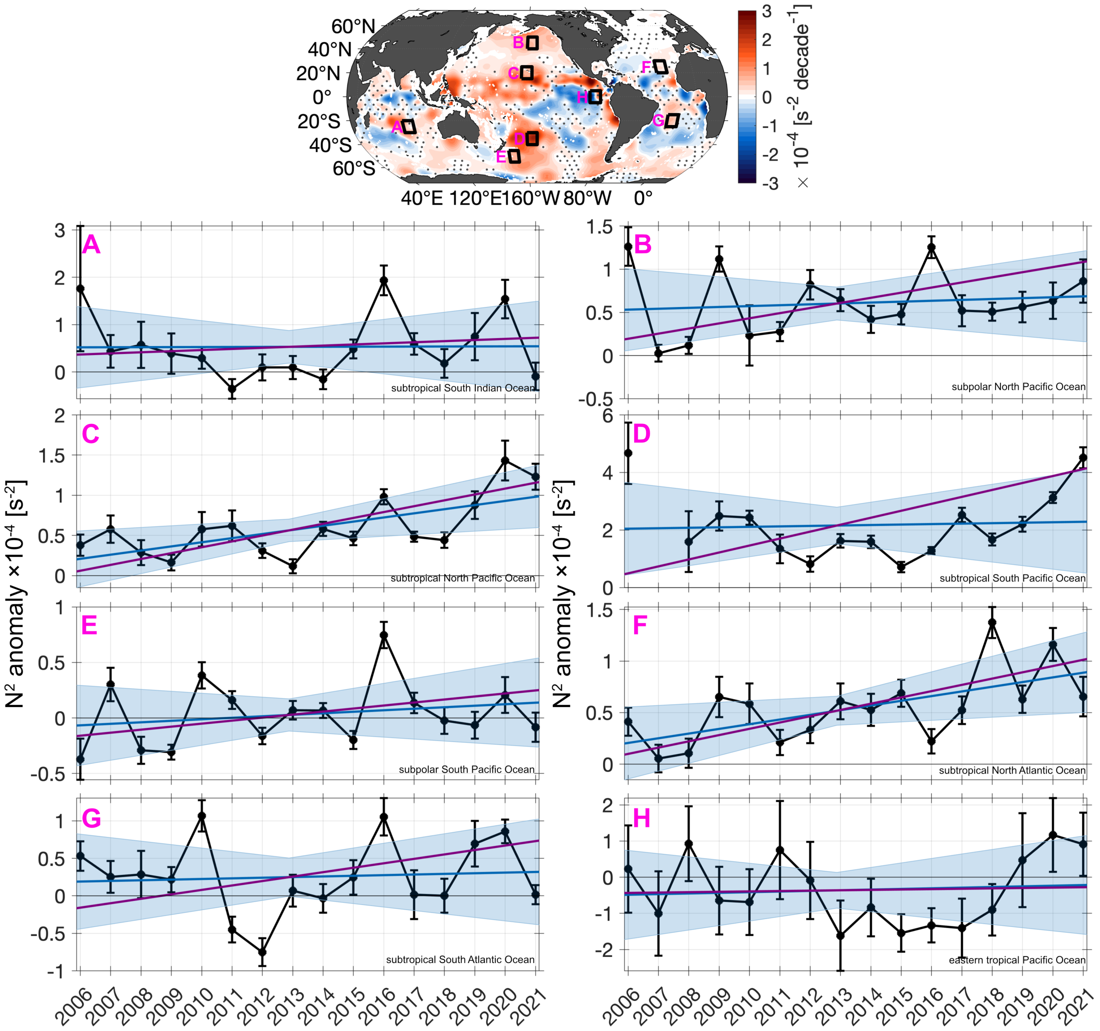

Supplementary Figure 4.19: Regional time series of vertical stratification maximum in January-March. Top: Trend of vertical stratification maximum in January-March (as in Figure 4.3c). Dotted areas show where the trend is not of 95 % significance. Black boxes with pink labels mark the corresponding regions for which the median time series (black) for January-March is shown below in **(A)-(H)**. Black lines with dots mark the January-March median anomaly for each year relative to the seasonal mean. Error bars denote the 95 % confidence interval. Blue lines indicate the corresponding trend of the January-March anomalies. Shading denotes its 95 % confidence level. Purple lines refer to the corresponding trend from our product we determined via the least square method (as in Figure 4.3c) for the center grid point within the respective regional box.

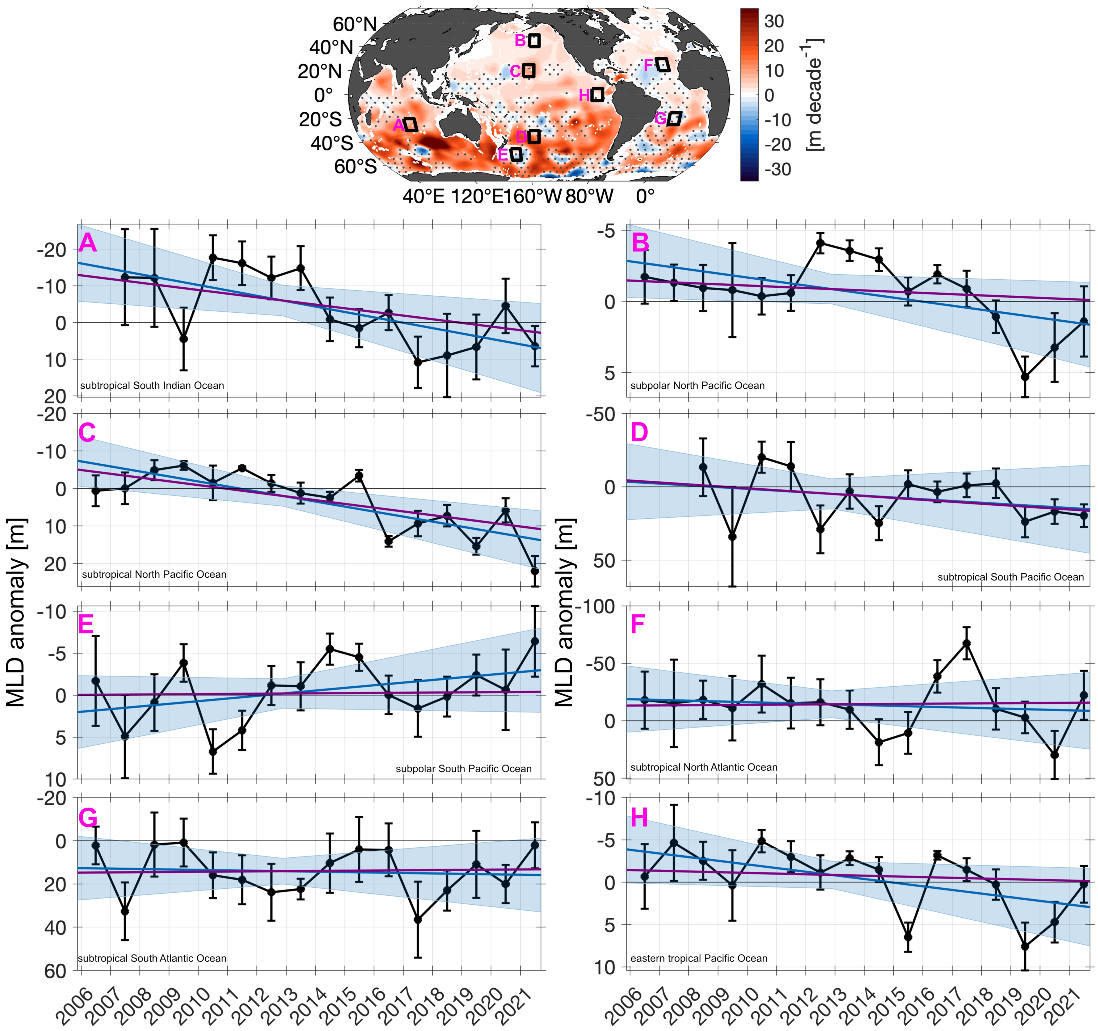

Supplementary Figure 4.20: Regional time series of mixed layer depth in July-September. Top: Trend of mixed layer depth in July-September (as in Figure 4.5a). Dotted areas show where the trend is not of 95 % significance. Black boxes with pink labels mark the corresponding regions for which the median time series (black) for July-September is shown below in **(A)-(H)**. Black lines with dots mark the July-September median anomaly for each year relative to the seasonal mean. Error bars denote the 95 % confidence interval. Blue lines indicate the corresponding trend of the July- September anomalies. Shading denotes its 95 % confidence level. Purple lines refer to the corresponding trend from our product we determined via the least square method (as in Figure 4.5a) for the center grid point within the respective regional box.

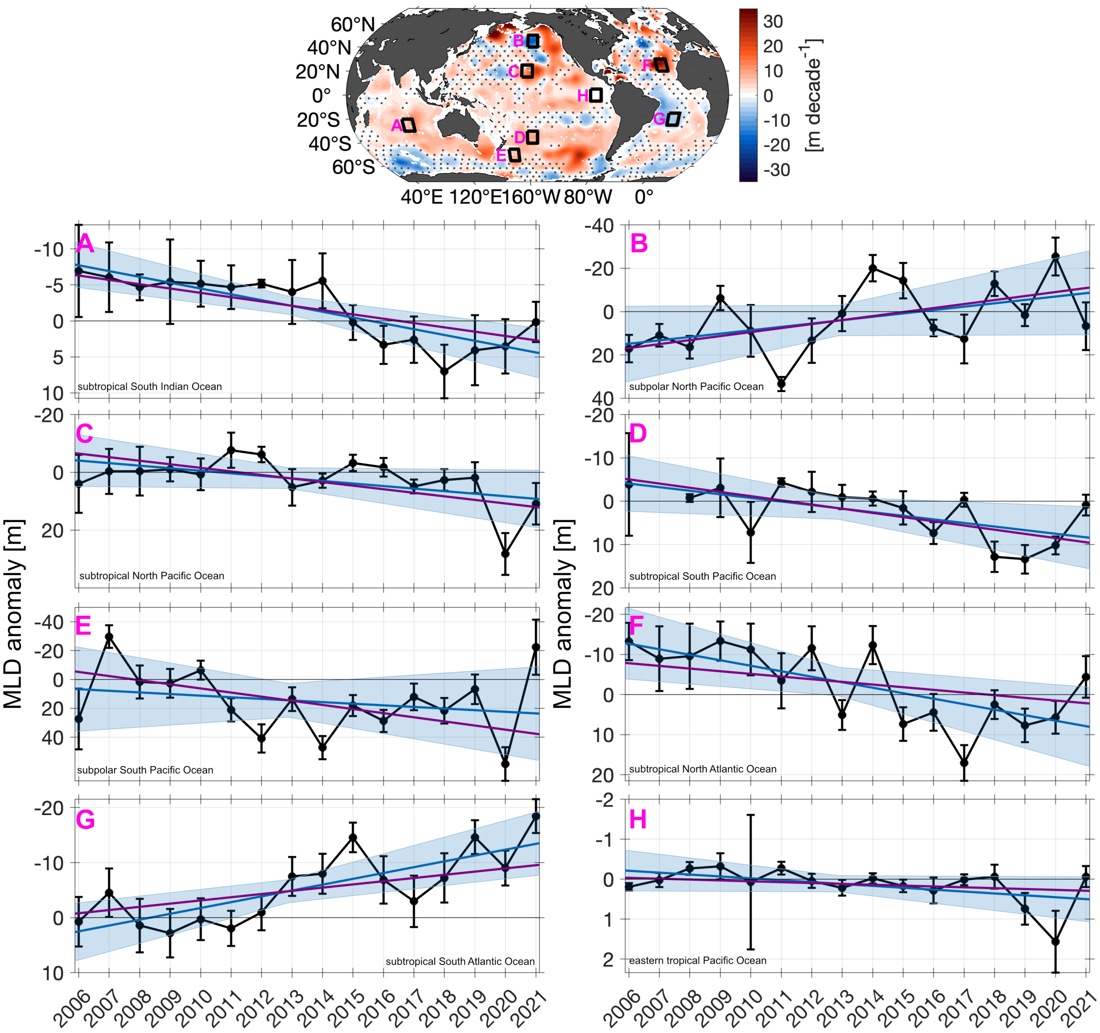

Supplementary Figure 4.21: Regional time series of mixed layer depth in January-March. Top: Trend of mixed layer depth in January-March (as in Figure 4.5c). Dotted areas show where the trend is not of 95 % significance. Black boxes with pink labels mark the corresponding regions for which the median time series (black) for January-March is shown below in **(A)-(H)**. Black lines with dots mark the January-March median anomaly for each year relative to the seasonal mean. Error bars denote the 95 % confidence interval. Blue lines indicate the corresponding trend of the January-March anomalies. Shading denotes its 95 % confidence level. Purple lines refer to the corresponding trend from our product we determined via the least square method (as in Figure 4.5c) for the center grid point within the respective regional box.

Chapter 5

Impact of the North Atlantic Oscillation on the decadal variability of the upper subtropical-tropical Atlantic Ocean

Chapter 3 and Chapter 4 have shown that the upper-ocean becomes more stratified in many regions of the world's oceans during the Argo period. In this Chapter, the analysis focuses on the decadal variability of the upper-ocean in the subtropical-tropical Atlantic. Variability associated with the North Atlantic Oscillation are compared to variations of isopycnal heave and potential vorticity. Possible impacts of a changing potential vorticity barrier in the northeastern tropical North Atlantic on the pathways of subducted water from the subtropics to the tropics are analyzed. Additionally, subduction and transport rates of the Equatorial Undercurrent are examined.

The manuscript is submitted to *Journal of Geophysical Research: Oceans.*

Roch, M., Brandt, P., Schmidtko, S., and Tuchen, F. P., (submitted to *Journal of Geophysical Research: Oceans*). Impact of the North Atlantic Oscillation on the decadal variability of the upper subtropical-tropical Atlantic Ocean.

The candidate carried out all the analyses described in the Sections 5.2.1-5.2.2, 5.2.4-5.2.5. Geostrophic velocities on the $26.0\,kg\,m^{-3}$-isopycnal in Section 5.2.3 were carried out by Philip Tuchen. The candidate performed the analysis in Section 5.2.6 based on the investigation by Brandt et al. (2021). She produced all the figures and authored the manuscript from the first draft to the final version.

Abstract

In the northeastern tropical Atlantic, a region of high potential vorticity (PV) determines the size of the exchange window for the interior thermocline flow of the subtropical cell via its variations in strength and extent. Variability of this PV barrier has the potential to impact the ventilation of the tropical Atlantic on decadal timescales. Here, the impact of the North Atlantic Oscillation (NAO) on isopycnals within the thermocline of the subtropical-tropical Atlantic Ocean is assessed from Argo observations for the time period of 2006-2022. Relative to the negative NAO phase from 2009-2010, during the positive NAO phase from 2014-2019, the North Atlantic subtropical high and the northeast trade winds are intensified. Satellite-derived wind stress curl shows increased upwelling/downwelling on the equatorward/poleward side of the trade wind zone, respectively. In the subtropical-tropical Atlantic, a symmetric pattern of isopycnal heave is observed: rising isopycnals within 20°N and 20°S and sinking poleward of that. With rising isopycnals, the PV barrier in the northeastern tropical Atlantic becomes stronger. Analyses of geostrophic velocities and the Sverdrup streamfunction in the tropical Atlantic show that during the positive NAO phase, associated with stronger a PV barrier, there are enhanced equatorward velocities at thermocline level along the western boundary and reduced equatorward supply of thermocline water through the interior. Moreover, intensified trade winds simultaneously lead to strengthened Equatorial Undercurrent (EUC) transport as observed at a mooring site at 0°, 23°W, likely via the pulling effect of the subtropical cells and enhanced subduction of thermocline waters supplying the EUC.

Plain Language Summary

In the North Atlantic Ocean, subducted water from the subtropics has two possible pathways within the thermocline toward the equatorial region: the interior pathway and the pathway along the western boundary. The size of the exchange window between subtropics and tropics depends on the strength of a barrier zone in the eastern part of the basin that is associated with wind-driven upwelling of density surfaces. The North Atlantic Oscillation (NAO) is the dominant atmospheric climate mode in the North Atlantic and in this study, we show how the NAO impacts the barrier for the equatorward thermocline flow in the tropical Atlantic Ocean. During positive NAO phases (e.g., 2014-2019), density surfaces become shallower and strengthening the barrier, while during negative NAO phases (e.g., 2009-2010) the barrier weakens. Geostrophic velocity analysis reveals that during positive NAO phases more/less thermocline water is transported equatorward via the western boundary/interior pathway. Additionally, observations from a mooring site at 0°, 23°W show stronger Equatorial Undercurrent transport as a result of intensified trade winds during positive NAO phases.

5.1 Introduction

The tropical Atlantic Ocean plays an important role in the global climate system as it is a gateway for the northward branch of the Atlantic Meridional Overturning Circulation (AMOC) that transports warm water from the South to the North Atlantic (Schott et al., 2004; Tuchen et al., 2022b; Martín-Rey et al., 2023). Additionally, the subtropical and tropical Atlantic are connected via shallow meridional overturning cells, so-called subtropical cells (STCs) (Liu et al., 1994; McCreary and Lu, 1994; Schott et al., 2004). Low potential vorticity (PV) water masses subducted by Ekman pumping in the subtropics are transported within the thermocline toward the equator. At the equator, the water is upwelled and transported back to the subtropics within the surface layer via poleward Ekman transport (Liu et al., 1994; McCreary and Lu, 1994; Schott et al., 2004).

The northeastern tropical Atlantic is under the influence of the northeast trade winds which generate positive wind stress curl south of the wind maximum and negative wind stress curl north of its maximum. Wind stress curl-driven Ekman suction south of the wind maximum, produces upwelling and doming of isopycnals, leading to a region of high PV on upper isopycnals ($< 26.4\,kg\,m^{-3}$, Figure 5.1) (Talley, 1988; Zhang et al., 2003). This zone of high PV acts as a barrier for the subducted water that flows from the subtropical North Atlantic toward the equator (Figure 5.1) (McCreary and Lu, 1994; Zhang et al., 2003; Schott et al., 2004). Therefore, the water subducted in the subtropics by Ekman pumping has to be advected around the PV barrier to reach the equator. Also, the southeastern tropical Atlantic contains an area of higher PV, but smaller in size and not as intense as in the North Atlantic and consequently, without a comparable effect on the equatorward thermocline flow. Therefore, and due to the larger basin size, thermocline water from the subtropical South Atlantic can take, besides from the western boundary pathway, a more direct route toward the equator.

As part of the STCs, two different exchange windows for subducted water from the subtropics to the tropics have been identified. The first exchange window allows pathways of subducted water through the interior of the basin (pathway (1) in Figure 5.1). The second one, includes equatorward pathways along the western boundary (pathway (2) in Figure 5.1) (Malanotte-Rizzoli et al., 2000). In the North Atlantic all pathways start with equatorward and westward flow in the region north of northeast trade wind maximum, where Ekman pumping results in the subduction of central water masses. These water masses, when leaving the directly wind-driven surface layer, are dominated by the presence of the North Equatorial Current (NEC, Figure 5.1), conserve their PV and follow geostrophic streamlines as analytically described in the ventilated thermocline theory by Luyten et al. (1983). On its way to the Equatorial Undercurrent (EUC), the interior pathway, first passes the PV barrier in the northeastern tropical Atlantic, before the water is deflected eastward due to the presence of the eastward flowing North Equatorial Countercurrent (NECC) and North Equatorial Undercurrent (NEUC, Figure 5.1) (Malanotte-Rizzoli et al., 2000). Before finally reaching the EUC, the flow path is bended again to the west at around 2°N as a result of the here-located westward flowing northern branch of the South Equatorial Current (nSEC, Figure 5.1) (Malanotte-Rizzoli et al., 2000; Schott et al., 2004). Besides this interior pathway, there is the western boundary pathway along which subducted water is first transported to the western boundary before it is further transported toward the equator. The subducted water reaches at the western boundary at around 10°N and reaches the North Brazil Current (NBC) retroflection at around 5°N-8°N (Figure 5.1) (Hazeleger et al., 2003). With the NBC retroflection, a part of the thermocline water is supplied into the NECC/NEUC or may reach the equator to supply the EUC (Figure 5.1).

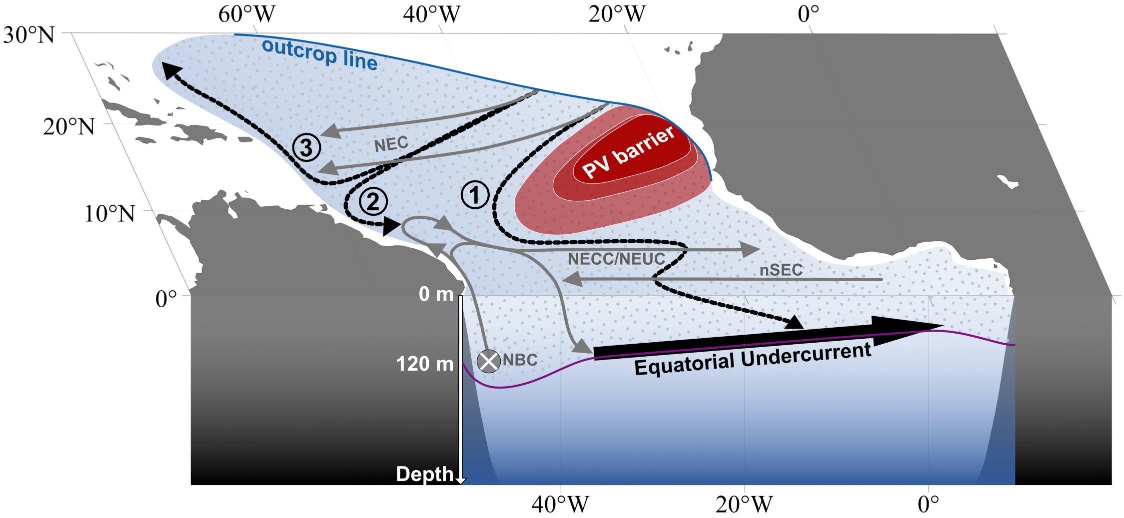

Figure 5.1: Schematic of the pathways of subducted water on an isopycnal surface (dotted area) outcropping in the subtropical North Atlanic (blue line marked as outcrop line). The depth of the isopycnal at the equator is indicated by the purple line. Subducted water generally follows the westward flow of the North Equatorial Current (NEC) with an additional equatorward component. Three different pathways are possible. (1) The interior pathway, that takes a detour around the potential vorticity (PV) barrier (red shading) in the northeastern tropical Atlantic before being deflected eastward due to the North Equatorial Countercurrent (NECC)/North Equatorial Undercurrent (NEUC) and westward due to the northern branch of the South Equatorial Current (nSEC), reaching the Equatorial Undercurrent (EUC) in the interior. (2) The western boundary pathway reaches the western boundaty north of the North Brazil Current (NBC) retroflection zone, from where the subducted water is eventually transported equatorward and eastward as part of the NBC retroflection. (3) The recirculation pathway follows the flow of the North Atlantic subtropical gyre. Note, this schematic only represents possible pathways of subducted water from the North Atlantic. It excludes pathways of South Atlantic water. However, the EUC is mostly supplied from the Southern Hemisphere with an important pathway being the northward flow of the NBC at the western boundary across the equator. Black stippled lines show the three different pathways, gray solid lines denote the mean surface-thermocline circulation field. This schematic is based on the circulation and pathway schemes in Stramma and England (1999); Zhang et al. (2003); Schott et al. (2004); Hahn et al. (2017); Tuchen et al. (2022b).

In general, the tropical Atlantic upper-ocean flow field is a combination of the STCs north and south of the equator, the western boundary current system and a complex zonal current system of equatorial and off-equatorial currents (Schott et al., 1998; Stramma and England, 1999; Brandt et al., 2015; Hahn et al., 2017). Moreover, tropical Atlantic water masses are mainly of South Atlantic origin, which is a consequence of the superimposed warm water return flow of the AMOC (Tuchen et al., 2022b). The South Equatorial Current (SEC) is supplying the northward flowing North Brazil Undercurrent (NBUC) at around 11°S with South Atlantic water masses. On its way to the equator, the surface flow of the NBUC intensifies at around 5°S, transforming the NBUC into the NBC (Figure 5.1) (Schott et al., 1998). North of the equator, the NBC retroflects to the southeast, feeding into the eastward flowing NECC/NEUC at around 5°N and the EUC at the equator (Schott et al., 1998; Hazeleger et al., 2003). A small contribution to the NBC retroflection was suggested to originate from the North Atlantic via the NEC (Bourlès et al., 1999) which form the western boundary pathway of the Northern Hemisphere STC, described above. A third pathway of subducted water, that does not participate in the STC, is the recirculation pathway where the water is trapped in the subtropical gyre (pathway (3) in Figure 5.1) (Liu et al., 1994; McCreary and Lu, 1994; Schott et al., 2004).

The zonal extent of the PV barrier in the northeastern tropical Atlantic determines the width of the interior window and thus, how much water is transported via the interior or western boundary pathway toward the equator (Figure 5.1). The PV barrier may adjust in magnitude and size due to wind stress curl or buoyancy changes. It has been suggested by a model study for the Pacific that in a warmer climate the PV barrier intensifies and extends further westward (Luo et al., 2009b). In this case, more water is transported closer to the western boundary while the total transport from the subtropics to the tropics may remain the same (Luo et al., 2009b). The redistribution of the subtropical-tropical exchange pathways toward the western boundary would result in an intensified EUC in the western and central part, and a weakened EUC in the eastern part (Luo et al., 2009b). We assume similar to occur in the Atlantic. In fact, the central Atlantic EUC has been shown to intensify at a rate of $3.3\,Sv\,\mathrm{decade}^{-1}$ from 2008 to 2018 (Brandt et al., 2021). Whether this is a result of climate warming or just part of natural climate variability remains an open question.

The Atlantic EUC is one of the most intense currents in the tropical Atlantic. It flows eastward along the equator and is part of the STCs and the AMOC, thereby, supplying the eastern equatorial Atlantic with saline and high-oxygen waters (Schott et al., 1998; Hazeleger and Drijfhout, 2006; Brandt et al., 2021; Tuchen et al., 2022a). The EUC is locally forced by easterly winds at the equator, creating an eastward pressure gradient (Qiao and Weisberg, 1997). With an assimilation model run of 50 years, it has been shown that the decadal variability of the Atlantic EUC is linked to decadal variations of the STCs forced by the trade winds away from the equator, typically taken at 10°N/S

(Rabe et al., 2008). Investigations of the decadal variability of the Atlantic STCs show that phases of weaker (stronger) interior transport generate higher (lower) equatorial sea surface temperatures (SST) and (Tuchen et al., 2020). For the intensifying Atlantic EUC from 2008-2018 it has been suggested to be related to a strengthening of the Atlantic STCs (Brandt et al., 2021). However, the trend of the Ekman divergence, caused by increased trade winds, is observed to be too small to be the only reason for the EUC transport increase (Brandt et al., 2021). Hence, another way of intensifying EUC transport rartes might be the redistribution of the subtropical-tropical pathways as a result of a changing PV barrier.

Although the STCs have been extensively studied, observational analysis on the North Atlantic PV barrier has fallen behind. Here, we aim to examine the decadal variability of isopycnals within the thermocline layer, connecting the subtropical with the tropical Atlantic Ocean by making use of the large amount of Argo profiles for the period of 2006-2022. Decadal variability of isopycnals is linked to the North Atlantic Oscillation (NAO) which is the leading atmospheric climate mode in the North Atlantic (Eden and Willebrand, 2001; Wanner et al., 2001; Pinto and Raible, 2012). The NAO mode is characterized by its impact on the North Atlantic subtropical high resulting in enhanced westerlies and northeast trades during positive NAO phases and reversed impact during negative phases (Chang et al., 2006). The northern tropical Atlantic variability is not only forced by the NAO but also by the El Niño Southern Oscillation (ENSO) (Czaja et al., 2002). While ENSO influences the northeast trades mainly on interannual timescales, the NAO impact dominates on decadal timescales and longer (Czaja et al., 2002). Here, we focus on decadal variability of the subtropical-tropical Atlantic Ocean. It is the first time to date, that variations of the PV barrier strength in the North Atlantic are investigated from observations and attributed to a redistribution of STC pathways. A changing PV barrier and therefore, variations of the ratio of transport of the interior and western boundary pathways of the equatorward STC flow, not only result in upper-ocean circulation changes, but potentially impact oxygen and nutrient distributions in the subtropical-tropical Atlantic

The present study is organized as follows: in Section 5.2 the data and applied methods are presented. Section 5.3 deals with the results of this study, starting with NAO composites of wind stress, wind stress curl and mixed layer temperature as well as the vertical displacement and PV of the 26.0 $kg\,m^{-3}$-isopycnal. The results are compared to composites of the Sverdrup streamfunction as well as geostrophic velocity on the 26.0 $kg\,m^{-3}$-isopycnal. Subduction rates of EUC density range are analyzed for the North and South Atlantic and related to the EUC transport series inferred from the mooring site at 0°, 23°W. In Section 5.4 the results are summarized and discussed.

5.2 Data and Methods

5.2.1 Argo observations

This study is conducted using Argo observations for the period of 2006-2022 (Argo, 2022). The Argo project is at play since the year 2000. However, it is solely since 2006 that the Argo coverage is large enough to allow for basin-scale mapping (Roemmich et al., 2015; Desbruyères et al., 2017). To date, the Argo array consists of almost 4,000 floats continuously providing hydrographic profiles of the upper $2,000\,m$ of the water column in the global oceans. Only data that pass the quality control, QC = 1, and have the adjusted mode are used for this analysis. Further quality checks have been carried out: Profiles have to contain continuous pressure profiles, reach at least $1,000\,dbar$ and no larger pressure difference than $150\,dbar$ of consecutive pressure measurements is allowed. In addition, profiles are excluded if they contain less than 20 sample points until $2,000\,dbar$ and if no mixed layer depth can be determined. The algorithm fails to define a mixed layer depth when the profile's shallowest measurement is located deeper than $20\,dbar$. Mixed layer characteristics (mixed layer depth, temperature and salinity) are estimated for each Argo profile following the Holte and Talley algorithm (Holte and Talley, 2009). Additionally, we restrict our analysis to the region of the 40°N-40°S in the Atlantic Ocean for most of the analyses which yields 252,725 available profiles. Only for the large-scale mixed layer temperature (MLT) anomalies and for the evaluation of subduction rates, all profiles within 60°N-60°S are included. Prior to further data handling, in situ measurements are converted to absolute salinity, conservative temperature and potential density following TEOS-10 (McDougall and Barker, 2011).

Profile handling, stratification measure and estimate of potential vorticity

We perform an interpolation on an isopycnal grid ($20.235 - 28.15\,kg\,m^{-3}$) with the modified Akima (Akima, 1970) piecewise cubic Hermite interpolation scheme (so-called makima method, (MathWorks Inc., 2019; MATLAB, 2019)). This interpolation scheme is a combination of the cubic spline and the piecewise cubic Hermite interpolating polynomial (pchip) (MathWorks Inc., 2019). The vertical resolution of the isopycnal grid increases for higher density levels. In total, we achieve 163 isopycnal levels. Original Argo profiles, where the vertical salinity gradient $dS/dP \geq 1\,g\,kg^{-1}\,dbar^{-1}$, and the corresponding adjacent pressure measurements are further apart than $2\,dbar$ ($dP \geq 2\,dbar$), are excluded as the interpolation scheme fails for these profiles. Finalizing the profile handling, those profiles that do not cover the full density range, are filled up with mixed layer characteristics above the shallowest measured density surface. This is solely a numerical way to handle outcropping isopycnals.

With these isopycnal-gridded profiles we are now able to determine the stratification of each profile. We use the squared Brunt-Väisälä frequency, $N^2 = g^2 \rho \frac{\beta dS_A - \alpha dT}{dP}$ (following TEOS-10 (IOC et al., 2010; McDougall and Barker, 2011)) as a measure for stratification. Here g is the gravitational acceleration, ρ is the potential density, α and β denote the thermal expansion and haline contraction coefficients, repectively. dS_A is referring to absolute salinity difference, dT to conservative temperature difference and dP to the pressure difference. Applying a vertical $dP =$ 15-dbar window to the calculation reduces small vertical-scale noise and errors. Note that therefore the Brunt-Väisälä frequency is derived from $7.5\,dbar$ to $1992.5\,dbar$ only.

As we can neglect the relative PV component in the open ocean, the PV reduces to: $PV = \frac{N^2 f}{g}$ (Talley, 1988). Using the derived squared Brunt-Väisälä frequency, we compute the PV depending on isopycnal surfaces. Here, we specifically focus on the $26.0\,kg\,m^{-3}$-isopycnal. This isopycnal outcrops in the subtropics between 25°-40°N/S (Zhang et al., 2003) and, at the equator, is close to the core depth of the EUC. Note, that the analysis could be easily done with any other isopycnal of interest. The PV barrier is present in the mean from the surface down to the $26.4\,kg\,m^{-3}$-isopycnal. Isopycnals within this density range show similar results.

Mapping procedures

We create maps of pressure and PV of the $26.0\,kg\,m^{-3}$-isopycnal, and MLT based on Argo observation with a 1° × 1° spatial resolution by making use of the least-squares fitting method. Fields to be mapped are the mean field, seasonal climatological mean fields and by utilizing the seasonal climatology, 6-month running mean anomalies. Mapping is performed by using all available data within ellipses around a corresponding grid point to be mapped. For the mean fields, the elliptic radii at the equator are equivalent to 3° in latitude and 8° in longitude. These take into account the near-equatorial predominantly zonal structures. The elliptic radii gradually transform to circles towards 20°N/S following an exponential approach. The area of ellipses (data area per grid point to be mapped) and circles is constant. On all data within such an ellipse, we apply an interquartile range (IQR) filter and exclude profiles outside 1.5 times the IQR above the third quartile or 1.5 times the IQR below the first quartile, in case of a normal distribution, this accounts to a standard deviation of 99.3 % of the data. For the least-squares fitting model, we account for each profile's distance to the corresponding grid point by applying a distance weighting using a normal (Gaussian) weighting with a spatial decorrelation scale (half folding width) of $350\,km$.

The least-squares model regression to estimate the mean field includes linear fits in longitude and latitude and a quadratic fit in latitude for each grid point. This preserves zonal and meridional structures within the data on scales significant smaller than the decorrelation scale. The large decorrelation scale on the other hand, ensures that small-scale and temporal variability is limited, but long-term stable features are preserved.

For the seasonal climatology and the 6-month running mean fields, the same procedure with larger mapping scales is chosen to obtain a well-defined mean field and to include more profiles: The area of the ellipses is starting with 6° in latitude and 14° in longitude at the equator and as before leveling out at 20°N/S to a circle. Furthermore, the decorrelation scale of the weighting function is increased to 450 km, to take the reduced data availability into account and focus on temporal/spatial anomalies of statistically significant scale.

For the seasonal mapping, a climatological year is created following the least-squares model regression using a 15-day spaced grid with data within a ±45-day window within the ellipse of the corresponding grid point. Again, applying linear fits in latitude and longitude and quadratic fit in latitude. The 90-day data window every 15 days is based on the data available for each 15-day grid timing ±45 days, i.e., overlapping time periods create the seasonal climatological means. This procedure results in a seasonal climatology with 25 temporal data points within the calendrical year (i.e., 0:15:365 days of a year) is created.

For the time period August 2006 to September 2022, a time varying field of anomalies is created. Mid-monthly anomalies are computed on a monthly $1° \times 1°$ spatial grid using data ±3 months. First, the seasonal cycle is removed from the data by interpolating the climatological seasonal cycle onto the data positions and times and residuals are derived. Then, the same spatial mapping scales as for the seasonal climatology are used to map the temporal evolution. Thus, the derived gridded temporal varying fields show the monthly anomalies to the mean ocean state from August 2006 to September 2022 without the mean seasonal cycle. Since each grid point includes data within a ±3-month window, the resulting monthly timeseries can be regarded as 6-month running mean smoothed.

Additionally, we perform empirical orthogonal function (EOF) analyses of the derived pressure of the 26.0 $kg\,m^{-3}$-isopycnal. For the EOF analysis, the gridded monthly timeseries is normalized by each grid points' standard deviation and detrended at each grid point separately. The latitude is cosine-weighted and the EOF analysis is done for regions only where the complete timeseries is available, i.e., moving outcrop regions are ignored.

The 1st principle component (PC) is compared to the NAO index from 2006-2022 (NOAA NCEI, 2023). The NAO index is defined by the sea level pressure difference between the subpolar low and subtropical high in the North Atlantic. During its positive phase the Low- and High-pressure systems are intensified, i.e., the pressure difference is enlarged. The index is based on the NAO loading pattern which is projected to the daily anomaly 500-millibar height field between 0°-90°N. The NAO loading pattern has been defined as the first rotated EOF mode using monthly mean 500-millibar height anomaly data from 1950-2000 between 0°-90°N (NOAA NCEI, 2023).

We perform a lag correlation between the 1st PC of the pressure of the $26.0\,kg\,m^{-3}$-isopycnal and the 2-year-running mean NAO timeseries. The significance of the correlation is tested with the Student t-test, taking the number of degrees of freedom into account which is determined from the autocorrelation of each timeseries.

Composite analysis

Based on the 2-year-running mean of the NAO index (NOAA NCEI, 2023), NAO composite analysis with the Argo observational dataset is performed and median fields of the corresponding 6-month running mean gridded anomalies of MLT, pressure and PV of the $26.0\,kg\,m^{-3}$-isopycnal for the positive phase and negative phase of NAO (± 0.2 NAO index, respectively) are produced. We define the difference between these two phases by subtracting the median field for the negative phase from that for the positive phase.

Annual maximum winter mixed layer depth and density

In order to calculate subduction rates, the annual maximum winter mixed layer depth (MLD), $\mathcal{H}$, and the corresponding mixed layer potential density (MLPD) are required. For each profile MLPD is estimated from MLT and mixed layer salinity derived from the Holte and Talley algorithm 2009. To derive annual maximum winter MLD and MLPD, first the seasonal climatology of the MLD and MLPD is computed with the same mapping method as described above. Second, the timing of each grid point's maximum MLD within the seasonal climatology is determined and third, by using the derived timing of the climatological maximum depth as mid-point, a 90-day mean for each year is calculated. Hence, timeseries of annual maximum winter MLD and corresponding MLPD are generated for each grid point. The mapping algorithm is the same as described above with mapping radii starting at the equator with 6° in latitude and 14° in longitude and a decorrelation scale of $450\,km$.

5.2.2 CMEMS wind stress data

The Global Ocean Monthly Mean Sea Surface Wind and Stress from scatterometer and model product from Copernicus Marine Environmental Monitoring Service (CMEMS) is used in this study. This product contains Level 4 monthly meridional and zonal wind stress on a $0.25° \times 0.25°$ horizontal resolution and is available from May 2007. The wind stress is derived from ECMWF ERA5 reanalysis and corrected by Level 3 scatterometer data from METOP-A, METOP-B and METOP-C ASCAT satellites. With the zonal and meridional wind stress components (τ^x and τ^y) the wind stress curl and Ekman pumping velocity are calculated following Cushman-Roisin and Beckers (2009c):

$$w_{Ek} = \frac{1}{\rho_0}\left(\nabla \times \frac{\vec{\tau}}{f}\right) = \frac{1}{\rho_0}\left[\frac{1}{f}\left(\frac{\partial \tau^y}{\partial x} - \frac{\partial \tau^x}{\partial y}\right) + \frac{\tau^x \beta}{f^2}\right] \tag{5.1}$$

with the Coriolis parameter $f = f_0 + \beta y$ (β-plane approximation), $f_0 = 2\Omega \sin \Phi_0$, and $\beta = \frac{2\Omega \cos \Phi_0}{r}$. Φ_0 is the corresponding latitude, Ω is the angular rotation rate of the Earth, ρ_0 is the reference density and r is the Earth radius.

By taking the mean of all available points within ±2° of each grid point, the data are transformed on a 1° × 1° horizontal resolution. This is done, in order to reduce noise of the data and to ensure to have consistent grid sizes among products.

For the time period from August 2007 to May 2022, 6-month running means of wind stress (τ^x, τ^y) and wind stress curl anomalies relative to the monthly climatological mean (created from monthly means per grid point from all years) are estimated. With the 6-month running mean anomalies, we also compute NAO composites for positive and negative NAO phases ($\pm 0.2\,$NAO index) and subtract the negative-phase fields from the positive-phase fields.

Sverdrup Streamfunction

The meridional Sverdrup transport is estimated based on the wind stress curl field, following Cushman-Roisin and Beckers (2009a):

$$V_{Sv} = \frac{1}{\rho_0 \beta}\left[\frac{\partial \tau^y}{\partial x} - \frac{\partial \tau^x}{\partial y}\right] \tag{5.2}$$

Integrating this equation zonally from the eastern to the western boundary yields the streamfunction of the Sverdrup transport. The anomalous streamfunction is determined from the 6-month running mean wind stress curl anomalies. Finally, NAO composites are calculated by subtracting the anomalous streamfunction for the negative NAO phase from that of the positive NAO phase.

5.2.3 Geostrophic velocities from Argo climatology data

Taking advantage of the hydrographic Roemmich-Gilson Argo climatology (Roemmich et al., 2009), monthly geostrophic velocities relative to an assumed level of no motion at 1000 *dbar* are estimated following the procedure of Tuchen et al. (2019, 2020). The meridional and zonal geostrophic velocities are inferred from the zonal and meridional dynamic height gradients, respectively, that are derived from temperature and salinity profiles. Here, an updated timeseries from the one used by Tuchen et al. (2020), now covering the time period from January 2006 to December 2022, is analyzed.

To examine NAO-induced changes of the STCs' equatorward thermocline pathways, NAO composites of meridional and zonal geostrophic velocities are derived for positive and negative NAO phases.

5.2.4 Near-surface velocity data

Additionally, near-surface geostrophic velocity data, estimated at $15\,m$ depth from a synthesis product of surface drifting buoy velocities and satellite-derived velocities from sea level anomalies and wind stress, are utilized to determine annual subduction rates (Lumpkin and Garzoli, 2011; Tuchen et al., 2022c). The latest version of this product is available annually from 1993-2021 and has a spatial resolution of $0.25^\circ \times 0.25^\circ$ (Perez et al., 2019). For consistency with the other products, we use the data of the time period of 2007-2021. In order to reduce noise, we transform the data on a $1^\circ \times 1^\circ$ grid by taking the mean of all available points within $\pm 2^\circ$ of each grid point. This is also required to have uniform grid sizes for all products.

5.2.5 Subduction

With the near-surface velocity product and the Ekman pumping velocity (Eq. 5.1) determined from the wind stress as well as from annual maximum MLD ($\mathcal{H}$) and MLPD (see Section 5.2.1), annual lateral induction ($\overline{\vec{u_g}} \cdot \nabla\mathcal{H}$), vertical pumping ($\overline{w_{\mathcal{H}}}$) and hence, the resulting annual subduction rates are computed following Marshall et al. (1993):

$$S_{ann} = -\overline{w_{\mathcal{H}}} - \overline{\vec{u_g}} \cdot \nabla\mathcal{H} = -\overline{w_{Ek}} + \frac{\beta}{f}\int_{-\mathcal{H}}^{0} \overline{v_g} dz - \overline{\vec{u_g}} \cdot \nabla\mathcal{H} \tag{5.3}$$

where $\vec{u_g} = (u_g, v_g)$ are the geostrophic velocities from the near-surface velocity product. The overbars define the annual mean of the corresponding variable.

We estimate the annual subduction rate and and its components, i.e., vertical pumping and lateral induction, for each year from 2007-2021. Within a density range of $\pm 0.1\,kg\,m^{-3}$ from 23:0.2:27.4 $kg\,m^{-3}$ we evaluate the median subduction rate as well as its two components per density bin per year for the North and South Atlantic, respectively. 24.5-26.4 $kg\,m^{-3}$ is the density range of water found in the EUC. The integration of the annual subduction rates over the area of their winter outcrops is defined as the total annual subduction rate of the EUC density range. This is done for the North and South Atlantic outcopping regions separately. Note that for this analysis negative values of vertical pumping and lateral induction are set to zero as these do not contribute to subduction.

5.2.6 EUC transport

Long-term velocity observations from moored acoustic Doppler current profilers (ADCPs) at $0°, 23°W$ are used to estimate the EUC transport following the procedure by Brandt et al. (2021). The mooring was first deployed in 2001 and it is since 2005 that we can determine the EUC transport (Brandt et al., 2014, 2021). For this study, we extended the timeseries by a new mooring observation period until July 2021. The total 20 years of full-depth current velocity observations at $0°, 23°W$ were recently reported by Tuchen et al. (2022a) and will be updated regularly when new mooring data become available. Prior to transport calculations, velocities are de-tided (40-hour-lowpass filter) and subsampled to a 12-hour resolution. Within the moored operation period, two additional off-equatorial moorings were installed for five years (2006-2011, 0°45'N and 0°45'S) to obtain a well-defined EUC transport timeseries. These three moorings were used to validate the reconstruction of the EUC transport with only the central mooring. The EUC transport is then determined by the integrated eastward velocity, u, with $u > 0$ of the reconstructed sections over latitude (1°12'N-1°12'S) and depth (30-300 m) (Brandt et al., 2021). Monthly mean timeseries are evaluated as well as a timeseries in which annual and semi-annual harmonics were subtracted and a 270-day lowpass filter was performed. For more details, see Brandt et al. (2021).

5.3 Results

5.3.1 North Atlantic Oscillation and comparison to heave of 26.0 $kg\,m^{-3}$-isopycnal

We aim to investigate the decadal variability of the upper subtropical-tropical Atlantic Ocean. Therefore, we perform an EOF analysis of the pressure of the 26.0 $kg\,m^{-3}$-isopycnal within 30°N-30°S, 60°W-20°E. The first EOF explains 14 % of the variance of the pressure of the density surface and particularly captures some of its decadal variability associated with spatially large-scale structures. The corresponding first PC compares well to the detrended 2-year-running mean timeseries of the NAO (Figure 5.2). Both timeseries show an about 10-year oscillation. The lag correlation between these two variables (Figure 5.2b) shows highest correlation ($r = 0.71$, significant at 95 % confidence interval) when the NAO index is leading by 5 months. The NAO is not the only force driving the isopycnal variability. However, the variabilities seem to be linked to each other.

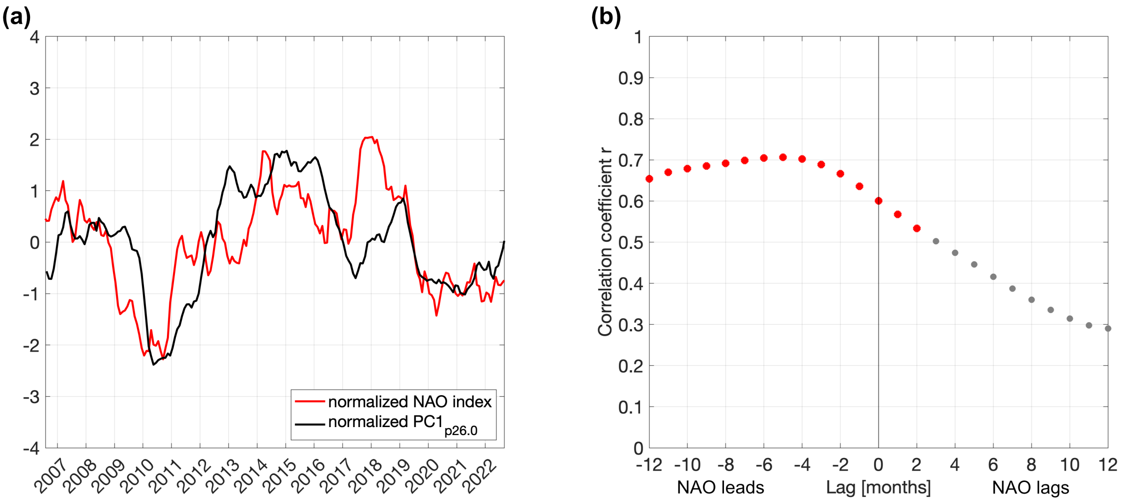

Figure 5.2: **(a)** First principal component (PC) as derived from an empirical orthogonal function (EOF) analysis of pressure anomalies of the 26.0 $kg\,m^{-3}$-isopycnal for the region 30°N-30°S, 60°W-20°E (black line). Before the EOF analysis, the pressure anomalies were derived relative to the climatology, smoothed by applying a 6-month running mean, normalized by each grid point's standard deviation and de-trended. The red line shows the 2-year-running mean detrended North Atlantic Oscillation (NAO) index, normalized by its standard deviation. **(b)** Lag correlation between 2-year-running mean NAO index and first PC of the pressure anomalies of the 26.0 $kg\,m^{-3}$-isopycnal. Negative lag indicate that the NAO index is leading. Red dots show where the correlation is significant, i.e. larger than 95 % significance level.

5.3.2 NAO composites

It is well-known that the NAO impacts the general atmospheric circulation over the North Atlantic (e.g., Visbeck et al., 2001; Hurrell et al., 2003; Pinto and Raible, 2012). Here, we examine the difference in wind stress and wind stress curl over the entire Atlantic between the positive and negative phases of the NAO in the form of a composite analysis. The composites are determined for when the NAO index exceeds ±0.2 for the positive and negative phases, respectively, occurring during the Argo period of 2006-2022 (Figure 5.3a). The negative NAO phase composite frames the years 2009-2011 (Figure 5.3a), covering a strong negative NAO event in winter 2010/2011 (Maidens et al., 2013). The positive NAO composites consists of the years 2014-2016, 2017-2019 (Figure 5.3a). Additionally, the same analysis is done for MLT anomalies to receive a first impression of the impact of the NAO on the upper-ocean.

In agreement with previous studies on the NAO-related wind anomalies (e.g., Marshall et al., 2001; Wanner et al., 2001; Pinto and Raible, 2012), the difference between positive and negative NAO phases indicates enhanced wind stress in the region of the Northern Hemisphere's westerlies but also in the area of the northeast trade winds (Figure 5.3b). Between 30°N-40°N, the wind stress is reduced. This pattern suggests an intensification of the North Atlantic subtropical high during positive NAO phases compared to negative NAO phases. Accordingly, we identify increased negative wind stress curl in the North

Atlantic subtropical subduction zone as well as strengthened positive wind stress curl in the tropical North Atlantic during the positive NAO phase compared to the negative NAO phases (Figure 5.3c). Only weak wind stress changes occur in the subtropical South Atlantic in response to the phase of the NAO. The southeast trades are slightly enhanced. The westerlies southward of 40°S intensify, producing large wind stress curl anomalies in this area.

The difference of MLT composites reveals a tripole pattern in the North Atlantic with a colder mixed layer in the subpolar region, a warmer mixed layer in the western subtropical gyre and again a colder mixed layer in the tropical gyre during the positive NAO phase compared to the negative NAO phase (Figure 5.3d). The MLT anomalies demonstrate a tripole pattern in the North Atlantic which is a well-known SST anomaly feature during positive NAO phases (e.g., Pinto and Raible, 2012). The negative MLT anomalies in the tropical gyre extend southward to 25°S (Figure 5.3d). Only along the eastern boundary south of the equator, a narrow band of mixed layer warming can be observed. Similarly to the North Atlantic, the South Atlantic subtropical gyre shows a warmer mixed layer during positive NAO phases compared to negative NAO phases during the Argo period

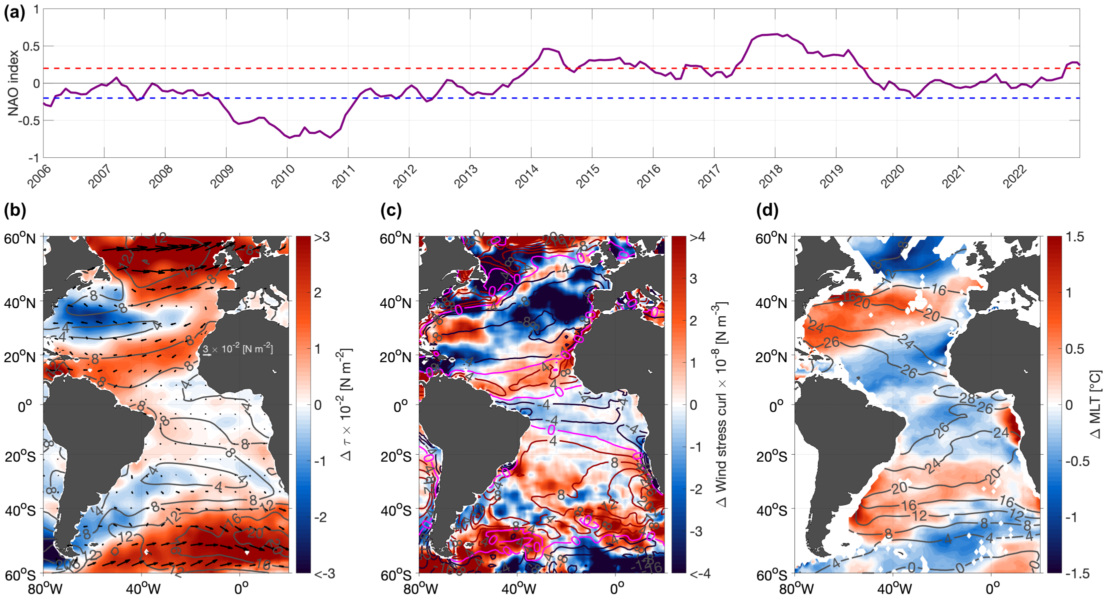

Figure 5.3: NAO composite analysis of wind and MLT. **(a)** 2-year-running mean North Atlantic Oscillation (NAO) index. Stippled red/blue lines mark ±0.2 NAO index threshold used to define positive and negative NAO phases for the composite analysis. **(b)** Difference between composites of wind stress anomalies of the positive and the negative NAO phases. Color shading denotes the difference in magnitude and arrows show the wind stress vector anomalies. Contour lines indicate the corresponding mean wind stress magnitude [$\times 10^{-2}\, N\, m^{-2}$]. **(c)** Same as in **(b)** but for wind stress curl. Contour lines indicate the corresponding mean field (blue denote where the mean curl is negative and red where the mean is positive). Pink contour lines mark the zero-wind stress curl. **(d)** Difference between composites of mixed layer temperature (MLT) anomalies from Argo observations of positive and negative NAO phases. Gray contour lines denote the corresponding mean field.

2006-2022. It should be noted however, that the variability in the South Atlantic is most likely not linked to the NAO, solely showing this pattern for the Argo observation period. In the South Atlantic, there exists a so-called South Atlantic Ocean Dipole (SAOD) which is identified by opposing SST anomalies in the southwest (25°S-40°S, 10°W-40°W) and in the northeast (0°-15°S, 20°W-10°E) South Atlantic (Nnamchi et al., 2011). A comparison of the timeseries of the SAOD (Nana et al. (2023), their Figure 4) to our NAO timeseries shows that the negative and positive phases of the NAO have opposing signs for the SAOD. The timeseries of Nana et al. (2023) indicates a positive SAOD from 2006-2011 and a negative SAOD from 2011-2016. Hence, there is a phase change from positive to negative SAOD during our observation period. A negative SAOD implies negative/positive SST anomalies in the northeast/southwest South Atlantic (Nnamchi et al., 2011). Thus, our observed MLT anomalies could result from this phase shift of the SAOD occurring at the same time as our phase changes of the NAO.

In order to identify how the NAO influences the upper isopycnals in the tropical Atlantic Ocean, we compute composites for the positive and negative NAO phases of pressure (i.e., isopycnal heave) and PV of the 26.0 $kg\,m^{-3}$-isopycnal. Since we identified the largest correlation at a 5-month lead of the NAO of the pressure anomalies of the 26.0 $kg\,m^{-3}$-isopycnal, we perform the analysis for a 5-month NAO lead. We then subtract the negative NAO phase composite from the one of the positive NAO.

From the negative to the positive NAO phase the 26.0 $kg\,m^{-3}$-isopycnal is mainly shoaling within the tropical Atlantic and sinking poleward of 20°N/S (Figure 5.4a). This rather symmetric isopycnal behavior indicates some wind stress related features (cf. Figure 5.3). The observed pattern is found to be very similar to the first EOF mode of pressure of the 26.0 $kg\,m^{-3}$-isopycnal (not shown).

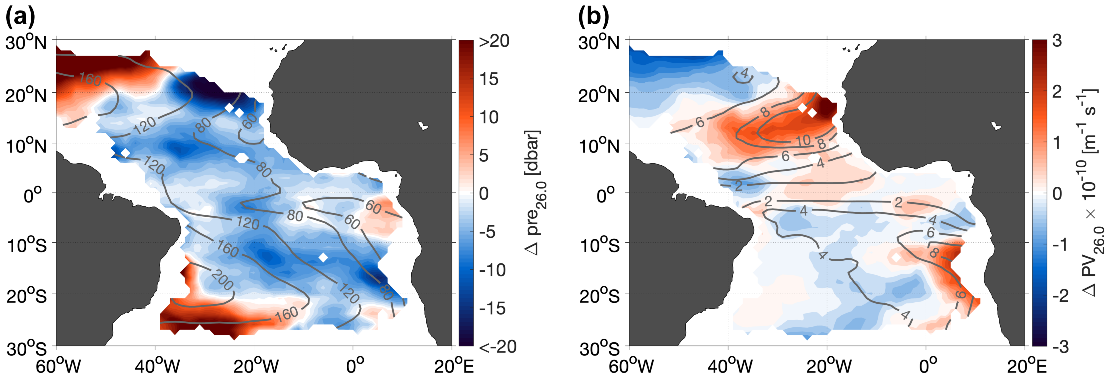

Figure 5.4: NAO composite analyses of pressure and PV anomalies. **(a)** Difference between composites of pressure anomalies of the 26.0 $kg\,m^{-3}$-isopycnal and of **(b)** the potential vorticity (PV) on the 26.0 $kg\,m^{-3}$-isopycnal of the positive and the negative NAO phases. Composites are calculated using a 5-month lead of the NAO. Contour lines show the corresponding mean fields.

The difference in PV anomalies on the 26.0 $kg\,m^{-3}$-isopycnal between the positive and negative NAO phases shows a distinct pattern in the North Atlantic: The PV within the tropical North Atlantic PV maximum area (i.e., PV barrier) is up to 20 % stronger in magnitude during the positive NAO phase compared to the negative NAO phase relative to the mean field (Figure 5.4b). Outside of the PV barrier, PV is mainly reduced during the positive NAO phase. Also, the South Atlantic PV barrier, which is in the mean less distinct than the one in the North Atlantic, intensifies during the positive NAO phase compared to the negative NAO phase.

In summary, changing wind patterns and associated wind stress curl changes lead to upwelling and downwelling anomalies in the respective regions during positive NAO phases relative to negative NAO phases. This produces stretching and squeezing of isopycnal layers and accordingly, changes of the vertical density gradient and PV.

5.3.3 Impact of North Atlantic PV barrier on the interior and western boundary pathways of the STC

The zonal extent of the PV barrier determines how much of the water, subducted in the eastern subtropics, is taking the interior pathway from the subtropics to the equator and how much water reaches the equator via the western boundary pathway (e.g., Zhang et al., 2003; Rabe et al., 2008). Hence, the PV barrier modifies the window width between the interior and western boundary pathways. Since we observe a stronger PV barrier during positive NAO phases compared to negative NAO phases (Figure 5.4b), we suggest that for periods of positive NAO phases subducted water from the subtropics is deflected more to the western boundary before reaching the equator.

In order to test this hypothesis, we show differences between positive and negative NAO phases of the Sverdrup streamfunction as well as of meridional and zonal geostrophic velocity on the 26.0 $kg\,m^{-3}$-isopycnal (Figure 5.5). The difference between NAO composites of the Sverdrup streamfunction, derived from the wind stress curl field (Figure 5.3c), illustrates an intensified tropical gyre (5°N-20°N, Figure 5.5a). This implies that the northward Sverdrup transport in the interior is enhanced and has to be compensated by a southward flow anomaly along the western boundary.

The meridional geostrophic velocity component derived from Argo data reveals negative velocity anomalies close to the western boundary in the latitude range of the tropical gyre (about 5°N-20°N) during positive NAO phases compared to negative NAO phases (Figure 5.5b). This implies that the southward velocity component is intensified. East of the western boundary circulation, positive anomalies can be observed, indicating weaker southward geostrophic velocities in the ocean interior during positive NAO phases compared to negative NAO phases. In a small area, close to the western boundary and equatorward of 5°N, positive anomalies occur during positive NAO phases compared to

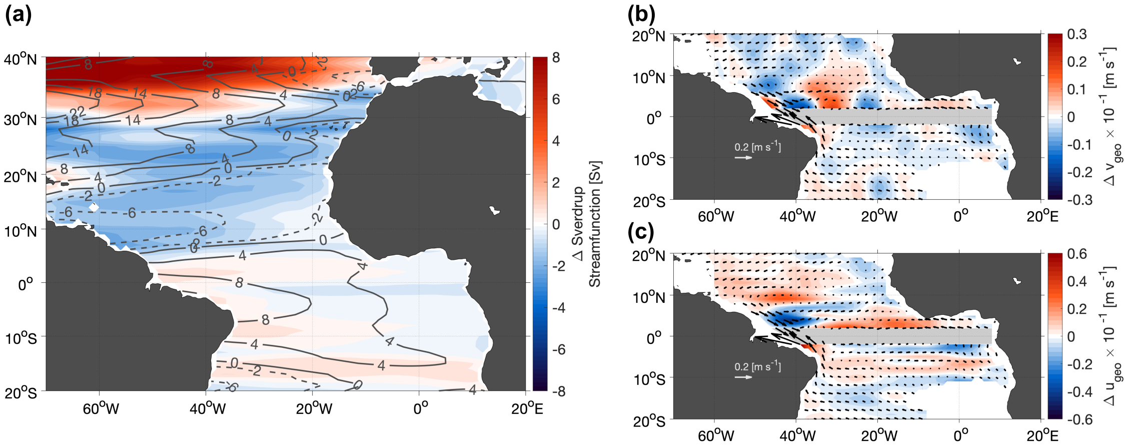

Figure 5.5: NAO composite analyses of Sverdrup streamfunction and geostrophic velocity. **(a)** Difference between composites of Sverdrup streamfunction anomalies of positive and negative NAO phases. Contour lines show the corresponding mean field. Solid contours denote where the mean field is positive and stippled contours where it is negative. **(b)** Difference between composites of meridional geostrophic velocities on the 26.0 $kg\,m^{-3}$-isopycnal of positive and negative NAO phases. **(c)** Same as in **(b)** but for zonal geostrophic velocity. Arrows in **(b)** and **(c)** show the mean absolute geostrophic velocity on the 26.0 $kg\,m^{-3}$-isopycnal. Composites are calculated at 0 lag between NAO, Sverdrup streamfunction and geostrophic velocity.

negative NAO phases. This could account for an intensified NBC coming from the South Atlantic. For completeness the zonal velocity component is shown as well (Figure 5.5c). Just north of the equator on the western side, negative (westward) velocities are enhanced, whereas east of 35°W, positive anomalies are observed (Figure 5.5c). Together with the meridional velocity anomalies, this indicates an anticyclonic circulation west of 35°W and an eastward velocity anomaly parallel to the equator east of 35°W.

5.3.4 Subduction of EUC water masses and comparison to EUC transport

Variations of the trade winds influence both, Ekman pumping and STCs (Rabe et al., 2008), and are therefore related to changes of subduction rates. In assimilation and coupled models a relation between STCs and EUC has been established, in which a stronger (weaker) Ekman divergence and thermocline convergence are associated with a stronger (weaker) EUC (Rabe et al., 2008; Fu et al., 2022). Here, we investigate changes of subduction rates for the density range of the EUC. Water masses advected by the EUC cover the density range of $24.5 - 26.4\,kg\,m^{-3}$. The subduction rate variations in the North and South Atlantic for this density range will be compared to the EUC transport timeseries inferred from moored velocity observations at 0°, 23°W.

The spatial distribution of the mean fields of annual vertical pumping, lateral induction and subduction rates (Figure 5.6) shows that the winter outcrop area of the EUC density range in the North Atlantic is largely characterized by positive vertical pumping

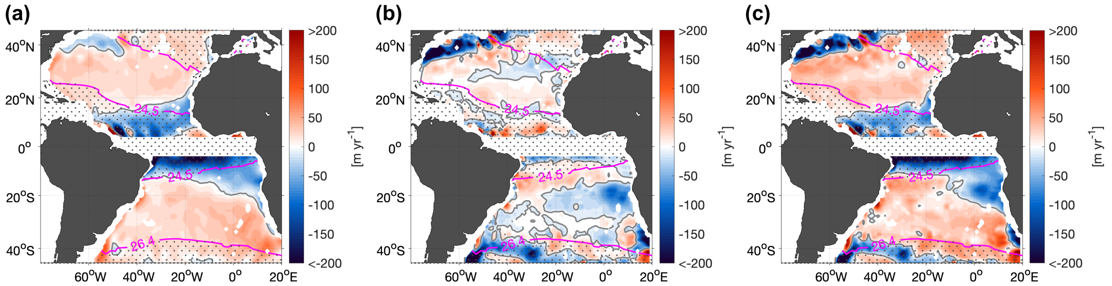

Figure 5.6: Mean of annual **(a)** vertical pumping, **(b)** lateral induction and **(c)** subduction rates averaged over the period of 2007-2021. The gray contour lines mark the zero-lines. The pink contour lines denote the mean location of the outcrops of $24.5\,kg\,m^{-3}$- and $26.4\,kg\,m^{-3}$-isopycnals during annual mean maximum (i.e., winter) mixed layer depth. This is the density range of water masses feeding into the Equatorial Undercurrent. Areas outside of this density range are stippled.

$(20 - 40\,m\,yr^{-1})$ which is the main contributor to the resulting pattern of mean annual subduction rates $(40 - 80\,m\,yr^{-1})$. For both terms only the southeastern and northwestern corners of the North Atlantic outcrop region are negative and therefore, no mean subduction takes place there. The lateral induction term reveals a different behavior: in between the southern boundary of the outcrop area and about 28°N the lateral induction is positive $(15 - 60\,m\,yr^{-1})$. In the center of the North Atlantic subtropical gyre, lateral induction is negative (up to $15\,m\,yr^{-1}$). Northwestward of the center of the outcrop area (north of about 30°N), lateral induction contributes to annual subduction rates of up to $80\,m\,yr^{-1}$. In the northwestern corner of the outcrop area, lateral induction is negative. These mean annual rates mirror the ones determined by earlier studies (Marshall et al., 1993; Qu et al., 2016).

The mean winter outcrop area of the EUC density range in the South Atlantic is mainly determined by vertical pumping. Especially in the southeast, vertical pumping rates exceed $80\,m\,yr^{-1}$. Lateral induction occurs only in small parts of the South Atlantic: mainly in a small band along the equatorward boundary of the outcrop region (around $40\,m\,yr^{-1}$). Overall, regions with negative lateral induction dominate the outcrop region in the Southern Hemisphere (Figure 5.6).

The year-to-year variability of annual subduction rates in the winter outcrop areas of the EUC density range $(24.5 - 26.4\,kg\,m^{-3})$ and its vertical pumping and lateral induction components are now investigated in more detail for the North and South Atlantic, individually. Note that for this analysis, negative rates are set to zero as they do not contribute to the annual subduction rate.

The total annual subduction rate of the EUC density range in the North Atlantic increased by about $8\,Sv$ from 2008-2018 (Figure 5.7a). After 2018, the total annual subduction rate slightly decreased again (Figure 5.7a) as well as vertical pumping. Although the magnitude of subduction is governed by the vertical pumping term, most of the sub-

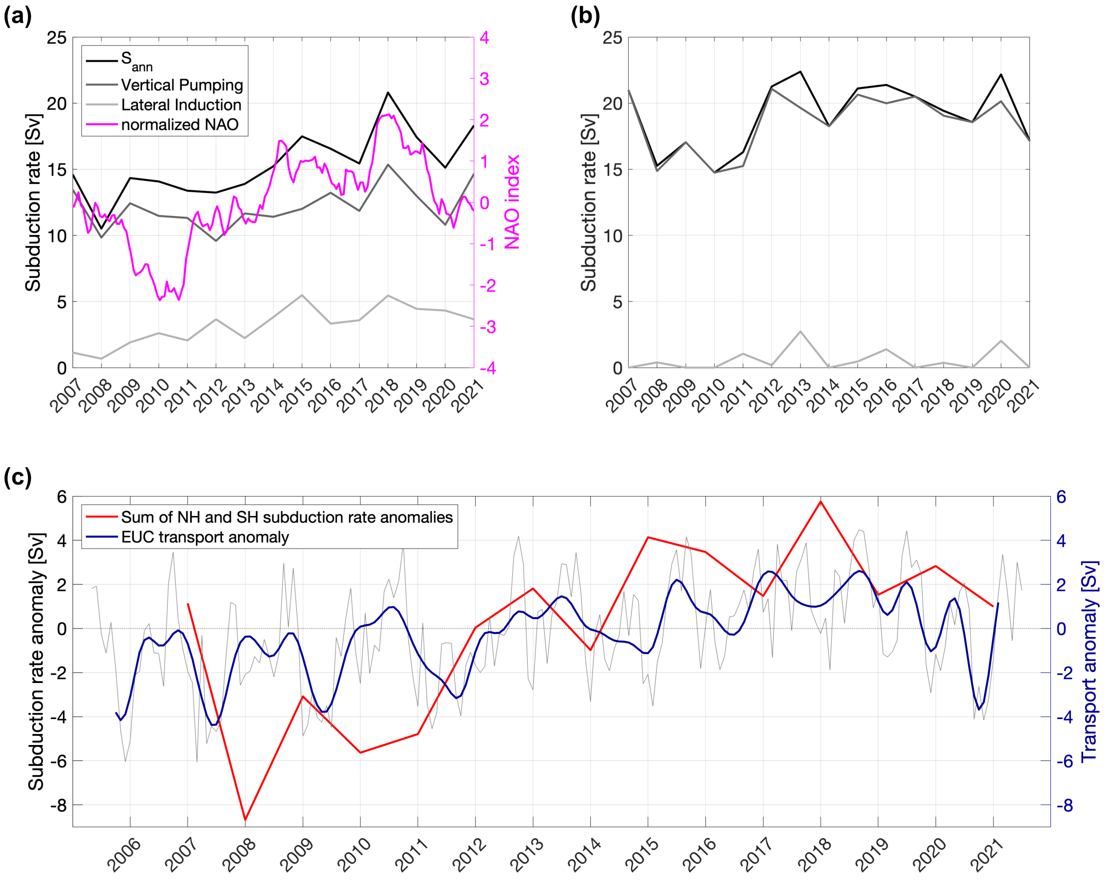

Figure 5.7: Total annual subduction rate (black), vertical pumping rate (dark gray) and lateral induction rate (light gray) for the density range of $24.5 - 26.4\,kg\,m^{-3}$ for the **(a)** North Atlantic and **(b)** South Atlantic. Additionally, in **(a)** is shown the normalized 2-year-running mean NAO index (pink). **(c)** Sum of total annual subduction rate anomalies from the North and South Atlantic shown in **(a)** and **(b)** (red) and EUC transport anomaly (thin grey line shows monthly data; thick blue line shows the data with annual and semi-annual harmonics subtracted and a 270-day low-pass filter applied). The EUC transport timeseries is the same as in Brandt et al. (2021), but extended by another mooring period.

duction rate change is due to lateral induction. Lateral induction amplified by about $5\,Sv$ from 2008-2018. Except for the first part of the derived timeseries, lateral induction increases during phases of increasing NAO index. Note that lateral induction is mainly determined by the winter MLD. Due to sparseness of Argo profiles before 2010, winter MLD might be biased. The outcrop area is evaluated to remain of similar size during the entire time period (Supporting Information, Supplementary Figure 5.8). Yet, standard errors of annual winter MLD are significantly reduced after 2012 (Supporting Information, Supplementary Figure 5.9).

In the South Atlantic, the total annual subduction was at a minimum between 2008-2011 (around $15\,Sv$, Figure 5.7b). From 2012 onwards the total annual subduction rate was between $18 - 22\,Sv$ and there is a tendency of a slight decrease towards the end of the timeseries. Variability as well as magnitude of subduction are mainly characterized by vertical pumping in the South Atlantic. As already determined from the spatial distribution of the lateral induction, for the outcrop area of the EUC density range, lateral induction was close to zero in the South Atlantic. Annual lateral induction rates remained below $3\,Sv$ throughout the timeseries (Figure 5.7b).

Summing up the total annual subduction contributions from the North and South Atlantic in the EUC density range, we observe an increase of about $8\,Sv$ from 2008-2018 (Figure 5.7c). From 2018-2021 the subduction rate reduces by $4-5\,Sv$. This can be compared to the EUC transport anomalies from moored observations at 0°, 23°W. Using an earlier record, Brandt et al. (2021) showed that the EUC transport increased by $3.3\,Sv$ between 2008-2018. The updated timeseries reveals that 2018 marks the maximum transport anomaly (Figure 5.7c). Since 2018, the EUC transport has been decreasing until the end of the timeseries.

5.4 Summary & Discussion

The main topic of this study was to improve the understanding of decadal changes of the upper-ocean density and circulation in the tropical-subtropical Atlantic during the Argo period from 2006-2022. We established a relation between the variability of upper isopycnals in the tropical Atlantic Ocean and the NAO. According to the NAO phases during the period of 2006-2022, the atmospheric patterns changed such that the North Atlantic subtropical high is intensified and shifted poleward during the positive NAO phase compared to the negative NAO phase in agreement with previous studies (e.g., Wanner et al., 2001; Pinto and Raible, 2012). This in turn impacts ocean dynamics: the intensified subtropical high of the North Atlantic was associated with enhanced northeast trade winds and led to intensified Ekman pumping in the subtropical subduction zones and increased Ekman suction equatorward of the trade wind maximum during the positive NAO phase compared to the negative NAO phase (Williams et al., 2015). As a result, deepening isopycnals poleward of 20°N and rising isopycnals to the south of this can be observed. During positive NAO phases, enhanced northeast trade winds drive isopycnal heave in the northeastern tropical Atlantic that strengthen stratification and the North Atlantic PV barrier.

It has been demonstrated by several studies that the anomalous wind-driven Ekman transport in the North Atlantic is linked to NAO-related atmospheric forcings (Leadbetter et al., 2007; Lozier et al., 2008; DiNezio et al., 2009). Williams et al. (2015) could further show that the thermocline depth (defined by the $27.5\,kg\,m^{-3}$-isopycnal) varies in accordance with the NAO phases: for a positive NAO phase the isopycnal depth is deeper in the subtropics and shallower in the subpolar gyre compared to the mean state (1950-2013). The opposite accounts for the negative NAO phase. These changes can be attributed to stronger/weaker northward Ekman transport from the tropics for positive/negative NAO phases, respectively (Williams et al., 2015). Williams et al. (2015) chose a deeper isopycnal than the 26.0 $kg\,m^{-3}$-isopycnal, utilized in this study which outcrops within the subtropical gyre. However, their investigation shows a slight upward movement of the isopycnal within the tropical basin for the positive NAO phase (cf. their Figure 4b (Williams et al., 2015)), mirroring our findings. Thus, large-scale vertical movement of isopycnals can be associated with subtropical Ekman pumping where we observe a downward displacement of the 26.0 $kg\,m^{-3}$-isopycnal and to equatorial Ekman divergence which contributes to shoaling of the 26.0 $kg\,m^{-3}$-isopycnal. In the northeastern tropical Atlantic, intensified wind stress curl-driven Ekman suction is leading to upward heave of isopycnals during positive NAO phases compared to negative phases. This does not happen constantly for a larger isopycnal range since the vertical velocity has a maximum in the subsurface. Ekman suction generates a squeezing of isopycnal layers above the depth of maximum vertical velocity and is thereby strengthening the PV barrier.

Nevertheless, Ekman pumping and Ekman suction do not solely follow the NAO patterns. Also, since not all NAO events are the same (Hilmer and Jung, 2000; Zhao and Johns, 2014). Hilmer and Jung (2000) found that the center of action of NAO interannual variability changes among periods. For instance, during 1978-1997 the center was displaced more to the east compared to prior decades and has been shown to impact the number of deep cyclones, air temperatures and air-sea interactions in the North Atlantic (Hilmer and Jung, 2000; Jung et al., 2003). Such a shift of the NAO center and therefore the atmospheric circulation could create different Ekman pumping/suction anomalies despite having a consistent positive NAO phase.

Our EOF analysis shows that the first EOF of the pressure anomaly of the 26.0 $kg\,m^{-3}$-isopycnal has an explained variance of 14 %, indicating that additional processes play a role in determining the vertical position of the isopycnal. Nevertheless, the corresponding first PC shows a similar 10-year oscillation as the filtered NAO timeseries. The variability of the vertical movement of the isopycnal cannot be solely related to the NAO forcing yet it plays a role on decadal timescales. Recently, it has been discovered from observations taken during 1900-2009 that the Atlantic climate follows an oscillatory mode with 10-15 years periodicity, which is termed the Pan-Atlantic Decadal Oscillation (Nnamchi et al., 2023). The Pan-Atlantic Decadal Oscillation changes are suggested to be imposed on the North Atlantic and then reach the tropical and South Atlantic via the oceanic and atmospheric teleconnections. Maximum variance of the 10-15 years oscillation is found to be connected to the thermocline feedback in the Atlantic cold tongue region which then supplements on to the NAO (Nnamchi et al., 2023). In the North Atlantic, the SST EOF pattern of Nnamchi et al. (2023) compares well to the tripole pattern of our MLT composite difference. The cooling MLT in the Northern Tropical Atlantic is most likely associated with intensified latent heat loss as a result of the increased northeast trades (cf.

wind-evaporation-SST (WES) feedback, Chang et al. (2006)). South of the equator, the study of Nnamchi et al. (2023) shows a dipole in SST compared to north of the equator. For the Argo period, we do not observe this structure in the difference between the NAO composites. However, Nnamchi et al. (2023) focused on much longer timescales than we are able to recover from Argo observations. The Pan-Atlantic Decadal Oscillation has been shown to act on timescales of 10-15 years, while on timescales of around 5 years the tropical Atlantic is characterized by anomalies of the same sign on both sides of the equator (Tanimoto and Xie, 1999). Additionally, it has been demonstrated that the South Atlantic climate variability oscillates on a 14-16 year period with variations of strength of the subtropical anticyclone followed by variations of a north-south SST dipole (Venegas et al., 1997). Hence, there is the potential, that for certain time periods, these modes of variability are combined into a pattern that corresponds to the NAO in the North Atlantic and the SAOD in the South Atlantic and thereby having MLT anomalies of the same sign north and south of the equator.

Furthermore, for long timeseries of SST (1870-2012) it has been shown that the NAO has a strong linkage to the Northern Tropical Atlantic SST in some decadal periods (Chen et al., 2015). This interdecadal change in the connection is suggested to be related to deviations from the mean SST in the Northern Tropical Atlantic, i.e., during warmer conditions, the SST anomalies in the Northern Tropical Atlantic are able to produce a larger wind response over the North Atlantic. As a result of the WES feedback, this leads to the tripole SST anomaly pattern in the North Atlantic Ocean which contributes to NAO-like atmospheric patterns (Chen et al., 2015). Besides, long-term satellite SST observations (1981-2018) show that the ocean surface is warming also in the tropical North Atlantic (Bulgin et al., 2020). Bulgin et al. (2020) split up the 37-year time periods into four sub-periods. The last period 2010-2018 reveals the typical positive NAO tripole SST pattern in the North Atlantic (cf., their Figure 1f), manifesting the hypothesis that the North Atlantic shifted more to a positive NAO stage in the recent decade.

However, the tropical Atlantic Ocean is not only influenced by the NAO. There exists a robust impact of El Niño on the trade wind zones north and south of the equatorial Atlantic (Lübbecke and McPhaden, 2012). El Niño forces weaker northeast trades but stronger southeast trades in the tropical Atlantic, yet the SST relation is not consistent (Lübbecke and McPhaden, 2012). For some periods ENSO and NAO influences are superimposing, while for other periods their forces are counteracting each other (Czaja et al., 2002). The impact of ENSO on the Northern Tropical Atlantic and the NAO cannot be neglected. Nonetheless, ENSO influence is mainly on interannual timescales while NAO acts on longer timescales (Czaja et al., 2002; Lübbecke and McPhaden, 2012).

We identified a stronger PV barrier during positive NAO phases as a result of intensified wind stress curl-driven upwelling in the northeastern tropical Atlantic and the thereby induced isopycnal heave. It has been suggested that, as part of the STC circulation, with a stronger PV barrier more of the subducted water from the subtropics has to take western boundary pathway toward the equator instead of following the interior pathway (Luo et al., 2009b). Our analysis shows that during positive NAO phases the tropical gyre in the North Atlantic is intensified. The wind stress curl-induced northward Sverdrup interior transport is thus enhanced and has to be balanced by the southward return flow along the western boundary. Hence, this could lead to an enhanced water mass transport from the subtropics toward the western boundary and further equatorward toward the equatorial region along the western boundary pathway. Meridional geostrophic velocities derived from Argo data confirm such flow pattern, showing southward flow anomalies at the western boundary as well as northward flow anomalies in the ocean interior. These results are in agreement with the hypothesis that during positive NAO phases with a stronger PV barrier, the window width between the interior and western boundary pathways of the STC is smaller. Thus, more of the interior thermocline flow is deflected toward the western boundary and thereby causing a redistribution among the STC pathways. Furthermore, the geostrophic velocity field suggests a stronger northward NBC flow until about 5°N as well as an intensified NBC retroflection flowing back to the equator. This matches the findings of a strengthened tropical gyre observed in the Sverdrup streamfunction during positive NAO phases compared to negative NAO phases.

The redistribution of STC pathways assumes at first that the subduction rates in the subtropics remain the same and as a result of the smaller window size, the same amount of water is just differently redistributed among the western boundary and interior pathway. Our results, however, indicate an increase of subduction of these water masses that are potentially flowing from the subtropical North Atlantic toward the equator within the STC. The vertical pumping term experiences a slight increase consistent with intensified wind stress-curl driven downwelling. Also, the lateral induction term is intensifying over time. The positive trend of total annual subduction is mainly established by the lateral induction term whereas the vertical pumping term sets the magnitude. The lateral induction term should be interpreted with caution in the beginning of the timeseries because the first few years reveal relatively large spatially varying winter MLDs and larger standard errors (Supporting Information, Supplementary Figure 5.9). It is only after 2012, that the standard errors are reduced. This could have a great impact on the lateral induction rates for which the zonal and meridional MLD gradients are required. Therefore, the lateral induction rate may slightly be biased from 2007-2010. Also, the number of profiles included in the mapping process increases after that (Supporting Information, Supplementary Figure 5.8). Interestingly, errors in the density outcrop areas should be relatively small, since the area size neither varies much over time nor shows a trend (Supporting Information, Supplementary Figure 5.8).

Moreover, increasing lateral induction after 2012 can be observed during positive NAO phases. Similar results have been shown for the annual subduction rates of the North

Atlantic Subtropical Underwater from 2007-2014 (Qu et al., 2016). Winter MLD sets the lateral induction variability. Qu et al. (2016) determined wind anomalies due to the NAO as the primary source of year-to-year variability of annual subduction rates of the North Atlantic Subtropical Underwater: during positive NAO phases enhanced trade winds produce cold SST anomalies in the northeastern tropical Atlantic, involving deeper mixed layers and enhancing lateral induction rates. This is mirrored by our findings. In the South Atlantic the subduction rate for the EUC density range is mainly driven by the vertical pumping term as lateral induction is barely existent (Figure 5.7b). Wind stress curl-driven Ekman pumping is most likely enhanced after 2012 (Figure 5.3).

Combining the annual subduction rates from the North and South Atlantic, we estimate an increase of the total annual subduction for the EUC density range from 2008-2018 of around $8\,Sv$ followed by a decrease of $4\,Sv$ until 2021. Prior to that, the annual subduction rate anomalies are largely negative which is most likely a result of the subduction rates of the South Atlantic, also showing a minimum during this time. However, lower lateral induction rates in the North Atlantic during this period superimpose on these weak subduction rates. The timings of increasing and decreasing total annual subduction mirror the evolution of the EUC transport timeseries. From 2008-2018 the EUC transport reveals a trend of $3.3\,Sv$ decade^{-1} (Brandt et al., 2021). It has been suggested that the STCs and the EUC are connected via a pulling effect in such way, that intensified trade winds lead in a first instance to a strengthened EUC via increased equatorial upwelling and finally the STCs adapt and amplify. This connection is found to be active on timescales of five years or longer (Rabe et al., 2008). Therefore, the enhanced annual subduction rates are most likely not the driving force of the strengthening EUC. Instead, the changes of the subduction rate are another consequence of intensifying trade winds. Also, it should be taken into account that not all of the subducted water is actually reaching the equator as there are three different pathways to take: recirculation pathway, western boundary pathway and interior pathway. Particles entering the recirculation pathway will not reach the inner tropics and are not part of the STC. Moreover, it is uncertain how much subducted water from the North Atlantic actually reaches the equator. Water that follows the western boundary pathway enters the NBC retroflection and either follows the NECC/NEUC or takes the tour to the equator. Indeed, it has been shown that the EUC and the NEUC have the same origins of water (Hüttl-Kabus and Böning, 2008). Similar flow paths must be the case for the interior pathway which crosses the NECC/NEUC (Figure 5.1) and subducted water following that pathway might not reach the equator.

On longer timescales, the variability of the EUC transport might be related to the NAO as a result of the associated variations of the North Atlantic subtropical high and the northeast trades. However, it remains unclear whether a stronger PV barrier contributes to an intensified EUC in the western and central Atlantic as suggested for the Pacific Ocean by a model simulation (Luo et al., 2009b). This would require EUC timeseries at different locations along the Atlantic equator, inn order to see whether the observed strengthening of the EUC decreases towards the eastern part of the basin.

To summarize, we found that during the Argo observation period the decadal variability of the vertical movement of upper isopycnals in the subtropical-tropical North Atlantic is related to the NAO. Positive NAO phase related wind stress changes produce isopycnal heave and wind stress curl-driven upwelling in the region of the North Atlantic PV barrier which enhance stratification and thereby strengthen the PV barrier for the equatorward thermocline flow within the North Atlantic STC. During positive NAO phases, stronger Additionally, the EUC transport increase is found to be related to stronger northeast trade winds during the positive NAO phase. Simultaneously, the enhanced trade winds cause an increase of annual subduction rates in the North Atlantic for the EUC density range.

5.5 Acknowledgements

This study was supported by the EU H2020 TRIATLAS project under grant agreement 817578. FP Tuchen was supported by a United States National Research Council Research Associateship Award held at NOAA's Atlantic Oceanographic and Meteorological Laboratory.

5.6 Data Availability Statement

The Argo observation dataset is available under Argo (2022). Argo float data and metadata from Global Data Assembly Centre (Argo GDAC) - Snapshot of Argo GDAC of December 10st 2022. SEANOE. https://doi.org/10.17882/42182#98126. The North Atlantic Oscillation Index is available via the National Centers for Environmental Information, National Oceanic and Atmospheric Administration: https://www.ncei.noaa.gov/access/monitoring/nao/. The Global Ocean Monthly Mean Sea Surface Wind and Stress from Scatterometer and Model. E.U. Copernicus Marine Environmental Monitoring Service (CMEMS) is available under https://doi.org/10.48670/moi-00181. The Argo climatology from Roemmich and Gilson can be obtained from https://sio-argo.ucsd.edu/RG_Climatology.html. The near-surface velocity data can be found at: ftp://ftp.aoml.noaa.gov/phod/pub/lumpkin/decomp/. For the moored observation data at 0°, 23°W previous observation periods and applied scripts for the EUC transport analysis can be accessed via https://doi.org/10.5281/zenodo.4478285. We extended the EUC timeseries for another mooring observation period available under https://doi.pangaea.de/10.1594/PANGAEA.960093.

5.7 Supporting Information

In order to estimate annual subduction rates, we made use of winter maximum mixed layer depth (MLD) and its density (MLPD). Winter maximum MLD is determined from the climatological deepest mixed layer for each grid point. A 90-day MLD mean around the time of climatological winter maximum MLD then gives the best measure of the winter maximum MLD. Figure 5.8 shows how many profiles were taken into account during the mapping procedure for each year from 2006-2021. Figure 5.9 and Figure 5.10 show for each winter the standard errors of the estimated MLD and of the MLPD, respectively. The number of profiles included in the mapping procedure are rather low in the first few years (2006-2009). These are also years, for which the standard errors of MLD and MLPD are higher than in the following years. Thus, the subduction and lateral induction rates should be taken with caution for these earlier years. Nevertheless, the size of the outcrop area defined by the isopycnals enclosing the Equatorial Undercurrent (EUC) density range does not vary much over time. Hence the error from the area size should be rather small.

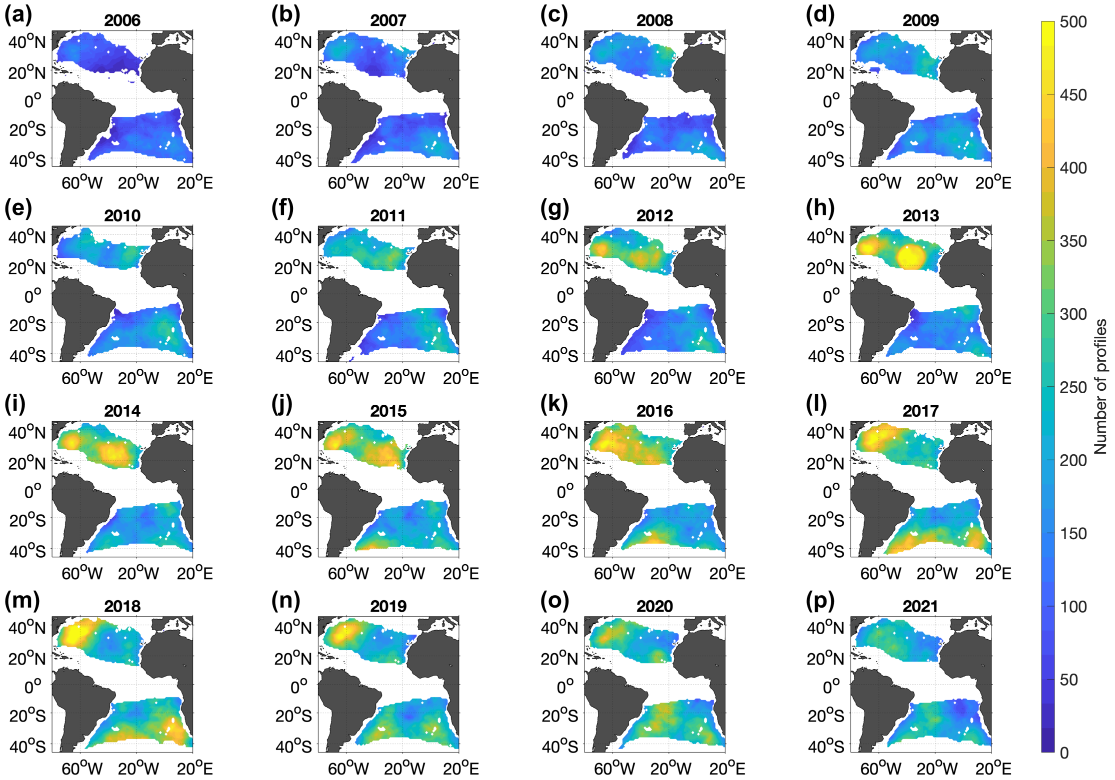

Supplementary Figure 5.8: Number of profiles taken into account during the mapping procedure for each winter MLD in the outcropping area defined by the isopycnals enclosing the Equatorial Undercurrent density range ($24.5 - 26.4\, kg\, m^{-3}$) from 2006-2021 (**(a)-(p)**)

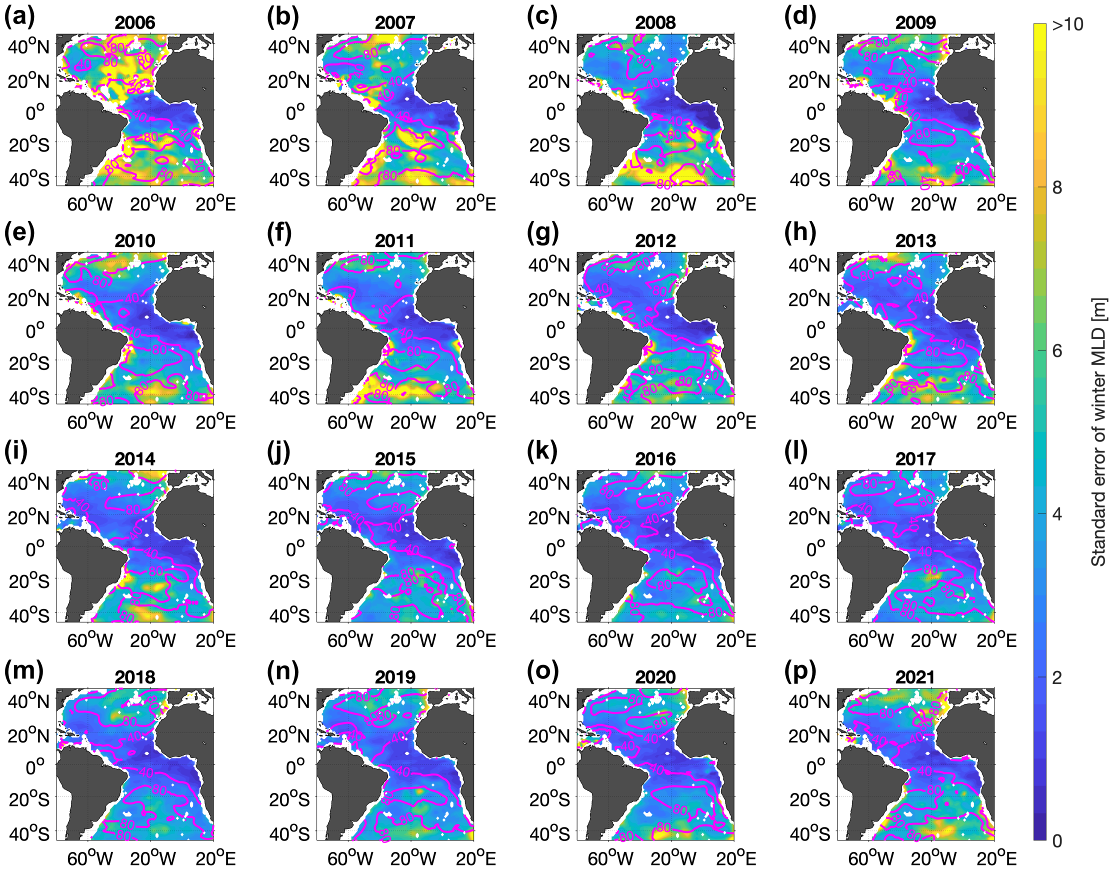

Supplementary Figure 5.9: Standard error for each winter's MLD from 2006-2021 (**(a)**-**(p)**). Pink contour lines mark the corresponding annual mean winter MLD.

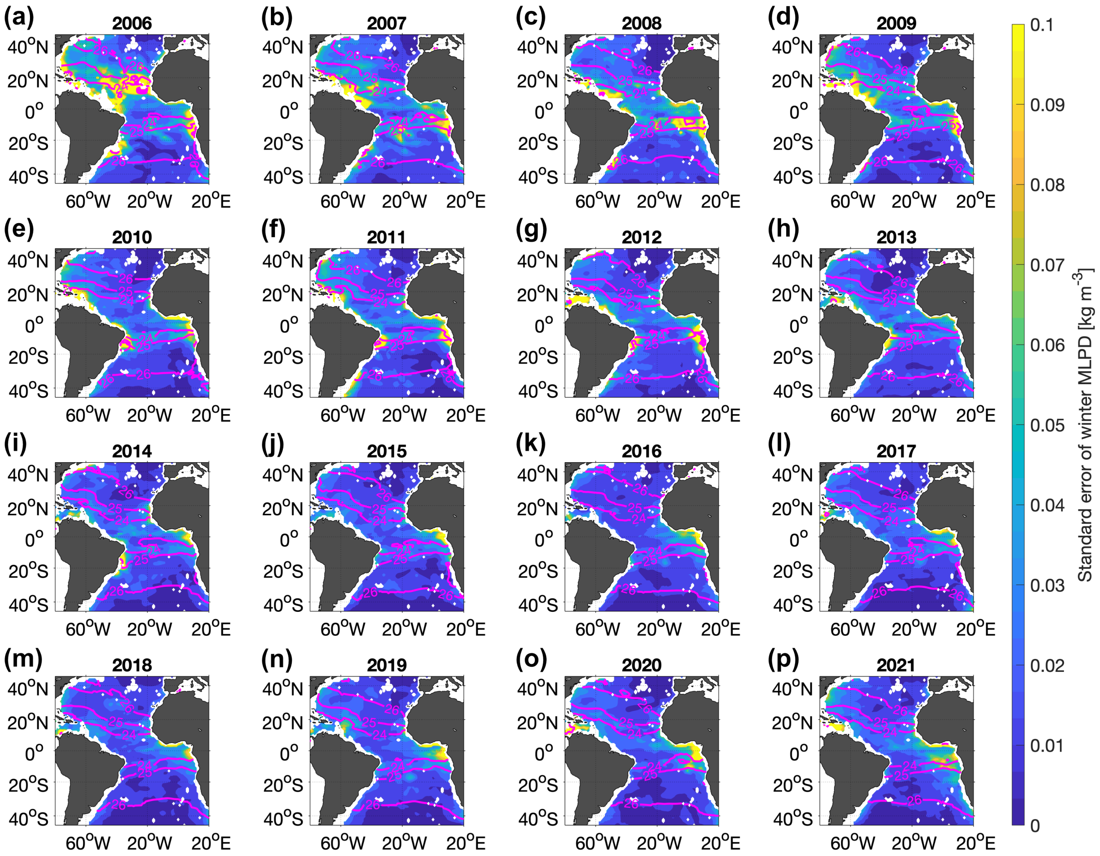

Supplementary Figure 5.10: Standard error for each winter's MLPD from 2006-2021 (**(a)**-**(p)**). Pink contour lines mark the corresponding annual mean winter MLPD.

Chapter 6

Synthesis

The aim of this thesis is to achieve an improved understanding of the recent changes of the upper-ocean during the Argo observation period in terms of climate variability. While it is not possible to directly link the observed changes to the on-going climate warming due to the rather short time period covered by Argo observations, it is important to perceive a better comprehension of the current state and recent changes of the upper-ocean.

Chapter 3 focused on the southeastern tropical Atlantic and how the underlying upper-ocean stratification has changed since 2006. The SETA region experienced the largest increase of the vertical stratification maximum during the period of 2006-2019 in the entire tropical Atlantic (Roch et al., 2021). This region off Angola and Namibia has previously received a lot of scientific attention. On seasonal timescales, the SETA region is affected by the passage of CTWs which mark the upwelling and downwelling seasons (e.g., Ostrowski et al., 2009; Bachèlery et al., 2016; Tchipalanga et al., 2018). On interannual timescales, extreme warm events, called Benguela Niños (Shannon et al., 1986), shift the ABF southward (Florenchie et al., 2004; Rouault et al., 2007, 2018; Lübbecke et al., 2010) and thereby bring tropical water masses more to the south (Lübbecke et al., 2010; Siegfried et al., 2019). Consequently, the productivity as well as the marine fish habitat in the SETA region can be affected (e.g., Gammelsrød et al., 1998). Chapter 3 now described for the first time observed large-scale stratification changes in the SETA region on decadal timescales, in particular, focusing on the open ocean region, since Argo does not cover shelf regions.

Investigations of the physical upper-ocean structure in this highly-productive ecosystem off the coast of Angola and Namibia are of great relevance. The study of Potts et al. (2014) found a poleward movement of some fish species habitats associated with increased warming. Local Angolan fishermen report vanishing fish species and less fish catches (Bearak and Mooney, 2019). This can have dramatic consequences as about one fourth of the Angolan's protein uptake relies on fish (FAO, 2023). Jarre et al. (2015) discussed possible biological consequences of climate warming on the Benguela upwelling system. However, they stress that relationships between hydrographic changes and marine ecosystem adaptations are not straight forward and further investigations are needed. In Chapter 3, a detailed analysis of large-scale upper-ocean changes in the SETA region is conducted: a continuous shift of the underlying subtropical stratification toward a more tropical stratification during 2006-2020 is observed (Roch et al., 2021). The physical findings are then discussed in terms of possible consequences on the marine ecosystem in the SETA region.

Additionally, Chapter 3 provided the base for an algorithm for detecting the vertical stratification maximum from Argo observations. This method was further developed in Chapter 4 and applied to the global oceans. The data product created for the analysis is freely available (Roch et al., 2023b). Furthermore, Chapter 4 was dedicated to analyze global changes of summer and winter vertical stratification maxima and relate these changes to mixed layer variations as well as to the heave mechanism during the period of 2006-2021. The physical mechanism responsible for the vertical stratification maximum can differ seasonally and regionally, as it can be part of the transition between the mixed layer and the seasonal or permanent pycnoclines or in summer, it can be integrated in the seasonal pycnocline itself. Despite that regionally and seasonally different processes are responsible for generating the vertical stratification maximum, it is a representative parameter for the coupling of the ocean surface and ocean interior. While observations indicate intensifying stratification of the ocean, in particular, of the upper $200\,m$ (Yamaguchi and Suga, 2019; Li et al., 2020), so far the vertical stratification maximum has not been examined in more detail. As it is a well-defined parameter in the water column and not as variable as the base of the mixed layer, the vertical stratification maximum might present a parameter that is well-comparable to models.

Chapter 4 presented the current mean state of the stratification maximum of the global oceans as well as the decadal changes during the time of 2006-2021. As the vertical stratification maximum acts as a gateway from the mixed layer to the ocean interior, it is closely related to mixed layer changes. For the Argo period, a de-coupling of the upper-ocean from the ocean interior is suggested as a result of an intensifying vertical stratification maximum (Roch et al., 2023a). The observed stratification increases are associated with mixed layer warming and partly freshening. This surface density reduction and therefore, intensifying stratification is consistent with climate projections and current knowledge (e.g., Capotondi et al., 2012; Rhein et al., 2013). However, the Argo period experiences a vast mixed layer deepening which is also observed on longer timescales for the summer mixed layer (Sallée et al., 2021), but is in contrast to what is expected as a result of global warming (e.g., Capotondi et al., 2012; Kwiatkowski et al., 2020; Rhein et al., 2013; Oschlies et al., 2018). Climate models focus on much longer timescales than the ones examined in Chapter 4. Nonetheless, these findings demonstrate that there are gaps in the knowledge of processes acting in the upper-ocean. Improved understanding of the de-coupling process of the mixed layer from the ocean interior is of great importance as it affects ocean ventilation and mixing, mode water formation and with that, it impacts the distribution of oxygen and nutrients and plays a role for biological productivity.

Chapter 3 and Chapter 4 focused on the upper-ocean stratification changes in association with mixed layer and heave variations. An altered stratification can affect many different processes. The model study by Luo et al. (2009b) suggested for the North Pacific that with surface warming and enhanced stratification, the PV barrier, located in the eastern parts of all tropical oceans, will become stronger in magnitude and larger in size. This is thought to have a severe impact on the subtropical-tropical pathways as part of the subtropical cells. The varying size of the PV barrier leads to a redistribution of the pathways (Luo et al., 2009b). The occurrence of a changing PV barrier in the North Atlantic was investigated in Chapter 5 based on observations. PV variability is highly related to the variations of the vertical density gradient. Therefore, the analysis focused on the decadal variability of the isopycnals in the subtropical-tropical Atlantic. The decadal variability of isopycnals could be related to the NAO. During positive NAO phases, intensified trade winds generate enhanced upwelling in the northeastern tropical Atlantic. This upwelling induces isopycnal heave and thereby squeezes isopycnal layers which enhances the upper-ocean stratification and strengthens the PV barrier in magnitude and size. Implications of the changing PV barrier on the subtropical-tropical pathways of the STC were examined. In addition, NAO-related wind stress changes were found to simultaneously cause anomalous EUC transport rates as well as subduction rates of the EUC density range. While Atlantic STCs have been extensively studied to date (e.g., Zhang et al., 2003; Tuchen et al., 2019, 2020), this is the first time that the variability of a PV barrier is investigated from observations and hence, Chapter 5 provided new insights on isopycnal and PV variability in the subtropical-tropical Atlantic Ocean.

In summary, within the framework of this thesis, the decadal variability of the upper-ocean structure has been assessed from Argo observations for the period of 2006-2022. This is the period of the to date, largest detected warming as part of the on-going climate change (e.g., Bulgin et al., 2020; Garcia-Soto et al., 2021). Therefore, increased knowledge of this particular period is required to improve our understanding of the processes involved in the observed variations but also to project future changes. In the following, the research questions raised in Chapter 1 are summarized and related to the results of the individual chapters. Finally, some open questions are discussed in the outlook.

6.1 Summary

Question 1

How did the upper-ocean stratification change in the southeastern tropical Atlantic during the Argo observation period? What are the reasons for the observed changes? How do they impact the marine ecosystem in the southeastern tropical Atlantic?

In Chapter 3, the southeastern tropical Atlantic Ocean (10°S-20°S, 5°W-15°E) was examined in terms of upper-ocean stratification trends for the period of 2006-2020 (Roch et al., 2021). Based on Argo observations, trends of the vertical stratification maximum were assessed and compared to the trends of mixed layer characteristics. During this period (2006-2020), the southeastern tropical Atlantic is the region that experiences the largest stratification increase (larger than 30 %) in the entire tropical Atlantic Ocean (30°N-30°S, Figure 3.4). The strengthening stratification is found to be accompanied by a surface density reduction that is driven by a warming and freshening of the mixed layer. Besides, the mixed layer is becoming thinner.

The study shows that the stratification increase is not solely related to the surface density reduction. According to the heave and spice decomposition by Bindoff and McDougall (1994), isopycnals are supposed to move downward in case of either a *pure warming/freshening* signal (cf. Chapter 2.3). Isopycnal analysis however, demonstrates rising isopycnals in the depth range of the vertical stratification maximum. This points toward an involvement of wind stress curl-driven changes. Indeed, satellite observations indicate intensified open ocean wind stress curl-driven upwelling which generates an upward displacement of isopycnals. The depth displacement does not happen constantly for all isopycnals, therefore the height difference between isopycnal layers changes. Isopycnals surrounding the vertical stratification maximum are observed to be squeezed together. This contributes to the observed stratification increase. Additionally, below the vertical stratification maximum, the layers between isopycnals are stretched and thus, stratification is reduced.

However, stratification is not only intensifying, it also changes its structure. Annual mean temperature and salinity values of the upper 200 m demonstrate a shift from a subtropical stratification (warm/saline water above cool/fresh water) toward a more tropical stratification which is characterized by a subsurface salinity maximum. Despite that the open ocean wind stress curl-driven upwelling is shown to be intensifying, coastal upwelling is reduced as a result of weakened alongshore southerly winds. However, this might have caused a more southward propagation of tropical waters.

Furthermore, the southeastern tropical Atlantic contains a highly-productive ecosystem. The observed changes of physical parameters are most likely associated with changes of the prevailing marine ecosystem. Yet, for the complexity of parameters and feedbacks involved in marine ecosystems, it remains uncertain, how exactly they are affected by intensifying stratification. The analysis of net primary production demonstrates a slight positive trend in the southeastern tropical Atlantic which is in contrast to most studies which suggest a reduced primary production as a response to intensifying stratification. Estimates of net primary production are based on satellite data and therefore, only surface values are analyzed. Consequently, the shoaling mixed layer might have led to a compression of productivity into a smaller volume which would relate to a negative trend of integrated primary production. Next to primary production also pelagic fishes might be affected. When tropical waters reach further south and shift the Angola-Benguela Front, this could further enhance the possibility of a southward migration of tropical fishes as for instance for the sardinellas *S. aurita* on an all year basis and not just seasonally when the Angola-Benguela Front is located more south.

To conclude, upper-ocean stratification in the southeastern tropical Atlantic seems to shift from subtropical to tropical conditions which can be explained by surface density reduction as well as isopycnal heave related to wind stress curl-driven upwelling (Roch et al., 2021). Implications on the marine ecosystems remain however unclear and require further investigations.

Question 2

What are common characteristics of the vertical stratification maximum in summer and winter season? How did the vertical stratification maximum and mixed layer characteristics change globally during the Argo observation period in summer and winter seasons, respectively? What causes the observed large-scale patterns and what are possible implications?

In Chapter 4, a global dataset of the vertical stratification maximum in summer and winter seasons based on Argo observations is presented, analyzed and compared to mixed layer characteristics. Recent changes of the vertical stratification maximum, its depth, MLT, MLS and MLD are investigated for the time period of 2006-2021 (Roch et al., 2023a). The extensive Argo observation dataset (Argo, 2021) allows to map summer and winter vertical stratification maxima of the past 16 years and to raise more knowledge of the decadal variability of summer and winter vertical stratification maxima during the last decade. The last decade has been subject to intensified ocean surface warming (Garcia-Soto et al., 2021).

The mean state of the vertical stratification maximum shows largest stratification values in the tropical oceans associated with minimum depths (Figure 4.2). Moving away from the tropics, the stratification maximum is subject to a seasonal cycle: highest stratification in the corresponding summer hemisphere co-located with shallower depth levels, while the winter stratification maximum is weaker and found deeper in the water column (Roch et al., 2023a). This fits to seasonal warming and cooling, respectively. Locations of the deepest vertical stratification maximum are the subpolar North Atlantic and the Southern Ocean, in the respective winter season.

For the 16 years of Argo observations, stratification maximum changes show regional differences. From trends of zonal means some general statements can be derived: the vertical stratification maximum is observed to strengthen in summer of both hemispheres while the winter stratification maximum intensifies in the Northern Hemisphere only (Figure 4.3). This is found to be accompanied in most regions by a mixed layer warming and partly freshening. Some areas even exceed mixed layer warming rates of 1.5°C decade^{-1} which corresponds to satellite SST observations that detect largest warming trends for the period of 2010-2018, regionally surpassing 4°C decade^{-1} (Bulgin et al., 2020). Besides the warming, isopycnal heave plays a role and results regionally in stronger vertical density gradients at the depth of the vertical stratification maximum. Isopycnal heave is most likely caused by wind stress curl-driven changes (e.g., Bindoff and McDougall, 1994; Huang, 2015; Roch et al., 2021). Contributions to strengthening stratification additionally arise from a large-scale mixed layer deepening observed during the Argo period (Figure 4.6). The mixed layer changes are observed to be symmetric on both hemispheres in the corresponding season: pronounced mixed layer deepening on the winter hemispheres with maximum deepening rates in the subpolar regions and weak but significant summer mixed layer deepening. Deeper mixed layers and strengthened stratification might be a paradox at first glance. Model studies suggest that the ocean warming and intensifying stratification will lead to shallower mixed layers as a result of less vertical mixing describing a stronger de-coupling of the mixed layer and the ocean interior (e.g., Capotondi et al., 2012; Oschlies et al., 2018; Luo et al., 2009a). Consistent with the here-presented findings, other observational studies, however, indicate deepening mixed layers on longer time periods (e.g., Sallée et al. (2021) for the period of 1970-2018).

Warmer and thicker mixed layers actually contribute to an intensifying stratification maximum: when the mixed layer becomes warmer due to surface forcing, the density reduces in this layer and the density gradient below the mixed layer increases, slightly enhancing the vertical stratification maximum, since the ocean interior has a slower warming rate. In the absence of wind forcing, this would lead to shallower mixed layers. However, if now wind forcing acts to deepen the mixed layer, the layer between the mixed layer base and the vertical stratification maximum squeezes, resulting in an upward movement and intensification of the vertical stratification maximum.

To finalize, the summer and winter vertical stratification maxima intensify globally by 7-8 % accompanied by a global winter and summer mixed layer deepening of 4 m during the Argo observation period (Roch et al., 2023a). There are regional differences, however, in general the results suggest a de-coupling of the upper-ocean from the ocean interior over the past 16 years due to the strengthening stratification of the vertical stratification maximum. Mode water formation processes, ventilated layers and mixing are expected to change consequently. An intensified seasonal cycle of the mixed layer depth might result in enhanced mode water production via lateral induction processes. Subtropical mode water volume has been shown to increase associated with isopycnal heave (Häkkinen et al., 2015, 2016). More mode water production and subduction of warmer mixed layer waters might have contributed to mode waters being the warming hot spots during the Argo period (Kolodziejczyk et al., 2019).

There are still many processes in the upper-ocean that are not well understood. The analysis and data product created during this thesis, can help identify and improve model-observation discrepancies in terms of the mixed layer characteristics and depth and the vertical stratification maximum.

Question 3

What is the impact of the North Atlantic Oscillation on the physical processes in the upper-ocean of the subtropical-tropical Atlantic Ocean? How is the decadal variability of isopycnals related to the potential vorticity barrier? Does the variability of the potential vorticity barrier have an influence on subtropical-tropical pathways?

In Chapter 5, the decadal variability of shallow isopycnals in the subtropical-tropical Atlantic Ocean is investigated and associated with the NAO for the Argo period between 2006-2022. With Argo observations and satellite wind products, it has been demonstrated that according to atmospheric circulation changes along with NAO phases, the isopycnals within the thermocline of the subtropical-tropical Atlantic are displaced in the vertical, changing the PV.

The analysis focuses mainly on the 26.0 $kg\,m^{-3}$-isopycnal which is part of the thermocline layer in the subtropical-tropical Atlantic Ocean and outcrops in the subtropical basins of the North and South Atlantic. The atmospheric patterns during the NAO phases are two well-established states in the North Atlantic: during positive NAO phases, the North Atlantic's subtropical high is intensified, leading to strengthened westerlies and northeast trades and during negative NAO phase the opposite occurs (e.g., Wanner et al., 2001; Pinto and Raible, 2012). The difference between composite analyses of satellite-derived wind stress for positive and negative NAO phases resembles the well-known patterns.

In accordance to the changing atmospheric circulation, the wind stress curl and the Ekman pumping/suction fields vary. During positive NAO phases, intensified wind stress curl-driven Ekman pumping in the subtropical subduction zones and strengthened Ekman suction in the northeastern tropical Atlantic can be observed. This has been shown to be associated with isopycnal heave changes: rising isopycnals equatorward of 20°N and deepening isopycnals poleward of that. Consequently, this induces height changes between isoypycnal layers which impact the PV field. The PV barrier in the northeastern tropical Atlantic is observed to be stronger during positive NAO phases than during negative NAO phases.

The zonal extent and the strength of the PV barrier influence the North Atlantic's subtropical-tropical exchange window of the STC: composite analyses of geostrophic velocities and the Sverdrup streamfunction depict enhanced equatorward velocities at thermocline level along the western boundary and reduced equatorward flow in the interior during positive NAO phases. Such a redistribution of the subtropical-tropical pathways has been suggested by Luo et al. (2009b) as a result of a warmer climate, when stratification is intensified and therefore, the PV barrier becomes stronger.

Not only the distribution of the subtropical-tropical pathways is influenced by the NAO phase-induced wind changes but also the subduction rates of the water with the density range entering the EUC from the North Atlantic. For the time of positive NAO in 2014-2019, the annual subduction rates are intensified. Also, the subduction rates of the EUC density range coming from the South Atlantic show variations, however, these do not follow the NAO pattern. Additionally, at the same time the EUC transport rate anomalies observed at the mooring site at $0°, 23°W$ are associated with the intensified trade winds. However, increasing subduction rates do not necessarily result in a strengthened EUC. This can be explained as follows: on timescales of five years and longer, the EUC and STCs are connected via a pulling effect, i.e., stronger trade winds lead to enhanced Ekman divergence and thermocline convergence, therefore strengthen the EUC transport and amplify the STCs (Rabe et al., 2008).

On these timescales the EUC might be related to the NAO as a result of variations of the northeast trade winds. The study of Luo et al. (2009b) suggested that with a stronger PV barrier and enhanced equatorward transport via the western boundary and reduced flow via the interior, the EUC will intensify in the western and central part of the basin. However, whether the here-observed variations of the PV barrier also contribute to EUC transport variability as it has been suggested by Luo et al. (2009b), remains uncertain.

The analysis of Luo et al. (2009b) focused on the Pacific Ocean which has a much larger basin size than the Atlantic Ocean and during in the mean state the interior pathway of the North Pacific has a larger contribution to the equator than in the Atlantic (e.g., Schott et al., 2004). Another possibility is that the considered time period is too short.

To summarize, Chapter 5 demonstrates NAO-related decadal variability of atmospheric circulation influences the upper-ocean structure in the subtropical-tropical Atlantic Ocean. Isopycnal heaving produces anomalous PV barriers which in turn lead to a redistribution of the subtropical-tropical pathways. Simultaneously, Atlantic EUC transport rates are adapted according to intensifying trade winds. Whether PV barrier variations contribute to the variability of the EUC remains unsolved.

6.2 Outlook

On the large-scale mixed layer deepening

The framework of this thesis contributes to enriching knowledge of the upper-ocean structure and its recent changes during the Argo period. The observed deepening mixed layers coinciding with intensifying upper-ocean stratification is at odds, even though deeper mixed layers do not contradict an enhancing stratification as discussed in Chapter 4. Reasons for the large-scale mixed layer deepening remain unsolved during this thesis, despite that wind changes likely contribute. Scaling analyses by Sallée et al. (2021) indicate that strengthening winds are indeed a potential force for the large-scale mixed layer deepening detected in observations. According to Sallée et al. (2021), wind-driven high-frequency internal-wave turbulence is probably the driving process as their scaling analyses propose that this mechanisms is highly-efficient in deepening mixed layers and the intensifying high-frequency winds are actually observed.

Nevertheless, the findings of this thesis raise questions on the connection between the mixed layer and upper-ocean stratification as the results do not mirror the climate model projections. Certainly, the Argo observation period (2006-2022) is too short to allow for a strong statement indicating that mixed layer changes because of enhanced stratification are wrongly simulated in coupled models. However, processes remain in this connection that are not yet fully understood. On seasonal timescales, the relation between the surface mixed layer and the stratification of the water column is clear: from winter to summer season, the surface mixed layer experiences heat input from the atmosphere, decreasing the ocean's surface density. After mixing, the mixed layer in summer will then be shallower than in winter bounded by enhanced stratification of the seasonal pycnocline. As the ocean surfaces loses heat in the following fall, the water column becomes unstable as the surface of the mixed layer increases in density, causing the water column to overturn and together with wind input, deeper mixed layers will develop until the end of winter (e.g., Talley et al., 2011d). During the Argo period, the seasonal cycle of the MLD amplified as winter mixed layers show a more pronounced deepening trend than summer mixed layers (Chapter 4). Hence, on seasonal timescales, the well-known mechanisms continue to occur.

The question is, what happens to the mixed layer if we continuously add heat to the the surface of the ocean. In this thought experiment, the warming rate is supposed to be smaller than the one associated with the seasonal cycle (Figure 6.1). The timeseries of the global median MLT anomalies in July-September and January-March inferred from Argo observations (applying the data product from Chapter 4) shows an increase of around 0.3°C from 2006-2021. The temperature increase during this period is still a lot smaller than the mean difference between winter and summer MLT in most regions (Figure 6.2).

Is there a maximum warming rate of the mixed layer until which wind forcing can still compensate the effect of a shoaling mixed layer and if the wind forcing is strong enough and/or increases could it then even lead to a deepening of the mixed layer? This might be a tipping point question. Maybe on the observational timescales, this tipping point

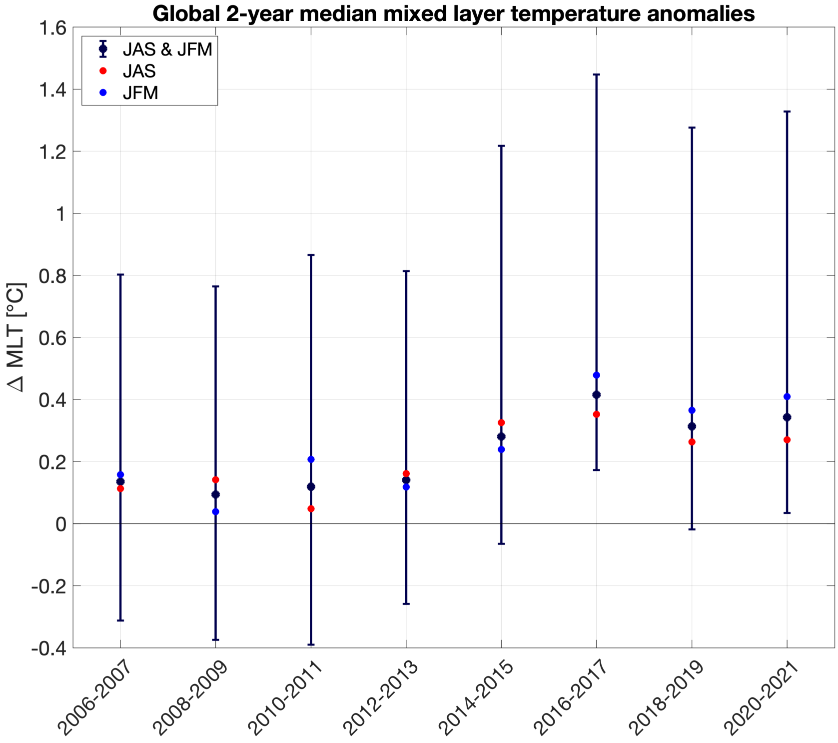

Figure 6.1: Global 2-year median timeseries of mixed layer temperature (MLT) anomalies in July-September and January-March from Argo observations for the time period of 2006-2021. This graph is created with the data product developed in Chapter 4 (Roch et al., 2023b). Anomalies are computed relative to the seasonal nearest grid point's mean. Dark blue bullets represent the median of both seasons combined (January-March, July-September), red bullets denote the median of July-September season and blue bullets refer to the median of January-March season. Bars show the corresponding upper and lower limits of the interquartile range.

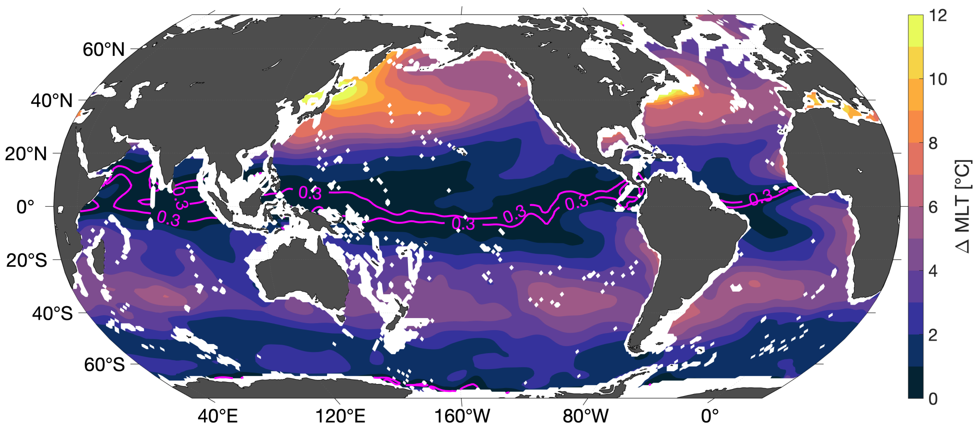

Figure 6.2: Mean difference between winter and summer mixed layer temperature (MLT) inferred from Argo observations for the time period of 2006-2021. This graph is created with the data product developed in Chapter 4. Pink line denotes the 0.3°C isotherm.

has not been reached yet compared to model projections which focus on much longer timescales (e.g., until 2100 as in Kwiatkowski et al., 2020). Kwiatkowski et al. (2020) find enhancing stratification in the upper 200 m of $0.13 \pm 0.05\,kg\,m^{-3}$ and a shoaling maximum MLD of $7 \pm 3.3\,m$ under the high-mitigation scenario SSP1-2.6 and $0.58 \pm 0.11\,kg\,m^{-3}$ and $19.5 \pm 2.6\,m$ under the high-emission scenario SSP5-8.5, respectively. These changes refer to the end-of-century model mean state in 2080-2099 relative to 1870-1899 (Kwiatkowski et al., 2020). Hence, the Argo observation period is way too short to compare to the model outputs. It would be of great value to test whether models can actually identify a mixed layer deepening and stratification increase on shorter timescales.

However, it has been shown that MLDs in Coupled Model Intercomparison Project (CMIP) are not well-represented even in the mean state. For instance, in CMIP5 summer mixed layers are found to be too shallow (e.g., Huang et al., 2014; Sallée et al., 2013) while winter mixed layers are often depicted too deep in deep-water-formation regions in both CMIP5 and CMIP6 (Fox-Kemper et al., 2023; Heuzé, 2021). Recently, Treguier et al. (2023) investigated MLDs in models with different resolution of the Ocean Model Intercomparison Project. Their findings indicate that in low-resolution models, winter mixed layers have large biases in deep-water-formation regions. Eddy-rich models show a smaller bias, however, not consistent across models and regions (Treguier et al., 2023). There is a need for a correct representation of the mean state and variability of the mixed layer in models before reliable projections are available.

On the potential impact of enhancing stratification and mixed layer deepening on marine ecosystems and biogeochemistry

Moreover, further investigation is needed on the impact of the mixed layer deepening and intensifying stratification on the biogeochemistry. Distributions of oxygen and nutrients are most likely to be influenced and thereby, the marine ecosystems are affected as well. Observations show a 2 % decrease of the global oxygen inventory since 1960 which has been attributed partly to the warming-induced solubility loss (Schmidtko et al., 2017) and partly to reduced ocean ventilation (Oschlies et al., 2018). This reduction in oxygen is, however, not homogeneous among basins and depths, but reflects oceanic volume, deep-water ventilation rates and bathymetry (Schmidtko et al., 2017). As a result of ocean warming and intensifying stratification, reduced ventilation is assumed which can lead to a decrease in oxygen (Keeling et al., 2010; Oschlies et al., 2018). Schmidtko et al. (2017) found the largest oxygen loss to be located in the North Pacific and Equatorial Pacific. Even though, their time series is much longer than the Argo period, the pattern of deoxygenation (cf. their Figure 1) is comparable to the increase of the vertical stratification maximum observed in the North Pacific in summer and winter seasons (Figure 4.3). Analyses on the relation between the vertical stratification maximum, oxygen and nutrients could contribute to improve the understanding of the suggested de-coupling process of the surface ocean from the ocean interior.

References

Adler, R. F., Sapiano, M. R. P., Huffman, G. J., Wang, J.-J., Gu, G., Bolvin, D., Chiu, L., Schneider, U., Becker, A., Nelkin, E., Xie, P., Ferraro, R., and Shin, D.-B. (2018). The Global Precipitation Climatology Project (GPCP) Monthly Analysis (New Version 2.3) and a Review of 2017 Global Precipitation. *Atmosphere*, 9(4):138, ISSN: `2073-4433`, DOI: `10.3390/atmos9040138`, https://www.mdpi.com/2073-4433/9/4/138.

Akima, H. (1970). A New Method of Interpolation and Smooth Curve Fitting Based on Local Procedures. *Journal of the ACM (JACM)*, 17(4):589–602, ISSN: `1557735X`, DOI: `10.1145/321607.321609`.

Argo (2019). Argo float data and metadata from Global Data Assembly Centre (Argo GDAC) - Snapshot of Argo GDAC of November 13st 2019. https://doi.org/10.17882/42182#68322.

Argo (2020). Argo float data and metadata from Global Data Assembly Centre (Argo GDAC) - Snapshot of Argo GDAC of November 25st 2020. https://doi.org/10.17882/42182#78698.

Argo (2021). Argo float data and metadata from Global Data Assembly Centre (Argo GDAC) - Snapshot of Argo GDAC of December 10st 2021. https://doi.org/10.17882/42182#90179.

Argo (2022). Argo float data and metadata from Global Data Assembly Centre (Argo GDAC) - Snapshot of Argo GDAC of December 09st 2022. https://doi.org/10.17882/42182#98126.

Argo (2023a). Argo's Mission. https://argo.ucsd.edu/about/mission/.

Argo (2023b). What is Argo? https://argo.ucsd.edu/about/.

Bachèlery, M. L., Illig, S., and Dadou, I. (2016). Forcings of nutrient, oxygen, and primary production interannual variability in the southeast Atlantic Ocean. *Geophysical Research Letters*, 43(16):8617–8625, ISSN: `19448007`, DOI: `10.1002/2016GL070288`.

Bakun, A., Black, B. A., Bograd, S. J., García-Reyes, M., Miller, A. J., Rykaczewski, R. R., and Sydeman, W. J. (2015). Anticipated Effects of Climate Change on Coastal Upwelling Ecosystems. *Current Climate Change Reports*, 1(2):85–93, ISSN: `21986061`, DOI: `10.1007/s40641-015-0008-4`.

Balaguru, K., Foltz, G. R., Leung, L. R., and Emanuel, K. A. (2016). Global warming-induced upper-ocean freshening and the intensification of super typhoons. *Nature Communications*, 7:13670, ISSN: `20411723`, DOI: `10.1038/ncomms13670`, http://dx.doi.org/10.1038/ncomms13670.

BCC (2012). Benguela Current Commission: State of Stocks Report. Report No. 2. http://www.benguelacc.org/index.php/en/component/docman/doc_download/120-sos-report-2012-low.

Bearak, M. and Mooney, C. (2019). 2°C beyond the limit. A crisis in the water is decimating this once-booming fishing town. https://www.washingtonpost.com/graphics/2019/world/climate-environment/angola-climate-change/.

Behrenfeld, M. J. and Falkowski, P. G. (1997). Photosynthetic rates derived from satellite-based chlorophyll concentration. *Limnology and Oceanography*, 42(1):1–20, ISSN: `00243590`, DOI: `10.4319/lo.1997.42.1.0001`.

Bentamy, A. (2020). Product User Manual For Wind Product - WIND_GLO_PHY_CLIMATE_L4_REP_012_003. https://resources.marine.copernicus.eu/documents/PUM/CMEMS-WIND-PUM-012-003.pdf.

Bentamy, A. and Fillon, D. C. (2012). Gridded surface wind fields from Metop/ASCAT measurements. *International Journal of Remote Sensing*, 33(6):1729–1754, ISSN: `13665901`, DOI: `10.1080/01431161.2011.600348`.

Bentamy, A., Piollé, J., Prevost, C., and Giesen, R. (2022). Product User Manual for Wind Product - WIND_GLO_WIND_L4_REP_OBSERVATIONS_012_006. https://catalogue.marine.copernicus.eu/documents/PUM/CMEMS-WIND-PUM-012-006.pdf.

Bindoff, N. L. and McDougall, T. J. (1994). Diagnosing Climate Change and Ocean Ventilation Using Hydrographic Data. *Journal of Physical Oceanography*, 24(6):1137–1152, ISSN: `0022-3670`, DOI: `10.1175/1520-0485(1994)024<1137:dccaov>2.0.co;2`.

Bingham, F. M., Busecke, J. J., and Gordon, A. L. (2019). Variability of the South Pacific Subtropical Surface Salinity Maximum. *Journal of Geophysical Research: Oceans*, 124(8):6050–6066, ISSN: `21699291`, DOI: `10.1029/2018JC014598`.

Bjerknes, J. (1969). Atmospheric teleconnections from the equatorial Pacific. *Monthly Weather Review*, 97(3):163–172, DOI: `10.1175/1520-0493(1969)097<0163:ATFTEP>2.3.CO;2`.

Boley, T. and Fréon, P. (1980). Coastal pelagic resources. In Troadec, J. P. and Garcia, S., editors, *The Fish Resources of the Eastern Central Atlantic. Part One: The Resources of the Gulf of Guinea from Angola to Mauretania. FAO Fisheries Technical Paper No. 186.1*, pages 13–76.

Bopp, L., Lévy, M., Resplandy, L., and Sallée, J. B. (2015). Pathways of anthropogenic carbon subduction in the global ocean. *Geophysical Research Letters*, 42(15):6416–6423, ISSN: `19448007`, DOI: `10.1002/2015GL065073`.

Bourlès, B., Gouriou, Y., and Chuchla, R. (1999). On the circulation in the upper layer of the western equatorial Atlantic. *Journal of Geophysical Research: Oceans*, 104(C9):21151–21170, ISSN: `21699291`, DOI: `10.1029/1999jc900058`.

Boyce, D. G., Lewis, M. R., and Worm, B. (2010). Global phytoplankton decline over the past century. *Nature*, 466(7306):591–596, ISSN: `14764687`, DOI: `10.1038/nature09268`.

Brandt, P., Bange, H. W., Banyte, D., Dengler, M., Didwischus, S. H., Fischer, T., Greatbatch, R. J., Hahn, J., Kanzow, T., Karstensen, J., Körtzinger, A., Krahmann, G., Schmidtko, S., Stramma, L., Tanhua, T., and Visbeck, M. (2015). On the role of circulation and mixing in the ventilation of oxygen minimum zones with a focus on the eastern tropical North Atlantic. *Biogeosciences*, 12(2):489–512, ISSN: `17264189`, DOI: `10.5194/bg-12-489-2015`.

Brandt, P., Funk, A., Tantet, A., Johns, W. E., and Fischer, J. (2014). The Equatorial Undercurrent in the central Atlantic and its relation to tropical Atlantic variability. *Climate Dynamics*, 43(11):2985–2997, ISSN: `14320894`, DOI: `10.1007/s00382-014-2061-4`.

Brandt, P., Hahn, J., Schmidtko, S., Tuchen, F. P., Kopte, R., Kiko, R., Bourlès, B., Czeschel, R., and Dengler, M. (2021). Atlantic Equatorial Undercurrent intensification counteracts warming-induced deoxygenation. *Nature Geoscience*, 14(5):278–282, ISSN: `17520908`, DOI: `10.1038/s41561-021-00716-1`, http://dx.doi.org/10.1038/s41561-021-00716-1.

Brochier, T., Auger, P. A., Pecquerie, L., Machu, E., Capet, X., Thiaw, M., Mbaye, B. C., Braham, C. B., Ettahiri, O., Charouki, N., Sène, O. N., Werner, F., and Brehmer, P. (2018). Complex small pelagic fish population patterns arising from individual behavioral responses to their environment. *Progress in Oceanography*, 164:12–27, ISSN: `0079-6611`, DOI: `10.1016/j.pocean.2018.03.011`.

Bulgin, C. E., Merchant, C. J., and Ferreira, D. (2020). Tendencies, variability and persistence of sea surface temperature anomalies. *Scientific reports*, 10(1):7986, ISSN: `20452322`, DOI: `10.1038/s41598-020-64785-9`, http://dx.doi.org/10.1038/s41598-020-64785-9.

Caesar, L., Rahmstorf, S., Robinson, A., Feulner, G., and Saba, V. (2018). Observed fingerprint of a weakening Atlantic Ocean overturning circulation. *Nature*, 556(7700):191–196, ISBN: `4158601800065`, ISSN: `14764687`, DOI: `10.1038/s41586-018-0006-5`.

Capotondi, A., Alexander, M. A., Bond, N. A., Curchitser, E. N., and Scott, J. D. (2012). Enhanced upper ocean stratification with climate change in the CMIP3 models. *Journal of Geophysical Research: Oceans*, 117(4):C04031, ISSN: `21699291`, DOI: `10.1029/2011JC007409`.

Chang, P., Yamagata, T., Schopf, P., Behera, S. K., Carton, J., Kessler, W. S., Meyers, G., Qu, T., Schott, F., Shetye, S., and Xie, S. P. (2006). Climate fluctuations of tropical coupled systems - The role of ocean dynamics. *Journal of Climate*, 19(20):5122–5174, ISSN: `08948755`, DOI: `10.1175/JCLI3903.1`.

Chapman, C. C., Lea, M. A., Meyer, A., Sallée, J. B., and Hindell, M. (2020). Defining Southern Ocean fronts and their influence on biological and physical processes in a changing climate. *Nature Climate Change*, 10(3):209–219, ISBN: `4155802007`, ISSN: `17586798`, DOI: `10.1038/s41558-020-0705-4`, http://dx.doi.org/10.1038/s41558-020-0705-4.

Chen, S., Wu, R., and Chen, W. (2015). The changing relationship between interannual variations of the North Atlantic Oscillation and northern tropical Atlantic SST. *Journal of Climate*, 28(2):485–504, ISSN: `08948755`, DOI: `10.1175/JCLI-D-14-00422.1`.

Church, J. A., White, N. J., Konikow, L. F., Domingues, C. M., Cogley, J. G., Rignot, E., Gregory, J. M., Van Den Broeke, M. R., Monaghan, A. J., and Velicogna, I. (2011). Revisiting the Earth's sea-level and energy budgets from 1961 to 2008. *Geophysical Research Letters*, 38(18):L18601, ISSN: `00948276`, DOI: `10.1029/2011GL048794`.

Clément, L., McDonagh, E. L., Marzocchi, A., and Nurser, A. J. (2020). Signature of Ocean Warming at the Mixed Layer Base. *Geophysical Research Letters*, 47(1):e2019GL086269, ISSN: `19448007`, DOI: `10.1029/2019GL086269`.

Cronin, Meghan, F., Weller, Robert, A., Lampitt, Richard, S., and Send, U. (2012). Ocean Reference Stations. In Rustamov, R., editor, *Earth Observation*, chapter Chapter 9. ISBN: `978-953-307-973-8`, DOI: `10.5772/27423`.

Cronin, M. F., Bond, N. A., Thomas Farrar, J., Ichikawa, H., Jayne, S. R., Kawai, Y., Konda, M., Qiu, B., Rainville, L., and Tomita, H. (2013). Formation and erosion of the seasonal thermocline in the Kuroshio Extension Recirculation Gyre. *Deep-Sea Research Part II: Topical Studies in Oceanography*, 85:62–74, ISSN: `09670645`, DOI: `10.1016/j.dsr2.2012.07.018`, http://dx.doi.org/10.1016/j.dsr2.2012.07.018.

Cushman-Roisin, B. and Beckers, J.-M. (2009a). 20.2.2 Sverdrup transport. In *Introduction to Geophysical Fluid Dynamics: Physical and Numerical Aspects*, chapter 20.2.2, pages 611–612. Academic press, 1. edition, http://repository.socib.es/repository/entry/show?entryid=18e5db9e-3383-4077-afb3-c16f109ffa32.

Cushman-Roisin, B. and Beckers, J.-M. (2009b). Homogeneous geostrophic flows. In *Introduction to Geophysical Fluid Dynamics: Physical and Numerical Aspects*, chapter 7.1, pages 187–189. Academic Press, 1. edition, http://repository.socib.es/repository/entry/show?entryid=18e5db9e-3383-4077-afb3-c16f109ffa32.

Cushman-Roisin, B. and Beckers, J.-M. (2009c). The surface Ekman layer. In *Introduction to Geophysical Fluid Dynamics: Physical and Numerical Aspects*, chapter 8.6, pages 230–233. Academic press, 1. edition, http://repository.socib.es/repository/entry/show?entryid=18e5db9e-3383-4077-afb3-c16f109ffa32.

Czaja, A., van der Vaart, P., and Marshall, J. (2002). A diagnostic study of the role of remote forcing in tropical Atlantic variability. *Journal of Climate*, 15(22):3280–3290, ISSN: `08948755`, DOI: `10.1175/1520-0442(2002)015<3280:ADSOTR>2.0.CO;2`.

Davis, R. E., Webb, D. C., Regier, L. A., and Dufour, J. (1992). The autonomous Lagrangian circulation explorer. *J. Atmospheric & Oceanic Technology*, 9(3):264–285, ISSN: `07390572`, DOI: `10.1175/1520-0426(1992)009<0264:TALCE>2.0.CO;2`.

de Boyer Montégut, C., Madec, G., Fischer, A. S., Lazar, A., and Iudicone, D. (2004). Mixed layer depth over the global ocean: An examination of profile data and a profile-based climatology. *Journal of Geophysical Research: Oceans*, 109(12):C12003, ISSN: `21699291`, DOI: `10.1029/2004JC002378`.

de Steur, L., Peralta-Ferriz, C., and Pavlova, O. (2018). Freshwater Export in the East Greenland Current Freshens the North Atlantic. *Geophysical Research Letters*, 45(24):13359–13366, ISSN: `19448007`, DOI: `10.1029/2018GL080207`.

Desbruyères, D., McDonagh, E. L., King, B. A., and Thierry, V. (2017). Global and Full-Depth Ocean Temperature Trends during the Early Twenty-First Century from Argo and Repeat Hydrography. *Journal of Climate*, 30(6):1985–1997, ISSN: `08948755`, DOI: `10.1175/JCLI-D-16-0396.1`.

DeVries, T., Holzer, M., and Primeau, F. (2017). Recent increase in oceanic carbon uptake driven by weaker upper-ocean overturning. *Nature*, 542(7640):215–218, ISSN: `1476-4687`, DOI: `10.1038/nature21068`, https://doi.org/10.1038/nature21068.

DiNezio, P. N., Gramer, L. J., Johns, W. E., Meinen, C. S., and Baringer, M. O. (2009). Observed interannual variability of the Florida current: Wind forcing and the North Atlantic Oscillation. *Journal of Physical Oceanography*, 39(3):721–736, ISSN: `00223670`, DOI: `10.1175/2008JPO4001.1`.

Durack, P. J. and Wijffels, S. E. (2010). Fifty-Year trends in global ocean salinities and their relationship to broad-scale warming. *Journal of Climate*, 23(16):4342–4362, ISSN: `08948755`, DOI: `10.1175/2010JCLI3377.1`.

Echevin, V., Aumont, O., Ledesma, J., and Flores, G. (2008). The seasonal cycle of surface chlorophyll in the Peruvian upwelling system: A modelling study. *Progress in Oceanography*, 79(2):167–176, ISSN: `0079-6611`, DOI: `https://doi.org/10.1016/j.pocean.2008.10.026`, https://www.sciencedirect.com/science/article/pii/S0079661108001705.

Eden, C. and Willebrand, J. (2001). Mechanism of interannual to decadal variability of the North Atlantic circulation. *Journal of Climate*, 14(10):2266–2280, ISSN: `08948755`, DOI: `10.1175/1520-0442(2001)014<2266:MOITDV>2.0.CO;2`.

Ekau, W., Auel, H., Hagen, W., Koppelmann, R., Wasmund, N., Bohata, K., Buchholz, F., Geist, S., Martin, B., Schukat, A., Verheye, H. M., and Werner, T. (2018). Pelagic key species and mechanisms driving energy flows in the northern Benguela upwelling ecosystem and their feedback into biogeochemical cycles. *Journal of Marine Systems*, 188(January 2017):49–62, ISSN: `09247963`, DOI: `10.1016/j.jmarsys.2018.03.001`, https://doi.org/10.1016/j.jmarsys.2018.03.001.

Ekman, V. W. (1905). On the influence of the earth's rotation on ocean currents. *Arkiv för Matematik, Astronomi och Fysik*, 2(11):1–53, ISSN: `10960783`, https://empslocal.ex.ac.uk/people/staff/gv219/classics.d/Ekman05.pdf.

Evans, D. G., Toole, J., Forget, G., Zika, J. D., Garabato, A. C., George Nurser, A. J., and Yu, L. (2017). Recent wind-driven variability in atlantic water mass distribution and meridional overturning circulation. *Journal of Physical Oceanography*, 47(3):633–647, ISSN: `15200485`, DOI: `10.1175/JPO-D-16-0089.1`.

Falkowski, P. G., Barber, R. T., and Smetacek, V. (1998). Biogeochemical Controls and Feedbacks on Ocean Primary Production. *Science*, 281(5374):200–206, DOI: `10.1126/science.281.5374.200`, https://doi.org/10.1126/science.281.5374.200.

FAO (2023). Fishery and Aquaculture Country Profiles. Angola, 2020. https://www.fao.org/fishery/en/facp/ago.

Fennel, W., Junker, T., Schmidt, M., and Mohrholz, V. (2012). Response of the Benguela upwelling systems to spatial variations in the wind stress. *Continental Shelf Research*, 45:65–77, ISSN: `02784343`, DOI: `10.1016/j.csr.2012.06.004`.

Fennel, W. and Lass, H. U. (2007). On the impact of wind curls on coastal currents. *Journal of Marine Systems*, 68(1):128–142, ISSN: `0924-7963`, DOI: `https://doi.org/10.1016/j.jmarsys.2006.11.004`, https://www.sciencedirect.com/science/article/pii/S0924796306003447.

Ferrari, R. and Boccaletti, G. (2004). Eddy-mixed layer interactions in the ocean. *Oceanography*, 17(3):12–21, ISSN: `10428275`, DOI: `10.5670/oceanog.2004.26`.

Feucher, C. (2016). Stratification structure in subtropical gyres and its decadal variability in the North Atlantic Ocean. http://archimer.ifremer.fr/doc/00366/47675/.

Feucher, C., Maze, G., and Mercier, H. (2019). Subtropical Mode Water and Permanent Pycnocline Properties in the World Ocean. *Journal of Geophysical Research: Oceans*, 124(2):1139–1154, ISSN: `21699291`, DOI: `10.1029/2018JC014526`.

Fiedler, P. C., Mendelssohn, R., Palacios, D. M., and Bograd, S. J. (2013). Pycnocline variations in the eastern tropical and north pacific, 1958-2008. *Journal of Climate*, 26(2):583–599, ISSN: `08948755`, DOI: `10.1175/JCLI-D-11-00728.1`.

Fiedler, P. C. and Talley, L. D. (2006). Hydrography of the eastern tropical Pacific: A review. *Progress in Oceanography*, 69(2-4):143–180, ISSN: `00796611`, DOI: `10.1016/j.pocean.2006.03.008`.

Florenchie, P., Reason, C. J., Lutjeharms, J. R., Rouault, M., Roy, C., and Masson, S. (2004). Evolution of interannual warm and cold events in the Southeast Atlantic Ocean. *Journal of Climate*, 17(12):2318–2334, ISSN: `08948755`, DOI: `10.1175/1520-0442(2004)017<2318:EOIWAC>2.0.CO;2`.

Folger, T. (1787). Chart of the Gulf Stream. In Franklin, B., editor, *Philosophical and Miscellaneous Papers*, page 122. London: C. Dilly.

Fox-Kemper, B., Hewitt, H. T., Xiao, C., Adalgeirsdottir, G., Drijfhout, S. S., Edwards, T. L., Golledge, N. R., Hemer, M., Kopp, R. E., Krinner, G., Mix, A., Notz, D., Nowicki, S., Nurhati, I. S., Ruiz, L., Sallee, J.-B., Slangen, A. B. A., and Yu, Y. (2023). Ocean, Cryosphere and Sea Level Change. *Climate Change 2021: The Physical Science Basis. Contribution of Working Group I to the Sixth Assessment Report of the*

Intergovernmental Panel on Climate Change, pages 1211–1362, ISBN: `9781009157896`, DOI: `10.1017/9781009157896.011`.

Franklin, B., Folger, T., Wright, E., Halley, E., Moll, H., Page, J. M., and Tho. (1768). Franklin-Folger chart of the Gulf Stream. *[London: Sold by Jno. Mount and Tho. Page] Retrieved from the Library of Congress*, https://www.loc.gov/item/88696412/.

Franzke, C. L. E., Barbosa, S., Blender, R., Fredriksen, H.-B., Laepple, T., Lambert, F., Nilsen, T., Rypdal, K., Rypdal, M., Scotto Manuel G, Vannitsem, S., Watkins, N. W., Yang, L., and Yuan, N. (2020). The Structure of Climate Variability Across Scales. *Reviews of Geophysics*, 58(2):e2019RG000657, DOI: `https://doi.org/10.1029/2019RG000657`, https://agupubs.onlinelibrary.wiley.com/doi/abs/10.1029/2019RG000657.

Franzke, C. L. E., Gugole, F., and Juricke, S. (2022). Systematic multi-scale decomposition of ocean variability using machine learning. *Chaos: An Interdisciplinary Journal of Nonlinear Science*, 32(7):73122, ISSN: `1054-1500`, DOI: `10.1063/5.0090064`, https://doi.org/10.1063/5.0090064.

Fu, Y., Brandt, P., Tuchen, F. P., Lübbecke, J. F., and Wang, C. (2022). Representation of the Mean Atlantic Subtropical Cells in CMIP6 Models. *Journal of Geophysical Research: Oceans*, 127(3):e2021JC018191, ISSN: `21699291`, DOI: `10.1029/2021JC018191`.

Fyfe, J. C. and Saenko, O. A. (2006). Simulated changes in the extratropical Southern Hemisphere winds and currents. *Geophysical Research Letters*, 33(6):L06701, ISSN: `00948276`, DOI: `10.1029/2005GL025332`.

Gammelsrød, T., Bartholomae, C. H., Boyer, D. C., Filipe, V. L., and O'Toole, M. J. (1998). Intrusion of warm surface water along the Angolan-Namibian coast in February-March 1995: The 1995 Benguela Nino. *South African Journal of Marine Science*, 19:41–56, ISSN: `02577615`, DOI: `10.2989/025776198784126719`.

Garcia-Soto, C., Cheng, L., Caesar, L., Schmidtko, S., Jewett, E. B., Cheripka, A., Rigor, I., Caballero, A., Chiba, S., Báez, J. C., Zielinski, T., and Abraham, J. P. (2021). An Overview of Ocean Climate Change Indicators: Sea Surface Temperature, Ocean Heat Content, Ocean pH, Dissolved Oxygen Concentration, Arctic Sea Ice Extent, Thickness and Volume, Sea Level and Strength of the AMOC (Atlantic Meridional Overturning Circula. *Frontiers in Marine Science*, 8(September):642372, ISSN: `22967745`, DOI: `10.3389/fmars.2021.642372`.

Gill, A. (1982). Use of Potential Temperature as a State Variable. In *Atmosphere-Ocean Dynamics*, chapter 3.7.4, pages 53–54. Academic Press, New York.

Hahn, J., Brandt, P., Schmidtko, S., and Krahmann, G. (2017). Decadal oxygen change in the eastern tropical North Atlantic. *Ocean Science*, 13(4):551–576, ISSN: `18120792`, DOI: `10.5194/os-13-551-2017`.

Häkkinen, S., Rhines, P. B., and Worthen, D. L. (2015). Heat content variability in the North Atlantic Ocean in ocean reanalyses. *Geophysical Research Letters*, 42(8):2901–2909, ISSN: `19448007`, DOI: `10.1002/2015GL063299`.

Häkkinen, S., Rhines, P. B., and Worthen, D. L. (2016). Warming of the global ocean: Spatial structure and water-mass trends. *Journal of Climate*, 29(13):4949–4963, ISSN: `08948755`, DOI: `10.1175/JCLI-D-15-0607.1`.

Hanawa, K. and Talley, L. D. (2001). Chapter 5.4 Mode waters. *International Geophysics*, 77(C):373–386, ISBN: `0126413517`, ISSN: `00746142`, DOI: `10.1016/S0074-6142(01)80129-7`.

Hazeleger, W., De Vries, P., and Friocourt, Y. (2003). Sources of the equatorial undercurrent in the Atlantic in a high-resolution ocean model. *Journal of Physical Oceanography*, 33(4):677–693, ISSN: `00223670`, DOI: `10.1175/1520-0485(2003)33<677:SOTEUI>2.0.CO;2`.

Hazeleger, W. and Drijfhout, S. (2006). Subtropical cells and meridional overturning circulation pathways in the tropical Atlantic. *Journal of Geophysical Research: Oceans*, 111(3):C03013, ISSN: `21699291`, DOI: `10.1029/2005JC002942`.

Hersbach, H., Bell, B., Berrisford, P., Biavati, G., Horányi, A., Muñoz Sabater, J., Nicolas, J., Peubey, C., Radu, R., Rozum, I., Schepers, D., Simmons, A., Soci, C., Dee, D., and Thépaut, J.-N. (2018). ERA5 hourly data on single levels from 1959 to present. *Copernicus Climate Change Service (C3S) Climate Data Store (CDS)*, DOI: `10.24381/cds.adbb2d47`, https://cds.climate.copernicus.eu/cdsapp#!/dataset/reanalysis-era5-single-levels?tab=overview.

Heuzé, C. (2021). Antarctic Bottom Water and North Atlantic Deep Water in CMIP6 models. *Ocean Science*, 17(1):59–90, DOI: `10.5194/os-17-59-2021`.

Hilmer, M. and Jung, T. (2000). Evidence for a recent change in the link between the North Atlantic Oscillation and Arctic sea ice export. *Geophysical Research Letters*, 27(7):989–992, ISSN: `00948276`, DOI: `10.1029/1999GL010944`.

Holte, J. and Talley, L. (2009). A new algorithm for finding mixed layer depths with applications to argo data and subantarctic mode water formation. *Journal of Atmospheric and Oceanic Technology*, 26(9):1920–1939, ISBN: `0739-0572`, ISSN: `07390572`, DOI: `10.1175/2009JTECHO543.1`, http://journals.ametsoc.org/doi/pdf/10.1175/2009JTECHO543.1.

Huang, C., Qiao, F., and Dai, D. (2014). Evaluating CMIP5 simulations of mixed layer depth during summer. *Journal of Geophysical Research: Oceans*, 119:2568–2582, ISBN: `2169-9291`, ISSN: `21699275`, DOI: `10.1002/2013JC009535`.

Huang, R. X. (2010a). A survey of oceanic circulation theory. In *Ocean circulation: wind-driven and thermohaline processes*, chapter 1.4, pages 45–62. Cambridge University Press, ISBN: `978-0-521-85228-9`.

Huang, R. X. (2010b). Subduction and obduction. In *Ocean circulation: wind-driven and thermohaline processes*, chapter 5.1.5, pages 512–536. Cambridge University Press, Cambridge, United Kingdom, ISBN: `978-0-521-85228-9`.

Huang, R. X. (2010c). The ventilated thermocline. In *Ocean circulation: wind-driven and thermohaline processes*, chapter 4.1.7, pages 315–336. Cambridge University Press, ISBN: `978-0-521-85228-9`.

Huang, R. X. (2015). Heaving modes in the world oceans. *Climate Dynamics*, 45(11-12):3563–3591, ISSN: `14320894`, DOI: `10.1007/s00382-015-2557-6`, http://dx.doi.org/10.1007/s00382-015-2557-6.

Hurrell, J. W. (1995). Decadal Trends in the North Atlantic Oscillation: Regional Temperatures and Precipitation. *Science*, 269(5224):676–679, ISSN: `00368075, 10959203`, http://www.jstor.org/stable/2888966.

Hurrell, J. W., Kushnir, Y., Ottersen, G., and Visbeck, M. (2003). An overview of the north atlantic oscillation. *Geophysical Monograph Series*, 134:1–35, ISBN: `9781118669037`, ISSN: `23288779`, DOI: `10.1029/134GM01`.

Hüttl-Kabus, S. and Böning, C. W. (2008). Pathways and variability of the off-equatorial undercurrents in the Atlantic Ocean. *Journal of Geophysical Research: Oceans*, 113(10):C10018, ISSN: `21699291`, DOI: `10.1029/2007JC004700`.

Imbol Koungue, R. A. and Brandt, P. (2021). Impact of intraseasonal waves on Angolan warm and cold events. *Journal of Geophysical Research: Oceans*, 126:e2020JC017088, DOI: `10.1029/2020JC017088`.

Imbol Koungue, R. A., Rouault, M., Illig, S., Brandt, P., and Jouanno, J. (2019). Benguela Niños and Niñas in forced ocean simulation from 1958 to 2015. *Journal of Geophysical Research: Oceans*, 124(8):5923–5951, DOI: `10.1029/2019JC015013`.

IOC, SCOR, and IAPSO (2010). The international thermodynamic equation of seawater – 2010: Calculation and use of thermodynamic properties. *Intergovernmental Oceanographic Commission, Manuals and Guides No. 56*, (June):1–196, www.TEOS-10.org.

Iselin, C. O. (1939). The influence of vertical and lateral turbulence on the characteristics of the waters at mid-depths. *Eos, Transactions American Geophysical Union*, 20(3):414–417, DOI: `10.1029/TR020i003p00414`.

Ito, T., Long, M. C., Deutsch, C., Minobe, S., and Sun, D. (2019). Mechanisms of Low-Frequency Oxygen Variability in the North Pacific. *Global Biogeochemical Cycles*, 33(2):110–124, ISSN: `19449224`, DOI: `10.1029/2018GB005987`.

Jarre, A., Hutchings, L., Kirkman, S. P., Kreiner, A., Tchipalanga, P. C., Kainge, P., Uanivi, U., van der Plas, A. K., Blamey, L. K., Coetzee, J. C., Lamont, T., Samaai, T., Verheye, H. M., Yemane, D. G., Axelsen, B. E., Ostrowski, M., Stenevik, E. K., and Loeng, H. (2015). Synthesis: Climate effects on biodiversity, abundance and distribution of marine organisms in the Benguela. *Fisheries Oceanography*, 24(S1):122–149, ISSN: `13652419`, DOI: `10.1111/fog.12086`.

Jiang, N. and Zhu, C. (2020). Tropical Pacific cold tongue mode triggered by enhanced warm pool convection due to global warming. *Environmental Research Letters*, 15(5):054015, ISSN: `17489326`, DOI: `10.1088/1748-9326/ab7d5e`.

Johnson, G. C., Hosoda, S., Jayne, S. R., Oke, P. R., Riser, S. C., Roemmich, D., Suga, T., Thierry, V., Wijffels, S. E., and Xu, J. (2022). Argo-Two Decades: Global Oceanography, Revolutionized. *Annual Review of Marine Science*, 14:379–403, ISSN: `19410611`, DOI: `10.1146/annurev-marine-022521-102008`.

Johnston, T. M. S. and Rudnick, D. L. (2009). Observations of the transition layer. *Journal of Physical Oceanography*, 39(3):780–797, ISSN: `00223670`, DOI: `10.1175/2008JPO3824.1`.

Jung, T., Hilmer, M., Ruprecht, E., Kleppek, S., Gulev, S. K., and Zolina, O. (2003). Characteristics of the recent eastward shift of interannual NAO variability. *Journal of Climate*, 16(20):3371–3382, ISSN: `08948755`, DOI: `10.1175/1520-0442(2003)016<3371:COTRES>2.0.CO;2`.

Kaminski, A. K., D'asaro, E. A., Shcherbina, A. Y., and Harcourt, R. R. (2021). High-resolution observations of the north pacific transition layer from a Lagrangian float. *Journal of Physical Oceanography*, 51(10):3163–3181, ISSN: `15200485`, DOI: `10.1175/JPO-D-21-0032.1`.

Kara, A. B., Rochford, P. A., and Hurlburt, H. E. (2000). An optimal definition for ocean mixed layer depth. *Journal of Geophysical Research: Oceans*, 105(C7):16803–16821, ISSN: `21699291`, DOI: `10.1029/2000jc900072`.

Karstensen, J. and Quadfasel, D. (2002a). Formation of Southern Hemisphere Thermocline Waters: Water Mass Conversion and Subduction. *Journal of Physical Oceanography*, 32:3020–3038, DOI: `10.1175/1520-0485(2002)032<3020:FOSHTW>2.0.CO;2`.

Karstensen, J. and Quadfasel, D. (2002b). Water subducted into the Indian Ocean subtropical gyre. *Deep-Sea Research Part II: Topical Studies in Oceanography*, 49(7-8):1441–1457, ISSN: `09670645`, DOI: `10.1016/S0967-0645(01)00160-6`.

Ke-xin, L. and Fei, Z. (2022). Effects of a freshening trend on upper-ocean stratification over the central tropical Pacific and their representation by CMIP6 models. *Deep-Sea Research Part II: Topical Studies in Oceanography*, 195(October 2021):104999, ISSN: `09670645`, DOI: `10.1016/j.dsr2.2021.104999`, https://doi.org/10.1016/j.dsr2.2021.104999.

Keeling, R. F., Körtzinger, A., and Gruber, N. (2010). Ocean deoxygenation in a warming world. *Annual Review of Marine Science*, 2(1):199–229, ISSN: `19411405`, DOI: `10.1146/annurev.marine.010908.163855`.

King, R. R., Lea, D. J., Martin, M. J., Mirouze, I., and Heming, J. (2020). The impact of Argo observations in a global weakly coupled ocean–atmosphere data assimilation and short-range prediction system. *Quarterly Journal of the Royal Meteorological Society*, 146(726):401–414, ISSN: `1477870X`, DOI: `10.1002/qj.3682`.

Kolodziejczyk, N., Llovel, W., and Portela, E. (2019). Interannual Variability of Upper Ocean Water Masses as Inferred From Argo Array. *Journal of Geophysical Research: Oceans*, 124(8):6067–6085, ISSN: `21699291`, DOI: `10.1029/2018JC014866`.

Kopte, R., Brandt, P., Claus, M., Greatbatch, R. J., and Dengler, M. (2018). Role of equatorial basin-mode resonance for the seasonal variability of the Angola Current at 11°S. *Journal of Physical Oceanography*, 48(2):261–281, ISSN: `15200485`, DOI: `10.1175/JPO-D-17-0111.1`.

Kopte, R., Brandt, P., Dengler, M., Tchipalanga, P. C., Macuéria, M., and Ostrowski, M. (2017). The Angola Current: Flow and hydrographic characteristics as observed at 11°S. *Journal of Geophysical Research: Oceans*, 122(2):1177–1189, ISSN: `21699291`, DOI: `10.1002/2016JC012374`.

Kuhlbrodt, T., Griesel, A., Montoya, M., Levermann, A., Hofmann, M., and Rahmstorf, S. (2007). On the driving processes of the Atlantic meridional overturning circulation. *Reviews of Geophysics*, 45(2):RG2001, ISSN: `87551209`, DOI: `10.1029/2004RG000166`.

Kwiatkowski, L., Torres, O., Bopp, L., Aumont, O., Chamberlain, M., R. Christian, J., P. Dunne, J., Gehlen, M., Ilyina, T., G. John, J., Lenton, A., Li, H., S. Lovenduski, N., C. Orr, J., Palmieri, J., Santana-Falcón, Y., Schwinger, J., Séférian, R., A. Stock, C., Tagliabue, A., Takano, Y., Tjiputra, J., Toyama, K., Tsujino, H., Watanabe, M., Yamamoto, A., Yool, A., and Ziehn, T. (2020). Twenty-first century ocean warming, acidification, deoxygenation, and upper-ocean nutrient and primary production decline from CMIP6 model projections. *Biogeosciences*, 17(13):3439–3470, ISSN: `17264189`, DOI: `10.5194/bg-17-3439-2020`.

Lamont, T., Barlow, R. G., and Brewin, R. J. (2019). Long-Term Trends in Phytoplankton Chlorophyll a and Size Structure in the Benguela Upwelling System. *Journal of Geophysical Research: Oceans*, 124(2):1170–1195, ISSN: `21699291`, DOI: `10.1029/2018JC014334`.

Latif, M. (2009). Klimadynamik. In *Klimawandel und Klimadynamik*, chapter 3, pages 82–132. UTB, Stuttgart, ISBN: `978-3-8252-3178-1`.

Latif, M., Bayr, T., Kjellsson, J., Lübbecke, J. F., Nnamchi, H. C., Park, W., Savita, A., Sun, J., Martin, T., and Dommenget, D. (2023). Strengthening atmospheric circulation and trade winds slowed tropical Pacific surface warming. *Communications Earth & Environment*, 4:249, DOI: `10.1038/s43247-023-00912-4`.

Latif, M. and Keenlyside, N. S. (2009). El Niño/Southern Oscillation response to global warming. *Proceedings of the National Academy of Sciences of the United States of America*, 106(49):20578–20583, ISSN: `00278424`, DOI: `10.1073/pnas.0710860105`.

Lavender, K. L., Davis, R. E., and Owens, W. B. (2000). Mid-depth recirculation observed in the interior Labrador and Irminger seas by direct velocity measurements. *Nature*, 407(6800):66–69, ISSN: `1476-4687 (Electronic)`, DOI: `10.1038/35024048`.

Leadbetter, S. J., Williams, R. G., McDonagh, E. L., and King, B. A. (2007). A twenty year reversal in water mass trends in the subtropical North Atlantic. *Geophysical Research Letters*, 34(12):L12608, ISSN: `00948276`, DOI: `10.1029/2007GL029957`.

Levitus, S., Antonov, J. I., Boyer, T. P., Baranova, O. K., Garcia, H. E., Locarnini, R. A., Mishonov, A. V., Reagan, J. R., Seidov, D., Yarosh, E. S., and Zweng, M. M. (2012). World ocean heat content and thermosteric sea level change (0-2000m), 1955-2010. *Geophysical Research Letters*, 39(10):L10603, ISSN: `00948276`, DOI: `10.1029/2012GL051106`.

Li, G., Cheng, L., Zhu, J., Trenberth, K. E., Mann, M. E., and Abraham, J. P. (2020). Increasing ocean stratification over the past half-century. *Nature Climate Change*, 10(12):1116–1123, ISSN: `17586798`, DOI: `10.1038/s41558-020-00918-2`, http://dx.doi.org/10.1038/s41558-020-00918-2.

Li, W., Li, L., Ting, M., and Liu, Y. (2012). Intensification of Northern Hemisphere subtropical highs in a warming climate. *Nature Geoscience*, 5(11):830–834, ISSN: `17520894`, DOI: `10.1038/ngeo1590`, http://dx.doi.org/10.1038/ngeo1590.

Li, Z. (2012). Interannual and decadal variability of the subtropical mode water formation in the South Pacific Ocean. *Ocean Modelling*, 47:96–112, ISBN: `1463-5003`, ISSN: `14635003`, DOI: `10.1016/j.ocemod.2012.02.001`, http://dx.doi.org/10.1016/j.ocemod.2012.02.001.

Lima, D. C., Soares, P. M., Semedo, A., Cardoso, R. M., Cabos, W., and Sein, D. V. (2019a). A Climatological Analysis of the Benguela Coastal Low-Level Jet. *Journal of Geophysical Research: Atmospheres*, 124(7):3960–3978, ISSN: `21698996`, DOI: `10.1029/2018JD028944`.

Lima, D. C., Soares, P. M., Semedo, A., Cardoso, R. M., Cabos, W., and Sein, D. V. (2019b). How Will a Warming Climate Affect the Benguela Coastal Low-Level Wind Jet? *Journal of Geophysical Research: Atmospheres*, 124(9):5010–5028, ISSN: `21698996`, DOI: `10.1029/2018JD029574`.

Liu, H., Yu, L., and Lin, X. (2019). Recent Decadal Change in the North Atlantic Subtropical Underwater Associated With the Poleward Expansion of the Surface Salinity Maximum. *Journal of Geophysical Research: Oceans*, 124(7):4433–4448, ISSN: `21699291`, DOI: `10.1029/2018JC014508`.

Liu, W., Xie, S. P., and Lu, J. (2016). Tracking ocean heat uptake during the surface warming hiatus. *Nature Communications*, 7:10926, ISSN: `20411723`, DOI: `10.1038/ncomms10926`.

Liu, Z., Philander, S. G. H., and Pacanowski, R. C. (1994). A GCM Study of Tropical-Subtropical Upper-Ocean Water Exchange. *Journal of Physical Oceanography*, 24:2606–2623, DOI: `10.1175/1520-0485(1994)024<2606:AGSOTU>2.0.CO;2`.

Llort, J., Lévy, M., Sallée, J. B., and Tagliabue, A. (2019). Nonmonotonic Response of Primary Production and Export to Changes in Mixed-Layer Depth in the Southern Ocean. *Geophysical Research Letters*, 46(6):3368–3377, ISSN: `19448007`, DOI: `10.1029/2018GL081788`.

López-Parages, J., Auger, P.-A., Rodríguez-Fonseca, B., Keenlyside, N., Gaetan, C., Rubino, A., Woldeyes Arisido, M., and Brochier, T. (2020). El Niño as a predictor of round sardinella distribution along the northwest African coast. *Progress in Oceanography*, 186:102341, ISSN: `0079-6611`, DOI: `https://doi.org/10.1016/j.pocean.2020.102341`, https://www.sciencedirect.com/science/article/pii/S007966112030080X.

Lozier, M. S., Dave, A. C., Palter, J. B., Gerber, L. M., and Barber, R. T. (2011). On the relationship between stratification and primary productivity in the North Atlantic. *Geophysical Research Letters*, 38(18):L18609, ISSN: `00948276`, DOI: `10.1029/2011GL049414`.

Lozier, M. S., Leadbetter, S., Williams, R. G., Roussenov, V., Reed, M. S., and Moore, N. J. (2008). The spatial pattern and mechanisms of heat-content change in the North Atlantic. *Science*, 319(5864):800–803, ISSN: `00368075`, DOI: `10.1126/science.1146436`.

Lozier, M. S., McCartney, M. S., and Owens, W. B. (1994). Anomalous Anomalies in Averaged Hydrographic Data*. *Journal of Physical Oceanography*, 24:2624–2638, DOI: `doi:10.1175/1520-0485(1994)024 < 2624:AAIAHD > 2.0.CO;2`.

Lübbecke, J. F., Böning, C. W., Keenlyside, N. S., and Xie, S. P. (2010). On the connection between Benguela and equatorial Atlantic Nios and the role of the South Atlantic Anticyclone. *Journal of Geophysical Research: Oceans*, 115(9):C09015, ISSN: `21699291`, DOI: `10.1029/2009JC005964`.

Lübbecke, J. F., Brandt, P., Dengler, M., Kopte, R., Lüdke, J., Richter, I., Sena Martins, M., and Tchipalanga, P. C. (2019). Causes and evolution of the southeastern tropical Atlantic warm event in early 2016. *Climate Dynamics*, 53(1-2):261–274, ISBN: `0123456789`, ISSN: `14320894`, DOI: `10.1007/s00382-018-4582-8`, http://dx.doi.org/10.1007/s00382-018-4582-8.

Lübbecke, J. F. and McPhaden, M. J. (2012). On the inconsistent relationship between Pacific and Atlantic Niños. *Journal of Climate*, 25(12):4294–4303, ISSN: `08948755`, DOI: `10.1175/JCLI-D-11-00553.1`.

Lukas, R. and Lindstrom, E. (1991). The mixed layer of the western equatorial Pacific Ocean. *Journal of Geophysical Research: Oceans*, 96(S01):3343–3357, DOI: `https://doi.org/10.1029/90JC01951`, https://agupubs.onlinelibrary.wiley.com/doi/abs/10.1029/90JC01951.

Lumpkin, R. and Garzoli, S. (2011). Interannual to decadal changes in the western South Atlantic's surface circulation. *Journal of Geophysical Research: Oceans*, 116(1):C01014, ISSN: `21699291`, DOI: `10.1029/2010JC006285`.

Lumpkin, R. and Speer, K. (2007). Global Ocean Meridional Overturning. *Journal of Physical Oceanography*, 37(10):2550–2562, DOI: `https://doi.org/10.1175/JPO3130.1`, https://journals.ametsoc.org/view/journals/phoc/37/10/jpo3130.1.xml.

Luo, Y., Liu, Q., and Rothstein, L. M. (2009a). Simulated response of North Pacific Mode Waters to global warming. *Geophysical Research Letters*, 36(23):L23609, ISSN: `00948276`, DOI: `10.1029/2009GL040906`.

Luo, Y., Rothstein, L. M., and Zhang, R. H. (2009b). Response of Pacific subtropical-tropical thermocline water pathways and transports to global warming. *Geophysical Research Letters*, 36(4):L04601, ISSN: `00948276`, DOI: `10.1029/2008GL036705`.

Luyten, J., Pedlosky, J., and Stommel, H. (1983). The ventilated thermocline. *Journal of Physical Oceanography*, 13(2):292–309, DOI: `10.1175/1520-0485(1983)013<0292:TVT>2.0.CO;2`.

Maidens, A., Arribas, A., Scaife, A. A., Maclachlan, C., Peterson, D., and Knight, J. (2013). The influence of surface forcings on prediction of the north atlantic oscillation regime of winter 2010/11. *Monthly Weather Review*, 141(11):3801–3813, ISSN: `00270644`, DOI: `10.1175/MWR-D-13-00033.1`.

Malanotte-Rizzoli, P., Hedstrom, K., Arango, H., and Haidvogel, D. B. (2000). Water mass pathways between the subtropical and tropical ocean in a climatological simulation of the North Atlantic ocean circulation. *Dynamics of Atmospheres and Oceans*, 32(3-4):331–371, ISBN: `0377-0265`, ISSN: `03770265`, DOI: `10.1016/S0377-0265(00)00051-8`.

Marshall, J., Kushnir Y., Battisti D., Chang P., Czaja A., Dichson R., Hurrell J., McCartney M., Saravanan R., and Visbeck, M. (2001). North Atlantic climate variability: phenomena, impacts and mechanisms. *International Journal of Climatology*, 21:1863–1898, DOI: `https://doi.org/10.1002/joc.693`.

Marshall, J. and Plumb, R. A. (2008). The wind-driven circulation. In *Atmosphere, Ocean, and Climate Dynamics: An Introductory Text*, chapter 10, pages 197–222. Elsevier Acadamic Press, ISBN: `978-0-12-558691-7`.

Marshall, J. C., Nurser, A. J., and Williams, R. G. (1993). Inferring the subduction rate and period over the North Atlantic. *Journal of Physical Oceanography*, 23(7):1315–1329, ISSN: `00223670`, DOI: `10.1175/1520-0485(1993)023<1315:ITSRAP>2.0.CO;2`.

Martín-Rey, M., Vallès-Casanova, I., and Pelegrí, J. L. (2023). Upper-Ocean Circulation and Tropical Atlantic Interannual Modes. *Journal of Climate*, 36(8):2625–2643, ISSN: `15200442`, DOI: `10.1175/JCLI-D-22-0184.1`.

MathWorks Inc. (2019). Help Center: Makima. https://de.mathworks.com/help/matlab/ref/makima.html.

MATLAB (2019). *9.7.0.1190202 (R2019b).* The MathWorks Inc., Natick, Massachusetts.

McCreary, J. P. and Lu, P. (1994). Interaction between the Subtropical and Equatorial Ocean Circulations: The Subtropical Cell.

McDougall, T. J. and Barker, P. M. (2011). Getting started with TEOS-10 and the Gibbs Seawater (GSW) Oceanographic Toolbox. *SCOR/IAPSO WG 127*, 127:1–28, ISBN: `978-0-646-55621-5`, www.TEOS-10.org.

McDougall, T. J. and Barker, P. M. (2014). Comment on "Buoyancy frequency profiles and internal semidiurnal tide turning depths in the oceans" by B. King et al. *Journal of Geophysical Research: Oceans*, (119):9026–9032, DOI: `10.1002/2014JC010066`.

Munk, W. H. (1950). ON THE WIND-DRIVEN OCEAN CIRCULATION. *Journal of Atmospheric Sciences*, 7(2):80–93, DOI: `https://doi.org/10.1175/1520-0469(1950)007<0080:OTWDOC>2.0.CO;2`, https://journals.ametsoc.org/view/journals/atsc/7/2/1520-0469_1950_007_0080_otwdoc_2_0_co_2.xml.

Nana, H. N., Tanessong, R. S., Tchotchou, L. A., Tamoffo, A. T., Moihamette, F., and Vondou, D. A. (2023). Influence of strong South Atlantic Ocean Dipole on the Central African rainfall's system. *Climate Dynamics*, (Dezfuli 2017), ISBN: `0123456789`, ISSN: `14320894`, DOI: `10.1007/s00382-023-06892-7`, https://doi.org/10.1007/s00382-023-06892-7.

Nnamchi, H. C., Farneti, R., Keenlyside, N. S., Kucharski, F., Latif, M., Reintges, A., and Martin, T. (2023). Pan-Atlantic decadal climate oscillation linked to ocean circulation. *Communications Earth and Environment*, 4(1):121, ISSN: `26624435`, DOI: `10.1038/s43247-023-00781-x`.

Nnamchi, H. C., Li, J., and Anyadike, R. N. (2011). Does a dipole mode really exist in the South Atlantic Ocean? *Journal of Geophysical Research Atmospheres*, 116(15):D15104, ISSN: `01480227`, DOI: `10.1029/2010JD015579`.

NOAA NCEI (2023). North Atlantic Oscillation. https://www.ncei.noaa.gov/access/monitoring/nao/.

Oschlies, A., Brandt, P., Stramma, L., and Schmidtko, S. (2018). Drivers and mechanisms of ocean deoxygenation. *Nature Geoscience*, 11(7):467–473, ISBN: `978-0-7695-4798-5`, ISSN: `17520908`, DOI: `10.1038/s41561-018-0152-2`, http://dx.doi.org/10.1038/s41561-018-0152-2.

Ostrowski, M. and Barradas, A. (2018). Report on the Evolution of the Angolan sardinella Stock in Relation to the Seasonal Coastally Trapped Waves Climatology and Interannual Equatorial Events 1994-2014, Extended Abstract, 2 pp. https://preface.w.uib.no/files/2018/11/PREFACE-D12.4-final-20180501.pdf.

Ostrowski, M., Da Silva, J. C., and Bazik-Sangolay, B. (2009). The response of sound scatterers to El Ninõ- and La Niña-like oceanographic regimes in the southeastern Atlantic. *ICES Journal of Marine Science*, 66(6):1063–1072, ISSN: `10543139`, DOI: `10.1093/icesjms/fsp102`.

Patricola, C. M. and Chang, P. (2017). Structure and dynamics of the Benguela low-level coastal jet. *Climate Dynamics*, 49(7-8):2765–2788, ISBN: `0123456789`, ISSN: `14320894`, DOI: `10.1007/s00382-016-3479-7`.

Peck, M. A., Alheit, J., Bertrand, A., Catalán, I. A., Garrido, S., Moyano, M., Rykaczewski, R. R., Takasuka, A., and van der Lingen, C. D. (2021). Small pelagic fish in the new millennium: A bottom-up view of global research effort. *Progress in Oceanography*, 191:102494, ISSN: `00796611`, DOI: `10.1016/j.pocean.2020.102494`.

Pendergrass, A., Wang, J.-J., and National Center for Atmospheric Research Staff, E. (2020). The Climate Data Guide: GPCP (Monthly): Global Precipitation Climatology Project. https://climatedataguide.ucar.edu/climate-data/gpcp-monthly-global-precipitation-climatology-project.

Perez, R. C., Foltz, G. R., Lumpkin, R., and Schmid, C. (2019). Direct Measurements of Upper Ocean Horizontal Velocity and Vertical Shear in the Tropical North Atlantic at 4°N, 23°W. *Journal of Geophysical Research: Oceans*, 124(6):4133–4151, ISSN: `21699291`, DOI: `10.1029/2019JC015064`.

Peterson, R. G. and Stramma, L. (1991). Upper-level circulation in the South Atlantic Ocean. *Progress in Oceanography*, 26(1):1–73, DOI: `10.1016/0079-6611(91)90006-8`.

Philander, S. G. H. (1983). El Niño Southern Oscillation phenomena. *Nature*, 302(5906):295–301, ISSN: `1476-4687`, DOI: `10.1038/302295a0`, https://doi.org/10.1038/302295a0.

Pinto, J. G. and Raible, C. C. (2012). Past and recent changes in the North Atlantic oscillation. *Wiley Interdisciplinary Reviews: Climate Change*, 3(1):79–90, ISSN: `17577799`, DOI: `10.1002/wcc.150`.

Potts, W. M., Henriques, R., Santos, C. V., Munnik, K., Ansorge, I., Dufois, F., Booth, A. J., Kirchner, C., Sauer, W. H., and Shaw, P. W. (2014). Ocean warming, a rapid distributional shift, and the hybridization of a coastal fish species. *Global Change Biology*, 20(9):2765–2777, ISSN: `13652486`, DOI: `10.1111/gcb.12612`.

Praveen Kumar, B., Vialard, J., Lengaigne, M., Murty, V. S., and McPhaden, M. J. (2012). TropFlux: Air-sea fluxes for the global tropical oceans-description and evaluation. *Climate Dynamics*, 38(7-8):1521–1543, ISSN: `09307575`, DOI: `10.1007/s00382-011-1115-0`.

Qiao, L. and Weisberg, R. H. (1997). The Zonal Momentum Balance of the Equatorial Undercurrent in the Central Pacific. *Journal of Physical Oceanography*, 27(6):1094–1119, ISSN: `00223670`, DOI: `10.1175/1520-0485(1997)027<1094:TZMBOT>2.0.CO;2`.

Qu, T., Zhang, L., and Schneider, N. (2016). North Atlantic Subtropical Underwater and Its Year-to-Year Variability in Annual Subduction Rate during the Argo Period. *Journal of Physical Oceanography*, 46(6):1901–1916, ISSN: `0022-3670`, DOI: `10.1175/jpo-d-15-0246.1`.

Rabe, B., Schott, F. A., and Köhl, A. (2008). Mean Circulation and Variability of the Tropical Atlantic during 1952–2001 in the GECCO Assimilation Fields. *Journal of Physical Oceanography*, 38(1):177–192, ISSN: `0022-3670`, DOI: `10.1175/2007JPO3541.1`, http://journals.ametsoc.org/doi/abs/10.1175/2007JPO3541.1.

Rahmstorf, S. (2002). Ocean circulation and climate during the past 120,000 years. *Nature*, 419(6903):207–214, ISSN: `00280836`, DOI: `10.1038/nature01090`.

Rhein, M., Rintoul, S., Aoki, S., Campos, E., Chambers, D., Feely, R., Gulev, S., Johnson, G., Josey, S., Kostianoy, A., Mauritzen, C., Roemmich, D., Talley, L., and Wang, F. (2013). Observations: Ocean. In Stocker, T., Qin, D., Plattner, G.-K., Tignor, M., Allen, S. K., and Boschung, J., editors, *Climate Change 2013: The Physical Science Basis. Contribution of Working Group I to the Fifth Assessment Report of the Intergovernmental Panel on Climate Change*, pages 255–316. Cambridge University Press, Cambridge, ISSN: `1672-5182`, DOI: `10.1017/CBO9781107415324.010`.

Risien, C. M., Reason, C. J., Shillington, F. A., and Chelton, D. B. (2004). Variability in satellite winds over the Benguela upwelling system during 1999-2000. *Journal of Geophysical Research: Oceans*, 109(3):C03010, ISSN: `21699291`, DOI: `10.1029/2003jc001880`.

Robinson, I. S. (2010). Primary production. In Bondel, P., editor, *Discovering the Ocean from Space: The unique applications of satellite oceanography*, chapter 7.3, pages 255–267. Springer Science & Business Media, Berlin, 1st edition, ISBN: `978-3-540-24430-1`, DOI: `10.1007/978-3-540-68322-3`.

Robson, J., Ortega, P., and Sutton, R. (2016). A reversal of climatic trends in the North Atlantic since 2005. *Nature Geoscience*, 9(7):513–517, ISSN: `17520908`, DOI: `10.1038/ngeo2727`.

Roch, M., Brandt, P., and Schmidtko, S. (2023a). Recent large-scale mixed layer and vertical stratification maxima changes. *Frontiers in Marine Science*, 10:1277316, DOI: `10.3389/fmars.2023.1277316`.

Roch, M., Brandt, P., and Schmidtko, S. (2023b). Software used in "Recent large-scale mixed layer and vertical stratification maxima changes" (Version 3). DOI: `https://doi.org/10.5281/zenodo.8382701`, https://doi.org/10.5281/zenodo.8382701.

Roch, M., Brandt, P., Schmidtko, S., Vaz Velho, F., and Ostrowski, M. (2021). Southeastern Tropical Atlantic Changing From Subtropical to Tropical Conditions. *Frontiers in Marine Science*, 8(November):748383, ISSN: `22967745`, DOI: `10.3389/fmars.2021.748383`.

Rodríguez-Fonseca, B., Suárez-Moreno, R., Ayarzagüena, B., López-Parages, J., Gómara, I., Villamayor, J., Mohino, E., Losada, T., and Castaño-Tierno, A. (2016). A Review of ENSO Influence on the North Atlantic. A Non-Stationary Signal. *Atmosphere*, 7(7):87, ISBN: `2073-4433`, DOI: `10.3390/atmos7070087`.

Roemmich, D., Boebel, O., Freeland, H., King, B., LeTraon, P.-Y., Molinari, R., Owens, W. B., Riser, S., Send, U., Takeuchi, K., and Wijffels, S. (1998). On The Design and Implementation of Argo: A Global Array of Profiling Floats. pages 1–32, https://argo.ucsd.edu/wp-content/uploads/sites/361/2020/05/argo-design.pdf.

Roemmich, D., Church, J., Gilson, J., Monselesan, D., Sutton, P., and Wijffels, S. (2015). Unabated planetary warming and its ocean structure since 2006. *Nature Climate Change*, 5(3):240–245, ISSN: `17586798`, DOI: `10.1038/nclimate2513`.

Roemmich, D., Gilson, J., Sutton, P., and Zilberman, N. (2016). Multidecadal change of the South Pacific Gyre circulation. *Journal of Physical Oceanography*, 46(6):1871–1883, ISSN: `15200485`, DOI: `10.1175/JPO-D-15-0237.1`.

Roemmich, D., Johnson, G., Riser, S., Davis, R., Gilson, J., Owens, W. B., Garzoli, S., Schmid, C., and Ignaszewski, M. (2009). The Argo Program: Observing the Global Oceans with Profiling Floats. *Oceanography*, 22(2):34–43, ISBN: `1042-8275`, ISSN: `10428275`, DOI: `10.5670/oceanog.2009.36`, http://www.aoml.noaa.gov/phod/docs/roemmich_et_al2009.pdf.

Rouault, M. (2012). Bi-annual intrusion of tropical water in the northern Benguela upwelling. *Geophysical Research Letters*, 39(12):L12606, ISSN: `00948276`, DOI: `10.1029/2012GL052099`.

Rouault, M., Illig, S., Bartholomae, C., Reason, C. J., and Bentamy, A. (2007). Propagation and origin of warm anomalies in the Angola Benguela upwelling system in 2001. *Journal of Marine Systems*, 68(3-4):473–488, ISSN: `09247963`, DOI: `10.1016/j.jmarsys.2006.11.010`.

Rouault, M., Illig, S., Lübbecke, J., and Imbol Koungue, R. A. (2018). Origin, development and demise of the 2010–2011 Benguela Niño. *Journal of Marine Systems*, 188(November 2016):39–48, ISSN: `09247963`, DOI: `10.1016/j.jmarsys.2017.07.007`, https://doi.org/10.1016/j.jmarsys.2017.07.007.

Roxy, M. K., Gnanaseelan, C., Parekh, A., Chowdary, J. S., Singh, S., Modi, A., Kakatkar, R., Mohapatra, S., Dhara, C., Shenoi, S. C., and Rajeevan, M. (2020). Indian Ocean Warming. In Krishnan, R., Sanjay, J., Gnanaseelan, C., Mujumdar, M., Kulkarni, A., and Chakraborty, S., editors, *Assessment of Climate Change over the Indian Region: A Report of the Ministry of Earth Sciences (MoES), Government of India*, pages 191–206. Springer Singapore, Singapore, ISBN: `978-981-15-4327-2`, https://doi.org/10.1007/978-981-15-4327-2_10.

Rühs, S., Oliver, E. C., Biastoch, A., Böning, C. W., Dowd, M., Getzlaff, K., Martin, T., and Myers, P. G. (2021). Changing Spatial Patterns of Deep Convection in the Subpolar North Atlantic. *Journal of Geophysical Research: Oceans*, 126(7):e2021JC017245, ISSN: `21699291`, DOI: `10.1029/2021JC017245`.

Sallée, J. B., Pellichero, V., Akhoudas, C., Pauthenet, E., Vignes, L., Schmidtko, S., Garabato, A. N., Sutherland, P., and Kuusela, M. (2021). Summertime increases in upper-ocean stratification and mixed-layer depth. *Nature*, 591(7851):592–598, ISSN: `14764687`, DOI: `10.1038/s41586-021-03303-x`, http://dx.doi.org/10.1038/s41586-021-03303-x.

Sallée, J. B., Shuckburgh, E., Bruneau, N., Meijers, A. J., Bracegirdle, T. J., and Wang, Z. (2013). Assessment of Southern Ocean mixed-layer depths in CMIP5 models: Historical bias and forcing response. *Journal of Geophysical Research: Oceans*, 118(4):1845–1862, ISSN: `21699291`, DOI: `10.1002/jgrc.20157`.

Schlitzer, R. (2021). Ocean Data View. odv.awi.de.

Schmidtko, S., Johnson, G. C., and Lyman, J. M. (2013). MIMOC: A global monthly isopycnal upper-ocean climatology with mixed layers. *Journal of Geophysical Research: Oceans*, 118(4):1658–1672, ISSN: `21699291`, DOI: `10.1002/jgrc.20122`.

Schmidtko, S., Stramma, L., and Visbeck, M. (2017). Decline in global oceanic oxygen content during the past five decades. *Nature*, 542(7641):335–339, ISSN: `14764687`, DOI: `10.1038/nature21399`.

Schott, F. A., Fischer, J., and Stramma, L. (1998). Transports and pathways of the upper-layer circulation in the western tropical Atlantic. *Journal of Physical Oceanography*, 28(10):1904–1928, ISSN: `00223670`, DOI: `10.1175/1520-0485(1998)028<1904:TAPOTU>2.0.CO;2`.

Schott, F. A., McCreary Jr., J. P., and Johnson, G. C. (2004). Shallow Overturning Circulations of the Tropical-Subtropical Oceans. In *Earth's Climate*, pages 261–304. American Geophysical Union (AGU), ISBN: `9781118665947`, DOI: `https://doi.org/10.1029/147GM15`, https://agupubs.onlinelibrary.wiley.com/doi/abs/10.1029/147GM15.

Sérazin, G., Tréguier, A. M., and de Boyer Montégut, C. (2023). A seasonal climatology of the upper ocean pycnocline. *Frontiers in Marine Science*, 10(March):1120112, ISSN: `22967745`, DOI: `10.3389/fmars.2023.1120112`.

Shannon, L. V., Agenbag, J. J., and Buys, M. E. (1987). Large- and mesoscale features of the Angola-Benguela front. *South African Journal of Marine Science*, 5(1):11–34, ISSN: `02577615`, DOI: `10.2989/025776187784522261`.

Shannon, L. V., Boyd, A. J., Brundrit, G. B., and Taunton-Clark, J. (1986). On the Existence of an El Nino-Type Phenomenon in the Benguela System. *Journal of Marine Research*, 44(3):495–520, ISSN: `00222402`, DOI: `10.1357/002224086788403105`.

Siegfried, L., Schmidt, M., Mohrholz, V., Pogrzeba, H., Nardini, P., Böttinger, M., and Scheuermann, G. (2019). *The tropical-subtropical coupling in the Southeast Atlantic from the perspective of the northern Benguela upwelling system*, volume 14. ISBN: `1111111111`, ISSN: `1932-6203`, DOI: `10.1371/journal.pone.0210083`, http://dx.plos.org/10.1371/journal.pone.0210083.

Somavilla, R., González-Pola, C., and Fernández-Diaz, J. (2017). The warmer the ocean surface, the shallower the mixed layer. How much of this is true? *Journal of Geophysical Research: Oceans*, 122(9):7698–7716, ISSN: `21699291`, DOI: `10.1002/2017JC013125`.

Sprintall, J. and Cronin, M. F. (2009). Upper Ocean Vertical Structure. In J.H., S., Thorpe, S., and Turekian, K., editors, *Encyclopedia of Ocean Sciences*, pages 217–224. Academic, San Diego, California, 2 edition, ISBN: `9780123744739`, DOI: `10.1016/B978-012374473-9.00627-5`.

Stommel, H. (1948). The westward intensification of wind-driven currents. *Trans. Am. Geophys. Union*, 29:202–206, DOI: `10.1029/TR029i002p00202`.

Stommel, H. (1979). Determination of water mass properties of water pumped down from the Ekman layer to the geostrophic flow below. *Proceedings of the National Academy of Sciences*, 76(7):3051–3055, DOI: `10.1073/pnas.76.7.3051`.

Stramma, L. and England, M. (1999). On the water masses and mean circulation of the South Atlantic Ocean. *Journal of Geophysical Research: Oceans*, 104(C9):20863–20883, DOI: `10.1029/1999JC900139`.

Sun, Q., Miao, C., Duan, Q., Ashouri, H., Sorooshian, S., and Hsu, K. L. (2018). A Review of Global Precipitation Data Sets: Data Sources, Estimation, and Intercomparisons. *Reviews of Geophysics*, 56(1):79–107, ISSN: `19449208`, DOI: `10.1002/2017RG000574`.

Sverdrup, H. U. (1947). Wind-driven currents in a baroclinic ocean: with Application to the Equatorial Currents of the Eastern Pacific. *Proceedings of the National Academy of Sciences*, 33(11):318–326, DOI: `10.1073/pnas.33.11.318`.

Talley, L. D. (1988). Potential Vorticity Distribution in the North Pacific. *American Meteorological Society*, 18(1):89–106, DOI: `10.1175/1520-0485(1988)018<0089:PVDITN>2.0.CO;2`.

Talley, L. D., Pickard, G. L., Emery, W. J., and Swift, J. H. (2011a). Depth Distribution of Potential Density. In *Descriptive Physical Oceanography - An Introduction*, chapter 4.4.3, pages 97–98. Elsevier, 6 edition, ISBN: `978-0-7506-4552-2`.

Talley, L. D., Pickard, G. L., Emery, W. J., and Swift, J. H. (2011b). Response to Wind Forcing. In *Descriptive Physical Oceanography - An Introduction*, chapter 7.5, pages 196–200. Elsevier, 6 edition, ISBN: `978-0-7506-4552-2`.

Talley, L. D., Pickard, G. L., Emery, W. J., and Swift, J. H. (2011c). S15 Climate and the Oceans. In *Descriptive Physical Oceanography - An Introduction*, chapter S15, pages 1–36. Elsevier, 6 edition, ISBN: `9780080939117`, https://booksite.elsevier.com/DPO/suppchapters.php.

Talley, L. D., Pickard, G. L., Emery, W. J., and Swift, J. H. (2011d). S7 Dynamical Processes for Descriptive Ocean Circulation. In *Descriptive Physical Oceanography - An Introduction*, chapter S7, pages 1–72. Elsevier, 6 edition, ISBN: `9780080939117`, https://booksite.elsevier.com/DPO/suppchapters.php.

Talley, L. D., Pickard, G. L., Emery, W. J., and Swift, J. H. (2011e). Typical Distributions of Water Characteristics - Temperature Distribution of the Oceans. In *Descriptive Physical Oceanography - An Introduction*, chapter 4.2, pages 69–72. Elsevier, 6 edition, ISBN: `978-0-7506-4552-2`.

Talley, L. D., Pickard, G. L., Emery, W. J., and Swift, J. H. (2011f). Typical Distributions of Water Characteristics - Thermocline, Halocline, and Pycnocline. In *Descriptive Physical Oceanography - An Introduction*, chapter 4.2.3, pages 76–79. Elsevier, 6 edition, ISBN: `978-0-7506-4552-2`.

Talley, L. D., Pickard, G. L., Emery, W. J., and Swift, J. H. (2011g). Wind-Driven Circulation: Sverdrup Balance and Western Boundary Currents. In *Descriptive Physical Oceanography - An Introduction*, chapter 7.8, pages 211–216. Elsevier, 6 edition, ISBN: `978-0-7506-4552-2`.

Tanimoto, Y. and Xie, S. P. (1999). Ocean-atmosphere variability over the Pan-Atlantic basin. *Journal of the Meteorological Society of Japan*, 77(1):31–46, ISSN: `00261165`, https://doi.org/10.2151/jmsj1965.77.1_31.

Tchipalanga, P., Dengler, M., Brandt, P., Kopte, R., Macuéria, M., Coelho, P., Ostrowski, M., and Keenlyside, N. S. (2018). Eastern boundary circulation and hydrography off Angola building Angolan oceanographic capacities. *Bulletin of the American Meteorological Society*, 99(8):1589–1605, ISSN: `00030007`, DOI: `10.1175/BAMS-D-17-0197.1`.

Tomczak, M. and Godfrey, J. (1994). Water mass formation, subduction and the oceanic heat budget. In *Regional Oceanography: An Introduction*, chapter 5, pages 51–62. Elsevier, pdf versio edition, https://www.geo.uni-bremen.de/~apau/dynamicclimate/course_materials_2015/Resources/tomczak_godfrey_1994.pdf.

Torralba, V., Doblas-Reyes, F. J., and Gonzalez-Reviriego, N. (2017). Uncertainty in recent near-surface wind speed trends: A global reanalysis intercomparison. *Environmental Research Letters*, 12(11):114019, ISSN: `17489326`, DOI: `10.1088/1748-9326/aa8a58`.

Treguier, A. M., De Boyer Montégut, C., Bozec, A., Chassignet, E. P., Fox-Kemper, B., McC Hogg, A., Iovino, D., Kiss, A. E., Le Sommer, J., Li, Y., Lin, P., Lique, C., Liu, H., Serazin, G., Sidorenko, D., Wang, Q., Xu, X., and Yeager, S. (2023). The mixed-layer depth in the Ocean Model Intercomparison Project (OMIP): impact of resolving mesoscale eddies. *Geoscientific Model Development*, 16(13):3849–3872, ISSN: `19919603`, DOI: `10.5194/gmd-16-3849-2023`.

Trenberth, K. E., Cheng, L., Jacobs, P., Zhang, Y., and Fasullo, J. (2018). Hurricane Harvey Links to Ocean Heat Content and Climate Change Adaptation. *Earth's Future*, 6(5):730–744, ISSN: `23284277`, DOI: `10.1029/2018EF000825`.

Trenberth, K. E. and National Center for Atmospheric Research Staff, E. (2020). The Climate Data Guide: Nino SST Indices (Nino 1+2, 3, 3.4, 4; ONI and TNI). https://climatedataguide.ucar.edu/climate-data/nino-sst-indices-nino-12-3-34-4-oni-and-tni.

Tuchen, F. P., Brandt, P., Hahn, J., Hummels, R., Krahmann, G., Bourlès, B., Provost, C., McPhaden, M. J., and Toole, J. M. (2022a). Two Decades of Full-Depth Current Velocity Observations From a Moored Observatory in the Central Equatorial Atlantic at 0°N, 23°W. *Frontiers in Marine Science*, 9(June):910979, ISSN: `22967745`, DOI: `10.3389/fmars.2022.910979`.

Tuchen, F. P., Brandt, P., Lübbecke, J. F., and Hummels, R. (2022b). Transports and Pathways of the Tropical AMOC Return Flow From Argo Data and Shipboard Velocity

Measurements. *Journal of Geophysical Research: Oceans*, 127(2):e2021JC018115, ISSN: 21699291, DOI: 10.1029/2021JC018115.

Tuchen, F. P., Lübbecke, J. F., Brandt, P., and Fu, Y. (2020). Observed Transport Variability of the Atlantic Subtropical Cells and Their Connection to Tropical Sea Surface Temperature Variability. *Journal of Geophysical Research: Oceans*, 125(12):e2020JC016592, ISSN: 21699291, DOI: 10.1029/2020JC016592.

Tuchen, F. P., Lübbecke, J. F., Schmidtko, S., Hummels, R., and Böning, C. W. (2019). The Atlantic Subtropical Cells Inferred from Observations. *Journal of Geophysical Research: Oceans*, 124(11):7591–7605, ISSN: 21699291, DOI: 10.1029/2019JC015396.

Tuchen, F. P., Perez, R. C., Foltz, G. R., Brandt, P., and Lumpkin, R. (2022c). Multidecadal Intensification of Atlantic Tropical Instability Waves. *Geophysical Research Letters*, 49(22):e2022GL101073, ISSN: 19448007, DOI: 10.1029/2022GL101073.

Venegas, S. A., Mysak, L. A., and Straub, D. N. (1997). Atmosphere-ocean coupled variability in the South Atlantic. *Journal of Climate*, 10(11):2904–2920, ISSN: 08948755, DOI: 10.1175/1520-0442(1997)010<2904:AOCVIT>2.0.CO;2.

Vincent, E., Emanual, K., Lengaigne, M., Vialard, J., and Madec, G. (2014). Influence of upper ocean stratification interannual variability on tropical cyclones. *Jounral of Advances in Modeling Earth Systems*, 6:680–699, DOI: 10.1002/2014MS000327.

Visbeck, M. H., Hurrell, J. W., Polvani, L., and Cullen, H. M. (2001). The North Atlantic oscillation: Past, present, and future. *Proceedings of the National Academy of Sciences of the United States of America*, 98(23):12876–12877, ISSN: 00278424, DOI: 10.1073/pnas.231391598.

Wang, C., Deser, C., Yu, J.-Y., DiNezio, P., and Clement, A. (2017). El Niño and Southern Oscillation (ENSO): A Review. In Glynn, P. W., Manzello, D. P., and Enochs, I. C., editors, *Coral Reefs of the Eastern Tropical Pacific. Coral Reefs of the World*, pages 85–106. Springer Netherlands, Dordrecht, ISBN: 978-94-017-7499-4, https://doi.org/10.1007/978-94-017-7499-4_4.

Wanner, H., Brönnimann, S., Casty, C., Gyalistras, D., Luterbacher, J., Schmutz, C., Stephenson, D., , and Xoplaki, E. (2001). North Atlantic Oscillation - Concepts and Studies. *Surveys in Geophysics*, 22(4):321–382, DOI: 10.1023/A:1014217317898.

Wentz, F., Scott, J., Hoffman, R., Leidner, M., Atlas, R., and Ardizzone, J. (2015). Remote Sensing Systems Cross-Calibrated Multi-Platform (CCMP) 6-hourly ocean vector wind analysis product on 0.25 deg grid, Version 2.0. *Remote Sensing Systems, Santa Rosa, CA*, www.remss.com/measurements/ccmp.

Williams, R., Marshall, J., and Spall, M. A. (1995). Does Stommel's mixed layer "demon" work? *Journal of Physical Oceanography*, 25(12):3089–3102, DOI: `10.1175/1520-0485(1995)025<3089:DSMLW>2.0.CO;2`.

Williams, R. G. and Meijers, A. (2019). Ocean Subduction. In Cochran, J. K., Bokuniewicz, H. J., and Yager, P. L., editors, *Encyclopedia of Ocean Sciences (Third Edition)*, pages 141–157. Academic Press, Oxford, third edit edition, ISBN: `978-0-12-813082-7`, DOI: `https://doi.org/10.1016/B978-0-12-409548-9.11297-7`, https://www.sciencedirect.com/science/article/pii/B9780124095489112977.

Williams, R. G., Roussenov, V., Lozier, M. S., and Smith, D. (2015). Mechanisms of heat content and thermocline change in the subtropical and subpolar North Atlantic. *Journal of Climate*, 28(24):9803–9815, ISSN: `08948755`, DOI: `10.1175/JCLI-D-15-0097.1`.

Wind and TAC (2018). WIND_GLO_PHY_CLIMATE_L4_REP_012_003 - Global Ocean Wind L4 Reprocessed Monthl Mean Observations. https://resources.marine.copernicus.eu/?option=com_csw&view=details&product_id=WIND_GLO_PHY_CLIMATE_L4_REP_012_003.

Wüst, G. (1949). Über die Zweiteilung der Hydrosphäre. *Deutsche Hydrografische Zeitschrift*, 2(5):218–225, ISSN: `1616-7228`, DOI: `10.1007/BF02226029`, https://doi.org/10.1007/BF02226029.

Wyrtki, K. (1964). The thermal structure of the eastern tropical Pacific Ocean. *Deutschen Hydrographischen Zeitschrift, Ergänzungsheft A*, 6:84.

Wyville Thomson, C. and Murray, J. (1885). The Voyage of H.M.S. Challenger 1873-1876. Narrative Vol. I. First Part. Chapter III. In *H.M.S. Challenger*. https://archimer.ifremer.fr/doc/00000/4751/.

Xue, T., Frenger, I., Prowe, A. E. F., José, Y. S., and Oschlies, A. (2022). Mixed layer depth dominates over upwelling in regulating the seasonality of ecosystem functioning in the Peruvian upwelling system. *Biogeosciences*, 19(2):455–475, DOI: `10.5194/bg-19-455-2022`, https://bg.copernicus.org/articles/19/455/2022/.

Yamaguchi, R. and Suga, T. (2019). Trend and Variability in Global Upper-Ocean Stratification Since the 1960s. *Journal of Geophysical Research: Oceans*, 124(12):8933–8948, ISSN: `21699291`, DOI: `10.1029/2019JC015439`.

Yu, J.-Y., Campos, E., Du, Y., Eldevik, T., Gille, S. T., Losada, T., McPhaden, M. J., and Smedsrud, L. H. (2020). Variability of the Oceans. In Mechoso, C. R., editor, *Interacting Climates of Ocean Basins: Observations, Mechanisms, Predictability, and*

Impacts, pages 1–53. Cambridge University Press, Cambridge, ISBN: `9781108492706`, DOI: `DOI: 10.1017/9781108610995.002`, https://www.cambridge.org/core/books/interacting-climates-of-ocean-basins/variability-of-the-oceans/3CA161E542A6B5C8E5C70BDBC22119BD.

Yu, L., Jin, X., and Liu, H. (2018). Poleward Shift in Ventilation of the North Atlantic Subtropical Underwater. *Geophysical Research Letters*, 45:258–266, DOI: `10.1002/2017GL075772`.

Yu, L., Jin, X., and Weller, R. A. (2008). Multidecade Global Flux Datasets from the Objectively Analyzed Air-sea Fluxes (OAFlux) Project: Latent and sensible heat fluxes, ocean evaporation, and related surface meteorological variables. Woods Hole Oceanographic Institution. Technical Report January.

Zeng, Z., Brandt, P., Lamb, K. G., Greatbatch, R. J., Dengler, M., Claus, M., and Chen, X. (2021). Three-Dimensional Numerical Simulations of Internal Tides in the Angolan Upwelling Region. *Journal of Geophysical Research: Oceans*, 126(2):e2020JC016460, ISSN: `21699291`, DOI: `10.1029/2020JC016460`.

Zhang, D., McPhaden, M. J., and Johns, W. E. (2003). Observational Evidence for Flow between the Subtropical and Tropical Atlantic: The Atlantic Subtropical Cells*. *Journal of Physical Oceanography*, 33(8):1783–1797, ISSN: `0022-3670`, DOI: `10.1175/2408.1`, http://journals.ametsoc.org/doi/abs/10.1175/2408.1.

Zhao, J. and Johns, W. (2014). Wind-forced interannual variability of the Atlantic Meridional Overturning Circulation at 26.5°N. *Journal of Geophysical Research: Oceans*, 119(1):2403–2419, DOI: `10.1002/ 2013JC009407`.

Zilli, M. T., Carvalho, L. M., and Lintner, B. R. (2019). The poleward shift of South Atlantic Convergence Zone in recent decades. *Climate Dynamics*, 52(5-6):2545–2563, ISBN: `0123456789`, ISSN: `14320894`, DOI: `10.1007/s00382-018-4277-1`, http://dx.doi.org/10.1007/s00382-018-4277-1.

Publications

- **Roch, M.**, Brandt, P., Schmidtko, S., Vaz Velho, F. and Ostrowski, M. (2021). Southeastern Tropical Atlantic Changing From Subtropical to Tropical Conditions. *Front. Mar. Sci.* 8; 748383. doi: 10.3389/fmars.2021.748383

- **Roch, M.**, Brandt, P., and Schmidtko, S. (2023). Recent large-scale mixed layer and vertical stratification maxima changes. *Front. Mar. Sci.* 10; 1277316. doi: 10.3389/fmars.2023.1277316

- **Roch, M.**, Brandt, P., Schmidtko, S., and Tuchen, F. P., (submitted to *Journal of Geophysical Research: Oceans*). Impact of the North Atlantic Oscillation on the decadal variability of the upper subtropical-tropical Atlantic Ocean.

- Brandt, P., Alory, G., Awo, F. M., Dengler, M., Djakouré, S., Imbol Koungue, R. A., Jouanno, J., Körner, M., **Roch, M.**, and Rouault, M. (2023). Physical processes and biological productivity in the upwelling regions of the tropical Atlantic. *Ocean Sci.*, 19; 581–601. doi: 10.5194/os-19-581-2023

Acknowledgements

First, I would like to thank my supervisor Peter Brandt for giving me the opportunity to conduct this thesis as a doctoral researcher within the Physical Oceanography department. I appreciate his great support, expertise and critical advice during my PhD as well as giving me the possibility to join four research cruises since my Master's studies and throughout my PhD. I am also very grateful for the productive online meetings we have had during the difficult times of the pandemic.

Second, I would like to thank my co-supervisor Sunke Schmidtko who always provided me very constructive feedback and a great scientific as well as moral support. We had many fruitful scientific discussions and I am very grateful for his patience with me, especially when I had a coding issue. Sunke kept on motivating me and supporting my ideas already since my Bachelor's studies and throughout my Master's studies. I really appreciate the work with him over all those years a lot.

I also want to thank Arne Biastoch and Martin Visbeck for accepting to examine this thesis.

Further, I would like to acknowledge all my colleagues from the Physical Oceanography department for a great support and some good moments throughout the time of my PhD. Special thanks go to Mareike, Tina, Rebecca, Daniel, Léo, Flo and Rodrigue. In particular, I would also like to thank all research cruise members for a really great time at sea. Many thanks go to Rebecca, Tina, Julia, Arthur, Daniel, Philip and Sunke for their truly helpful comments on parts of this thesis.

Moreover, I would like to thank my friends who might not always understood what I am doing but who were morally supporting me anyway. Especially, I also want to thank Neele who is truly the best friend I could wish for and who supported me through all highs and lows.

Finally, I am really grateful and thankful for my parents' support and for their help wherever they could and for giving me the opportunity to do what I dream of. My parents have been motivating and calming me down throughout all times. Thank you for always having my back. Last but not least, I would like to thank Kim for always being there, defying my most odd moods and pushing me to take my sailing, windsurfing and wingfoiling breaks whenever I needed them.

Declaration

I hereby declare that - apart from my supervisor's guidance and acknowledged assistance - the content and design of this thesis is my own work. This thesis has not been submitted either partially or wholly as part of a doctoral degree to another examining body and has not been published or submitted for publication except for the chapters where this is explicitly stated. This thesis has been prepared in accordance with the Rules of Good Scientific Practice of the German Research Foundation. An academic degree has never been withdrawn from me.

Kiel, October 2023, 25.10.2023

(Marisa Roch)